2010-12-16

Chemical and Acoustic Emission Evaluation Studies of Concrete Bridge in Marine Environment

Alexander Boudewijn Suma
University of Miami, alexandersuma@gmail.com

UNIVERSITY OF MIAMI

CHEMICAL AND ACOUSTIC EMISSION EVALUATION STUDIES OF CONCRETE BRIDGE IN MARINE ENVIRONMENT

By

Alexander Boudewijn Suma

A DISSERTATION

Submitted to the Faculty
of the University of Miami
in partial fulfillment of the requirements for
the degree of Doctor of Philosophy

Coral Gables, Florida

December 2010

UNIVERSITY OF MIAMI

A dissertation submitted in partial fulfillment of
the requirements for the degree of
Doctor of Philosophy

CHEMICAL AND ACOUSTIC EMISSION EVALUATION STUDIES OF CONCRETE BRIDGE IN MARINE ENVIRONMENT

Alexander Boudewijn Suma

Approved:

_____
Antonio Nanni, Ph.D.
Professor and Chair of Civil,
Architectural, and
Environmental Engineering

_____
Terri A. Scandura, Ph.D.
Dean of the Graduate School

_____
Brian Metrovich, Ph.D.
Associate Professor of
Civil Engineering
Case Western University

_____
Jacqueline James, Ph.D.
Assistant Professor of
Civil, Architectural, and
Environmental Engineering

_____
Fabio Matta, Ph.D.
Assistant Professor of
Civil and Environmental
Engineering
University of South Carolina

_____
Masoud Sanayei, Ph.D.
Professor in Civil and
Environmental
Engineering
Tufts University

SUMA, ALEXANDER BOUDEWIJN (Ph.D., Civil Engineering)
Chemical and Acoustic Emission Evaluation Studies of Concrete Bridge in Marine Environment. (December 2010)

Abstract of a dissertation at the University of Miami.

Dissertation supervised by Professor Antonio Nanni.
No. of pages in text. (244)

A field investigation of the Fair Isle Bridge, Miami, Florida consists of a nondestructive evaluation program including physical and acoustic emission (AE) assessment. The bridge is situated in a marine environment and its deck consists of PC and RC sections. Chemical evaluation is performed prior to strengthening with CFRP laminates and consists of visual inspection, carbonation, pH evaluation, chloride content, and steel corrosion detection by half-cell potential. After repair, three additional physical assessments are performed: crack mapping, thermography, and AE. These combined techniques provide sufficient information to create layered maps to evaluate the condition of the bridge structure. Within the maps, areas of interest are explored and compared for high probability of corrosion and concrete damage. Through spatial analysis of physical and chemical evaluation data, areas with significant potential difference are identified. These areas are the focus of a load test while monitoring strain, load and AE. The AE program components consist of in-service traffic monitoring and a load test in the elastic range. An experimental program was also conducted in a controlled laboratory environment where beams were subjected to corrosion conditioning and cyclic loading to failure. The NDT methods studied in this thesis are correlated by means of spatial analysis and provide a novel method for field inspections.

With love and gratitude

to my children Sarah & Ruben

and my parents Martin & Yolande

Acknowledgements

During my Ph.D. studies, I spent many moments thinking about how to express my deep appreciation to the exceptional individuals who supported me over the last three years. I have met so many people, with whom I shared many different experiences and who have supported me in many different ways. I speak from personal experience: One cannot complete a Ph.D. study without the help and support of family, friends, and good advisors who challenge and can convince one to keep the faith. I would like to deeply thank these individuals; they all have contributed to this very moment where I find myself in the University of Miami library writing my statement of gratitude after successfully defending my thesis and ending it all with a big smile.

Above all, my two beautiful children, Sarah and Ruben, have made the greatest sacrifice. In their young years of life, they had to miss their father for long periods. Almost every day we had telephone contact, chatted by webcam. Fortunately, I managed to not miss one of their birthdays by flying over to spend time with them. I have seen them grow up as very talented, intelligent, and happy children and have all the confidence they will be very successful in life. I hope that the pursuit of my Ph.D. will serve as an example for them to follow their dreams and to make a contribution to the world with the talents they are given.

My parents, Martin and Yolande, have taught me to be a free thinker and they have believed in me from the beginning. Without their lessons to use my strengths, belief in my capabilities, and their unconditional support, I would never have been able to develop my ambitions. My father's pride and my mum's love have been the one certainty

in life that I could always build on. Our family's typical jokes, but also supportive chats, have been very important. I could also build on my sister, Joyce, and my two brothers, Kevin and Christoffel. Their support during one of the toughest periods of my life will never be forgotten. Chris even came over for several weeks. A special thanks goes to them as it is a treasure to have siblings.

During my Ph.D. study, I was blessed to meet a wonderful person to whom I grew closer and closer. Rossella Ferraro is a very smart and loving person who has not only helped me to keep believing in myself, but has been there for me at every moment where the mountain sometimes seemed too high. Without her, I would not have been able to finish this study. I would like to give her a big kiss and special thanks for being such a strong and beautiful person. Together with little Spartacus, they were my joyful lights.

I would like to give highest appreciation to my advisors, Dr. Antonio Nanni and Dr. Brian Metrovich. They have given me exceptional guidance. On several occasions, I found myself in situations where I needed the type of help which is not typically found on the advisors job description. They never hesitated to be understanding and made extraordinary exceptions to support me in even the most uncommonly difficult situations. Their support has my greatest respect and I am happy that they have become such close friends. Next to my Ph.D. studies, I have worked with Dr. Nanni on many projects and I would like to let him know that I admire him as a person on both a technical and personal level. Appreciation and gratitude also goes to the committee members, Dr. Fabio Matta, Dr. Jacqueline James, and Dr. Masoud Sanayei. Their technical contributions and friendships are gratefully acknowledged. Special appreciation goes to Dr. Sanayei who lifted the level of my study by his guidance during the last months.

I would like to thank the people and institution for their support to make this research possible and especially the National Science Foundation, Doug Ruggiano of Metric Engineering, FYFE Company for supplying strengthening materials, and the Grove Isle Owners Association.

There are a couple of individuals that absolutely deserve to be mentioned. Hetty and Co van de Kreeke have supported me especially in the first and toughest year. Without their exceptional help, I would not have made it. Hetty is not without reason known as “Happy Hetty” and, thanks to Co, I was able to come first time to Miami with a scholarship from the Netherlands Florida Scholarship Foundation in 2007. Mieke Grayson has been the kindest person helping me to travel to my children several times per year. Without her help, I cannot imagine how I would have survived. Dr. Pamela Deroian has become a dear friend and I would like to thank her and Patricia Rodriguez Gilmore for the liberating and positive talks we had throughout the last two years. My sincere gratitude goes also to President Donna Shalala and Dr. Patricia Whitely for their support and trust when it was so much needed. Dr. Monique Bakker and Professor Frans van Herwijnen have guided me through my Master’s studies, and they have also been my examples in Miami.

On activities not directly connected to this study, I was blessed to work with Dr. Bart Chernow, Dr. Elizabeth Fenjves, Dr. Alexey Titov, and Dr. Christine Neipert. Dr. Chernow is a very exceptional individual who I greatly thank for his trust and belief in me. It has been the greatest honor to work with them and I hope we can together continue developing the integrated roof wind energy invention.

Great memories are connected with my time in Miami. I have established many friendships. Sean October has become a very close friend, as well as Angelica Echavarria, Antonio De Luca, Tommy Kiger, Matthew Trussoni, Navid Nem, Tayla Aryai, Daniela Delgado, Carole Kavooras, Bill Jacobs and so many more. Dr. Carol Hays, Dr. Rodrigo Mora, and Dr. Fernando Tinoco are thanked for their support and friendship. My roommate, Nicola Saner, is thanked for all her help during this last semester. I wish her great success in pursuing her business degree. Keen appreciation is felt for the valuable assistance and friendship of especially Derek Schesser and Tom Makowski, and my students Stephanos Stephani, Ben Schulte, Santiago Rodriguez, Caitlin Lundell, Ida Qu, and Brian Law. I have made many more friends with whom I shared wonderful Orange-Green times during UM and ASCE activities, which bring me to my final words: “GO CANES!”

Table of Contents

List of Figures

List of Tables

Chapter 1

1. Introduction

1.1 Preface

Concern about the condition of concrete bridges in the United Stated is an issue that involves safety, high repair cost, and has an immense impact on social wellbeing and economic growth if bridge structures need to be closed or posted [Alkhrdaji and Frye, 2009]. Estimates show that over 180,000 bridges will exceed the age of their design life span of 50 years within the next 15 years [Alampalli et al., 2002]. Today, one in five has already exceeded that age and one in four bridges is rated as deficient, either in need of repair or rehabilitation for increasing traffic loads [AASHTO, 2008]. At the publishing date of the AASHTO Report "Bridging the Gap" in July 2008, the rehabilitation cost of all bridges in the US was estimated up to $140 billion dollars. Similarly in Europe, investigations conclude that bridges from the age of 25 to 35 years show signs of deterioration and major maintenance is required [Colombo et al., 2005].

To contribute to a solution to this worldwide problem, new methods for assessment and monitoring techniques need to be studied. In 2008, a research proposal was funded by the National Science Foundation under the aegis of the [I/UCRC TIE] program to perform a cross-disciplinary integration of knowledge and technology on the physics of bridge damage, bridge load testing and monitoring systems. The case study of a bridge in deteriorated condition in an aggressive marine environment was identified. By combining

experimental non-destructive evaluation (NDE) techniques and making use of a mapping tool, it is intended to spatially verify and correlate the different evaluation results from physical, chemical, and acoustic emission (AE) results.

Routine inspection is the most common form of highway bridge inspection to satisfy the requirements of the National Bridge Inspection Standard [NBIS, 1996; Phares et al., 2004].Routine bridge inspections typically consist of visual inspection [Moore at al., 2001]. This method relies heavily on subjective assessments. Nondestructive testing (NDT) methods range from hammer tapping to dynamic load testing and rely on qualitative observations and measurements. Chemical investigation techniques, included in this research, are not part of routine concrete bridge inspections [The Manual for Bridge Evaluation, 2008]. However, corrosion and carbonation are processes of great structural impact. Corrosion of the embedded steel reinforcement ranks among the most significant adversely acting damage mechanisms [Korenska et al., 2008].

One of the novel inspection methods in the area of nondestructive structural health monitoring for bridges is acoustic emission. An AE signal is the generation, propagation and detection of transient elastic strain waves in solid materials as they undergo dislocation, deformation or fracture [Carpinteri et al., 2008]. AE makes use of piezo-electric sensors in passive (receiving) mode where acoustic surface (Rayleigh) waves are recorded as a voltage signal [Matta et al., 2010]. Its usefulness is found in preliminary warning of impending failure or damage progression that may not be detected as effectively through other methods. Sensors can be placed within a certain distance from sensitive areas or other locations of interest for global monitoring, depending on the structure's geometry, material composition and interface conductivity properties.

The AE method is in advanced stage of development for steel structures. However, due to the heterogeneous nature of concrete, further development in accuracy, the ability to identify wave forms, and attenuation of acoustic wave signals is still desired [Colombo et al., 2005; Korenska et al., 2008]. AE has long been used for fatigue, impact loads, stress corrosion and catastrophic crack growth detection and for nearly 60 years in the cracking assessment of ships [Glennie and Summerscales, 1986]. Recently an increasing number of case studies have been performed on concrete bridge structures, but due to the dominant influences of body shapes, mix designs, noise conditions, aggregate sizes, and loading patterns and history, there has been difficulty comparing and creating a fundamental knowledge base. Previous work has been reviewed, where the majority of studies are performed under laboratory conditions on concrete bridge girders [Schechinger and Vogel, 2007; Lovejoy, 2008], which due to shape and size are not comparable to slab structures. However, significant progress has been found in field testing for development and the use of AE together with strain, displacement and load measurement to deploy recognition of AE characteristics like Kaiser and Felicity Effect [ASTM E1316, 2010] in concrete structures [Matta et al., 2010]. More recent applications are found in fatigue evaluations of FRP bridge components [Cole et al., 2006] and the long term live-load monitoring of hybrid FRP bridge structures [Lui and Ziehl, 2009]. Because AE is very sensitive to crack growth it is an ideal candidate for quantifying the effect of damage both prior to and after strengthening. [Ziehl, 2008]. As an inspection method, AE has already been recognized worldwide as the most promising method for the inspection and evaluation of concrete bridge structures [Korenska et al. 2008].

This study contributes to the development and recognition of AE as a structural health monitoring (SHM) system for the assessment of concrete bridges. Through chemical evaluation, visually undamaged areas, both repaired and unrepaired, are compared to provide examples for future studies and inspections. A method used in this investigation is a division of the deck soffit in a 24 by 24 in. [610 by 610 mm] grid. At each grid point, a series of physical and chemical assessment methods are performed before and after repair, and strengthening with Carbon Fiber Reinforced Polymers (CFRP) laminates occurred. Before repair, the bridge deck showed areas with spall of the concrete cover which created the opportunity to perform the following evaluations: visual inspection, concrete carbonation, pH level evaluation, probability of steel corrosion by half-cell potential, and chloride content analysis. After repair, consisting of grout patching and strengthening with two layers CFRP, three additional physical assessments were performed: crack mapping, thermography, and AE attenuation conductivity. The 192 grid points create a map to spatially correlate data collected from chemical evaluations with AE monitoring while sensors are placed on the grid points. Verification and correlation of the chemical and acoustic data is the main goal of this combination of techniques. Additionally, the map offers a visual aid providing an example for future bridge studies. Spatial correlation study is conducted by making use of a statistical method adopted from the field of Geography [Hu et al., 2009]. Supported with numerical evaluation and the software ArcGIS ESRI, areas with high damage potential are identified.

1.3 Objectives

This dissertation consists of three individual studies, where two are related to field investigations and one is performed under laboratory conditions. The overall objectives of this dissertation are to:

- Create and evaluate spatial mapping tools for concrete bridges in marine environments for structural and material deterioration, composed by a pallet of physical and chemical methods and AE;
- Analyze corrosion induced damage in controlled laboratory conditions to develop recognition and prediction of AE patterns;
- Contribute to the improvement of NDE techniques to examine the conditions of concrete bridges for decision making on maintenance, repair and replacement.

1.4 Significance

Contribution to science is made by introducing a mapping technique for a pallet of chemical, physical and AE evaluation methods which are spatially correlated for the assessment of the condition of concrete structures. This investigation provides a case study to indicate and localize deteriorated areas in concrete structures before and after repair with CFRP laminates with a higher level of confidence than single assessments.

1.5 Dissertation Outline

Study I starts with a series of nondestructive chemical investigations before repair where the physical condition of a bridge in marine environment is evaluated and results are mapped in a 24 by 24 in. [610 by 610 mm] grid. The combined results are visually compared to identify areas of potential deterioration. AE monitoring during in-service traffic follows and concentrates on the PC portion of the deck.

Study II includes three additional physical assessment layers conducted after repair and strengthening. Seven layers are combined by numerical and spatial analysis with ArcGIS to identify areas of high potential damage. A crawl speed truck load test at service load level is conducted while monitoring load, strain and AE. Correlation is investigated between strain and AE trends. In addition, statistical parameters for AE activity and intensity are used to localize areas of high stresses and local deteriorated condition in relation to the spatial analysis outcomes.

Study III is performed under laboratory conditions. Three different corrosion stages are induced to assess changes in physical properties and AE attenuation. Spatial analysis is conducted to localize areas of potential damage. After repair and strengthening, the four specimens are subjected to four-point bending testing with increasing load cycles until failure. AE and spatial assessment outcomes are used to indicate inferior areas and are compared to the eventual failure location.

Table 1.1 shows how the outcomes of this research have or will be developed. A total of three journal papers will be submitted to the listed aimed journals. One paper is currently in press as special publication.

Table 1.1 - Overview of publications

Study	Title	Journal	Status
Study I	Non Destructive Evaluation Techniques and Acoustic Emission for Damage Assessment of Concrete Bridge in Marine Environment	ACI-Special Publications	In Press
Study II-1	Probabilistic Identification of Corrosion Damage in a Concrete Deck	Materials in Civil Engineering	Writing
Study II-2	Bridge Load Test of RC Deck Marine Environment	Structural Engineering	Writing
Study III	CFRP Strengthened RC Beams at Different Corrosion Stages	Construction and Building Materials	Writing

Chapter 2

2. Study I – Physical Assessment Studies and In-Service Monitoring with Acoustic Emission

Synopsis

Non-destructive evaluation techniques are used to assess the condition of a 40-year old concrete bridge operating in an aggressive marine environment. The bridge's superstructure includes both reinforced (RC) and prestressed concrete (PC) one-way slabs, and experienced widening, repairs, and recently strengthening by means of externally bonded Carbon Fiber Reinforced Polymer (CFRP) laminates. Phase I of the investigation focuses on evaluating deterioration of concrete and steel reinforcement by means of in-situ and laboratory testing. A 24 in. by 24 in. [610 by 610 mm] grid was marked on the bottom surface of the supporting slabs to map indicators of concrete, corrosion and physical damage. Visual inspection, measurement of carbonation, pH level, chloride content, and active corrosion potential evaluation were implemented and rendered as layered maps to identify areas with high potential damage. Phase II includes acoustic emission (AE) monitoring under service loads. AE Amplitude, Duration, Energy and Number of Hits were analyzed to identify structural activity associated with damage phenomena, such as concrete cracking, slip between corroded reinforcement and surrounding concrete, and debonding of CFRP laminates. The database acquired from Phase I and Phase II was used for damage assessment. Combined results from the

different techniques show promise in determining areas of concern with higher certainty than when using a single measurement technique. Moreover, physical assessment results indicated specific structural elements to be in more severe deteriorated condition and additionally were found to have higher AE signal intensity and activity.

2.1. Background

According to the AASHTO Report "Bridging the Gap" [AASHTO, 2008], bridge rehabilitation costs in the US alone are estimated to exceed $140 billion with numerous bridges reported needing maintenance and repair. To contribute to the solution of this worldwide problem and reduce the likelihood of similar situations in the future, new methods for assessment and monitoring techniques need to be studied. By combining different non-destructive evaluation (NDE) techniques and a spatial mapping tool, the research project presented in Study I introduces the ability to spatially verify and correlate different chemical and physical evaluation results on the condition of a concrete bridge operating in a highly aggressive marine environment and associate them with acoustic emission (AE) parameters acquired through bridge testing. This case study is a contribution towards making field inspection methods more effective, accessible, efficient and economical.

The combination of physical and structural evaluation techniques used in this research are not typically found on the agenda of bridge inspections. However, concrete carbonation and corrosion of the steel reinforcement are physical and chemical processes that may have relevant structural implications. Corrosion is among the most significant adversely acting damage mechanisms [Korenska et al., 2008].

In the case of exposure to marine (chloridic) environments, the likelihood of corrosion damage has high potential. Through physical and chemical assessment, visually damaged and undamaged areas can be investigated for carbonation and active corrosion.

This study presents five physical and chemical evaluation methods performed prior to repair; visual inspection, carbonation detection, active steel corrosion potential, pH level evaluation, and chloride content evaluation. The objective of these studies is to visually compare the layered maps, which contain the results of each layer, to identify areas with high damage potential. As the structure of the PC section of the bridge consists of 8 PC slabs, the comparison is focused on two slabs with different damage potential and similar loading patterns. With support of AE monitoring, these slabs are compared for AE activity and trends to verify the outcomes of the physical and chemical assessment.

2.1.1. Literature Review

An Acoustic Emission (AE) signal is the generation, propagation and detection of transient elastic strain waves in solid materials as they undergo dislocation, deformation or fracture [Carpinteri et al., 2008]. Its usefulness is in the preliminary warning of impending failure that may not be detected as effectively through other methods. AE has long been used for fatigue, impact loads, stress corrosion and catastrophic crack growth detection, and has been applied for nearly 60 years in the cracking assessment of ships [Glennie and Summerscales, 1986]. It is recognized as an effective method for steel structures, but needs to be further investigated for its capabilities in concrete elements. Due to the heterogeneous nature of concrete, accuracy, identification of wave forms, and attenuation of AE wave signals are still areas where development is desirable [Colombo et al., 2005; Korenska et al., 2008]. Recently, an increasing number of case studies have

been performed on concrete bridge structures. However, due to the uniqueness of signal transmission and other characteristics, the effects of mixture design, body shape, size, reinforcement type, aggregate type and size, loading path and history, transducer type and external noise conditions, it is difficult to develop a fundamental knowledge base and therefore more case studies are desirable [Hearn and Shield, 1997]. The majority of previous studies were performed on concrete I-type bridge girders [Schechinger et al., 2007; Lovejoy, 2008], which due to size and shape are not comparable to slab structures. As this study focuses on a one-way slab span, signals from AE data have characteristics due to their travel path through the element which depends on length of path, obstructions due to element shape and material type and density.

2.1.2. Objectives

- Examine physical and chemical evaluation techniques together with AE as non-destructive evaluation techniques for the assessment of physical and structural deterioration of concrete bridges in marine environments;
- Introduce a novel mapping tool that offers spatial verification and correlation of physical and chemical assessment results;
- Identify areas of urgent concern for concrete damage and steel reinforcement corrosion by different layers;
- Employ a case study with AE monitoring to examine the performance after repair with CFRP laminates and to serve as an example study for field structural health monitoring of slab bridges in marine environments regardless of its complexity of different materials, types of concrete mixtures, aggressive marine exposure with the use of a spatial layered mapping tool.

2.1.3. Fair Isle Bridge

The bridge, as the subject of this thesis, is located in Coconut Grove, Florida, along the coastline of Biscayne Bay and is the only connection between the main land and Fair Isle, called The Fair Isle Bridge (Figure 2.1 and Figure 2.2). This bridge is an ideal case for investigating corrosion damage, age deterioration, repairs during life history, and strengthening with CFRP laminates with non-destructive evaluation (NDE) techniques. The bridge super structure consists of reinforced concrete (RC) and prestressed concrete (PC) sections with inspection reports indicating damage due to the corrosion of both prestressed strands and reinforcement bars. This damage is thought to be caused by a combination of the aggressive marine environment air content, spraying of ocean water, contact height from the ocean, and dynamic impact loading. The bridge consists of 28 spans with an overall length of 711 ft. [217m]. The span of interest is Span 28 which is adjacent to the island. This span contains significant visual damage before repair due to the corrosion of the reinforcement and spalling of the concrete cover in critical areas.

The unique and complex structural configuration of the Fair Isle Bridge can best be explained by its history. Original construction and subsequent widening and repairs have been studied through permit plans to determine how the structure was designed, built and modified over time (Table 2.1). The bridge was originally built in 1961, and widened from 22.5 ft. [6.86 m] to 33.25 ft. [10.13 m] in 1972 [Ruggiano, 2008]. The original structure consisted of 9 PC one-way slabs of 30 in. [760 mm] width, 15 in. [380 mm] height, and 3 in. [76 mm] cover, each reinforced with 9 prestressed strands with 0.5 in. [13 mm] diameter. All members are connected with shear keys. The superstructure was expanded on the North side with a RC section having a width of 8.5 ft. [2.6 m], a depth of

18 in. [460 mm] and reinforced with 1.25 in. [32 mm] diameter steel bars spaced at 6 in. [152 mm] on-center. The added RC section was cast between the eight existing PC beams and the ninth PC beam, which was relocated to the North end of the span (Figure 2.3). A 3 in. [76 mm] concrete deck was cast on top of the PC members. The increased structural capacity is substantial if the deck acts compositely with the supporting members; otherwise it only functions to redistribute loads in the transverse direction.

Table 2.1 - Original design, expansions and repair details

	Original Construction 1961	Expansion 1972	Repair 1998	Repair 2008
Total width (ft)	22.5	33.25	No change	No change
Section width (in.)	30	10.75	No change	No change
Section height (in.)	15	18	Repair spall	Repair spalled concrete
Cover (in.)	3	3	Patching	Patching
Top deck [in.]	0	3	Fill cracks	No change
Design	PC	RC	Patching	Patching, CFRP strengthening
Bar diameter (in.)	0.5	1.25	Shear strengthening	Adhesively bonded CFRP laminates
Number of bars/foot	3.6	3	No replacement	No replacement

Repairs were carried out in 1998 and 2008. The first repair consisted of removing loose concrete, adding epoxy coated steel shear reinforcement, and patching with grout. Most recent repair consisted of removing loose concrete and patching, and strengthening the complete deck with two layers of externally bonded CFRP laminates, each with a thickness of 0.04 in. [1.02 mm]. Due to the complex combination of RC and PC structural members, materials and repairs performed at different times, this bridge is an interesting case study; unique in history, but representative for field investigations.

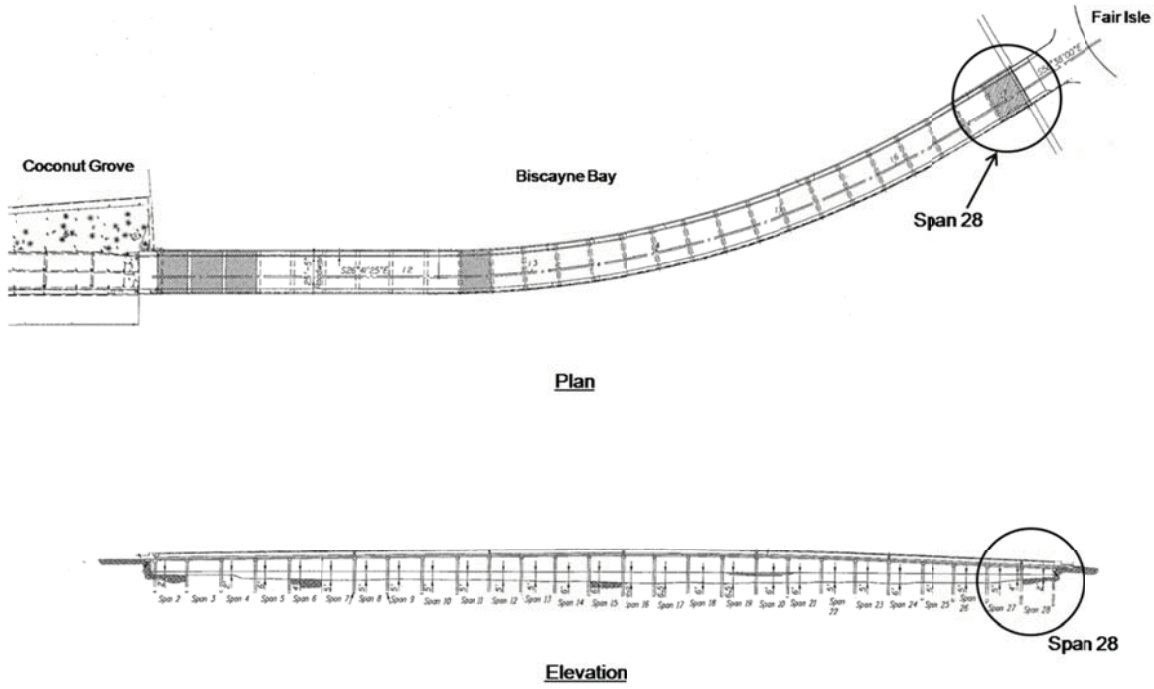

Figure 2.1 - Adopted plan and elevation of Fair Isle Bridge

Figure 2.2 - Fair Isle Bridge from South-East direction

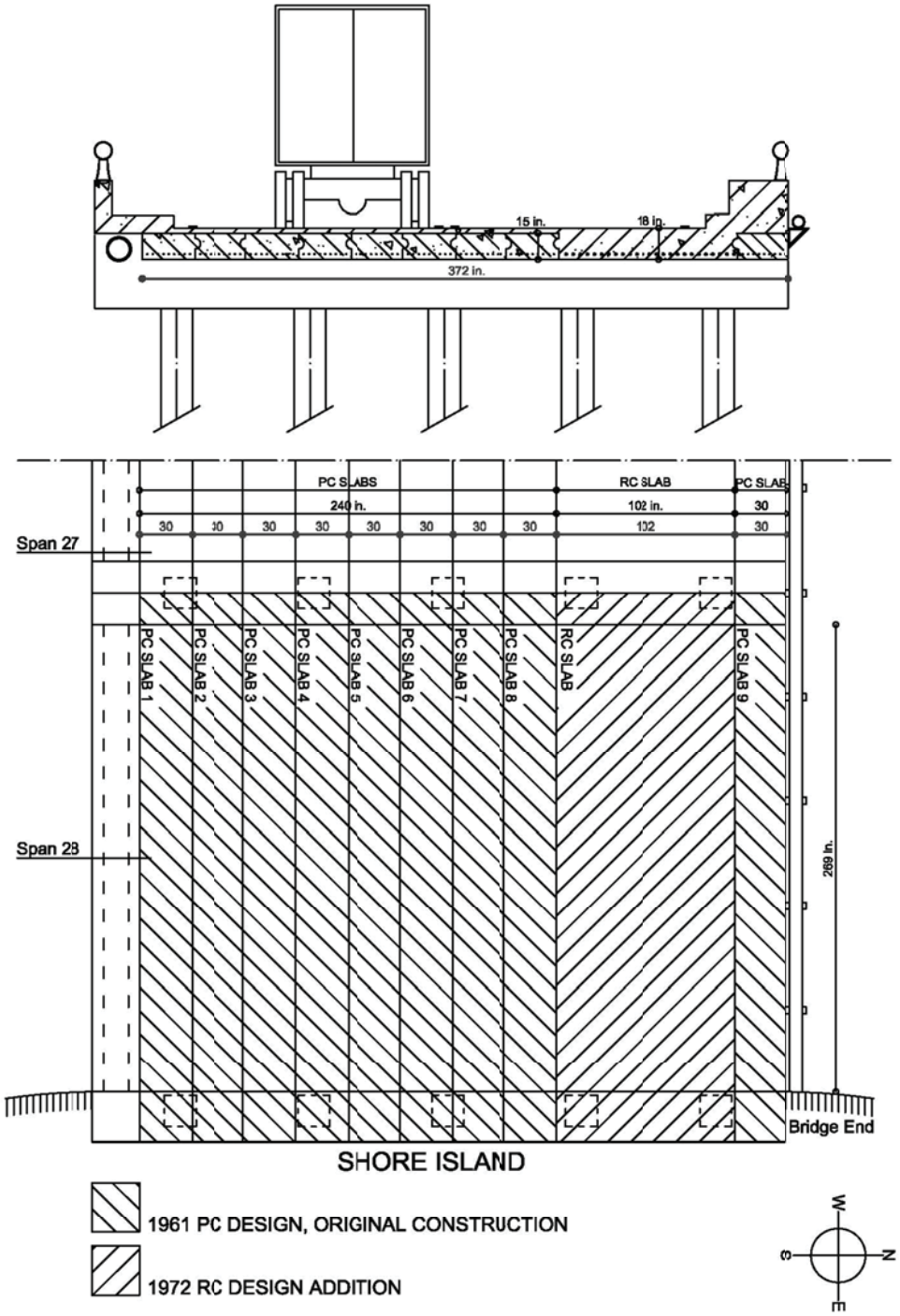

Figure 2.3 - Cross section and plan of PC and RC section

2.2 Phase 1 – Assessment Studies before Repair

The degree of concrete carbonation and steel reinforcement corrosion directly relate to strength and may rapidly deteriorate over time under adverse environments. A 24 by 24 in. [610 by 610mm] grid was marked on the deck soffit of the bridge superstructure for mapping purposes (Figure 2.4). At each of the 192 grid points, chemical and physical NDE field tests as summarized in this section were performed and small samples were collected for laboratory testing. Each implementation of the physical and chemical NDE techniques provides one layer of a superimposed map describing the condition of the superstructure. Together, all layers provide a database suitable for the possibility of visual comparison and spatial correlation of damage (with respect to the marked grid). The NDE field evaluations conducted in Phase I were performed before the damaged members were repaired and then strengthened with externally bonded CFRP laminates to define areas of interest for monitoring by means of AE in Phase II.

2.2.1. Physical Evaluation Methods

The following NDE methods were implemented to address concrete deterioration and steel reinforcement corrosion and are explained in the following paragraphs: (A) visual inspection, (B) evaluation of concrete carbonation, (C) estimation of steel corrosion probability via half-cell potential measurement by in-situ (field) tests, (D) measurement of pH level, and (E) measurement of chloride content by laboratory tests.

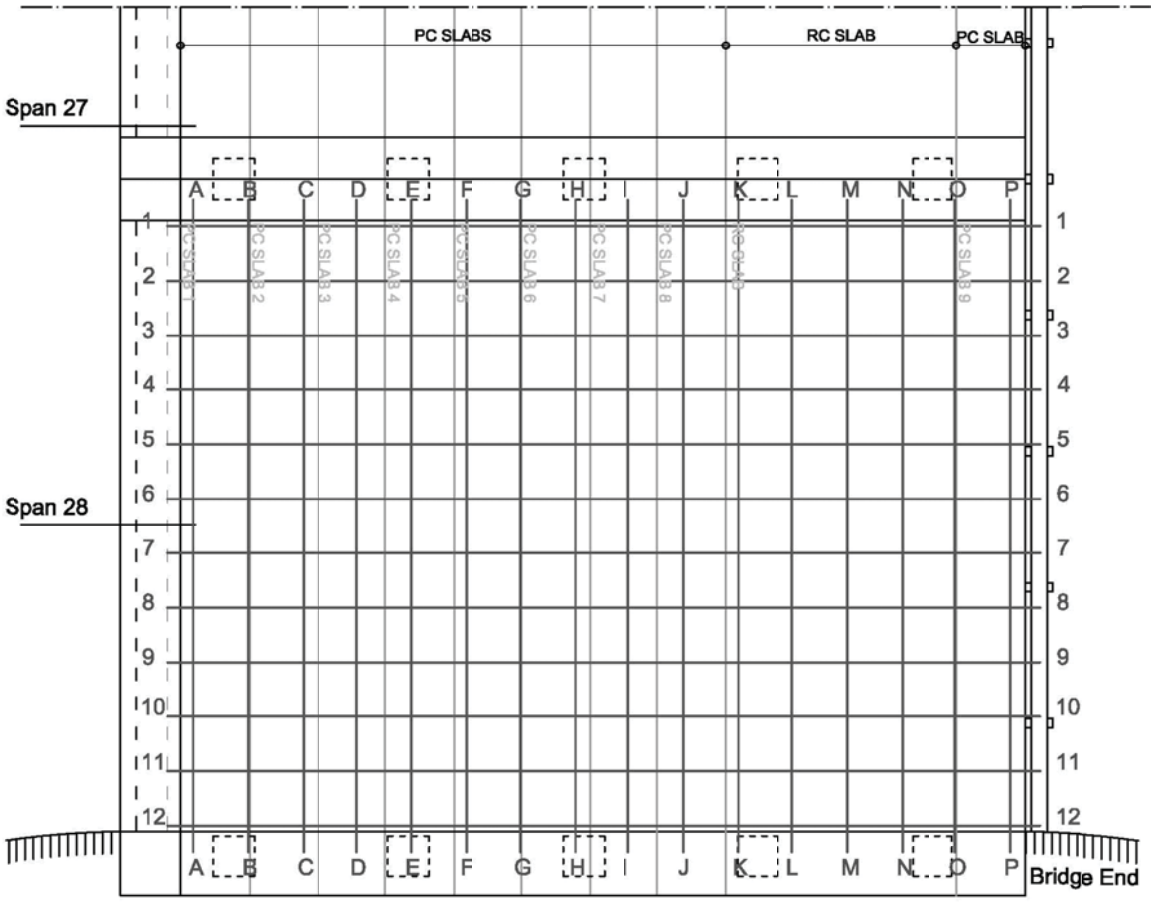

Figure 2.4 - 24 by 24 in. [610 by 610 mm] grid on deck soffit

(A) Visual inspection – A visual inspection was conducted prior to repair to develop a map of cracks, corrosion bleeding, spalling, remaining reinforcement bars and prestressing strands in the areas exposed. Preliminary inspection indicated large pieces of the concrete cover had spall, which allowed for examination of the condition of the exposed reinforcement.

(B) Concrete carbonation – Carbonation is the process of developing calcium carbonate in concrete resulting from the carbon dioxide reacting with concrete caused by the presence of water which results in a less porous but stronger cement paste [Verma and Balasubramaniam, 2009]. However, carbonation creates a reduction of concrete alkalinity and lowers the pH level. This results in protection loss against steel corrosion [Grubb et al., 2007]. Fresh concrete has a pH level of at least 12.5, which creates a passive, protective layer against corrosion as the corrosion process is only able to develop at a pH level below 9 [Matsushita et al., 2000]. Carbonation drops the pH level below the passivation threshold for steel reinforcement; this may result in a pH as low as 7 [Chang and Chen, 2004].

A 1% phenolphthalein in ethanol solution was used to detect carbonation [Minor and White, 1988]. First, the solution was sprayed directly onto the concrete and coloration was captured with photographs, and later visually evaluated and mapped. Sprayed areas turn pink when the pH level exceeds 9, highlighting non-carbonated areas [Otsuki et al., 2003]. Areas where the color does not change are affected by concrete carbonation and have a pH level lower than 9, which indicate a corrosion prone environment.

Spall and removed concrete cover areas offered the opportunity to evaluate carbonation at deeper level in the concrete cover. The findings offer information on large areas about how far the carbonation process was able to develop vertically into the cover.

In the second part of this task, 5 mg samples were taken at each grid point by drilling with a 0.5 in. [13 mm] concrete bit. The drilled holes offered a fresh surface at a depth of approximately 0.2 in. [5 mm]. Again, carbonation traces were captured with photographs and mapped. Similar tests were performed at an average depth of 3 in. [76 mm] in the areas where the concrete was removed for repair work. The outcomes of this study were rendered in a separate layered map.

(C) Steel corrosion potential – The probability of active corrosion of uncoated steel reinforcement was estimated inside the cover by means of half-cell potential measurement using a copper-copper sulfate reference electrode following ASTM C876. The device used was the “James Cor Map” from James Instruments. The reinforcement was directly contacted at one end, and measurements were taken on the concrete surface in the remaining area to measure potential difference. As indicated by Elsener and Böhni [Elsener and Böhni, 1988], there is no indication of active corrosion when values are at measured higher than -200 mV, inconclusive when between -200 and -350 mV, and with 90% probability of active corrosion when less than -350 mV. More negative readings indicate that the reinforcement has more excess electrons and therefore higher likelihood of active corrosion [Malnotra and Carino, 2004]. Three readings were taken, averaged and mapped into a new layer. The concrete cover was partially removed prior to repair operations, providing access to steel reinforcement in each individual slab. This access allowed measurements to be taken even at locations where the cover was still intact.

(D) pH level – Together with the mapping of carbonation and corrosion potential, pH level measurements indicate the extent and depth to which the concrete cover has deteriorated. As the pH level decreases due to exposure to chloride particles from the ocean environment (chloride induced corrosion) [Neville, 1995] and carbon dioxide particles in air (carbonation) [Bary and Sellier, 2004], depassivation of the concrete cover takes place. pH measurements were conducted in agreement with ASTM F 710 [2008; Räsänen and Penttala, 2003]. Powdered samples of 5 mg were obtained by drilling with a 0.5 in. [13 mm] concrete bit at the grid points till a depth of approximately 0.2 in. [5 mm]. Relative to this weight, several drops of distilled water were added and laboratory measurements were taken with paper pH measurement strips from Indigo Instruments with a pH range of 1 to 14. A three-sample average was obtained and mapped into a new layer. The same procedure was carried out at the level of reinforcement (3.0 in. [76 mm] depth) where concrete was removed or spalled.

(E) Chloride content – Corrosion of the steel reinforcement is often caused by exposure to chlorides, typically from contact with deicing salts or marine environments [Sergi and Glass, 2000]. The corrosion level may differ for different concrete mixtures as chloride ions will bond differently [Xinying and Zhang, 2001]. As evaluation of the chloride content provides an estimate of the concentration of chloride particles that have penetrated the concrete cover. The chloride content was compared to evaluations available in open literature [Thomas, 2004; Lindvall, 2007]. Ten single 3 g. samples of size 0.4 by 0.4 in. [10 by 10 mm] were taken only from spalled areas located at the level of reinforcement (3.0 in. [76 mm]) with different material types, design types and repairs, and construction dates. The laboratory analysis was performed according to ASTM

1152M [2004] with “James CL-2000” chloride testing system from James Instruments. The concrete age is important to correlate the analysis outcomes with the degree of carbonation. The found chloride content percentages were mapped into a fifth layered map (E) and compared to those available in literature in relation to depth and construction dates.

2.2.2 Physical Evaluation Results

(A) Visual inspection – Large areas of spalled concrete typically situated at shore end of Span 28 were observed. Cover cracks and steel bleeding were found mainly in this area. It is likely that the dynamic loading of vehicles, which have a relatively greater impact entering and leaving the bridge while accelerating uphill, were the cause of the increased number of cracks. This was observed by the spring action of passing vehicles. Concrete cracks have allowed air and water containing chloride to penetrate which could cause to accelerate corrosion development. In areas where concrete did not spall or was not removed, the concrete cover looked intact and only minor cracks were observed.

Figure 2.5 shows the first layered map (A) with areas of spalled concrete and included the remaining reinforcement bars and prestressed strands present before repair. The PC superstructure was in severe condition and several strands were severely corroded (Figure 2.6). Slab 3 was observed to be in the worst condition, where only two out of nine strands (22%) were found to be intact. The remaining seven strands were corroded and severed completely. The capacity of this member was estimated to be insufficient.

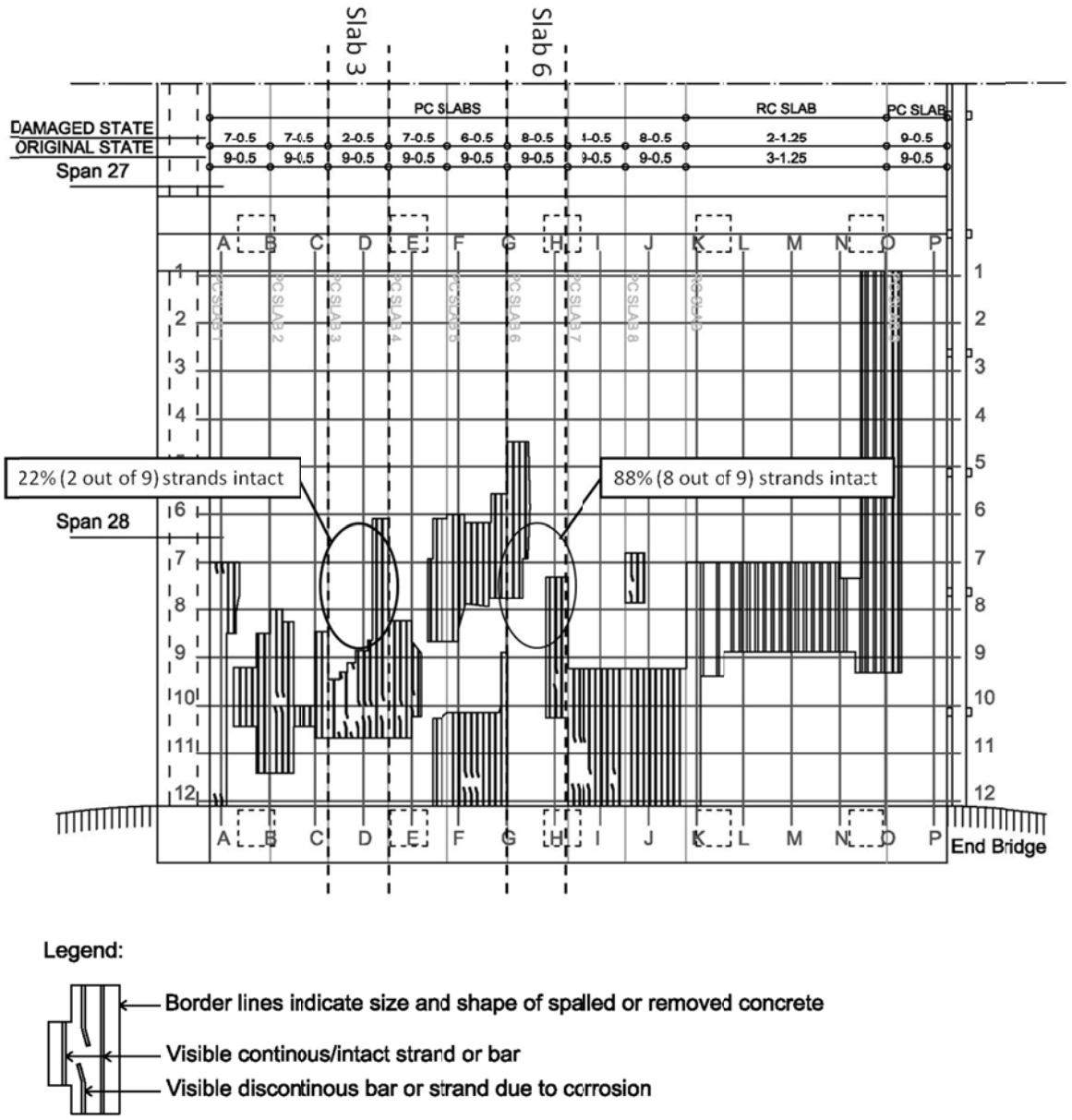

Figure 2.5 - Layer (A): Visual inspection map

Figure 2.6 - Areas with spalled concrete and damaged strands

Figure 2.7 - Field exploration for carbonation detection

The wheels of passing vehicles are typically positioned in a travel lane above slab 3 and 6 (Figure 2.3), as verified during field monitoring (this is key to analyzing AE events considered in this study, as reported in the next section). The NDE results for slab 6 provide a useful dataset for correlating chemical and physical evaluation results with AE monitoring. Figure 2.5 shows slab 6 still has 88% of its strands intact (seven out of nine), with only a few areas of concrete cover spalled over the span length. Visual inspections indicate that slab 6 is in much better condition than slab 3 with a resulting increase in residual strength. Chemical evaluations of carbonation and corrosion potential will be used to assess the validity of the visual inspection outcomes. As the traffic loads are positioned directly on top of these members, the structural response will concentrate on these areas, particularly in the area of maximum moment. This midspan (maximum positive bending moment) zone is a favorable location to mount AE sensors and compare the physical outcomes for these two parent members under similar loads and structural design, but in different states of deterioration.

(B) Concrete carbonation – As the repair work began and the loose concrete was removed, the spraying of 1% phenolphthalein in ethanol solution showed that deeper areas freshly exposed to air did not show as much carbonation as the surface areas (Figure 2.7). In the core of the exposed portion, the pink color indicated that no carbonation developed. This method was shown to be a good tool for preliminary field investigations by its accessibility and ability to provide results quickly.

Freshly exposed surfaces were created by drilling at all grid points to a depth of approximately 0.2 in. [5 mm]. The second layered map (B) (Figure 2.8) shows that areas in the South-East and North-West side indicate presence of carbonation. It is clear that

more carbonation is present in slab 3 than in slab 6. Slab 3 indicates carbonation differently than slab 6, especially at midspan. Additional measurements were taken at greater depth after the concrete cover was removed as part of the repair work. The freshly exposed areas showed only a few carbonated spots on the North-East side, confirming the outcomes of field tests where freshly exposed concrete at the depth of the steel reinforcement had limited carbonated areas.

(C) Steel corrosion potential – The mapped results of steel corrosion potential are given in the third layered map (C) (Figure 2.9). Areas with values less than -350 mV are left blank as there is no indication of active corrosion. Especially on the East side close to the shore support, much active corrosion seems to be present. High corrosion potential is also measured in the North-West section. Both slab 3 and 6 show active corrosion. However, slab 3 has more exceeding values in the center zone till approximately -400 mV. It is likely that the degree of active corrosion is higher in slab 3 [Malhotra and Carino, 2004]. The bottom-up use of the device was experienced as poor and labor-intensive.

(D) pH level – The fourth map contains pH measurement results (Figure 2.10). The map shows several areas on the North-West side to have a pH level of 9 or less. Areas on the East side with lower pH levels are found close to the shore support. Slab 3 has more areas with relatively low pH levels in the maximum moment zone than slab 6. In addition, measurements at the reinforcement depth were taken, with the pH being always higher than 9 (Appendix I.A). These outcomes are consistent with the carbonation map.

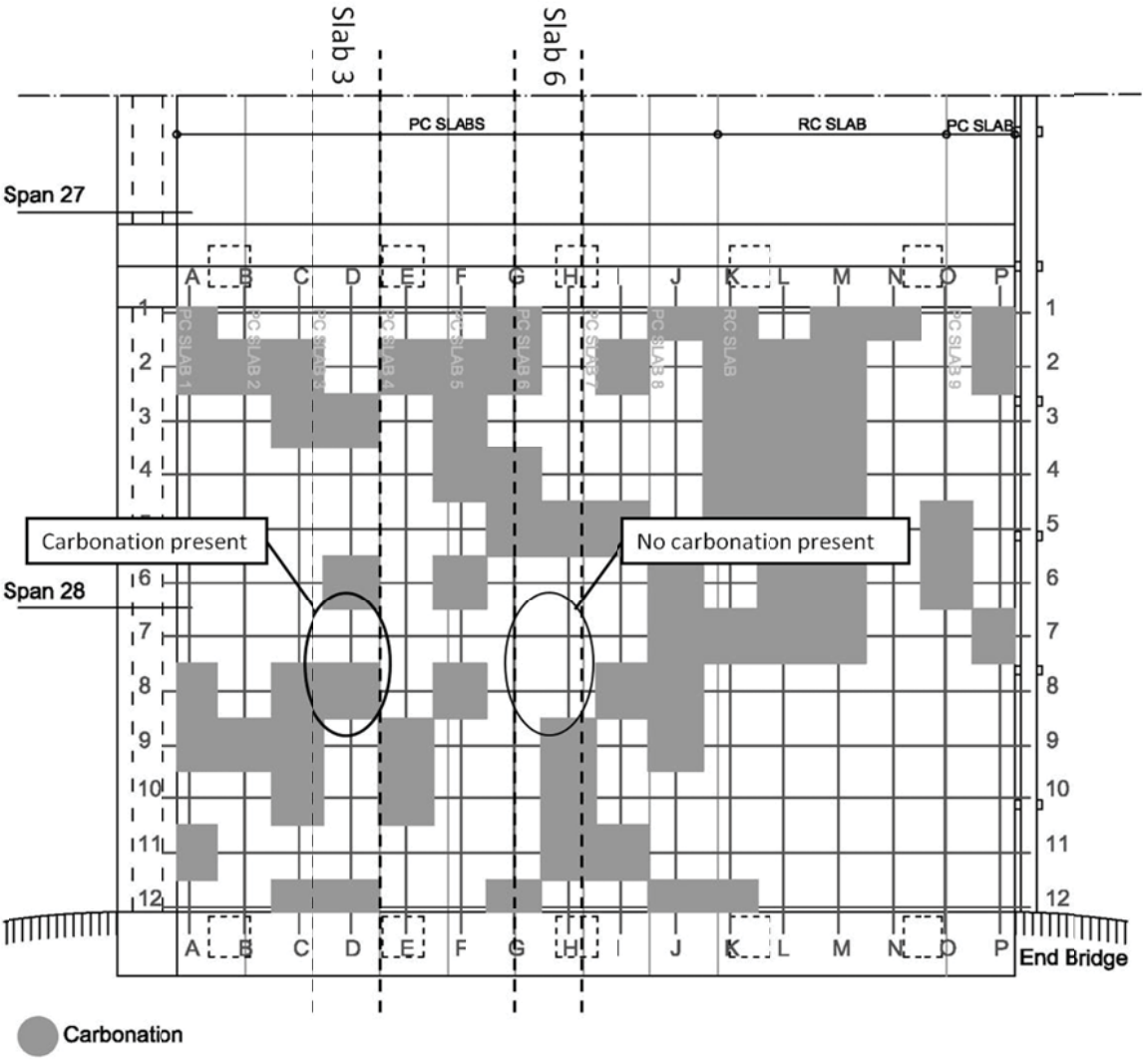

Figure 2.8 - Layer (B): Carbonation map

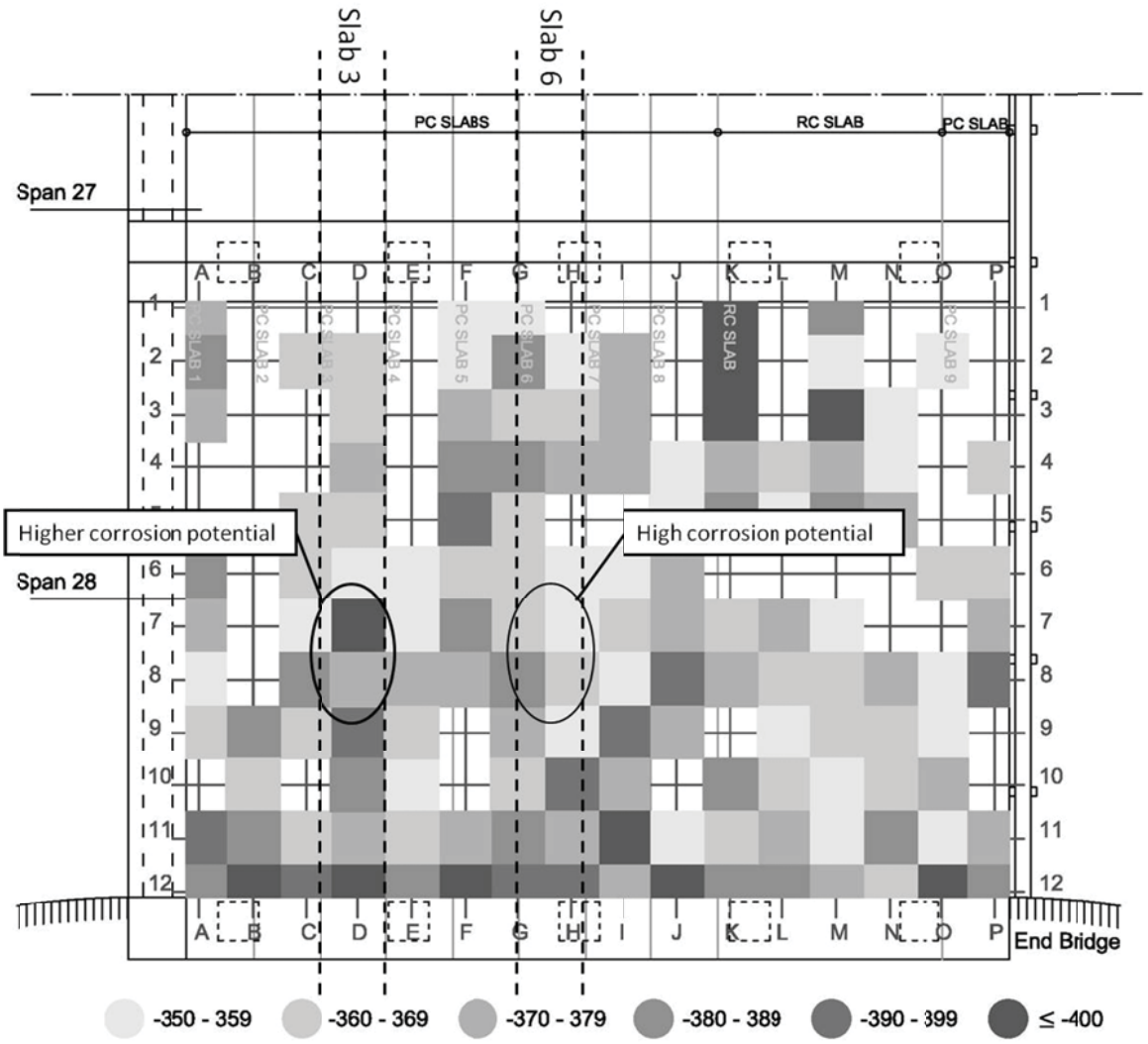

Figure 2.9 - Layer (C): Active steel corrosion potential map

(E) Chloride content – Chloride content results were mapped for ten grid points in the fifth layered map (E) (Figure 2.11). All samples have chloride content above 2% of concrete mass, except sample 7 from the East side of the RC area, and sample 14 from PC slab 5. Results for material type, temperature of prepared specimen and chloride content are reported in Appendix I.B and are in agreement with case studies [Thomas, 2004; Lindvall, 2007], where values ranging from 2.0-3.5% were reported for samples taken at a depth of less than 0.4 in. [10 mm] with marine exposure for more than 10 years and tested at a temperature of about 62°F [20°C]. The resulting map contains a smaller number of samples compared to the other layered maps. This partial information doesn't contradict the collected data in the other assessments and confirms its location with high concentrations of chloride exposure. Samples in this case study showed comparable results at a depth of 3.0 in. [76.2 mm]. No samples were taken from slab 3 and 6 before repair.

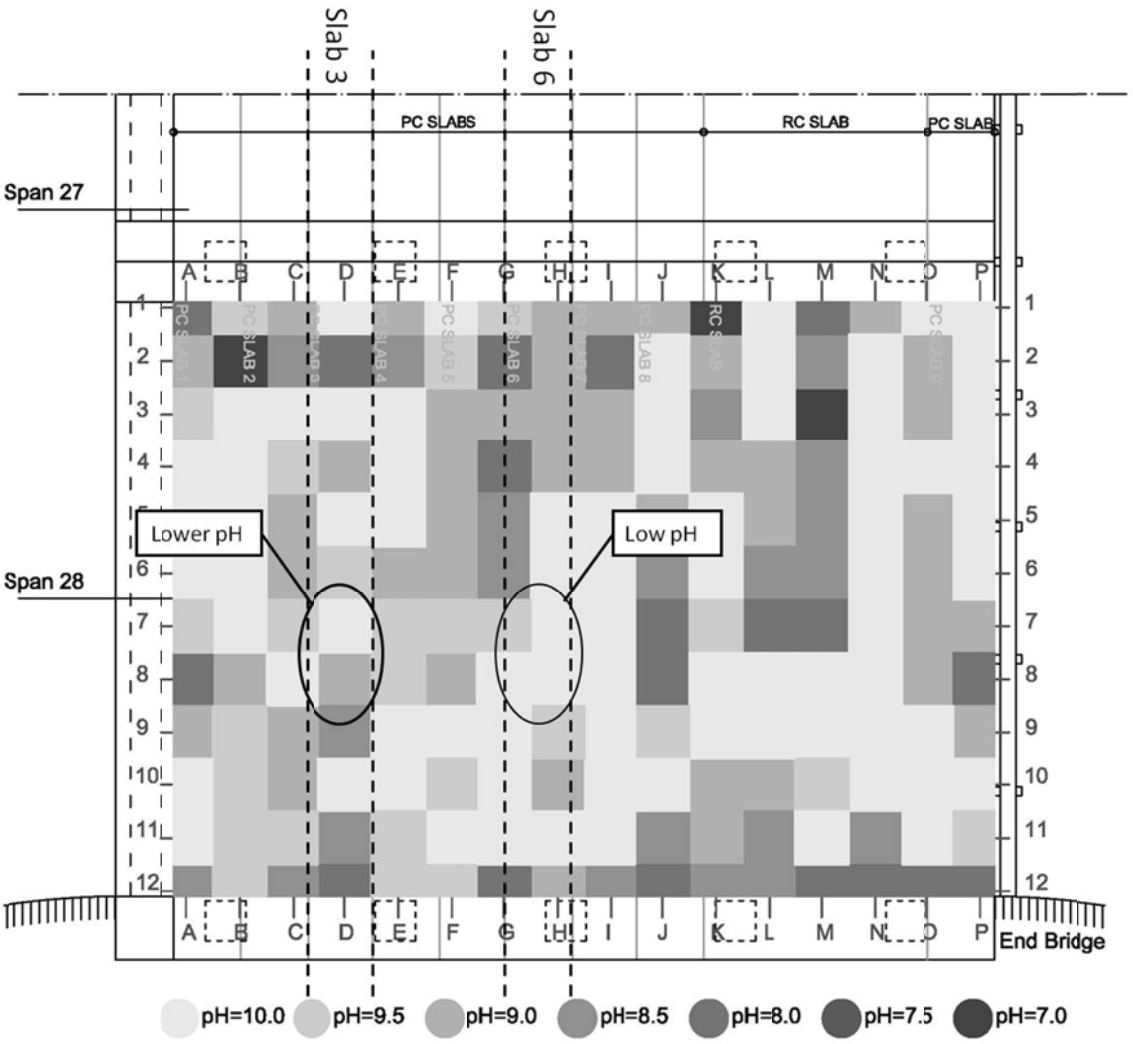

Figure 2.10 - Layer (D): pH level map

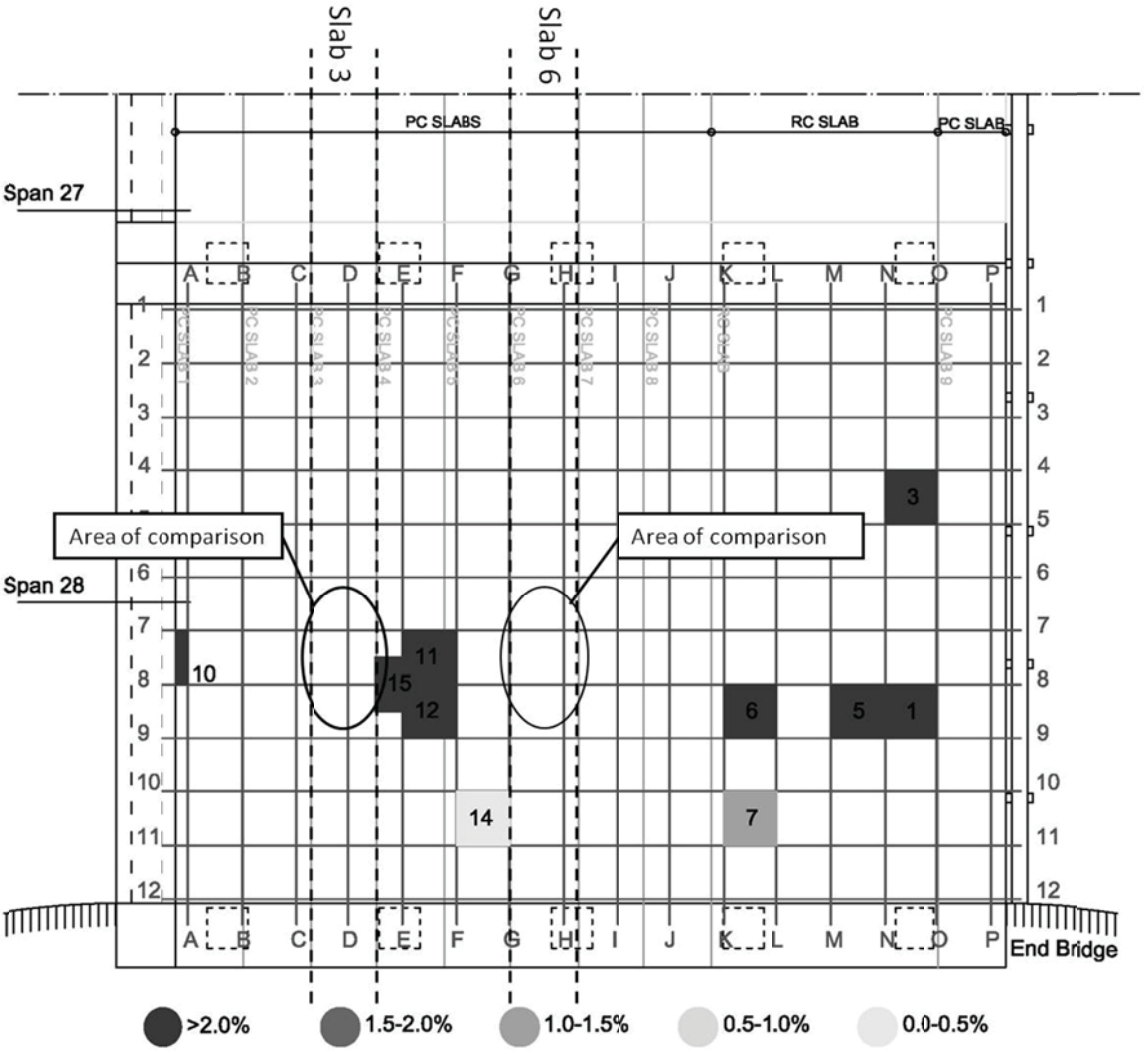

Figure 2.11 - Layer (E): Chloride content map

2.2.3. Discussion of Deteriorated Condition in Slab 3 and 6

Different chemical and physical measurements indicated visual correlation in the layered maps. A 24 in. by 24 in. [610 by 610 mm] grid provides a sufficiently dense grid to evaluate the condition of Span 28. Visual inspection showed similar results with regards to corrosion as the half-cell potential measurements. By visually comparing maps, it can be seen that active corrosion potential also occurs in areas where the cover appears visually undamaged. Carbonation studies provide similar indication as pH level mapping results at the surface and at the depth of reinforcement. In addition, the chloride content of surface samples confirmed the aggressiveness of the marine environment, consistent with the pH level and the carbonation measurements. Finally, carbonated and low pH level areas were strong indicators of areas of active corrosion due to depassivation. An overview of threshold levels to indicate severe conditions related to physical properties is given in Table 2.2

Table 2.2 - Threshold levels indicating corrosion/concrete damage

Layer	Assessment method	Threshold
(A)	Visual Inspection	Bars missing (%)
(B)	Carbonation detection with 1% phenolphthalein in ethanol solution	no pink coloration
(C)	Active steel corrosion potential	< -350 mV
(D)	pH level	≤ 9.0
(E)	Chloride content	> 2%

Areas of maximum positive moment in slab 3 and 6 are selected as focus of study due to their difference in physical and external visual condition, although they experience similar loading patterns and are structurally comparable. After collecting, interpreting and visually comparing layered maps with chemical and physical evaluation outcomes, the

condition of both areas were identified relative to a state of deterioration. To select two areas of interest for this study, all chemical and physical evaluation results were mapped and compared. Visual inspection indicated severe damage on slab 3, where only 22% of the original prestressed strands were left. Slab 6 showed less damage, with 88% of the original prestressed strands remaining intact. The layered carbonation map indicates that slab 3 has carbonated areas at midspan, where slab 6 does not. The third layered map (C) indicated active corrosion potential in both members, with a higher probability of corrosion in slab 3. This beam has areas with pH levels lower than 10 while beam 6 indicated no areas at this level. The chloride content evaluation was not performed on slab 3 and 6. Measurements made close to the areas of interest indicate that the chloride content lies above 2%. By visual analysis and comparison of layered maps, the physical NDE investigation has shown that the midspan region of slab 3 is in a higher level of deterioration than slab 6 indicated by active corrosion potential, carbonation and pH-level.

2.4 Phase 2 - Acoustic Emission

Layered chemical and physical NDE evaluation maps were compared to localized signals from AE monitoring for Phase II. AE monitoring under service loads was conducted after repairs were performed in order to compare areas in different conditions. On several occasions, monitoring was performed for one hour durations at low traffic hours with high loading events. The main purpose of using this combination of techniques is verification and correlation of chemical and acoustic data. Additionally, the maps offer a visual aid, providing the possibility of becoming an example for future bridge studies.

2.4.1 AE Monitoring

In-service AE monitoring concentrated on the PC section of the superstructure, containing eight repaired and strengthened PC one-way slabs. Monitoring was performed using an 8 channel digital AE system, Micro SAMOS (PAC). One piezoelectric resonant sensor type R6I was mounted on each of the 8 PC members in the maximum positive moment zone at midspan on top of the bonded CFRP laminates (Figure 2.3). As selected in Phase I, the areas of interest for AE monitoring lie at the midspan of slab 3 and 6. The CFRP laminates cover the entire span and acoustic waves propagate from the source through the CFRP laminate interface to the sensors. Each sensor was secured in place with aluminum brackets and lightly pushed by a screw against the surface where grease was used as a contact agent (Figure 2.12). AE-Win software was used to collect, decode and process AE data into usable parameters. The AE parameters used for the analysis are: Amplitude, Energy, Duration, and Number of Hits. Together they provide an indication of identifiable event activity. Based on the outcomes of preliminary tests aimed at evaluating the ambient noise level, the AE amplitude threshold was set at 30 dB. Low traffic hours offered identifiable events, in particular from heavy trucks. Time was reported and pictures were taken to estimate the loading level.

During in-service monitoring, several events occurred where high loads may be related to high AE activity. Recorded event data was analyzed and related to log events. Figure 2.13 gives the results recorded for Amplitude versus time for all eight AE sensors. Sensor 7 and 8 were mounted on the last two PC members on the North side (the opposite lane). When identifying events, these beams cannot be taken into consideration as they bear loads for different traffic and are too far away from the monitored event.

Figure 2.12 - AE sensors on deck soffit of the bridge

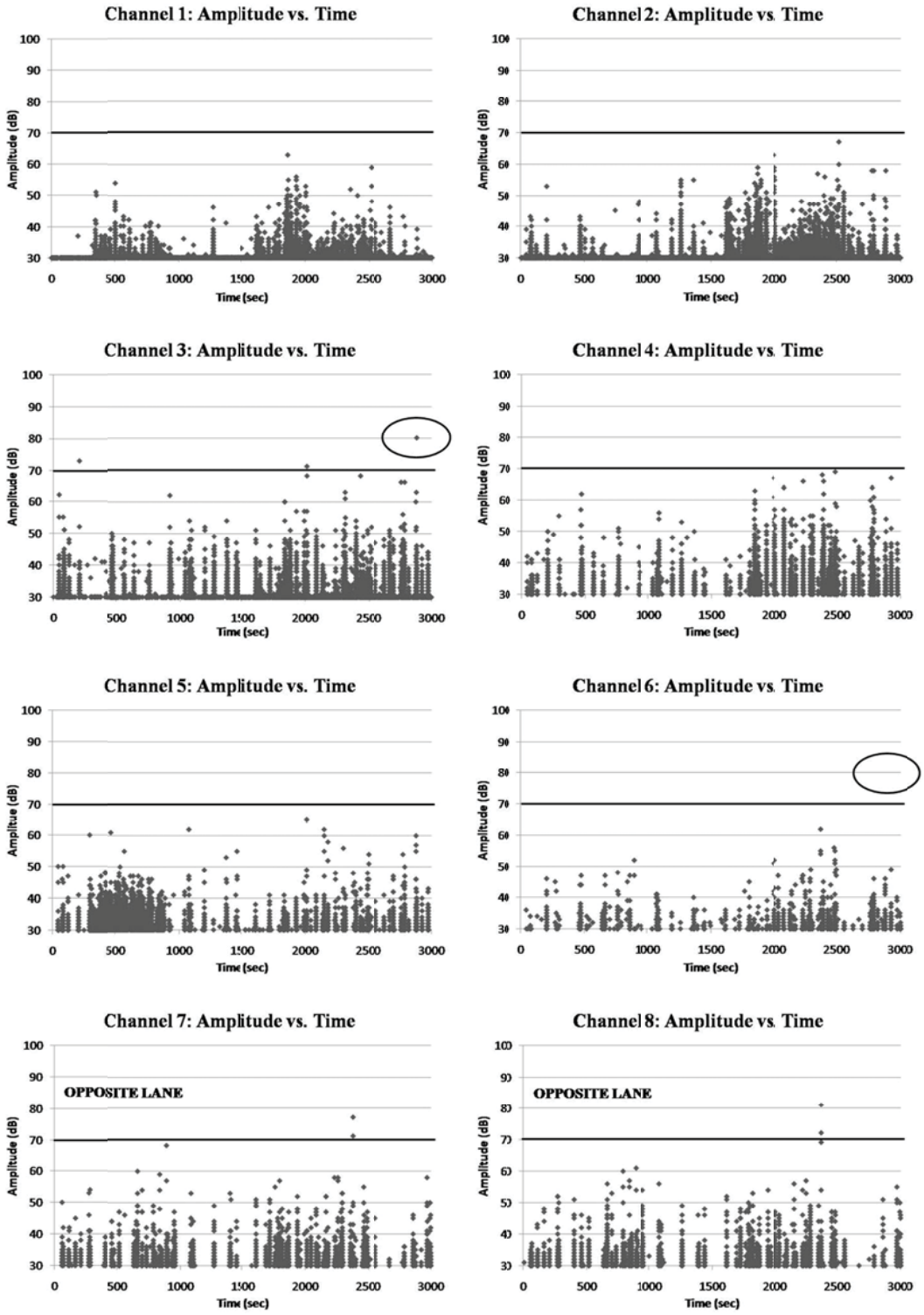

Figure 2.13 - AE Amplitude for sensors 1 to 8

An event at time t = 2,884 seconds, marked with a circle in Figure 2.13, has an Amplitude of approximately 80 dB and consists of 59 hits. The Number of Hits with the same amplitude occurring at the same time, indicate AE activity from the same or close source location [Shigeishi et al., 2001]. The CFRP laminates were applied continuously across the structural elements, allowing signals to travel from one member to the adjacent ones by propagating through the CFRP fiber matrix, depending on the fiber orientation [Degala et al., 2009]. However, previously performed attenuation tests on the bridge indicated that the maximum transmission distance is approximately 2 ft. [610 mm] with acoustic waves attenuating rapidly due to multiple layers of materials including two layers of CFRP laminates. Decreases in AE Amplitude relate to the attenuation properties related to material (propagating medium) and distance. Therefore, it is likely that AE events during monitoring will occur within the sensor capture range as the dominating mechanism is positive bending moment in the midspan zone where the sensor is mounted.

Figure 2.13 shows graphs where Amplitude is plotted against time for comparing results of selected zones on slabs 3 and 6. These graphs indicate that there is relatively more activity and higher peak Amplitudes recorded by sensor 3 on slab 3. A threshold level is drawn in the graphs to point out events with Amplitudes higher than 70 dB. Sensor 3 on slab 3 is the only sensor where signals exceeding 70 dB were recorded during events that were logged as having heavy trucks present.

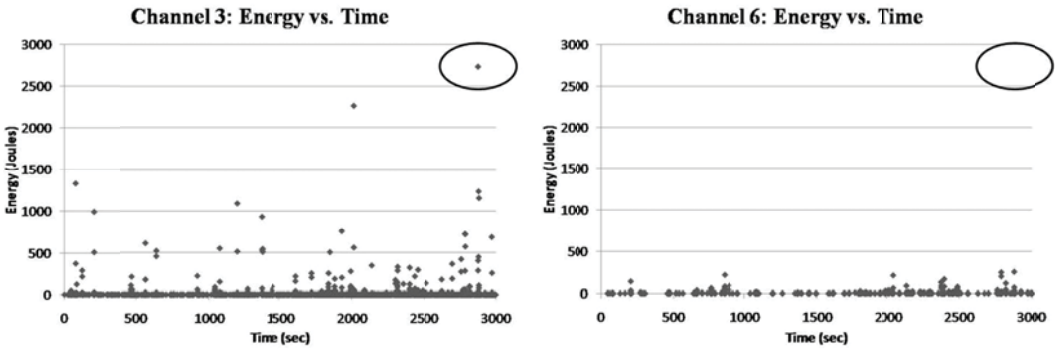

Figure 2.14 - AE Energy vs. Time for sensors 3 and 6

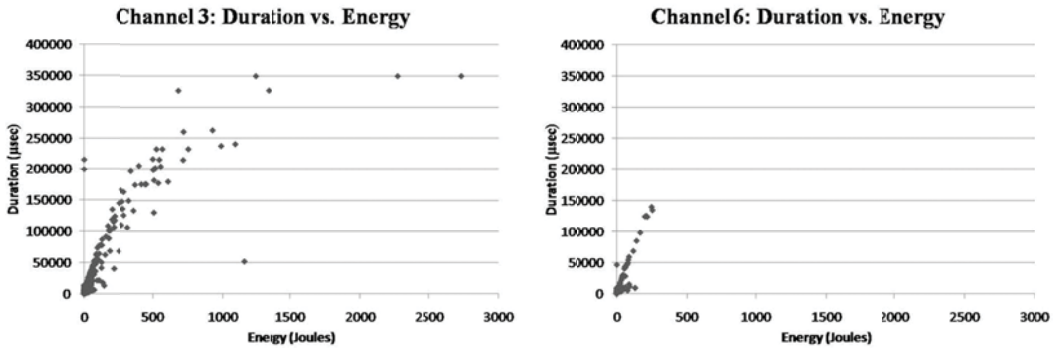

Figure 2.15 - AE Duration vs. Energy for sensors 3 and 6

To identify and verify the intensity of the event at t = 2,884 seconds, the parameters Energy and Duration were also taken into consideration. Figure 2.14 shows plots of Energy against time for slabs 3 and 6. Energy is evaluated as integral of the volt-squared function over time (ASTM E 1316, 2010). These graphs confirm the event intensity in slab 3 by showing that the measured energy value E = 2,736 J is higher than signals recorded by sensor 6 on slab 6. Graphs of slabs 3 and 6 for Duration against Energy are plotted in Figure 2.15. The Duration of the event at t = 28884 seconds is recorded with the highest value of 349 milliseconds in slab 3, confirming a higher intensity for this event in slab 3 relative to slab 6.

2.4.2 Discussion of AE Results

AE monitoring as a NDE method under service loads indicated that PC slab 3 has more acoustic stress wave activity than slab 6 under similar load histories. The AE parameters Amplitude, Energy, Duration and Number of Hits served to isolate meaningful events by activity and intensity. Through preliminary attenuation testing, the Amplitude level indicated that signal sources were most likely situated at midspan of the PC members where the AE sensors were mounted and likely to come from the same slab where data were recorded. Amplitude and Number of Hits were sufficient to identify different levels of activity between slab 3 and 6. Duration and Energy were used to confirm the intensity of events (heavy truck loading), in agreement with field logs. Through the selection of zones of interest in Phase I, effective AE sensor locations were determined. AE signal characteristics and distribution reinforced the observation from Phase I that slab 3 may be in a more deteriorated condition than slab 6. Intense AE activity may have been caused primarily by reduced structural capacity due to corrosion

of the steel reinforcement in slab 3. Due to the reduced contribution of the steel reinforcement, the externally bonded CFRP laminates may carry a larger component of the tensile forces, which may also lead to higher activity and intensity of acoustic events.

2.5 Conclusions

Based on the comparison between physical NDE observations and AE monitoring on a 40 year old concrete bridge operating in a highly aggressive marine environment, the following conclusions are drawn:

- Complexity of different material types, concrete designs and marine exposure deterioration were overcome by using a spatial mapping tool providing possibility for spatial comparison, correlation and visual verification of chemical and physical NDE results;
- Physical relations of carbonation, pH and chloride content were confirmed by visually comparing different layered maps conducted at surface level and deeper reinforcement level. Moreover, together they provide significantly more information about the physical condition than conducting visual inspection only. Additionally, visual inspections and active corrosion potential were related and confirmed by the visual comparison of layered maps;
- Different chemical and physical NDE measurements combined with visual inspection, enabled the identification of regions of structural concern for carbonation and corrosion damage with less uncertainty by visually comparing layered maps;

- Relationship between deteriorated physical and diminished structural conditions of concrete members was shown per location by making use of chemical and physical evaluation and AE monitoring. Moreover, the physical assessment method provides a rational preliminary indication of areas with high AE activity to provide estimates regarding the structural condition and point out locations for AE monitoring;
- AE amplitude and number of hits allowed for identification of events of comparatively high acoustic stress wave activity. Amplitude, duration and energy were used to evaluate the overall intensity of events. The combined evaluation of these AE parameters allowed for the isolation of areas of concern for structural performance;
- CFRP laminates as interface for AE sensors post repair did not prevent nor complicate the effective acquisition and analysis of acoustic data;
- Using spatial visualization, contributions to field inspections and health monitoring was provided for concrete bridges in marine environments by introducing an accessible visual evaluation tool which simplifies decision making on maintenance, repair and replacement of concrete bridge structures and may serve as a practical communication tool;
- Combination of chemical and physical evaluation with AE monitoring offered an improved assessment capability. Through results and analysis, this study serves as a case study for future assessment.

Chapter 3

3. Study II - Probabilistic Identification of Corrosion Damage in a Concrete Deck

Synopsis

A spatial analysis technique is used to combine and evaluate statistical correlations for a range of chemical assessment methods before and after repair of a RC bridge structure to identify areas of concern for corrosion and concrete damage. This method combines results of spatial layered maps such as visual inspection, pH level measurement, concrete carbonation, corrosion potential, chloride content, deck cracks, thermography and acoustic emission (AE) attenuation conductivity and response. A spatial comparison was made through numerical evaluations as well as Geographic Information System (GIS) software ArcGIS. Two structural identical areas for location and loading pattern were identified on the bridge structure where one area was opened, inspected and repaired and the other area remained untouched. After repair, the entire deck soffit was strengthened with two plies of Carbon Fiber Reinforced Polymers (CFRP) laminates. A layered map was created by performing pencil break tests while monitoring AE signals to attempt to evaluate this complex system of different materials, compositions, additions and repairs. The study was followed by a service level truck crawl speed load test at strategic locations on the RC deck to locate active regions for comparison with the chemical evaluation spatial analysis outcomes. Correlation was

found between AE results and strain data. Moreover, areas rated by spatial analysis for highest damage potential identified showed spatial correlation with localized AE statistical indicators in terms of cumulated activity and signal intensity.

3.1 Background

Routine concrete bridge inspections are typically completed using visual inspection and rely heavily on subjective assessments made by bridge inspectors [Phares et al., 2004]. To detect loose fitting concrete in the vicinity of spall areas, hammer tapping or chain dragging is the common method by listening, identifying and localizing hollow sounds [Manual for Bridge Evaluation, 2008]. The deck soffit is visually inspected for cracks, concrete spalls, bleeding and exposed corroded steel reinforcement. When the concrete cover is not spalled, but corrosion of the reinforcement is active and has reached a visually undetectable but concerning state, the currently available inspection methods do not offer indisputable results. As stated in the Manual for Bridge Evaluation published by AASHTO [2008], corrosion detection methods are rated as “good” for electrical methods [ASTM D3633, 2006], “good” beneath bituminous surfacing by sonic techniques [ASTM D4580, 2003], and “good” for detecting delamination through corrosion by thermography [ASTM D4788, 2007] and radar detection. Ultrasonic methods like acoustic emission (AE) monitoring with piezoelectric sensors [ASTM E1316, 2010] are rated as “fair” for corrosion detection.

Different material testing methods have been developed and successfully used to supplement routine field testing methods when more information is desired [Barde et. al., 2009; Cusson et al., 2009; Robertson et al., 2009]. As these methods are complex and often require specialized instrumentation, they are less accessible for routine inspections.

Material testing methods are most often semi-destructive in nature, meaning that small samples have to be collected from the actual structure. In the case of RC bridges, this is usually done in the concrete cover until the reinforcement is reached and, therefore, there is no structural impact if the holes are filled appropriately to prevent chloride penetration. These types of physical and chemical testing methods were performed prior to repair and strengthening and documented in Study I; (A) visual inspection layer, (B) concrete carbonation layer, (C) steel corrosion potential layer, (D) pH level layer, and (E) chloride content layer. The results were mapped in a 24 by 24 in. [610 by 610 mm] grid on the entire span and arranged in separate layers to be overlaid in order to identify areas of structural deficiency. AE monitoring during service verified that more activity was present at locations tagged as most critical by other test methods.

The strengthening repair work of the bridge span includes the application of two plies of Carbon Fiber Reinforced Polymers (CFRP) laminates on the deck soffit to replace and supplement corroded and missing steel reinforcements. As a result, the soffit of the deck is covered and no physical information can be obtained from the concrete substrate without harming the CFRP. In addition to the assessment layers conducted in Study I, three additional layers of nondestructive tests (NDT) are generated to provide more information. Mapping of deck cracks (F) is performed to differentiate areas for crack density and crack direction which may provide information about the loading history, structural mechanism and structural contribution of the deck. Thermography (G) is a method used to identify air voids under FRP laminates.

These voids are considered an application deficiency which speaks for maintenance and repair [Hawkins et al., 1998]. AE conductivity by pencil lead break testing (H) [Hsu, 1976; Nielsen, 1980] offers information about the structure's composition and repair.

As Study I focuses on the Prestressed Concrete (PC) section of the bridge structure, the attention of Study II focuses on the Reinforced Concrete (RC) portion which is located on the North side of the span (Figure 2.3, Study I). By combining the layered maps from Study I and including three extra layers conducted after repair, spatial correlation studies are performed in an attempt to introduce a method that offers more reliable identification of damaged areas. Main objective of this study is to create and test improved evaluation methods using mapping techniques, and to introduce a tool for decision making on maintenance, repair and replacement of concrete bridges.

3.1.1 Literature Review

Several techniques that go beyond the scope of routine field testing [The Manual for Bridge Evaluation, 2008] have been included to spatially identify areas for structural or physical diminished conditions. Among others, one of the successful methods is damage localization and quantification using non-destructive load tests to minimize the residuals of analytical and measured strains to update FEM models for localizing damaged areas [Sanayei et al., 1996; Sanayei et al., 2006; Santini-Bell et al., 2007]. This method is identified as complementary to visual inspection and other NDT techniques. Another successful spatial investigation method is half-cell potential mapping of concrete slabs to identify areas with high probability of active corrosion [ASTM C876, 2009]. Spatial corrosion potential maps in color plots are shown by Elsener et al., [2003] and supply an accessible and interpretable tool for inspectors in the field. However, Gulikers and

Elsener [2009] acknowledge the debate on the appropriate level of confidence to allow for distinction between passively and actively corroding steel, as they introduce a more reliable statistical treatment to indicate areas with active steel corrosion. Huston et al., 2007 studied the physical condition of two case study bridges by visually comparing and overlaying maps of Ground Penetrating Radar (GRP), acoustic elastodynamic measurement in the form of Impact Echo (IE), and corrosion potential mapping to indicate the bridge condition and detect delaminations. These studies and methods offer well developed tools to give information about the structural and physical condition of a concrete structure. The presented study aims to complement existing evaluation methods by introducing a higher level of confidence that combines physical assessment studies using spatial analysis to localize areas with high probability for concrete and corrosion damage.

Spatial analysis is defined as a formal technique to study entities using their topological, geometric, or geographic properties [O'Sullivan et al., 2002; Fotheringham et al., 2002]. A tool to spatially correlate layered maps is available in the field of Geography. The Geographic Information System (GIS) software ESRI ArcGIS was developed to analyze and store geographic maps and to produce predictions with “one click” available statistical analysis tools. GIS was first time used by civil engineers in the 1950’s during a collaborative study of geographers and transportation engineers at the University of Washington [Miles and Ho, 1999]. Today, the software is used for urban planning and decision making [Stevens et al., 2007], earthquake prediction models [Yamazaki, 2001], hydrology [Vafeidis, 2007], emergency planning [Carroll, 2007], traffic analysis [Kumaresan, 2009], and is experiencing rapid development by being

combined with other software programs like Computational Fluid Dynamics (CFD) to create endless possibilities including pollution models in urban areas [Zheng et al., 2010]. However, GIS software is typically used for analysis and identification of trend behavior of large scale areas such as urban areas and nation maps. No study was yet found where the software was used on the scale of a single bridge span to statistically identify areas with corrosion damage.

AE signals (transient elastic waves) are generated in a structure by a rapid release of energy from a localized source or sources within a material [ASTM E1316, 2010]. The subject of study presented is unique for its loading path and history, age, body shape, composition, mixture designs, aggregate type and size, repairs, strengthening, and state of local corrosion deterioration. Today, many damaged bridges are repaired with external CFRP laminates and desire life time AE monitoring to assess delamination and fiber rupture during service [Kaiser and Karbhari, 2004]. This study aims to contribute to the understanding of the unique AE signatures of a repaired and strengthened concrete bridge, and to identify areas with more AE activity, independent of the structures composition or knowledge about its history.

3.1.2 Structure of Study

Part 1 of Study II consists of a spatial analysis of the layered maps introduced in Study I with the inclusion of three new layers performed after repair. The spatial analysis to detect areas of concern for corrosion damage is carried out with guidance of GIS Software and complemented by numerical analysis to identify areas with a higher probability of damage. The second part of Study II consists of observations obtained with a service level load test at strategic locations. Measured and analytical strains are

compared with AE events over time. The intent is to correlate the AE activity response to measured and analytical strains and to evaluate correlation by location with the spatial analysis outcomes of Part 1 of Study II.

3.1.3 Objectives

- Evaluate and compare chemical assessment methods with AE monitoring to localize areas of concern, both repaired and unrepaired, for corrosion and concrete damage;
- Employ statistical spatial analysis to demonstrate the advantages of establishing more statistical confidence on localizing structural and physical properties and to apply a smaller number of AE sensors on predetermined strategic locations;
- Evaluate the potential advantages of pencil lead break testing on complex composed concrete bridge structures with a history of expansion, repairs and strengthening with different materials and structure design types rated for corrosion damage;
- Evaluate correlation between strain and AE activity during a nondestructive isolated load test, both static and ambient at service level loading;
- Evaluate numerical correlation of AE trends and activity by sensor location with the areas that are identified for high potential damage by spatial assessment.

3.2 Part 1 - Physical Assessment Studies after Repair

The different data layers collected and described in Study I are typical assessment studies performed before repair. Three new layers introduced in Study II are performed after repair; (F) deck cracks layer, (G) thermography layer, and (H) AE attenuation conductivity layer. After the CFRP laminates were applied and paint protected, the same 24 by 24 in. [610 by 610 mm] grid was drawn on the entire deck soffit to allow for similar measurement points. All investigation procedures of after repair studies are nondestructive field tests performed on site.

(E) Cracks in Deck Surface - The bridge deck consist of a North and South lane as illustrated in Figure 3.1, where the RC portion is marked by a dashed square. Deck cracking can be due to a number of effects such as temperature shrinkage or loading paths in relation to the thickness of the 18 in. [457 mm] solid poured concrete element [Hadidi et al., 2005; ACI 224R, 2008]. A layered map of deck cracks (F) is created to assess crack density and to verify the separation crack between the PC and RC sections. Visual cracks in the RC section were documented in x-y coordinates and mapped. Figure 3.1 shows that the South lane has far more cracks than the North lane. Overlay decks are known to suffer increased crack propagation compared to monolith bridge decks [Darwin et al., 2004]. A major crack in the North lane evidently illustrates separation between prestressed beam PC-8 and the monolith RC slab. Cracking occurring in this section has structural impact as these cracks may provide access to chloride containing air and water to the steel reinforcement. Although cracks on the deck soffit are more recognizable as structural defects, cracks in the top surface should be taken into account for identification of areas of concern for corrosion damage.

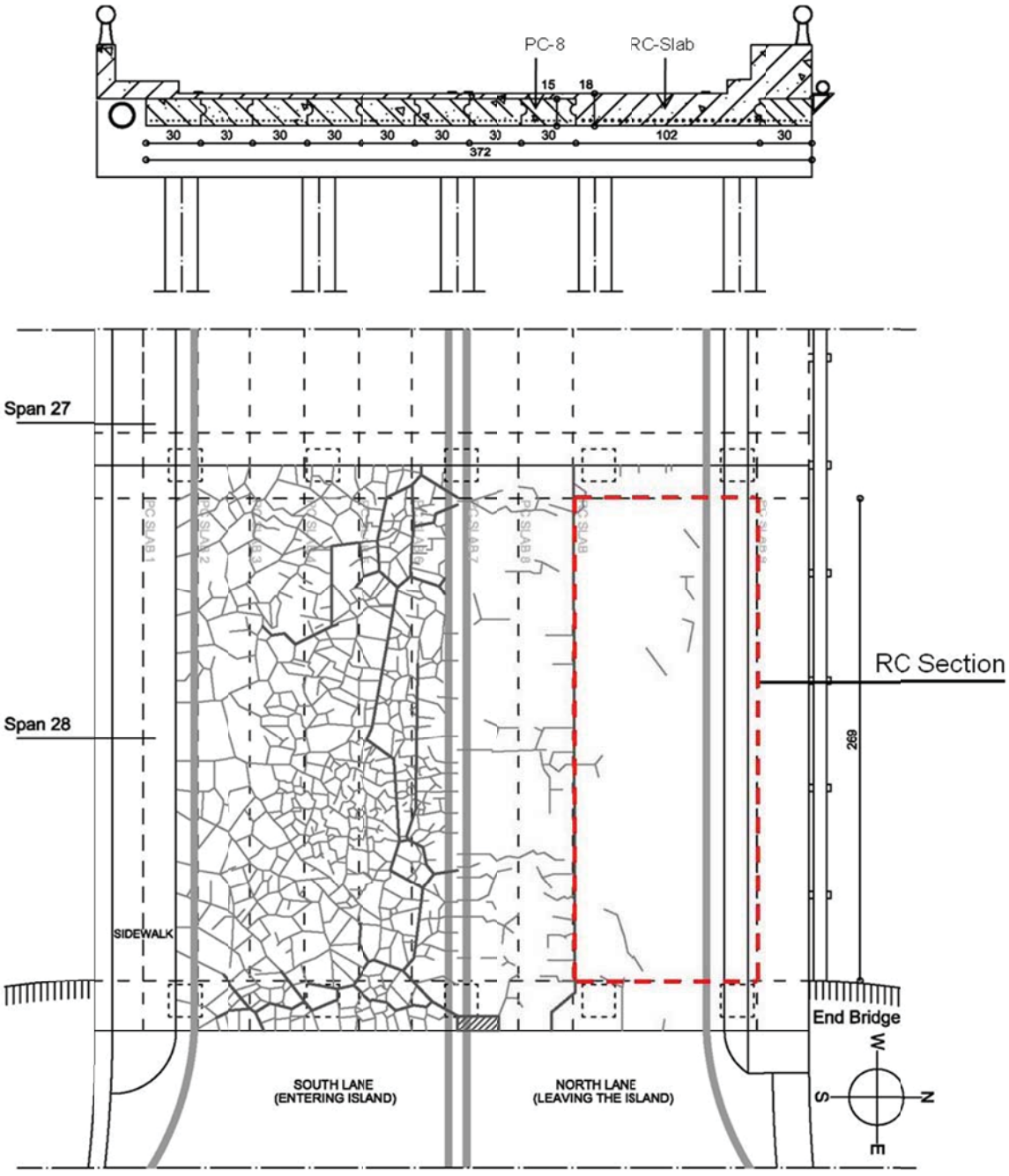

Figure 3.1 - Plan view and deck cracks

The cracks are translated in a crack density map in Figure 3.2, where only the RC portion is illustrated. The figure gives small squared areas in a mini grid of 6 by 6 in. [150 by 150 mm] with a total number of 16 possible areas in the existing 24 by 24 in. 610 by 610 mm] grid. The dashed square in grid point M-5 illustrates the area and crack density cells that can be linked to this grid point to allow for spatial comparison with other layered maps. All crack lengths are measured and classified by grey tints relating to the length in the mini grid cell which can be found in the accompanying graph. The crack lengths per mini cell in the RC section range from 1 to 12 in. [25 to 304 mm]. Cracks are mainly found in the shear areas of the span, but the direction and shape of cracks do not obviously demonstrate a shear failure mechanism. A complete crack density and direction vector map is given in Appendix II.A where cracks ranging between 6 and 9 in. [150 and 230 mm] are weighed as more significant as they may indicate a single crack spanning a 6 by 6 in. [150 by 150 mm] cell in a straight line.

(F) Air Voids under CFRP Laminates - An assessment layer with mapped air voids under the CFRP laminates is included as one of the layers for spatial analysis. Even though air voids are not a result of physical degradation, but rather an application defect, the layer is included to overall evaluate for future maintenance and repair. Investigation is performed 18 months after application by Infrared Flash Thermography [ASTM E2582, 2007]. Detection is performed by heating a square for several second in the 24 by 24 in. [610 by 610 mm] grid on the double layered laminate bottom surface. For this investigation, two Revlon RV484 blowers with a performance of 1875 Watt, 125 VAC and 60 Hz were used simultaneously. The FLIR Hand Held Infrared Thermal Imager monitors the surface, while it cools, to discover areas with high heat radiation.

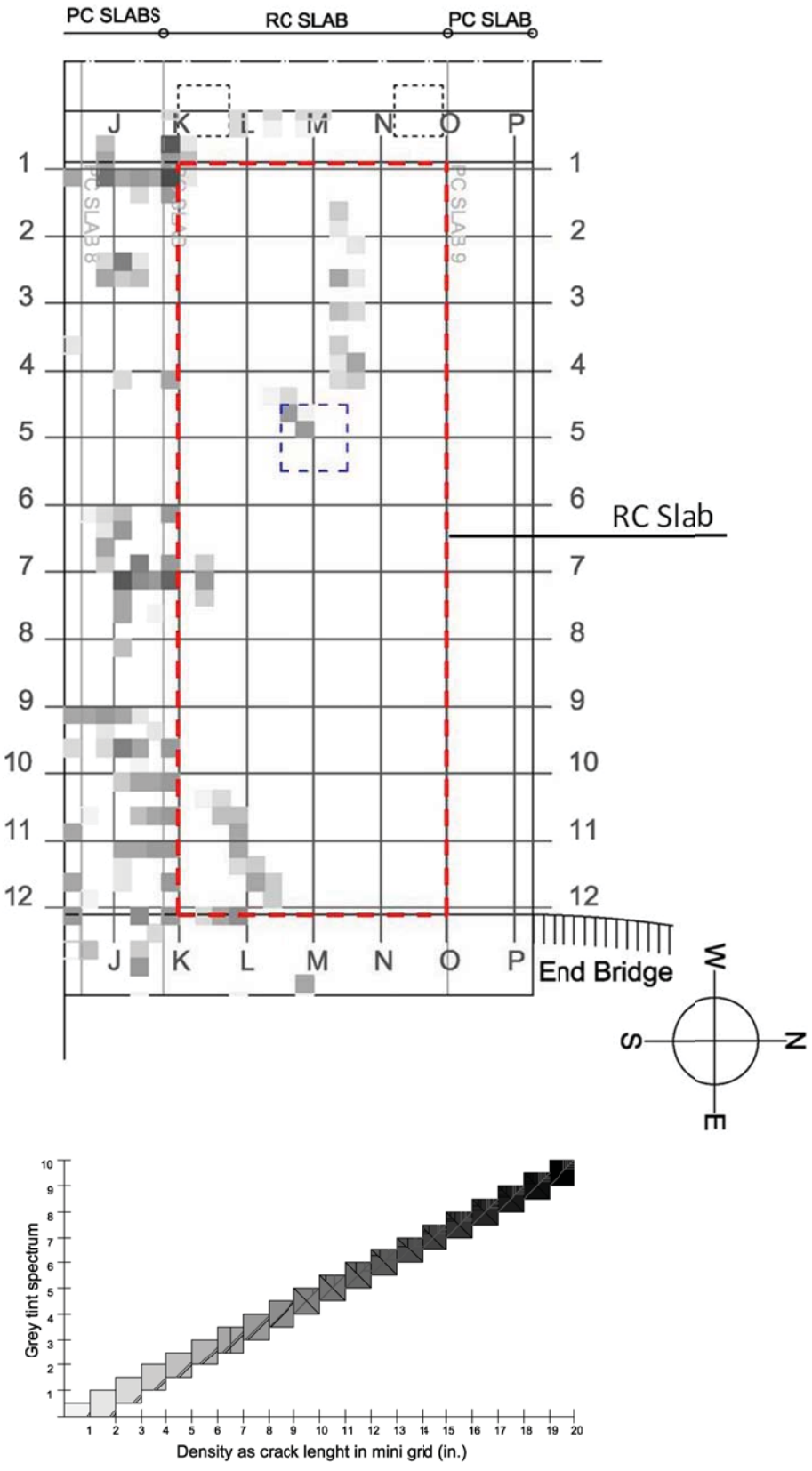

Figure 3.2 - Layer (F): Density specified deck cracks map

The difference in heat flux in the CFRP material is illuminated in the area with higher temperature differential through the camera view port. When the CFRP plies hold a void or delamination, the composition has a different heat flux as it cannot transfer its heat to the underlying concrete material. While holding and looking through the camera pointed at the investigated area, illuminated areas were marked on the actual surface, photographed using Infrared imaging as well as regular camera and by reporting void dimensions to later draw them in a new layered thermography map (G) (Figure 3.3). A complete bridge map of voids is given in Appendix II.B.

According to ACI-440.R2 [2008] (Table 3.1); an air bubble smaller than 2 in^2 [13 cm^2] can be ignored (blue), except when there are 10 or more in 10 ft^2 [1 m^2] (red dash-dotted square); an air void with an area between 2 and 25 in^2 [13 and 160 cm^2] should be filled with resin (magenta); and air voids with an area larger than 25 $in.^2$ [160 cm^2] are required to be cut out locally and replaced (red). The accompanying Infrared images and photographs show how the voids can be detected and gives example of two of the most concerning voids with a size larger than 25 in^2 [160 cm^2] in area O-2 and L-6. Also one 10 ft^2 [1 m^2] area with 10 voids or more is identified in area M-N-3-4. Associated infrared images show clear evidence of changes in heat flux for the specified areas.

Table 3.1 - Repair actions for FRP blisters and delamination spots

Area of air void	Action [ACI-440.R2, 2008]
< 2 in^2	Acceptable
10 spots <2 in. per 10 ft^2	Inject or Replace
2 to 25 in^2	Inject
> 25 in^2	Replace

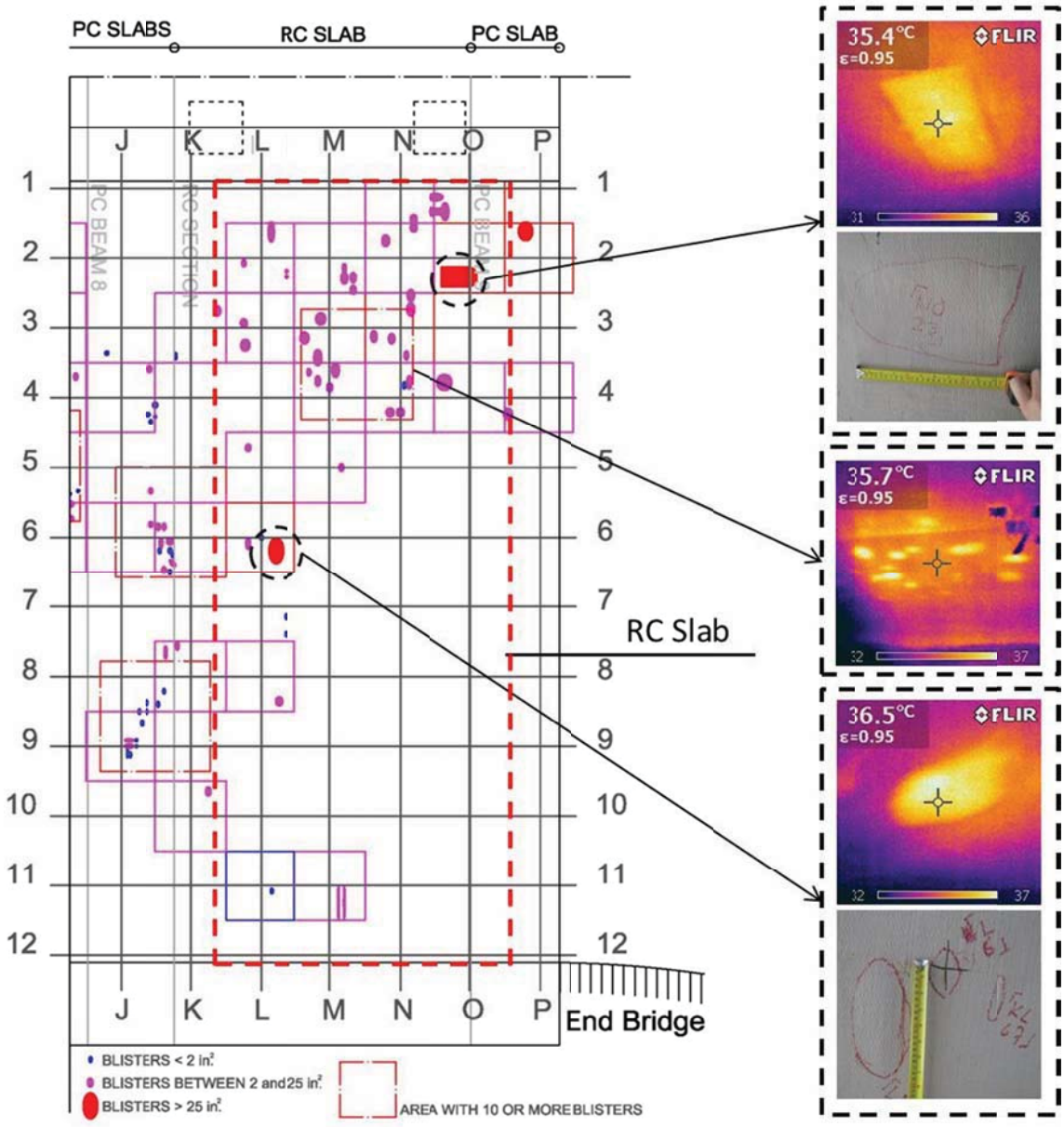

Figure 3.3 - Layer (G): Air voids under CFRP laminates map

AE Attenuation Conductivity - To assess the composition properties in terms of AE signal transmission, a new layered map (H) is developed using AE attenuation conductivity testing. The aggregate size, concrete cover spall, removal and patching, as well as existing cracks or delaminated CFRP can cause energy absorbance or losses of AE signal transmission through CFRP laminates [Jacobs and Owino, 2000]. By standardized pencil lead breaking on the CFRP laminates, properties of the complete composition of the original, repaired and patched underlying concrete with the CFRP laminate interface become visible. Pencil lead break testing is a standardized technique [ASTM E976, 2010] to simulate an intense, quite similar to natural AE source, acoustic signal by breaking the brittle graphite lead of 0.3 mm diameter pencil lead, approximately 0.12 in. [3 mm] from its tip, against the surface of the monitored material [Hsu, 1976; Nielsen, 1980]. Attenuation is assessed before load testing to report noise level and find determine the appropriate recording Amplitude threshold. In accordance, decisions can be made on sensor spacing and placement. Additionally, attenuation is compared for transmission in parallel, diagonal and random directions to the CFRP fiber string matrix to detect any blockages in the composite deck by visualization of results. AE sensors were placed on spread, triangularly arranged locations in the existing 24 by 24 in. [610 by 610 mm] grid for direct comparison with other layered maps (Figure 3.4).

A total of 15 AE sensors were placed on the RC slab while the 16th control sensor was placed on neighboring PC slab 8; 20.5 in. [508 mm] South of sensor 8. RC slab sensors had a minimum spacing of 48 in. [1219 mm] and maximum 53.7 in. [1364 mm]. All AE sensors made contact to the CFRP interface with the same aluminum brackets and vacuum grease contact agent as previously used in Study I (see also Figure 3.20).

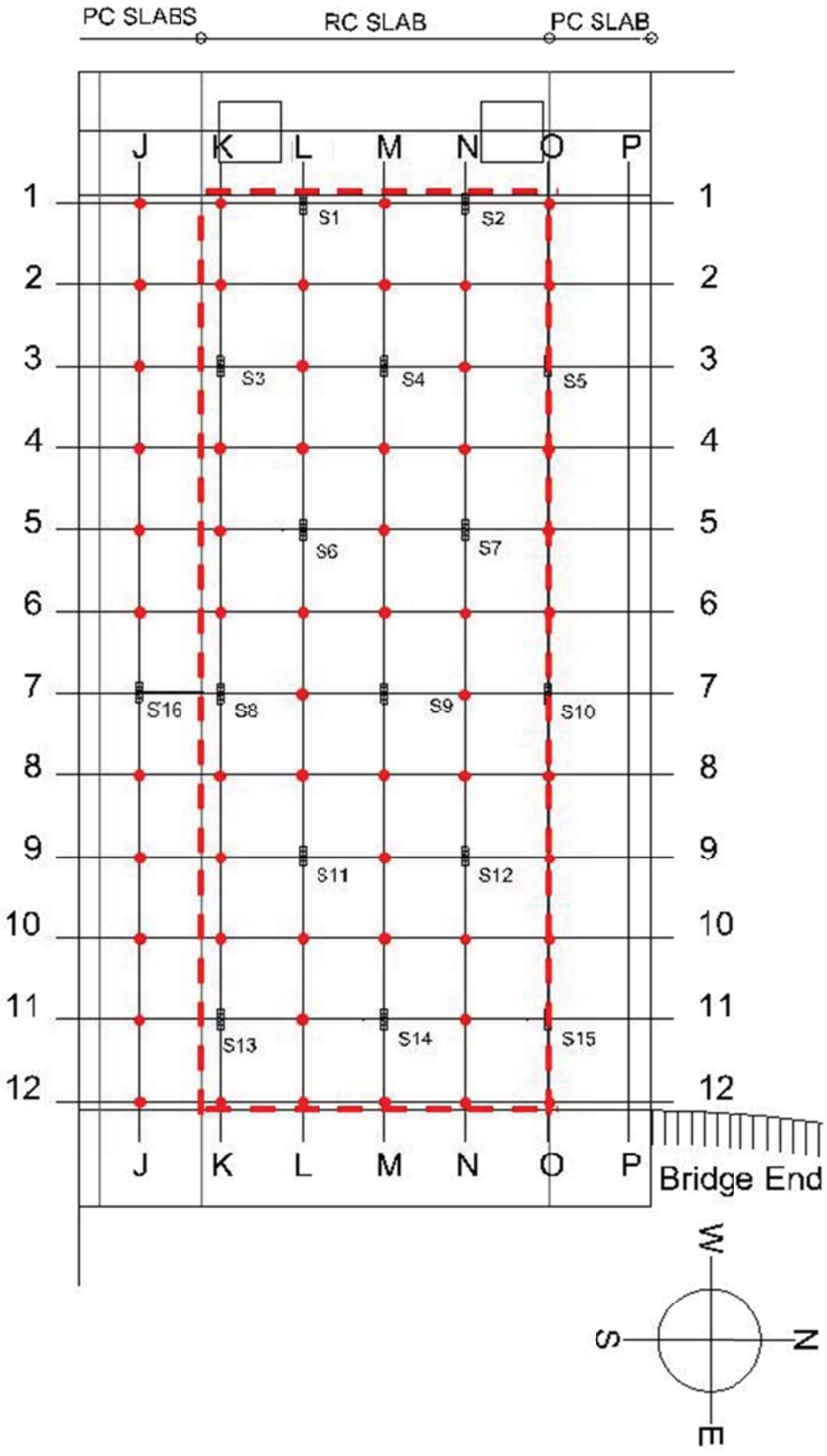

Figure 3.4 - AE sensor and pencil lead break locations

Pencil lead break testing with 0.3 mm graphite lead is performed starting from grid point 1 (J-12) in the South-East corner to grid point 57 (O-1) in the North-West corner. Strategic breaking and placement allowed for the repetition of signals at similar distances and in different directions; parallel, diagonal and in random direction in relation to the grid and CFRP matrix.

Monitoring of AE signals was performed with a 16-channel Sensor Highway II System™ with piezoelectric resonant sensors type RI6. Recording and data processing were carried out using AE-Win software. Amplitude (dB) is used as the governing parameter to approach attenuation. As illustrated in Figure 3.4, the location of sensor S16 was foreseen to assess contact between PC slab 8 and the RC slab. Noise was eliminated as much as possible during the pencil lead break test by waiting for zero traffic moments and with a recording threshold of 30 dB. Low recording of Amplitude can be caused by reduced contact between the sensor, contact agent and the CFRP interface, but was evaluated by running the Automatic Sensor Test (AST) prior to testing. The recorded Amplitude (dB) results are given in Appendix II.C for all 57 break events and 16 recording sensors. Each pencil lead break event could be recorded by more than just the closest sensor and offered evaluation opportunities to assess one event from more distances and different angles. Average Amplitudes with standard deviations are sorted by break location, recording sensor, distance and direction of transmission and is shown by figures and tables in Appendix II.C.

Figure 3.5 shows attenuation data of all pencil lead breaks for average Amplitude (dB) against traveling distance (in.) for all sensors and traveling directions. The dashed line has a pencil lead break location at 3.5 in. [90 mm] resulting in an Amplitude of 99

dB recorded by sensor 16. Shortest distance for sensors on the RC slab is 24 in. [610 mm]. As shown in the graph, all sensors together show a clustered trend which is relatively wide spread. It shows attenuation variances ranging from ~49 dB in sensor 12 to ~69 dB in sensor 7 at a distance of 24 in. [610 mm]. At a distance of 48 in. [1,220 mm], the lowest recording again takes place in sensor 12 with Amplitude 34 dB and the highest recording in sensor 13 with Amplitude 64 dB, which visually peaks out the trend in the figure. At distances larger than 100 in. [2.5m] the data becomes inconstant an inconsequential.

To offer a better indication of average AE signal attenuation in the RC slab, Figure 3.6 shows average Amplitude attenuation for sensor 1 to 15, and additionally the PC slab mounted sensor 16, in terms of distance. The sensors on the RC slab and the sensor on the PC slab show almost similar attenuation behavior, where PC slab sensor 16 has a higher standard deviation. Sensors 1 to 15 attenuate from an Amplitude of ~60 dB at 24 in. [610 mm] to ~50 dB at 48 in. [1,220 mm] distance with a standard deviation of relatively 6.5 and 8.42 dB, where sensor 16 attenuates from an Amplitude of 63 dB at 24 in. [610 mm] to 56.50 dB at 48 in. [1,220 mm] distance with a standard deviation of relatively 0 to 6.36 dB. However, after extensive sorting and processing data, these graphs give enough support to determine signal distance range and applicable threshold level to eliminate noise. Appendix II.D shows 3D visualized plots of the AE signals by pencil breaks transposed to their source location to visually identify the range of the recording threshold.

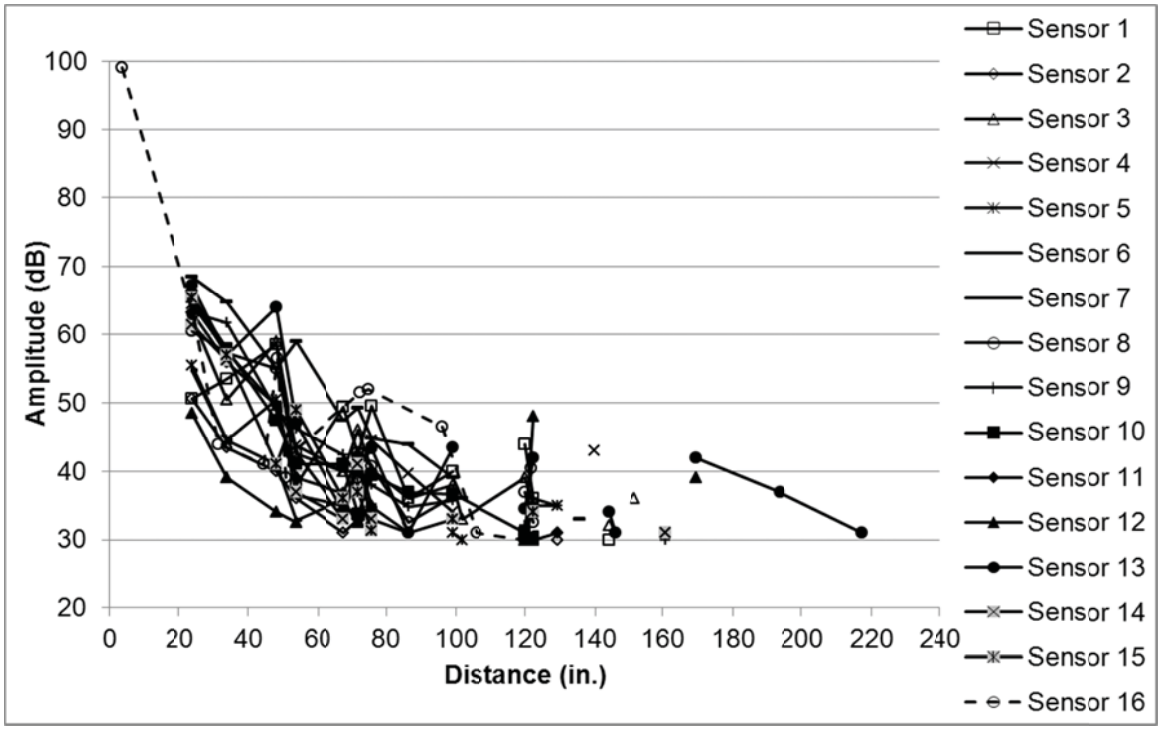

Figure 3.5 - Average Amplitude attenuation vs. traveling distance

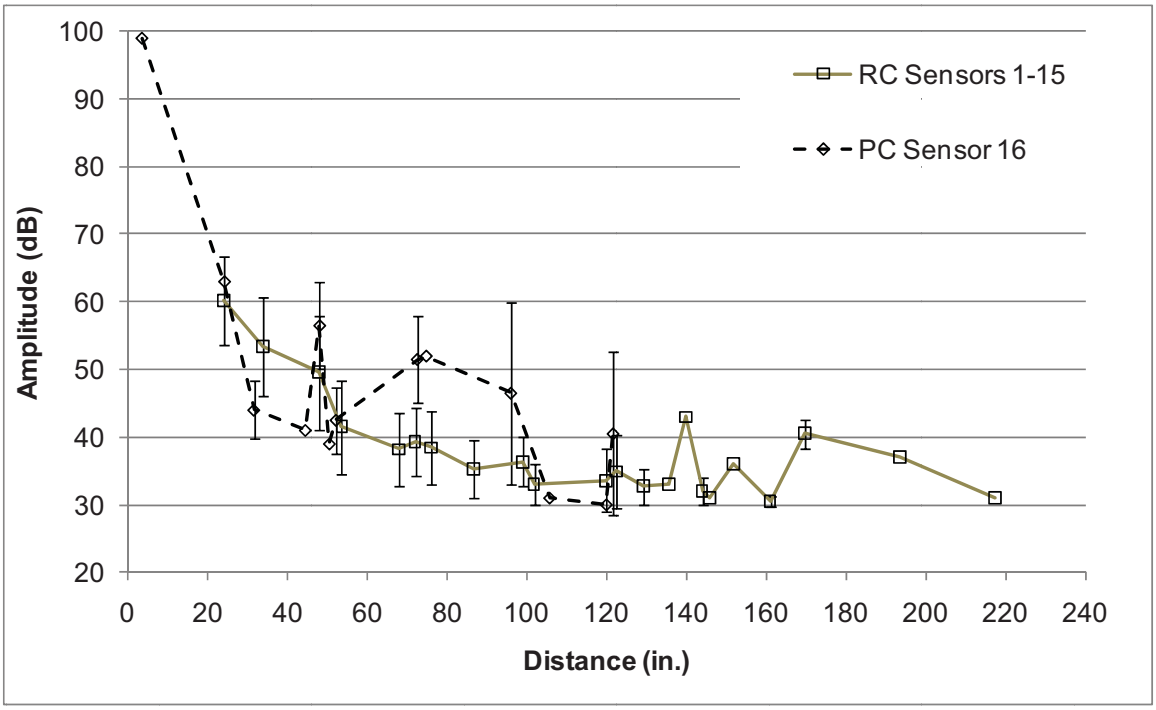

Figure 3.6 - Comparison AE attenuation RC slab with PC slab 8

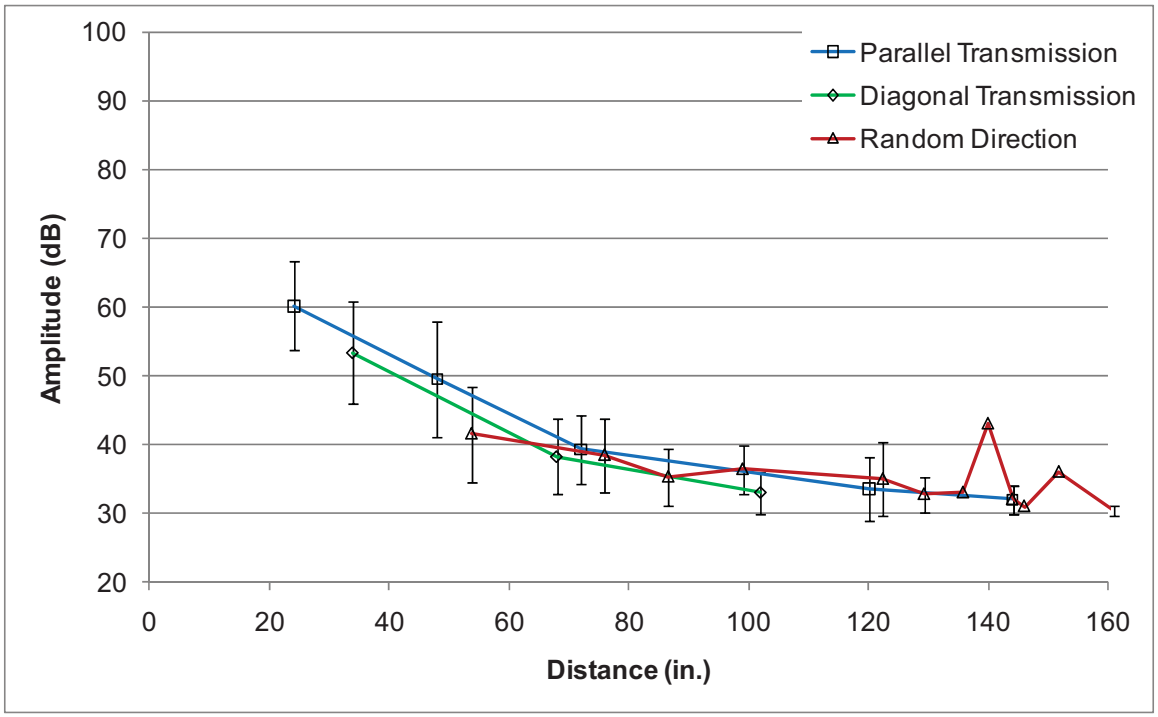

Figure 3.7 - Comparison parallel, diagonal and random direction

The CFRP laminate matrix consists of a weaving pattern of carbon fiber strings in two directions. Each of the two plies has a thickness of 0.04 in. [1.02 mm] per laminate. As the AE signal is generated on the structure's surface, the acoustic wave travels as a surface wave (Rayleigh) and will be partially converted into a guided wave transferred through CFRP fibers [Degala et al., 2009; Chen et al., 2001]. As carbon materials allow faster traveling and reduced signal attenuation, the strings in the CFRP matrix may serve as wave guides [Chen and Wissewapaisal, 2000]. This can create a difference in signal attenuation when events are in parallel, diagonal or in another (random) direction to the sensor locations and CFRP matrix. To evaluate possible differences, the Amplitudes are assessed separately by direction and given in Figure 3.7. The graph shows the average Amplitude (dB) against traveling distance (in.) for all three distinct directions with standard deviations indicated at each measurement point. No considerable variance is seen between the directions of transmission. This could also mean that the matrix spacing is too small to create significant traveling distances which could influence signal intensity. This also shows that string to string connections do not create significant signal losses, as in addition, the laminates are saturated with resin during application which should create sufficient contact.

In order to make the attenuation testing and data reading more accessible for field applications, an attempt is made to contribute to this effort by visualizing Amplitude signal reach and responses in three dimensions. Figure 3.8a shows a top view of a volumetric plot of signal ranges of sensor 9. Each recorded Amplitude signal has been drawn vertically in the bridge plan on the grid point where the event was created by pencil lead breaking. Since pencil lead breaking is a standardized test [ASTM E976,

2010], each given impulse has comparable intensity at its starting point, but will lose a certain amount of energy during its travel path depending on the medium properties. With this information, the volumetric plot now provides visual guidance by its shape for areas and travel paths that for conductivity of AE signals. The complete composite system of repaired concrete with the external CFRP laminates together determines conduction properties of the travel path. Sensor 9 in Figure 3.8a is placed in the center region of the RC slab and can pick up pencil lead break events from almost any location on the entire slab with a recording threshold of 30 dB. Limited by the pattern of pencil lead breaking grid points, it tries to complete its range in circular shape which would be the ideal case if the material was more conductive like steel. With this visualization tool; the signal range, appropriate sensor spacing, and recording threshold become more accessible and interpretable for field applications.

Figure 3.8b illustrates the volumetric signal range of sensor 16. This sensor is placed on neighboring PC slab 8 and records the same pencil lead break events as the sensors placed on the RC slab. The longitudinal shape of the range plot is clearly visible. Only three signals are able to travel from the RC slab to the sensor on the PC slab. Its volumetric shape gives indication of a separation crack between PC slab 8 and the RC slab which was already detected by deck cracks (Figure 3.1) and visual inspection (Study I). The signal ranges of sensor 2 and sensor 5 are given in Figure 3.8c and d. Comparing the volumetric signal range of both sensors with for example sensor 9 (Figure 3.8a) or sensor 13 (Figure 3.8c), we see that their range is somewhat limited. Comparing sensor locations with the information collected in the visual inspection study (Figure 2.5), we see that a long strip of concrete was removed and replaced. A small separation crack due

to the patched concrete can be the cause of limited signal transmission. Another cause of signal interruption can be the dense arrangement of air voids under the CFRP laminate in the North West corner of the RC slab (Figure 3.3). These discontinuities may partly block AE signal transmission or absorb their energy. This information is considered useful for designing sensor locations for AE monitoring and testing. The volumetric plots of the other sensors can be found in Appendix II.E.

Per sensor location, the surrounding properties of the material with composite arrangement can now be evaluated to support other methods, hypotheses and observations. AE signal conductivity relates to the typical density property of the composite arrangement. Reflection of waves takes place between laminates and concrete, even though the recorded wave is named a surface wave (Rayleigh). The deck soffit is completely covered with CFRP laminates and gives no visual access for inspection. If little information is known about the bridge structure, this technique is able to provide more understanding and clarification about the composition of material and structure and can offer a visual guide.

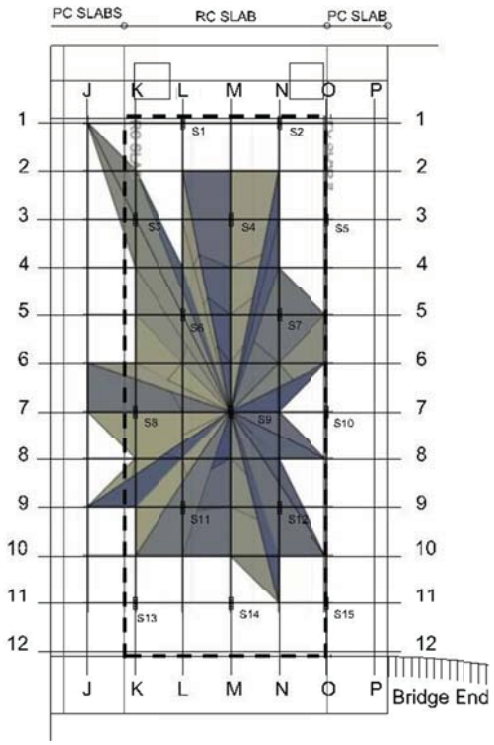

(a) sensor 9

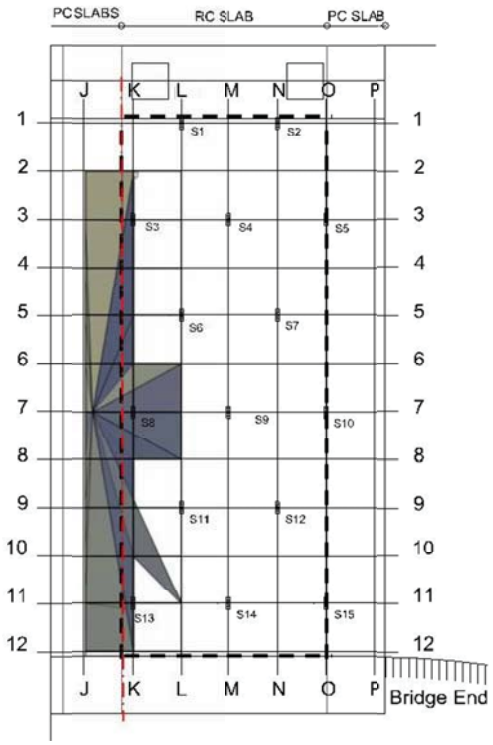

(b) sensor 16

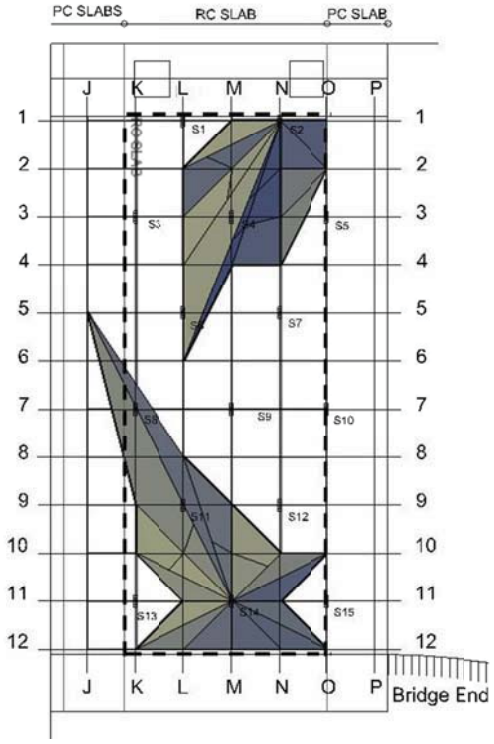

(c) sensor 2 (top) and 14 (bottom)

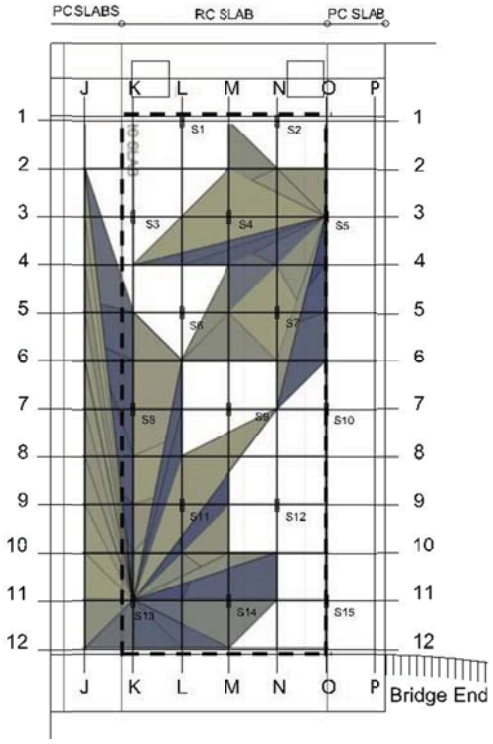

(d) sensor 5 (top) and 13 (bottom)

Figure 3.8 - AE attenuation volumetric visualized ranges

3.3 Spatial Analysis

Assessment layers from Study I (A to D) and the three additional layers from Study II (F to H) are combined in spatial analysis of the RC slab by making use of the grid intersection points as data points. Each method offers a different perspective on the condition of the bridge. By combining these methods and results, areas of concern can be identified with increased confidence. The spatial analysis is divided in the combination of layers conducted before repair (Figure 3.9) and after repair (Figure 3.10). Numerical investigation is first performed by block statistics and later computerized with guidance from the Software ESRI ArcGIS.

3.3.1 Numerical Spatial Analysis

The method followed in the numerical spatial analysis is block statistics. Before comparison takes place, each layer is translated into a normalized identity for every grid point to indicate the degree of damage in relation to the specific parameter. Reason to not include the Chloride Content layer (E) is that measurements could only be taken at a few grid points, which offers only partial information of the RC slab. To maintain an equivalent measurement, each layer ought to have complete coverage of all grid points in the selected area. Chloride content measurements confirm with bridge condition and aggressive environment in Study I.

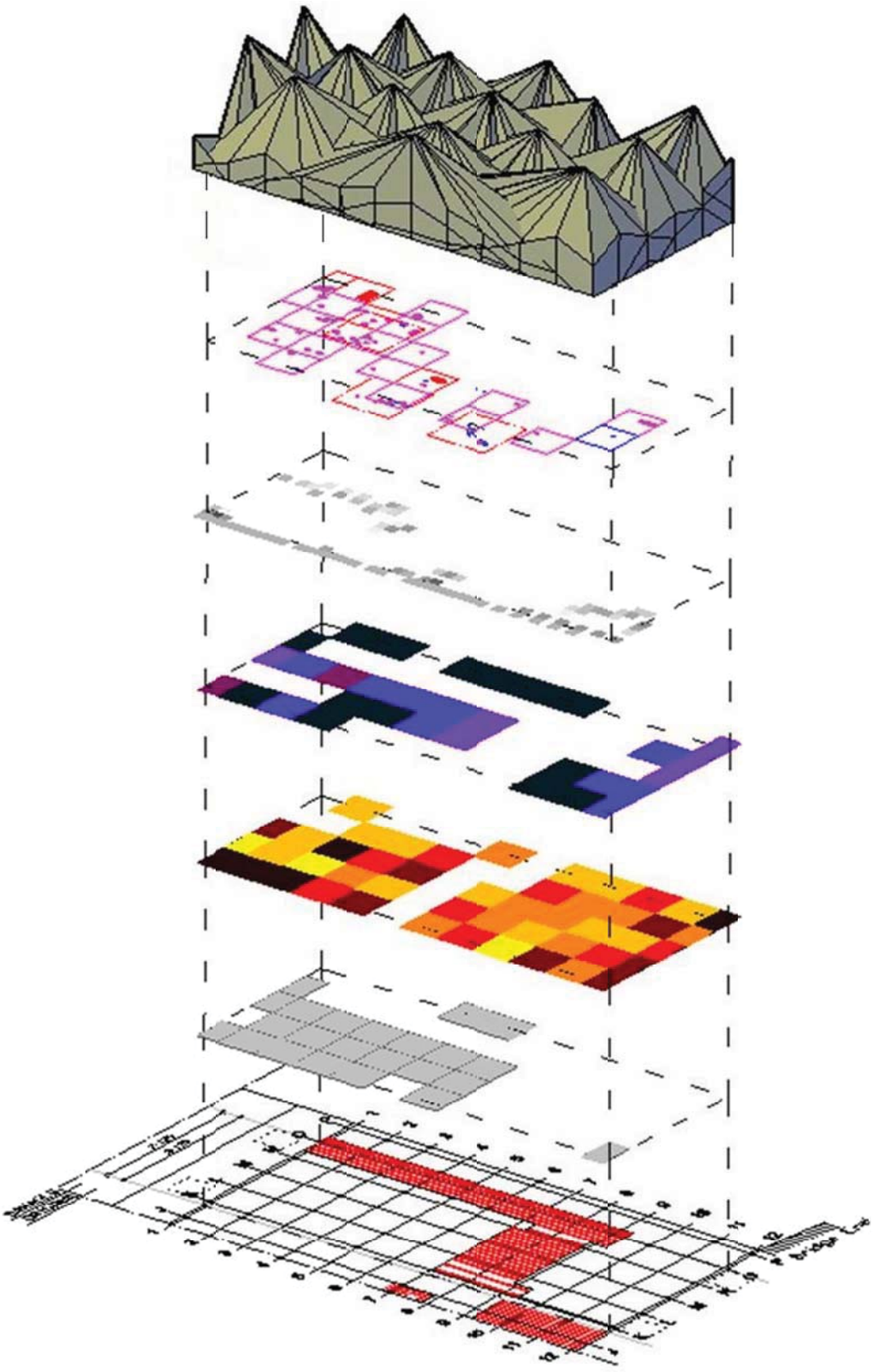

Figure 3.9 - Layered maps before and after repair, (A) to (H)

The translation of grid data points into normalized values on a scale from 0 to 1.0 where 0 indicates non-concerning damage probability and 1.0 is highly concerning. The degree of concern is determined by code and literature qualification (Table 3.2).

Table 3.2 - Thresholds indicating corrosion or concrete damage

	Layer	Assessment method	Threshold
Study I	(A)	Visual Inspection	Bars missing (%)
	(B)	Carbonation detection	no pink coloration
	(C)	Active corrosion potential	< -350 mV
	(D)	pH level	≤ 9.0
	(E)	Chloride content	> 2%
		(not included)	
Study II	(F)	Deck cracks	Relative density ratio
	(G)	Air voids under CFRP	≥ 2 in^2, or 10 per 10 ft^2
	(H)	AE attenuation conductivity	Relative Number of Hits ratio

Table 3.3 shows the translation of remaining reinforcement (A) in the RC slab ($RC_{n,m}$). The original design calls for three #9 (1.25 in. [25 mm]) steel reinforcing bars per foot width [30cm]. Each lost bar is translated as one third of damage. The translation of concrete carbonation layer (B) is simplified to “yes” and “no” for pink coloration in the grid points ($CA_{n,m}$) to relatively 1.0 or 0 (Table 3.4). Layer (C) with active corrosion potential ($CP_{n,m}$) indicates active corrosion with 90% probability when values are measured -350 mV or lower. Although, Elsener and Böhni [1988] explained that lower measured values indicate a higher corrosion potential, these values are not quantitatively verified and are therefore not used in the applied scale (Table 3.5). Last included layer before repair is pH level layer (D) in the RC slab which resulted in a range of 7.67 to 10.00. In the case that pH level is lower than 9.0, a corrosion friendly environment exists which is translated in parameter ($pH_{n,m}$) with a damage probability of 1.0 (Table 3.6).

Table 3.3 - Numerical translation lost reinforcement

Observation	$RC_{n,m}$
0	0
1	0.33
2	0.66
3	1

Table 3.4 - Numerical translation carbonation

Observation	$CA_{n,m}$
Yes	0
No	1

Table 3.5 - Numerical translation active corrosion potential

Observation	$CP_{n,m}$
≥ -350	0
< -350	1

Table 3.6 - Numerical translation pH level

Observation	$pH_{n,m}$
> 9.00	0
≤ 9.00	1

The first assessment layer after repair describes crack density (F) and is interpreted by total length of each mini-grid crack density cell $n_{n,i}$ times the length indicated in the specific mini grid cell $L_{n,m}$ (in.) (Table 3.7). The crack density ratio ($CD_{n,m}$) is found in equation (1) by dividing total length in the grid cell by highest crack length found on the RC slab. This allows for relative crack density scaling; classifying cells with highest and lowest concern.

$$CD_{n,m} = \frac{\sum n_{n,m} * L_{n,m}}{\sum n_{max} * L_{max}} \quad (1)$$

The second assessment layer (G) describes the locations of air voids. With guidance of the ACI 440.R2 [2008] code, measured air void sizes are translated to parameter ($AV_{n,m}$) as given in Table 3.8. An assumption is made to distinguish damage level of air voids with an area between 2 and 25 in^2 [13 and 160 mm^2] and with a single air void area of 25 in^2 [160 mm^2] or larger. The code recognizes differences in repair methods, and this is reflected in the appointed damage level in the scale.

Table 3.9 translates AE attenuation activity per grid point from layer (G). Using attenuation testing and 3D visualized sensor range plots, each grid point is counted for its total Number of Hits from a threshold of 40 dB. The normalization of the parameter $AE_{n,m}$ is calculated by dividing the Number of Hits counted per grid point $N_{n,m,hits}$ by the maximum Number of Hits detected in the RC slab (2), which was found in grid point L-6 or pencil lead break location 31. This method allows for relative scaling of the complete RC structure and its AE activity parameter. It also includes the sensor locations, as the 3D visualized sensor range also covers these locations. Additionally, this method is not inclined by the slabs geometry or edge grid point locations as the volumetric interpretation continues to the edge which includes these grid points.

$$AE_{n,m} = 1 - \frac{N_{n,m,hits}}{n_{max}} \quad (2)$$

Table 3.7 - Numerical translation deck crack density

Observation	$CD_{n,m}$
Length cracks	CD Ratio by equation (2)

Table 3.8 - Numerical translation air voids

Observation	$AV_{n,m}$
< 2 in.	0
2 to 25 in.	0.5
> 25 in.	1
≥10 spots/10 ft^2	1

Table 3.9 - Numerical translation AE conductivity

Observation	$AE_{n,m}$
Number of Hits	Hits Ratio by equation (1)

The mean value of the combined and normalized data of all layers in equation (3) is calculated to offer a suggestion of grid points and regions with low and high damage potential. In Table 3.11, calculated mean values are given for a combination of 7 layers. The option exists to give weighed values to specific layers to better estimate potential damage considering corrosion, FRP application or concrete deterioration, but ample investigation is required in order to verify adequate values.

$$\bar{x}_{n,m} = \frac{\sum RC_{n,m} + CA_{n,m} + pH_{n,m} + CP_{n,m} + AV_{n,m} + AE_{n,m} + CD_{n,m}}{n_{layers}} \quad (3)$$

$$s_{n,m} = \sqrt{\frac{1}{N}\sum_{i=1,j=1}^{N}(XX_{i,j} - \bar{x})^2} \quad (4)$$

Table 3.12 gives standard deviation from equation (4) in which XXi,j, represents the identity of any specified assessment layer. Combining the two tables, one can identify cells with high mean and low standard deviations to indicate locations with the highest damage potential. Selected mean values higher than 0.7 and between 0.6 and 0.7 are given in Table 3.10. Grid point K-3 (red) has the highest damage potential and is situated in the South-West corner of the RC slab, as well as K-1 and K-12 (orange) with a value higher than 0.70, and K-5 higher than 0.6 (yellow). These numbers point out that column K has highest indication of damage potential. When the selection is expanded to values between 0.5 and 0.6, the number of selected data points increases rapidly, but is still mostly found in columns K, L and M. This specifies the highest damage potential in the South-West region of the RC span.

Table 3.10 - Cells with highest mean with standard deviations

	$\bar{x}$> 0.70				0.60 < $\bar{x}$ < 0.70	
	K-1	K-3	K-12	M-4	K-5	M-3
Mean	0.74	0.73	0.74	0.72	0.61	0.65
Standard Deviation	0.36	0.26	0.36	0.39	0.41	0.45

Table 3.11 - Mean values before and after repair combined

	K	L	M	N	O
1	***0.74***	0.17	0.37	0.45	0.24
2	0.53	0.48	0.59	0.16	0.37
3	***0.73***	0.32	***0.65***	0.36	0.11
4	0.50	0.54	***0.72***	0.41	0.15
5	*0.61*	0.58	0.56	0.17	0.33
6	0.36	0.48	0.33	0.06	0.52
7	0.59	0.52	0.49	0.10	0.11
8	0.51	0.32	0.19	0.22	0.24
9	0.39	0.24	0.21	0.19	0.22
10	0.50	0.41	0.21	0.22	0.27
11	0.45	0.49	0.29	0.38	0.27
12	0.74	0.50	0.38	0.40	0.41

Table 3.12 - Standard deviations before and after repair combined

	K	L	M	N	O
1	***0.36***	0.34	0.48	0.46	0.42
2	0.42	0.41	0.42	0.22	0.48
3	***0.26***	0.37	***0.45***	0.45	0.29
4	0.42	0.45	***0.39***	0.47	0.26
5	0.41	0.42	0.44	0.37	0.47
6	0.39	0.50	0.47	0.17	0.50
7	0.45	0.47	0.50	0.25	0.29
8	0.41	0.37	0.38	0.40	0.42
9	0.40	0.37	0.39	0.38	0.40
10	0.37	0.44	0.39	0.40	0.46
11	0.43	0.42	0.40	0.49	0.46
12	***0.36***	0.42	0.49	0.50	0.52

The number of grid points and area size of the RC slab used in the analysis is relatively small. In field applications, it may be more common to have larger areas or more dense grids, while both result in a higher number of data points. In these cases, cells with high damage potential cannot be selected manually and statistical tools are needed to investigate larger regions. The method used in this investigation is "Blocking". This technique creates block shaped groups of grid points and considers different statistical parameters, like mean, standard deviation, median, etc. Many spatial variations are possible to divide the grid into blocks. Figure 3.10 shows the block shapes options in the RC grid with equation reference for blocking 1x3 as determined in equation (5) and (6).

$$\overline{[\iota, J]}_{n+i,m+j} = \frac{\sum XX_{n+i,m+j}}{n_{layers}} \tag{5}$$

$$\overline{[1,3]}_{n,m+2} = \frac{\sum XX_{n,m+2}}{n_{layers}} \tag{6}$$

Appendix II.F gives the numerical blocking results of mean and standard deviation of assessment combinations before repair, after repair, and combined. Figure 3.11 shows a 3D spatial analyses column graph with 1x1 cells. Figure 3.12 shows the results of 1x3 cells after blocking. Both figures illustrate similar indication of highest damage potential in the South-West corner of the RC slab. The 1x1 cell graph in Figure 3.11 shows cells with highest mean values by the colors red, orange and yellow relating to Table 3.10. For larger areas, this 1x1 cell graph is not clear enough to appoint regions with highest damage potential without color indication. The 3x2 blocking results (Figure 3.12) is stronger to identify larger regions with high damage potential. In case of high number of grid points, this statistical method offers enhanced interpretation and understanding.

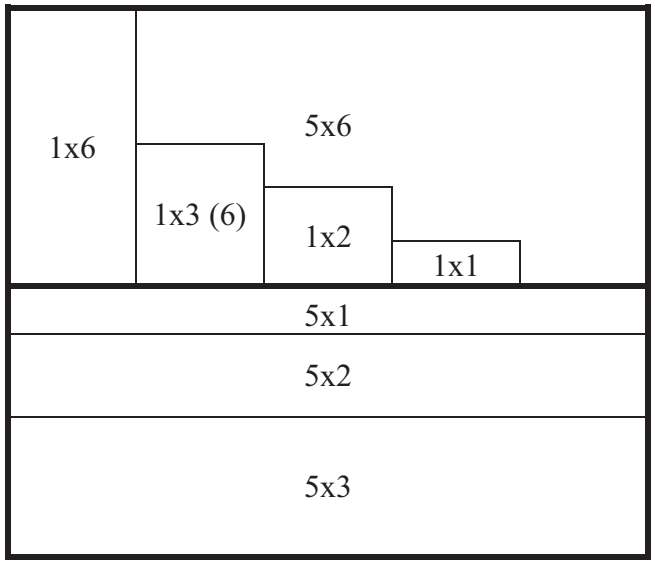

Figure 3.10 - Deviation RC deck for Blocking Statistics

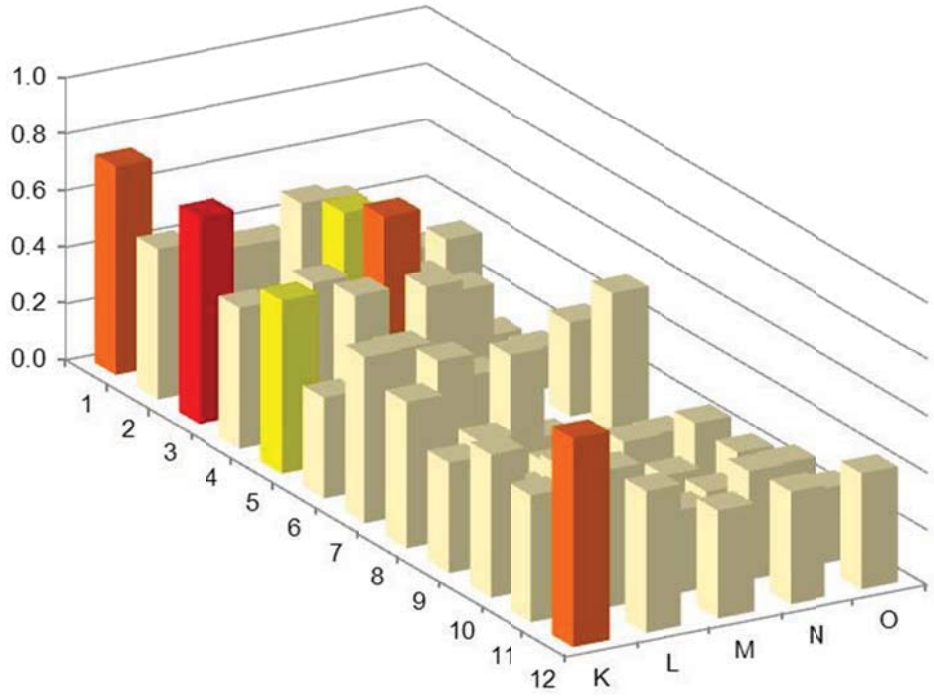

Figure 3.11 - Mean values with 1x1 spatial analysis

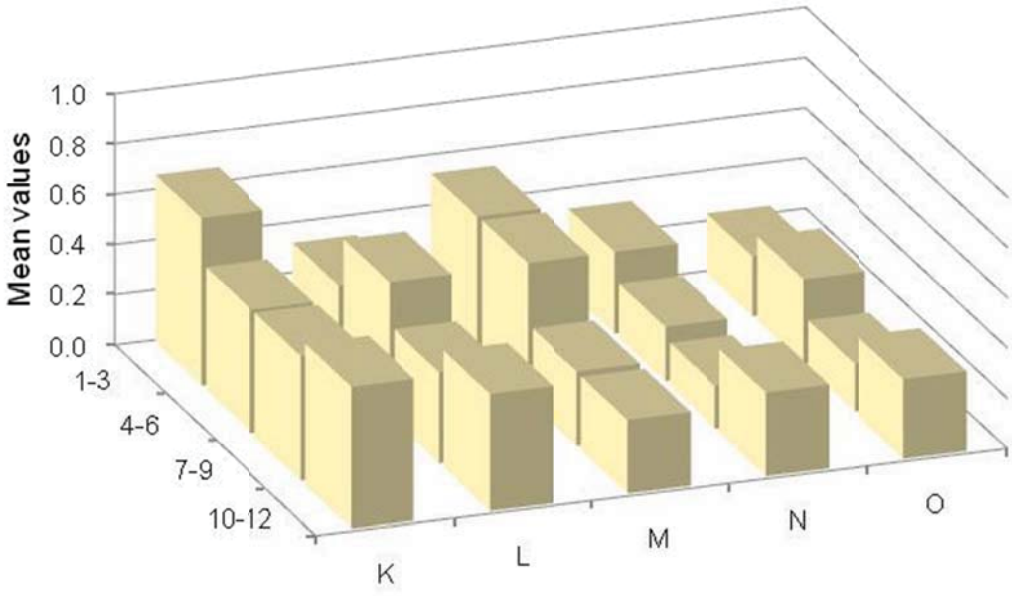

Figure 3.12 - Mean values with 1x3 spatial analysis

3.3.2 ArcGIS Spatial Analysis

A computerized method to evaluate spatial information in the form of points, floating points, polygons and polylines is ArcGIS 10 (ESRI) which is adapted from the field of Geography to evaluate the bridge condition and perform spatial analysis of layered assessment maps. In its most common application, this software is used to upload existing geographic maps which contain separate layers of altitude, urban zoning, and transportation which together can be analyzed for most efficient routes for a new piping network [Chang et al., 2010; Ormsby et al., 2008]. This study makes use of a specific developed raster grid with several layers of physical information on the scale of a single bridge span.

The ArcGIS Desktop applications used for analysis are ArcCatalog 10 and ArcMap 10. ArcCatalog is used to organize and convert data files. An Excel input was chosen where the raw assessment data were linked to x-y raster coordinates. After converting the file into a Shapefile, the data was opened in ArcMap which has visual output and analysis tools available. Before separate layers can be viewed and used, each layer needs to be imported by using “Conversion Tools” to convert the raster linked data with “From Feature to Raster”. From this point, each layer can be viewed separately or as a combination. As the layers still have raw data values, they cannot be compared or combined yet. The Spatial Analyst Tools option “Reclassify” enables the translation of raw data into usable, comparable parameters as previously performed in the numerical analysis. During the reclassification process, the ordering, separation and translation of field values is done by “Manual Method”.

Statistical parameters are already given during the analysis process; count, minimum, maximum, sum, mean and standard deviation. For each layer, reclassification classes with their statistical parameters are given in Tables 3.13 to 3.19, and visual outputs for each layer are given in Appendix II.G.

The combination of reclassified layers can be done with the "Map Algebra" option "Raster Calculator", which offers most common algebraic expressions. Only the "Addition" function is used, but "Multiplication" might be useful in the weighting of layers. New-formed identities are "Before Repair", "After Repair", and "Before and After Repair", of which the output of the last combination is given in Figure 3.13 and the first two are documented in Appendix II.G. The maximum output by combining all layers in simple addition has a cell range of 700 in the case that all 7 layers indicate maximum damage. The actual maximum is found in cell K-1, K-3 and K-12 at the level of 516, which is 73.7% of the maximum. K-1, K-3 and K-12 have equal numerical values. Other relevant statistical parameters are an overall mean of 281.63 with standard deviation of 120.12.

Table 3.13 - Reclassification lost reinforcement bars

Data	Classes	Reclass	Count	Min	Max	Sum	Mean	St. Dev.
0	0	0	36					
1	0-33	0.33	12	0	66	1188	19.8	26.62
2	33-66	0.66	12					

Table 3.14 - Reclassification pH level

Data	Classes	Reclass	Count	Min	Max	Sum	Mean	St. Dev.
10	9.01-10	0	36	0	100	2400	40	49.40
7.67	7.67-9	100	24					

Table 3.15 - Reclassification carbonation

Data	Classes	Reclass	Count	Min	Max	Sum	Mean	St. Dev.
No	0	0	37	0	100	2300	38.33	49.03
Yes	0-1	100	23					

Table 3.16 - Reclassification active corrosion potential

Data	Classes	Reclass	Count	Min	Max	Sum	Mean	St. Dev.
330	0-349.9	0	15	0	100	4500	75	43.66
434	350-435	100	45					

Table 3.17 - Reclassification air voids

Data	Classes	Reclass	Count	Min	Max	Sum	Mean	St. Dev.
0	0-49	0	37					
50	50-99	50	12	0	100	1700	28.33	39.45
100	99-250	100	11					

Table 3.18 - Reclassification AE conductivity

Data	Classes	Reclass	Count	Min	Max	Sum	Mean	St. Dev.
0-10	0-10	10	1					
10-20	10-20	20	0					
20-30	20-30	30	5					
30-40	30-40	40	10					
40-50	40-50	50	12	10	90	3460	57.66	18.44
50-60	50-60	60	10					
60-70	60-70	70	12					
70-80	70-80	80	4					
80-90	80-90	90	6					
90- 00	90-100	100	0					

Table 3.19 - Reclassification deck cracks

Data	Classes	Reclass	Count	Min	Max	Sum	Mean	St. Dev.
0-10	0-10	10	39					
10-20	10-20	20	5					
20-30	20-30	30	1					
30-40	30-40	40	4					
40-50	40-50	50	5	10	100	1350	22.5	20.96
50-60	50-60	60	3					
60-70	60-70	70	2					
70-80	70-80	80	0					
80-90	80-90	90	0					
90- 00	90-100	100	1					

Numerical cell values in a range of 700 still require knowledge of the assessment layers included. To make the damage potential level clearer, reclassification is used to divide the “Before and After Repair” layer in 10 classes by “Equal Interval”. Figure 3.13 gives similar outputs as the unclassified layer, except that the attached values are different. Cell K-1, K-3 and K-12 now have a value of 10 where the overall mean value is 5.37 with a standard deviation of 2.55. With this ten scale division, it is less complicated to decide what level of combined assessment classes should decide for areas that influence decision making on further inspection, immediate repair, maintenance or complete replacement when unacceptable large areas of high levels are found. An example is given in Figure 3.14 where cells are displayed from the level of 6. In addition, the accompanying values are written in the cell which is not an available option in the software. In a few moments, the data can be manipulated for the visual analysis and identification of the most severe cells or groups with the highest probability of damage.

The greatest advantage of this automated tool can be found in applications with high numbers of data points. Manual numerical analysis is not feasible when the number of data points becomes larger than in this study and automated tools become a necessity. Each action in the software considers all data points and processing is performed relatively fast with today's available computing capacity. In this study, "Blocking Statistics" appears useful to identify larger regions by combining cells in block shapes. Figures 3.15 and 3.16 show the visual output by ArcGIS of a 1x3 blocking exercise withy mean values and standard deviations. The software suggests using a classification of five classes, which makes the output less defined, but allows for rapid identification. By visually analyzing both figures, the regions with highest mean values can easily be selected and again lead to the same conclusion as the single cell evaluation and the numerical analysis method. Following the 1x3 cells with highest mean value and finding the associated low standard deviation values will point out the region with highest damage potential. Although cell K-1-3 has the highest mean value of 9.0, the most severe 1x3 cell is visually identified in L-4-6 by similar class and lowest standard deviation class. The actual mean value in cell L-4-6 is 7.67 with a standard deviation of 0.47. This method simplifies the calculation process, but caution has to be taken for an existing error.

In conclusion, it was found from Figures 3.13 to 3.16 that cell K-12 and the region from column K to M to rows 1 to 5 have the highest damage probability, which are both found in the unrepaired areas of the bridge span. These regions will be the focus of the load testing of the bridge.

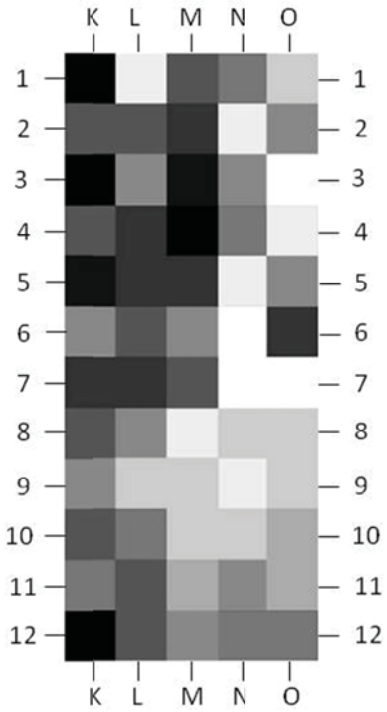

Figure 3.13 - ArcGIS output before and after repair combined

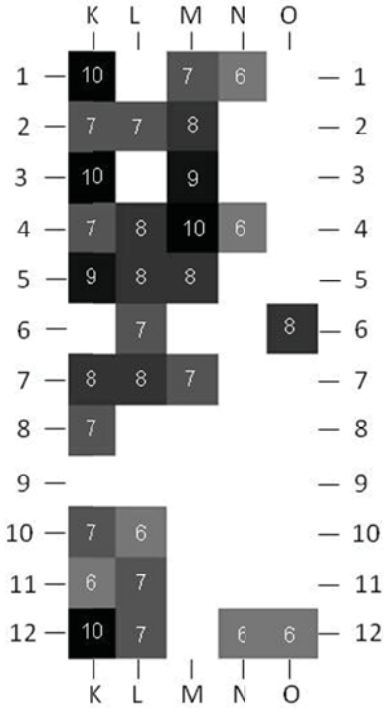

Figure 3.14 - ArcGIS output 10 class reclassification (6 to 10)

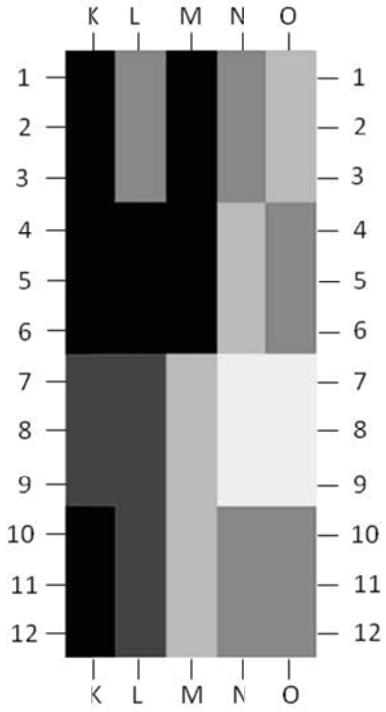

Figure 3.15 - 1x3 mean Blocking Statistics (ArcGIS)

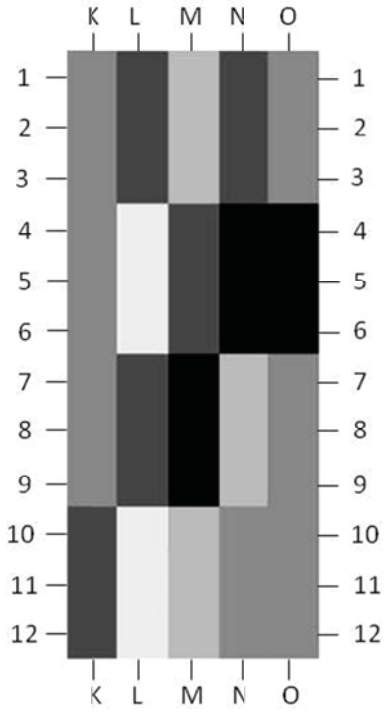

Figure 3.16 - 1x3 standard deviation Blocking Statistics (ArcGIS)

3.4 Part 2 - Bridge Load Test

The second part of Study II consists of a nondestructive load test with service level loading. The load is kept within the regular level of daily service (posted limit of 15 kips [67 kN]) with the main objective to correlate strain performance of the CFRP strengthened RC slab with AE activity. Strain and AE field monitoring where loads are within the lower bound of the elastic range is reflected in this study as it is found in many occasions in practice. As an example, Sanayei et al. [2010-1] successfully used static truck load tests for baseline finite element model updating of a three span continuous bridge with steel girders and composite concrete slab. Both static tests with truck stop locations and truck moving at a crawl speed were performed on the bridge.

Appendix II.H shows the truck load test results with measured strains and AE. For the low truck weight, as expected, static testing did not provide significant strain and AE response. Measured strains at midspan and analytically calculated structural response [ACI 440.R2, 2008] are used to evaluate correlation with the AE parameters Amplitude, Energy, Duration and Cumulative Hits; expressed in time. Active areas for AE activity in terms of cumulative values of parameters and peak values are compared to the previously appointed areas for high damage potential.

3.4.1 Fair Isle Bridge Test Setup

The field test is performed with preparation by attenuation testing and physical assessment studies as described in Part 1. The outcomes of these two studies offered guidance on the placement of sensors, strain gauges, static load locations and crawl loading pathways (Figure 3.17). Loading during testing is implemented by a water truck with a total weight of 13.64 kips [60.7kN] (Figure 3.19) (Appendix II.I). The back axle is

weighed separately at 7.22 kips [32kN] (3.61 kips [16kN] per wheel) which results in a load of 6.42 kips [29kN] (3.2 kips [14.5kN] per wheel) at the front axle. The length of the bridge is 268 in. [6.8m]. Spacing between the front and back axles is 151 in. [3.85m] and between the wheels 81 in. [2m] and 73 in. [1.85m] respectively for front and back wheels. The back axle has double wheels each with a width of 10.5 in. [27cm] and spacing from the center of 11.5 in. [30cm].

AE sensor placement, numbering, type, and contact agent were consistent with the attenuation test (Figure 3.4 and 3.17). Strain gauges were adhered to the CFRP laminates after removing paint and smoothing the surface by sanding. Strain gauges were placed in the center of the slab; RC-b and RC-d (Figure 3.17). In addition, strain gauges were placed on neighboring PC beams, to verify the crawl path. RC-b is located 28.5 in. [72.4cm] North from the separation between PC slab 8 and the RC slab. RC-d is located 45 in. [114cm] North from strain gauge RC-b. Strain was recorded with a 12 channel Data Acquisition System (DAQ) and Mat Lab software with a rate of 100 samples per second. As the AE recording equipment was not directly linked to the DAQ, recording was started manually and simultaneously on both.

3.4.2 Crawl Speed Truck Load Testing

A truck crawl speed test was performed in July 2010 with an average speed of 2.11 mph [0.94 m/s]. The span length is 275 in. [7 m], so from when the front wheel entered to when it left took an average time of 7.42 seconds, from East to West. The complete loading took 11.49 seconds as the back wheel enters and leaves the span 151 in. [3.85 m] later. Three travel lanes were defined on the bridge deck before the start of the test.

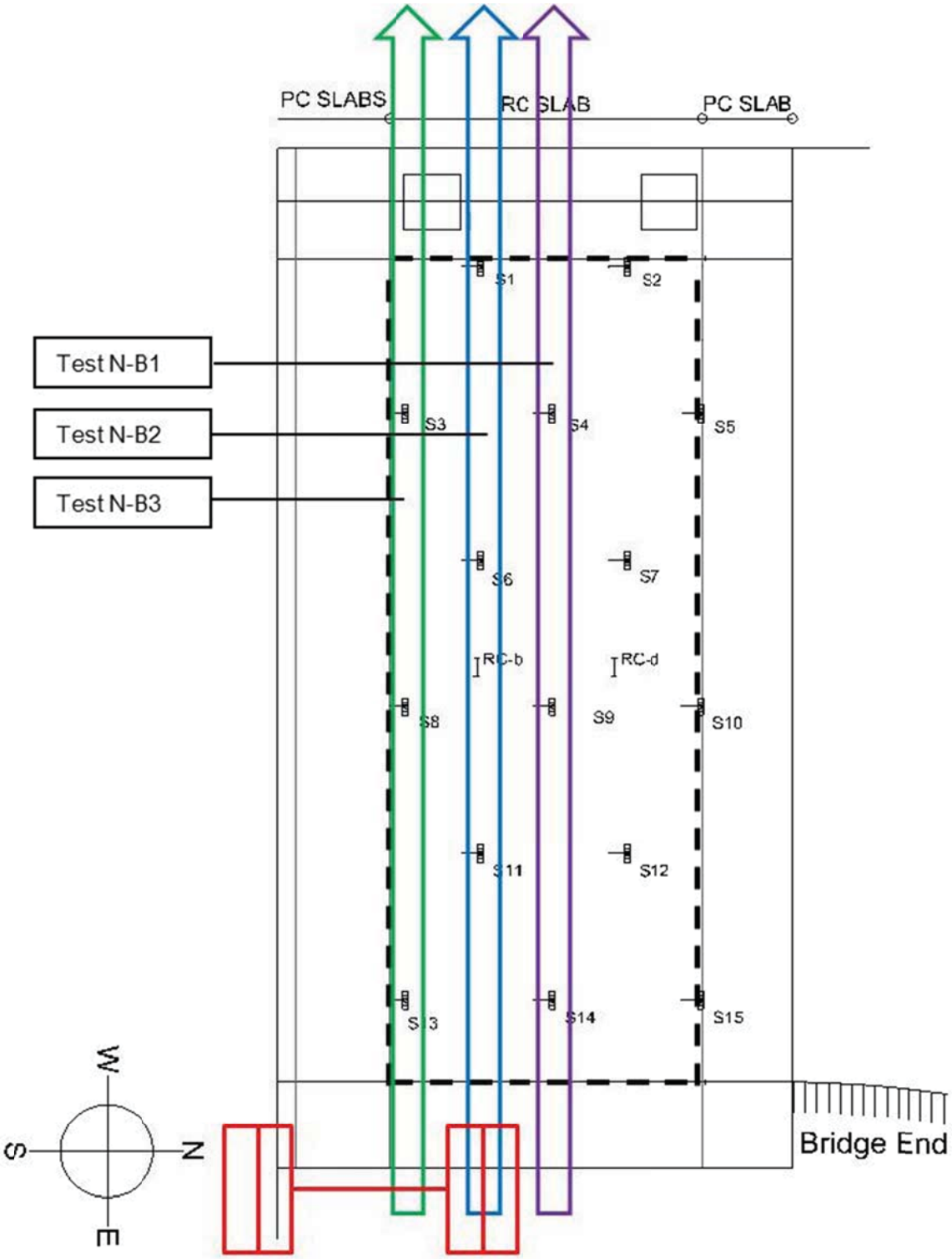

Figure 3.17 - Test setup crawl speed truck load test

Figure 3.18 - Load truck for load testing

Figure 3.19 - AE sensors and strain gauges on the deck soffit

Test N-B1, N-B2 and N-B3 are shown in Figure 3.18 by the colors magenta, blue and green respectively. The large arrows point the travel paths of interest on the RC slab. The thin arrows with same colors show the path of the truck's left wheel rolling over the PC section. The loading on the RC slab is assumed isolated. In following order, test N-B1 rolls over sensor S14, S9 and S4, test N-B2 over sensor S11, S6 and S1, and test N-B3 over S13, S8 and S3. Strain gauge RC-b is directly located under travel lane N-B2 at midspan. Recording of strains and AE started simultaneously several seconds before the truck entered the span. At the time of entering; a time mark was executed to identify the start of loading. Each test is repeated three times and analyzed individually.

3.4.3 Structural Response

The structural capacity of the RC slab is determined analytically [ACI 440.R2, 2008] in 3 conditions as found during visual inspection; (a) not corroded; (b) 33%; and (c) 66% steel reinforcement loss. An overview of analytical results of these different states is given in Table 3.20. The load response from the truck is based on a solid slab from the separation crack at PC-8 till the north end, which results in an 11 ft. [3.35 m] wide slab with a height of 18 in. [460 mm] (Figure 3.20). The dead load moment in the center of the slab is estimated with Timoshenko and Woinowski-Krieger [1959] on 15.70 kip-ft/ft. [11.6 kNm/30cm]. Calculations based on beam theory result in 14.76 kip-ft. [10.9 kNm/30cm]. The internal response to the point load of the truck wheel is also derived by Timoshenko and Woinowski-Krieger [1959] on 3.86 kip-ft/ft. [2.85 kNm/30cm] at the location RC-b. This strain gauge lies directly under the path for structural and AE evaluation.

Table 3.20 - CFRP strengthened RC deck capacity

Steel loss %	Situation	Moment ft-kip/ft.	EI lb/in^2/ft.	w midspan in.	V_c kip
0%	Cracking	22.825	8.11E+10	0.032	23.75
	Yielding	80.99	5.22E+09	1.761	
33%	Cracking	21.789	8.40E+10	0.029	
	Yielding	67.88	4.51E+09	1.707	
66%	Cracking	20.62	8.85E+10	0.026	
	Yielding	54.56	3.76E+09	1.648	

The loading path is translated to influence lines (Figure 3.21). Corresponding bending and shear responses are given for different truck locations rolling from East to West with one or two axles on the span. The moment including dead and live load is indicated with the solid line. The moment solely including the live load; with a dashed line. The dead load moment location RC-b is smaller than the moment in the center of the span. This moment is goniometrically transposed to location RC-b and results in 10.65 kip-ft/ft [7.85 kNm/30cm]. The back axle with 3.61 kip [16 kN] positioned in the center of the span, is found dominating on this crawl path to give highest moment of 3.86 ft-kip/ft [2.85 kNm/30cm], which translates as 14.5 ft-kip/ft [10.7 kNm/30cm], including the dead load. Measured strains are compared with live load analytical strains in the span center as a function of time. The estimated maximum moment is approximately 18%, 21% and 27% of the yielding moment for the section with 0%, 33% and 66% steel loss.

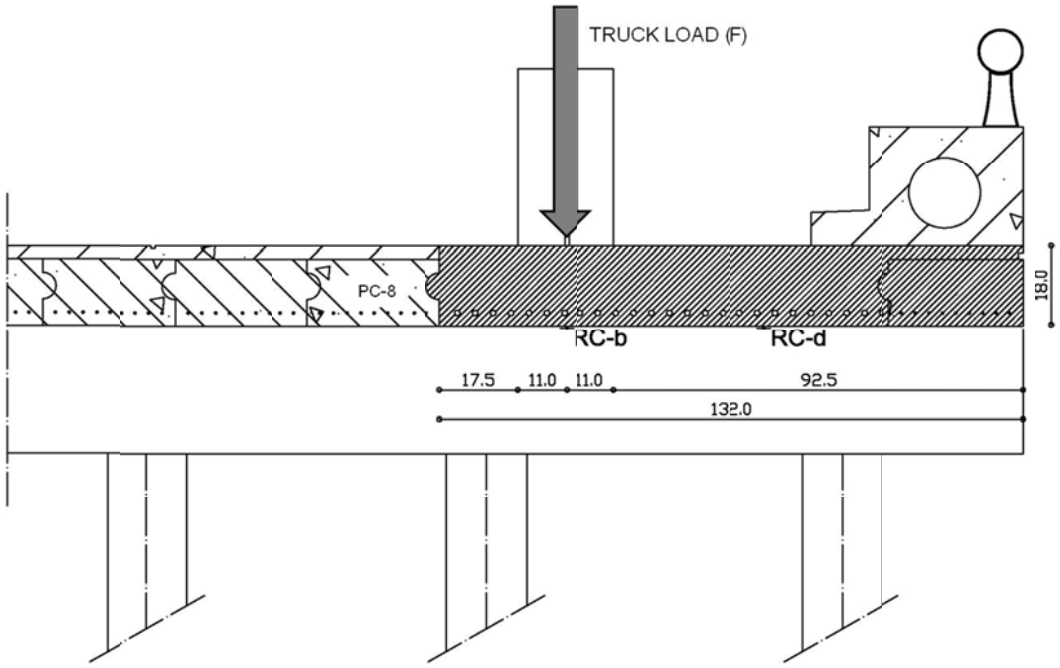

Figure 3.20 - Slab section and load position

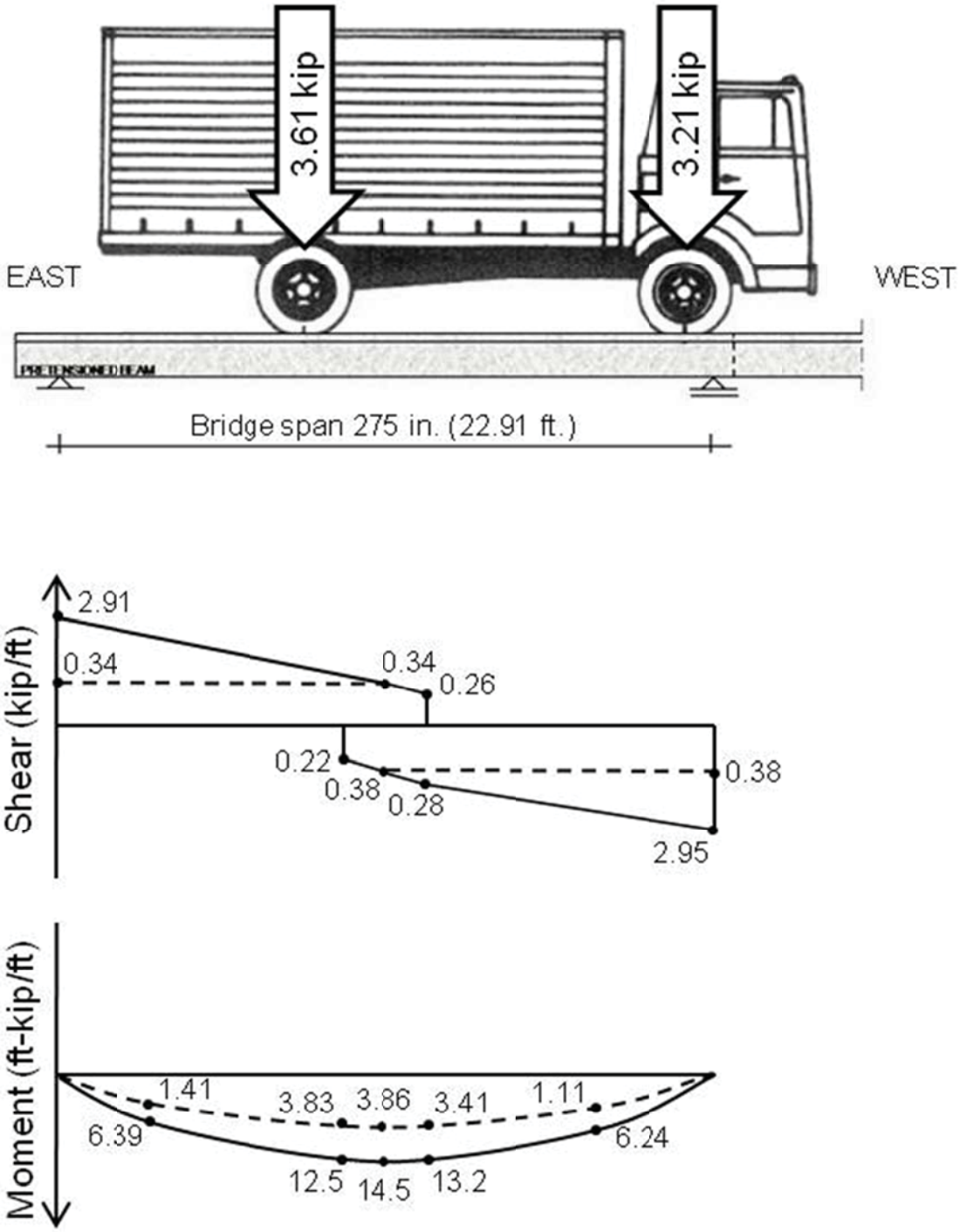

Figure 3.21 - Influence lines

3.4.4 Results and Discussion of Strain and AE Relation

Filtering by Linear Moving Average of 100 samples offered a smoothened strain evolution without losing important characteristics, like magnitude, time accuracy and peak [Sanayei et al., 2010-2]. Different sampling amounts are evaluated and compared in Appendix II.J. The recording sample rate of 100 Hz and average test duration of 20 seconds made sure no important characteristics were lost. The Moving Average method is similar to a digital low-pass filter [Chen et al., 2009]. As previously done by Sanayei et al., a strain vs. time relation was found by translating the implemented load of the truck for location and speed into its resulting strain response for a 3-span continuous bridge [Sanayei et al., 2010-3]. This method allows for direct comparison between measured strains and analytical strains as shown in Figure 3.22. This figure shows strains expressed over time of the crawl speed truck load test N-B2a in the experimental field program. This test is most representable for its travel path which is directly located on top of strain gauge RC-b and AE sensors. Appendix II.K shows all other test recordings. In the figure, strains of RC-b and RC-c are shown. Similarities in the evolution of time and the occurrence of peaks are recognized.

The figure also shows analytical strain for two possible conditions estimated with 66% remaining steel reinforcement: (a) cracked section, and (b) uncracked section. These two conditions are given as the strain gauge can be positioned on three possible locations, being (i) on top of an existing crack, (ii) directly next to an existing crack, or (iii) far away from cracks. These three locations influence the strain readings directly where in the first location (i) the strain readings would correspond to a cracked section (a) as the crack would open during testing and result in higher strains. The second location (ii)

would result in a zero reading of strain as the stresses would be carried solely by the steel which results in zero strain at the external edge of the crack. And finally, the third location (iii) would result in strain reading as if the section is uncracked (b). Because the deck soffit is covered with CFRP laminates, location (i) and (ii) would also require local debonding of laminates. It appears from Figure 3.22 that the strain gauges were not located on top or in the vicinity of a crack.

The shape of analytical strain evolutions shows two peaks (Figure 3.22). The first positive slope corresponds to the front wheel entering the bridge after 1.5 seconds and rolling until midspan from East to West with a constant speed of 2 mph [0.89m/s], where the second largest positive moment and corresponding strain is reached. After a small symmetric down slope, when the front wheel has passed the center, the back wheel enters the bridge to increase the moment with a positive slope. At the time instant the positive slope changes into a steeper slope, the front wheel has left the bridge span and the back wheel starts to move towards the center of the span. At the second peak the back wheel is positioned exactly at the center of the span where the largest moment occurs and the largest midspan strains are measured. A final down slope follows as the back wheel leaves the bridge span.

Significant correlation between the analytical and measured strains is observed in Figure 3.22. The light blue line represents the strain measured directly under the truck load path which shows most correlation in terms of strain magnitude, especially in the second and highest peak. The strains measured in the other tests are given in Appendix II.K which show similar results and all stay in the range of 0 to 7 μ-strain.

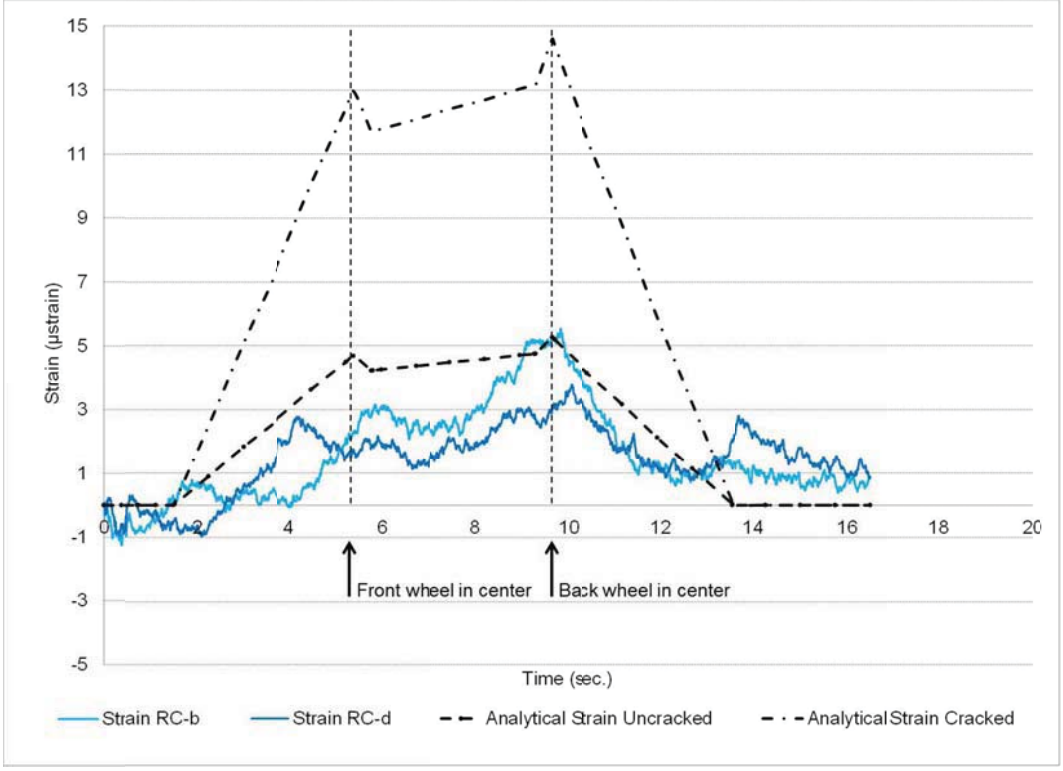

Figure 3.22 - Measured and analytical strains (N-B2a)

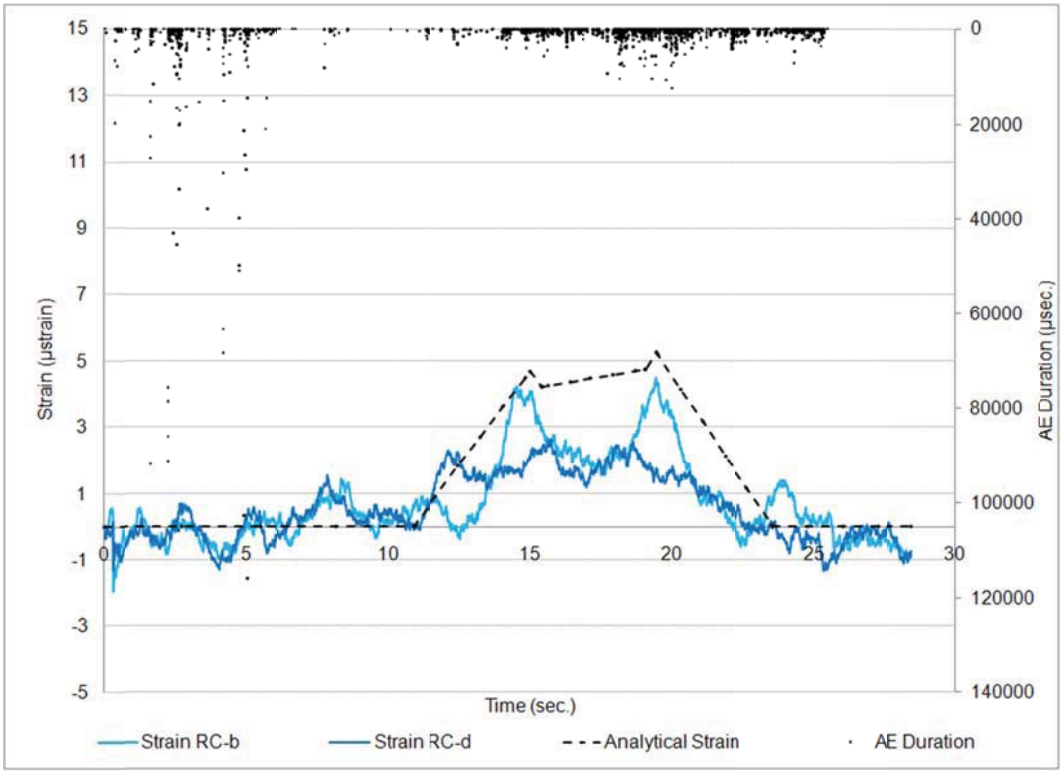

Figure 3.23 - Strains and unfiltered AE Duration (N-B1b)

Nair and Cai [2010] describes that in general, AE can be classified into primary and secondary emissions, where primary emissions are those originated from within the material of interest, while secondary emissions refer to all other emissions generated from external sources. AE signal sources cannot always be identified. The lower bound loading doesn't give the expectation of concrete cracking, but in the case that steel reinforcement is partially lost, it appears that the composition of damaged and repaired concrete, strengthened with CFRP fibers show more AE signal activity as if they need to contribute more to the structure's strength capacity [Suma et al., 2010; Mirmiran et al., 2000]. By analyzing the data, it was found that a distinction can be made by looking at the AE data collection before and during the span loading.

Figure 3.23 shows an example (Test N-B1b) where hits with long Duration (>13,000) were recorded before the truck entered the span, as was also seen in the field concrete bridge test of Golaski et al. [2002]. In the graph, strain (μ-strain) is given on the left axis to indicate the loading pattern of the span with the horizontal time axis, while the AE Duration (μ-sec.) is given upside-down and measured on the right axis but following the same time progression. This approach of combining graphs is chosen to show events at time instances without overlapping points and lines. The Duration of a wave signal is specified as the length of time of a pulse wave, measured in μ-seconds, between the AE signal starts and the AE signal ends but limited by the threshold [ASTM E1316, 2010]. Long Duration signals before loading were also found in tests N-B1a, N-B3a, and N-B3b with characteristic Durations above 15,000, 9000, and 9000 μ-seconds respectively. As the bridge was not loaded and free of traffic, signals with this type of Duration were identified as secondary emissions and digitally filtered with AE-Win software.

Amplitude is analyzed as first indicator of AE activity (Figure 3.24). The right side vertical-axis expresses Amplitude in a range of 40 dB (threshold) to 100 dB (recording limit). The first peak Amplitude of 62 dB at t=3.75 seconds is recorded during the first positive strain slope. During the second positive slope, a new but slightly lower peak Amplitude of 58 dB is measured at t=7.14 seconds when the strain magnitude is increasing and shows an irregularity with a peak performance. The highest peak Amplitude of 67 dB is found at t=9.11 seconds. This peak occurs when analytical strain overtops the first peak and when measured strain shows peaks. A last Amplitude peak of 56 dB at t=9.76 seconds is recorded when measured and analytical strains have a highest peak when the back wheel is at the span center to implement the highest moment. Signal Amplitude intensity decreases as moment and strain responses decrease. Similar load and AE activity relations were found by Korenska et al. [2008] during a concrete bridge load test where the focus remained on frequency analysis.

The magnitude of Amplitude gives the impression of being relatively low compared to laboratory conducted beam tests (Study III). Concrete bridge field tests of Golaski et al. [2002] and Nair and Cai [2007] conclude that AE Amplitudes recorded on field bridges below 55 dB indicates no danger for the structural integrity while strong AE hits exceeding 80 dB indicate a critical value for danger. All crawl tests performed recorded peak Amplitudes higher than 55 dB and lower than 80 dB, except Test N-B1b with a hit of 80 dB at t=19.98 sec. Results of Amplitude and strain of all tests show similar results and are given in Appendix II.K.

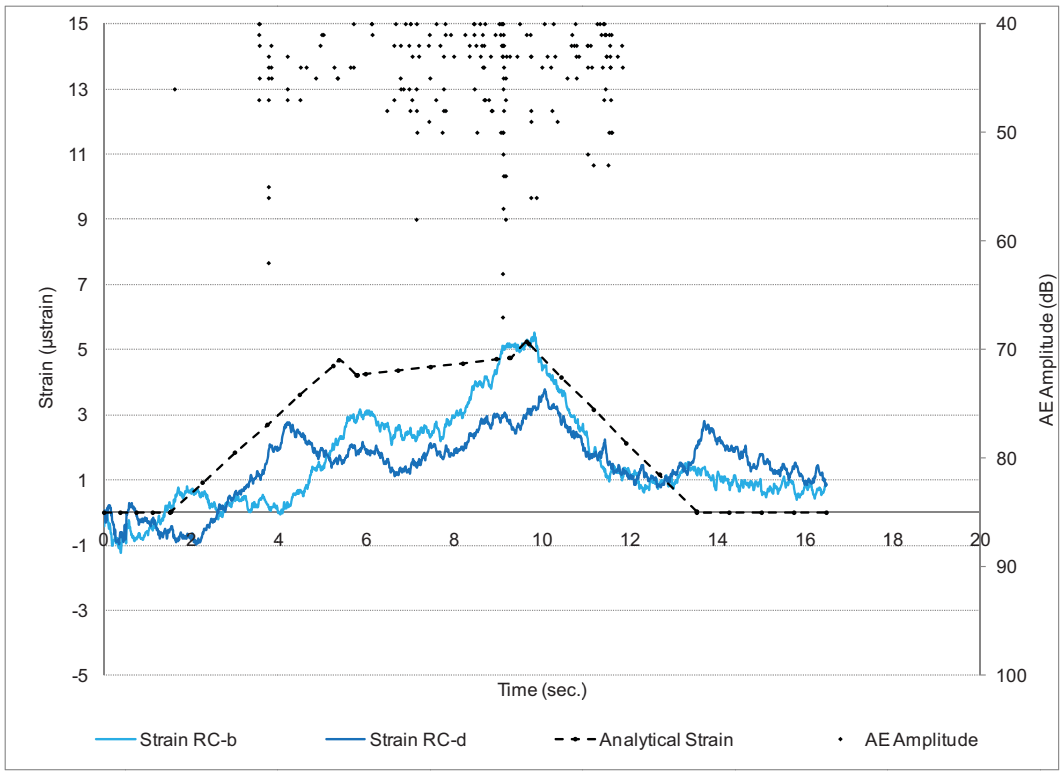

Figure 3.24 - Strain and AE Amplitude (N-B2a)

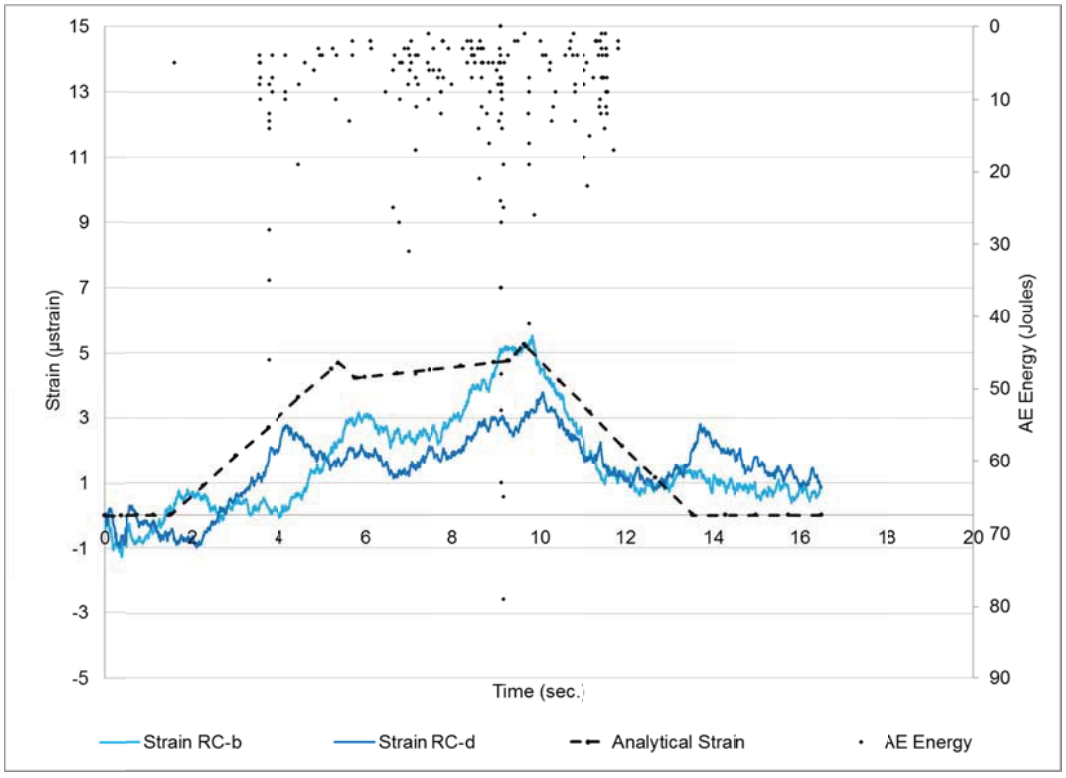

Figure 3.25 - Strain and AE Energy (N-B2a)

Another indicator of signal intensity is Energy (Joules) which is given in the same context as the previous graph in Figure 3.25. Energy is expressed upside down in Joules on the right axle and similar behavior is found. Energy of a wave signal is evaluated as integral of the volt-squared function over time [ASTM E 1316, 2010]. In other words, Energy is an integral function of Duration and Amplitude where the area under the Amplitude wave peaks is calculated over the length of the wave signal duration [Nair and Cai, 2010]. When signals have high Amplitude and long Duration, calculated Energy is high. When signals have low Amplitude and long Duration, the Energy is also high. As long Duration signals were previously indicated as secondary emissions, caution is advised by interpreting Energy to assess the AE signal rating. High Energy hits are recorded at the same time instances high Amplitudes are recorded. In this case, Energy verifies the intensity of the AE signals to indicate important events with primary status.

The duration of AE hits is given in Figure 3.26. where the same concept of graph interpretation is used with the AE Duration on the right side axis expressed in μ-seconds. Comparing this graph with Amplitude recording (Figure 3.24) and Energy (Figure 3.25), a relationship can be found between high Amplitude, high Energy and long Duration of the event at t=9.11 seconds. When all three parameters have relatively high values, it is likely that an event with high intensity took place and is most likely a primary event from within the structure. Primary events occurring within the structure may come from different possible sources, such as concrete cracking, crack opening and closing, crack propagation, concrete patch movement in separation cracks, CFRP laminate debonding, CFRP fiber stretching or moving friction, resin cracking or local yielding, or resin slip. Some are more likely to occur than others considering the load magnitude.

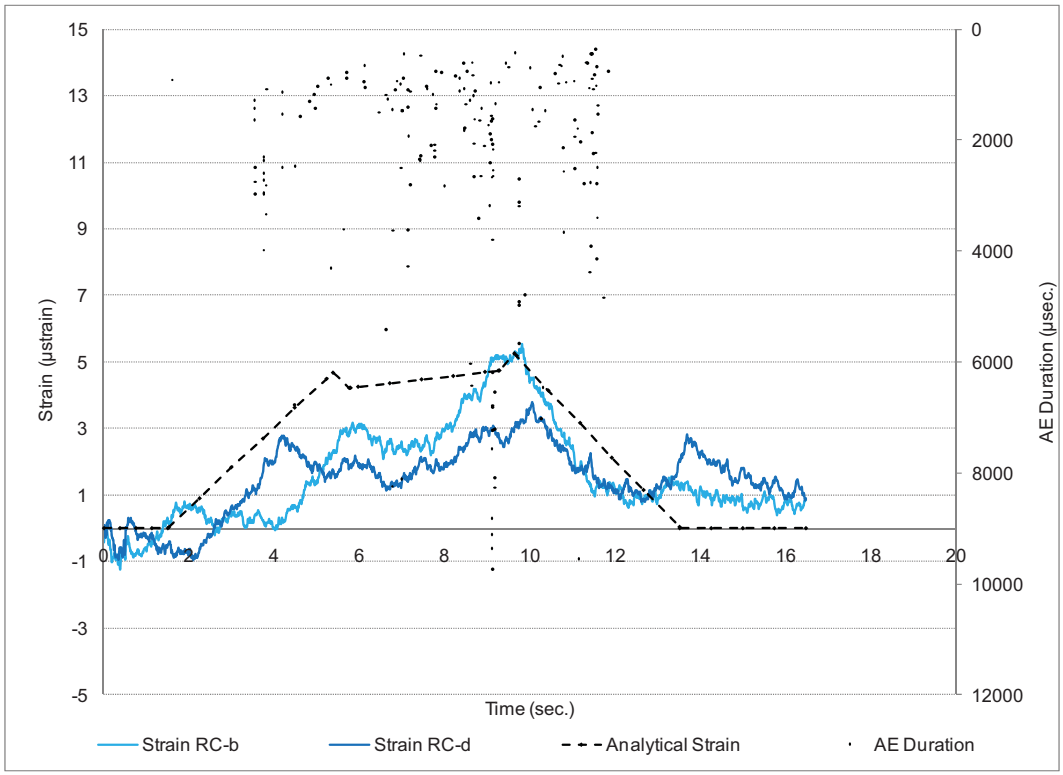

Figure 3.26 - Strain and AE Duration (N-B2a)

Cumulative Hits and Cumulative Energy are given in Figure 3.27 and 3.28, where similar setup of graphs is used to show the AE parameters on the right side axis. These graphs do not have an upside-down vertical right side measurement. As seen in the figures, both graphs have a normalized cumulative axis which allows for trend comparison of different tests (Appendix II.K). Both graphs show similar behavior and at the time instant t=9.11 seconds, the highest increase occurs. This vertical jump includes about 15% of the recorded hits and about 30% of the total Energy. Not only do the highest intensities for Amplitude, Duration and Energy occur during this event, but also an increased Number of Hits independent of magnitude and intensity. The two events at earlier times, t=3.75 and t=7.14 seconds, are recognized by both Cumulative Hits and by the Cumulative Energy by respectively about 10% of total Hits and about 10% of total Energy for each event. The peak previously mentioned at the highest strain recording at t=9.76 second shows a smaller increase of an estimated 3% of total hits and 5% of total Energy. Together with the lower recorded Amplitude of 56 dB, this signal should still be classified as a primary emission, but with a lower indication of danger.

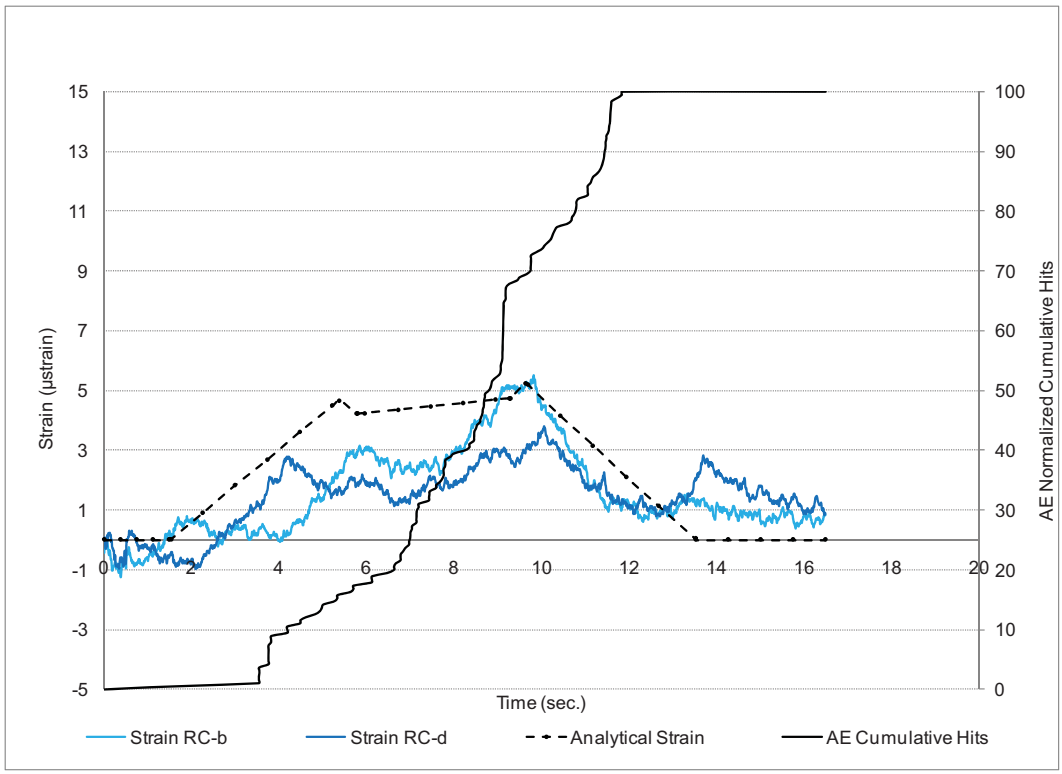

Figure 3.27 - Strain and AE Normalized Cumulative Hits (N-B2a)

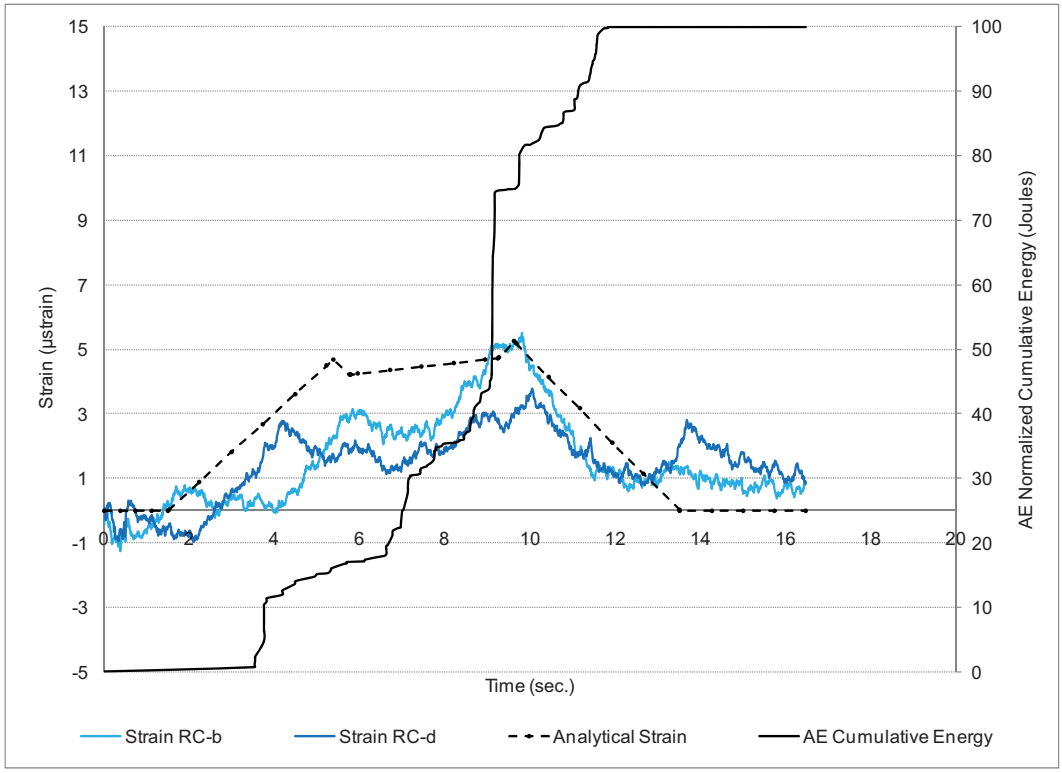

Figure 3.28 - Strain and AE Normalized Cum. Energy (N-B2a)

3.4.5 Results and Discussion of Spatial Analysis and AE

A selection of areas with the highest potential damage at the level of 7 or more on a 1 to 10 scale was made in the end of Part 1 of Study II. These most concerning cells are found in the clustered area K-M-1-5 and cell K-12. These locations are on top of or in the vicinity of Sensor 1, 3, 4 and 6 for the clustered area in the South-West side and Sensor 13 for the single cell K-12 in the South-East corner (Figure 3.29). The analysis to find spatial correlation of between AE activity and physical spatial analysis results is approached by stating a hypothesis. The hypothesis states that higher AE activity is found in areas and cells rated with high potential of physical damage. This is tested by means of the AE parameters Amplitude, Energy, Duration and Number of Hits through numerical evaluation of the statistical identities peak, sum and average to find spatial correlation.

Each truck crawl speed test is analyzed where peak, mean and sum were calculated. AE data was filtered in AE-Win software to only include data points from the time instant the truck entered until it left the span. Table 3.21 gives an overview of selected parameters to establish comparison for correlation. The first column gives the peak Amplitude of each test, followed by the mean value which is calculated by dividing the parameter's sum by total Hits. Similar approach is used for Energy and Duration. The last column, Number of Hits, shows first the Sum to show the total activity of each test and then the Number of Hits per second for the time span the bridge was loaded. Evaluation of this data is performed by complying with similar viewpoints as was done in strain and AE comparison. The Amplitude is found to be most significant for the highest peak coupled with the highest mean of each test and test cycle. For example in travel path N-A1 this was found to be Test N-A1b and is identified in the table by *italic* and **bold** font.

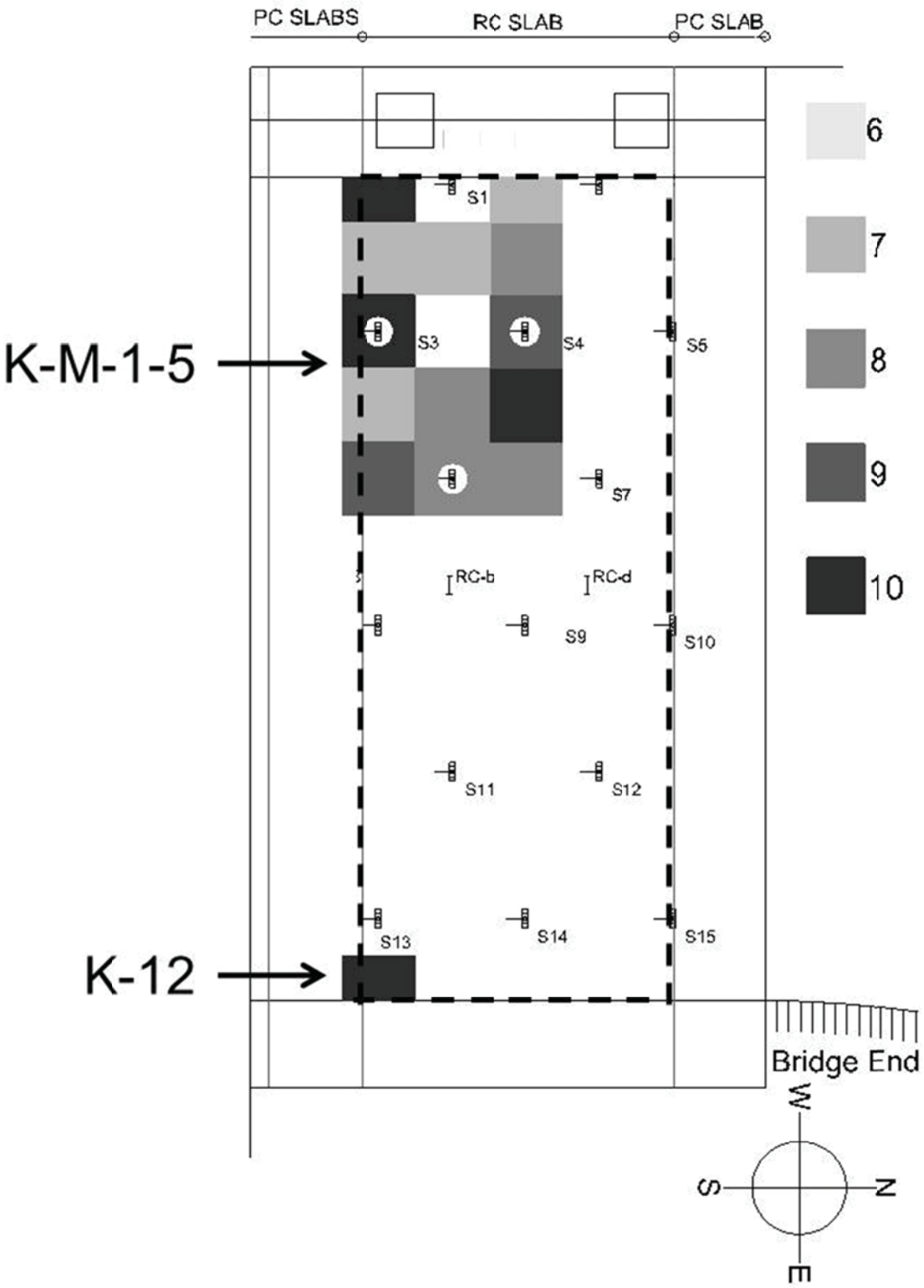

Figure 3.29 - Potential damaged areas and sensor locations

Table 3.21 - AE Peak and mean values selection per test

	Amplitude (dB)		Energy (J.)		Duration (μsec.)		Nr. of Hits	
Test	Peak	Mean	Peak	Mean	Peak	Mean	Sum	Mean
N-B1a	69	47	167	17.3	9414	2756	39	1.37
N-B1b	***80***	***45***	***513***	***17.1***	***7774***	***2200***	52	1.83
N-B1c	65	45	72	9.2	9478	2624	***49***	***2.06***
N-B2a	67	17	***79***	***3.2***	***9736***	***816***	***113***	***6.85***
N-B2b	***61***	***44***	75	7.6	8914	1242	36	1.84
N-B2c	58	43	58	9.5	8349	2467	19	1.02
N-B3a	58	46	33	13.1	7553	2594	17	0.81
N-B3b	***71***	***45***	86	9.7	***8242***	***2386***	***31***	***1.29***
N-V3c	67	43	***146***	***14.9***	12028	1954	17	1.13

Table 3.22 - Sensor selection highest AE activity per test

		Crawl Speed Tests (N)								
		B1a	B1b	B1c	B2a	B2b	B2c	B3a	B3b	B3c
Peak	Amplitude	4	6	13	6	6	13	6	13	8
	Energy	4	6	13	6	6	13	3	13	8
	Duration	6	9	13	3	9	6	3	13	8
Cumulative	Amplitude	1	1	1	1	3	1	3	13	3
	Energy	1	6	1	6	3	1	3	13	8
	Duration	1	1	1	6	1	6	3	13	6
	Hits	1	1	1	1	3	1	3	13	3
Result	Peak Sensors	4	6	13	6	6	13	3	13	8
	Cum. Sensor	1	1	1	1	3	1	3	13	3

For test cycle N-A2, the highest Amplitude is found in N-A2a, but the accompanying mean was significantly lower and selection of N-A2b seemed more reasonable. Energy is evaluated similarly for highest peak together with highest calculated average. Duration, on the other hand, is a parameter related to Amplitude and Energy. This parameter is more significant when relating Amplitude and Energy are high and when Duration is

lower in peak and mean value. Tests are selected in correspondence to this evaluation to exclude secondary emissions, and needs to be considered as a subordinate evaluation criterion. Last evaluation parameter is Number of Hits, which creates dominancy for highest sum and mean. This identity is also a subordinate parameter as the Number of Hits may include secondary emission hits.

To locate high activity per sensor, peaks and summation of each parameter was used to establish a selection of the most active sensors during the tests. Table 3.22 shows the parameters used in this evaluation and are created in a similar fashion as Table 3.21. In the row labeled “peak”, sensors that have highest peaks are listed. Analyzing the numbers, it is found that most of the tests indicate the same sensor for peak in Amplitude as in Energy. Only Test N-B3a doesn’t comply with this statement, but after analysis of the peak data for Amplitude and Energy in Figure 3.30 and 3.31, it appears that Sensor 3 has a peak value of 57 dB which is one decibel lower than the peak of sensor 6 where the Energy related to this hit is three times higher for sensor 3 (Figure 3.31). For this reason, sensor 3 in Test N-B3a is chosen as most active and more significant.

The next row shows cumulative values for all the parameters including Number of Hits. The tests N-B1a, N-B1c, N-B2b, N-B2c, N-B3a and N-B3b all agree on the highest sums of Amplitude, Energy and Number of Hits. Test N-B1b and N-B3c follow the sensor numbers with highest frequency of dominating sum. Test N-B2a shows only high Energy related with long Duration. Therefore, high Amplitude is a more important parameter on this occasion. The dominating sensors for both peak and sum evaluation are repeated in the last row (Table 3.22) named “results” to point out the sensors with highest activity.

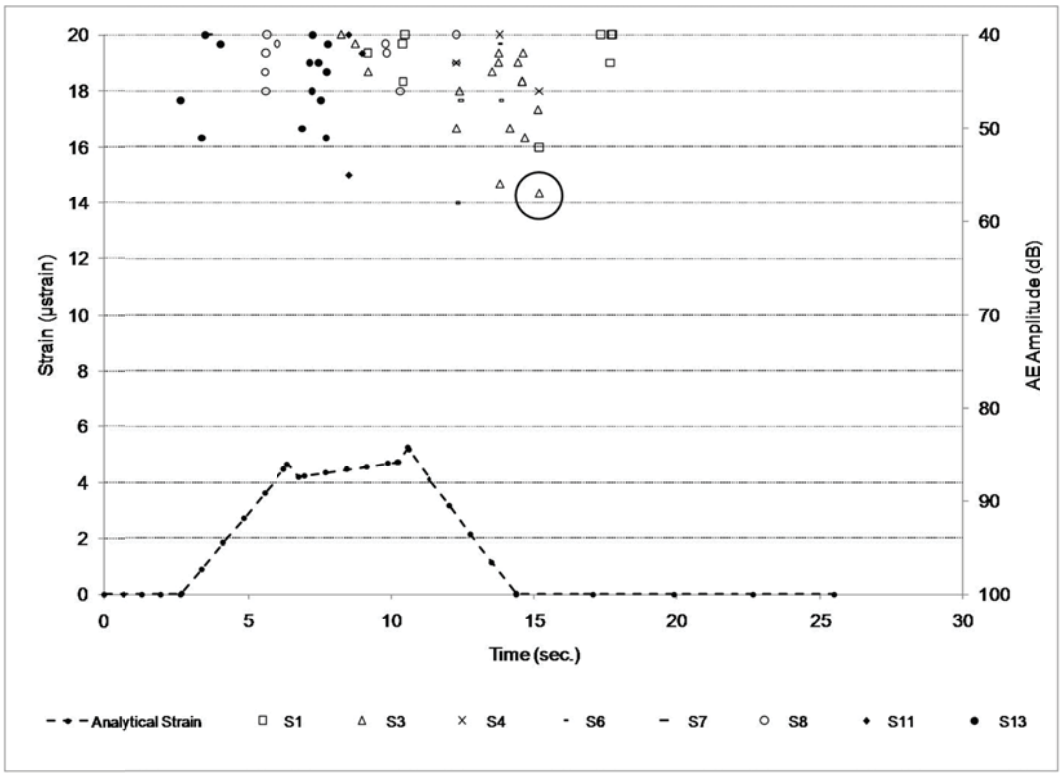

Figure 3.30 - AE Amplitude hits per sensor (N-B3a)

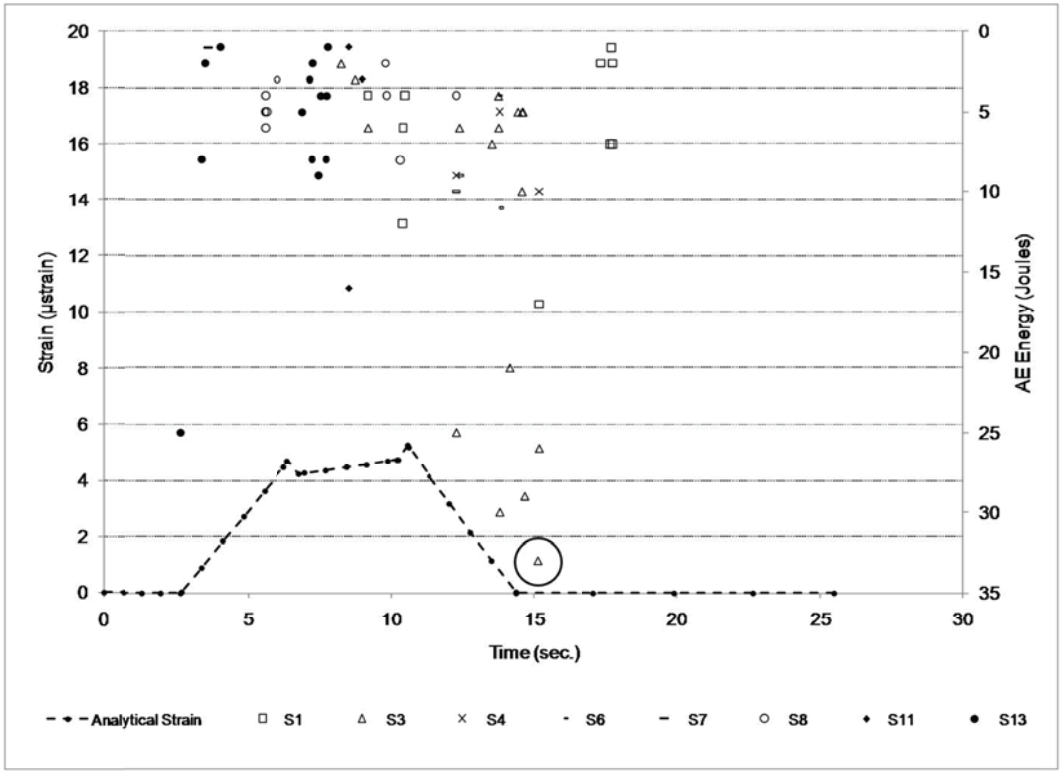

Figure 3.31 - AE Energy hits per sensor (N-B3a)

Due to the numerical complexity and high number of tests and data, visualization offers more understanding of correlation between the most active sensors and specific areas listed for the highest probability of damage. Figure 3.32 shows the same grey scale signature for potential damaged areas as in Figure 3.13 and 3.29. In addition, the crawl speed load test travel paths are added and each sensor listing in Table 3.23 is marked with a circle around the specific sensor for both highest peak activity and highest cumulative activity. The same color code is used to identify the three different load paths together with the most active sensor responses. This method offers clear evaluation of sensor activity correlated with the travel path and with the highest damaged potential areas.

The first travel path N-B1 (magenta) shows 3 circles for the most activity in sensor 1 and 3 single circles for sensor 4, 6 and 13. Sensor 1, 4 and 6 lie in the clustered area of concern and sensor 13 is close to cell K-12. The second travel path N-B2 (blue) shows two circles in sensor 1, 2 circles in sensor 6 and 2 single circles in sensor 11 and 13. Here the travel path is followed, but again more circles are found in the clustered area for high damage potential and close to cell K-12. The last travel path N-B3 shows 3 circles in sensor 3, 2 circles in sensor 13 and a single circle in sensor 8. The travel path is followed with AE activity, but the highest activity is found in the clustered area and the sensor closest to cell K-12.

In overall perspective, the figure shows that with three equal travel paths at different locations, most activity was found in the clustered area K-M-1-5. Sensors 3 and 4 are on top of cells ranked at level 9 and 10 on scale 1 to 10 for damage potential where sensor 4 is the only sensor with high activity in the travel path going over sensor 4, 9 and 14.

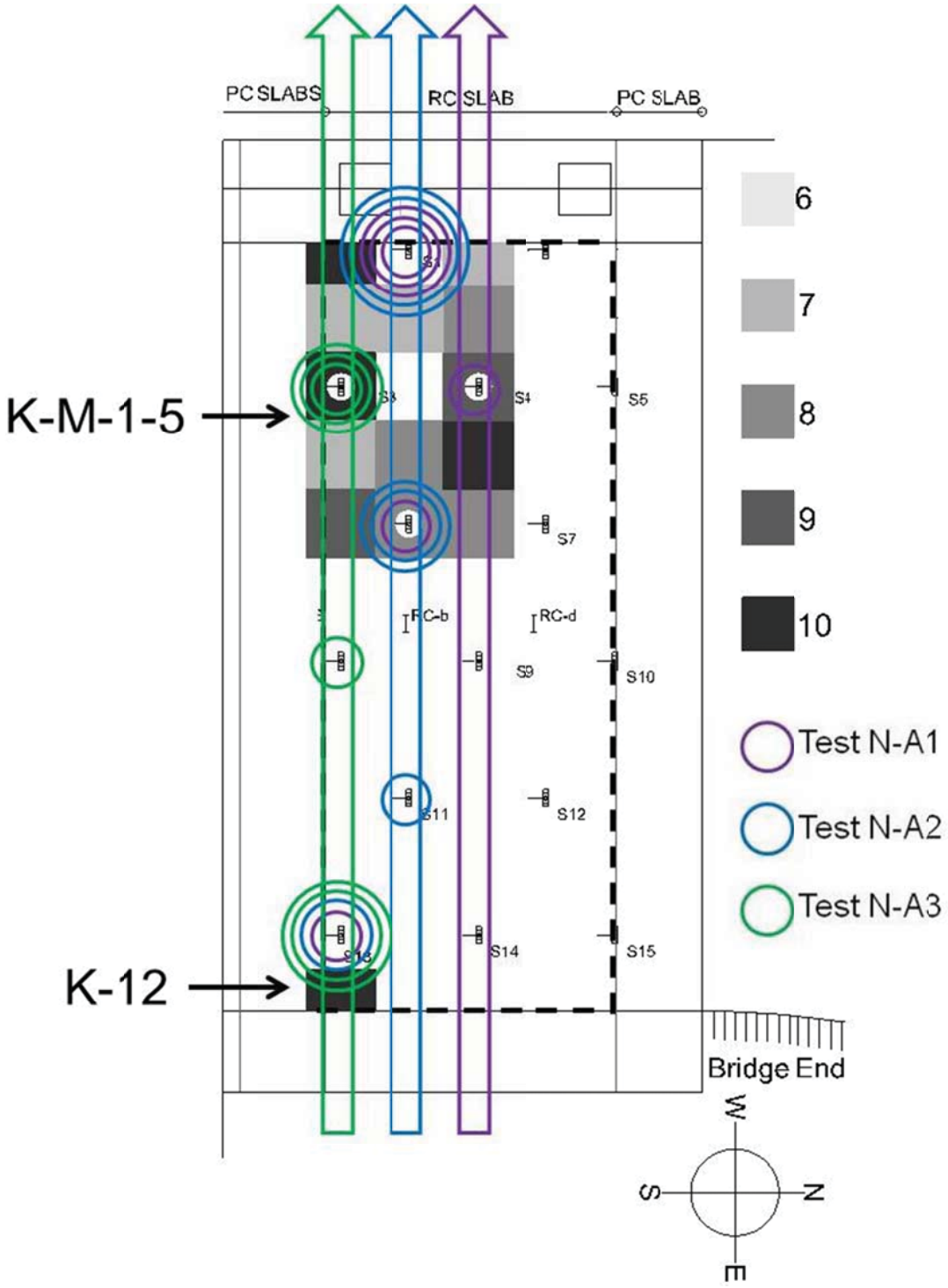

Figure 3.32 - Most active sensors per crawl speed test

Sensor 6 is on top of a cell ranked at level 8 on scale 10 and has a relatively high number of circles (3). Sensor 1 and 13 have the highest activity of all sensors and find themselves next to cell K-1 which is ranked with damage potential level 10 on a scale of 1 to 10. One might consider that the supports create secondary emissions by friction which may create peak hits and cumulative high activity, even though these type of emissions have low Amplitudes (<55 dB) with long Durations (>~15,000). If this was the case, sensor 2 and sensor 14 should also have been selected for high activity. Finally, while midspan flexure was found to be the dominant mechanism for structural activity, the sensors in the midspan zone did not show extensive activity, although the sensors in the zones with high damage probability did. For these reasons, the hypothesis is accepted as true.

3.5 Conclusions

- Performing spatial analysis prior to AE monitoring enables to locate areas of concentration for deeper assessment and with a smaller number of AE sensors on predetermined areas;
- Combination of physical assessment results by spatial analysis enables to indicate corrosion and concrete damage probability for areas that are concealed and give no visual access;
- Numerical AE signal activity correlation with spatial assessment outcomes could be performed with the parameters Amplitude, Energy, Duration and Number of Hits;
- Clustered South-West area (unrepaired) and cell K-12 on the South-East side which were rated as having a high probability of concrete and corrosion damage

by the spatial analysis showed significantly higher AE activity for sensors placed on top or in vicinity of these regions;

- Repaired area with a lower probability of concrete and corrosion damage did not show as much AE activity as unrepaired areas;
- Nondestructive service level loading by means of crawl speed truck tests were able to indicate time and intensity relationships between strain and AE parameters;
- Attenuation testing offers a tool to investigate the composition and repair quality, independent of its composition and history, by AE signal conductivity on visually unreachable and undetectable areas covered with CFRP laminates;
- Parallel, diagonal and signal transmission in random direction compared to the double layered CFRP fiber matrix did not show noteworthy differences in Amplitude attenuation;
- ArcGIS appears a useful and accessible tool for assessments with layered maps and large numbers of data points.

Chapter 4

4. Study III - CFRP Strengthened RC Beams at Different Corrosion Stages

Synopsis

Laboratory experiments are performed to simulate bridge field conditions with respect to reinforcement corrosion. Four RC beams are tested at various stages of corrosion. Section dimensions are 6 by 12 in. [150 by 300 mm] with a total length of 12 ft. [3.65 m], reinforced with three steel #4 bars [12.7 mm] and 1 in. [25 mm] cover. Three different corrosion stages of steel reinforcement were induced by a voltage and different time durations. A nondestructive evaluation program included visual inspection, pH level, concrete carbonation, active corrosion potential, chloride content, mapping of cracks, and AE attenuation conductivity. A spatial analysis of combined evaluation layers is performed to identify the most severe concrete damage locations and most probable failure locations under loading. A repair of laboratory specimens is performed after corrosion; removing of spall and loose fitting concrete without replacing steel reinforcement, patching with grout, and strengthening with two plies of CFRP laminates. The four beams are subjected to four-point bending load tests, starting from relatively low loads and increasing until failure. AE and physical assessment outcomes are used to indicate inferior areas and compare to the eventual failure location. Beams at different stages of corrosion damage showed different failure modes with essential impact on

repair success. The laboratory tests are used to calibrate readings from various tests with actual deterioration/damage for a better understanding of similar measurements on deteriorated full-scale bridges.

4.1 Background

Steel reinforced concrete beams and slabs exposed to salty and ocean environments are subjected to increased concrete damage and deterioration due to accelerated steel corrosion progression. Corrosion of steel reinforcement is one of the major causes affecting the long-term performance of reinforced concrete (RC) structures [El Maaddawy and Soudki, 2003]. Over the last 50 years, extensive research and a considerable number of papers have been produced to understand the corrosion process and the cathodic and anodic reactions [Broomfield, 2007]. In particular, chloride induced corrosion is recognized as the most common cause of degradation of reinforced concrete as many concrete structures are exposed to marine environment or extensive use of de-icing salts [Angst et al., 2009].

To address steel reinforcement corrosion, an emerging alternative has been found in the use of fiber reinforced polymers (FRP) for both rehabilitation and new construction [Nanni, 2000; Van den Einde et al. 2003; Bakis et al. 2002]. Glass fiber (GFRP), carbon fiber (CFRP) and Aramid Fiber Reinforced Polymers (AFRP) are materials commonly used for strengthening applications where in-service durability is key [Hollaway, 2010]. Some successful applications for rehabilitation include externally bonded CFRP rods for bridge deck strengthening [Nanni, 2000], confinement and wrapping of circular and non-circular RC columns [De Luca et al., 2010; Rocca et al., 2008], strengthening of masonry walls with FRP bars [Galati et al., 2005], improved shear capacity of RC beams with

external strengthening sheets [Khalifa et al., 1998], external flexural strengthening of RC beams [Ashfour et al., 2004], and enhanced flexural performance with externally bonded CFRP laminates on slab structures [Arduini et al., 2004].

4.1.1 Literature Review

Previous work on the structural testing of specimens with different corrosion damage levels strengthened with an external reinforcement layouts are studied to develop a base line of expectations. El Maaddawy and Soudki [2005] compare the strength behavior of corroded, uncorroded, unrepaired, and repaired in two different schemes of flexural strengthening, of RC beams with dimensions 6 by 10 in. [150 by 250 mm] and length 10.5 ft [3.2 m]. The testing program consists of corrosion conditioning with and without sustained loading, followed by four-point bending testing. Induced corrosion levels have a range of 8.7 to 30.5% steel mass loss, measured after failure. Concluded is that CFRP repaired corroded RC beams have increased ultimate strength compared to uncorroded, unstrenghtened beams. Soudki et al. [2007] investigate 11 RC beams; 6 by 10 in. [150 by 250 mm] and 8 ft [2.4 m] length. The research program consists of accelerated corrosion by means of wetting-drying cycles in the presence of salt with electrical potential measurement of active corrosion, followed by four-point bending to failure. Masoud et al. [2001] performed structural load tests on corroded specimens by monotonic loading. Six beams are strengthened with a single CFRP ply and corroded, while one is uncorroded-unstrengthened, with dimensions 4.7 by 6.9 in. [120 by 175 mm] and 70.8 in [1.8 m] span. The ultimate monotonic load of strengthened-corroded specimens increased 37 to 87% above the unstrengthened-corroded specimen. The corrosion level was estimated by Faraday's law on 9% steel mass loss for all specimens. Benjeddou et al. [2007] discuss

failure mechanisms of experimental studies with damaged RC beams externally CFRP strengthened. Four-point bending tests are conducted on beams with dimensions 4.7 by 6 in. [120 by 150 mm], spanning 6 ft [1.8 m]. The laminates' width results in different failure mechanisms where 2 in. [50 mm] wide single CFRP plies result in interfacial debonding and 4 in. [100 mm] wide strips result in peeling off of the laminate including the concrete cover. These studies all use single sheet CFRP plies and do not include spatial analysis with nondestructive evaluation (NDT) testing and AE monitoring.

An AE monitored study of repaired CFRP strengthened RC beams under four-point bending tests is performed by Degala et al. [2009]. The analysis approach includes Intensity Analysis (IA) which is a time based technique that makes use of the History Index (HI) and Severity (Sr) [Gostautas et al., 2005]. HI is a ratio comparison of signal strength between recent emissions and all emissions. Sr is the average of the largest signal strength emissions, related to new structural damage. Both parameters depend on unique material properties. IA is found suitable for field applications when a high number of sensors are placed. Maji and Sahu [1994] studies AE characteristics of 10 RC beams; 4 by 4 in. [100 by 100 mm] and span 67 in. [1.7 m], under 3 point bending. His findings are that AE sensors placed at midspan on the bottom surface record more AE activity with more intense signals than sensors attached to rebars at the beam ends. Peak activity for Number of Hits occurs after 80 to 90% of the ultimate load is reached. Results indicate that micro cracking is recorded as soon as load is applied. Ohtsu et al. [2002] performs four-point bending on unstrenghtened RC beams by prescribed cyclic loading monitored with AE. The analysis makes use of the Kaiser Effect [Tensi, 2004; Kaiser, 1950] to evaluate sudden increases of Number of Hits in relation to load levels and reload cycles.

4.1.2 Structure of Study III

The structure of the study is found in Figure 4.1. The physical assessment program consist of (A) visual inspection, (B) pH level measurement, (C) concrete carbonation, (D) corrosion potential, (E) chloride content, (F) crack mapping, and (G) AE attenuation conductivity. Corrosion conditioning is induced by an impressed current to establish three different corrosion levels verified by monitoring AE activity and visual inspection. One specimen remains uncorroded. NDT is repeated to discover changes in physical parameters at different corrosion levels. The beams are repaired as per the same repair and strengthening methods as on the field bridge, followed by attenuation testing. Attenuation tests are performed before corrosion and after repair to assess conductivity differences. The fourth and final stage consists of subjecting all four beams to four-point bending where a threefold series of cycling service level loads are built up until failure is reached. The structural tests are monitored for load, strain, deflection at midspan and AE activity.

4.1.3 Objectives Study III

- Assess performance of RC beams under laboratory conditions with corrosion damage, repair, and CFRP strengthening;
- Evaluate AE response in relation to strain, deflection at increasing and repeating load cycle series;
- Evaluate failure modes and ultimate strength of CFRP strengthened RC beams under different stages of corrosion;
- Indicate areas of higher activity by sensor location related to loading type, failure location and areas previously rated for high potential damage.

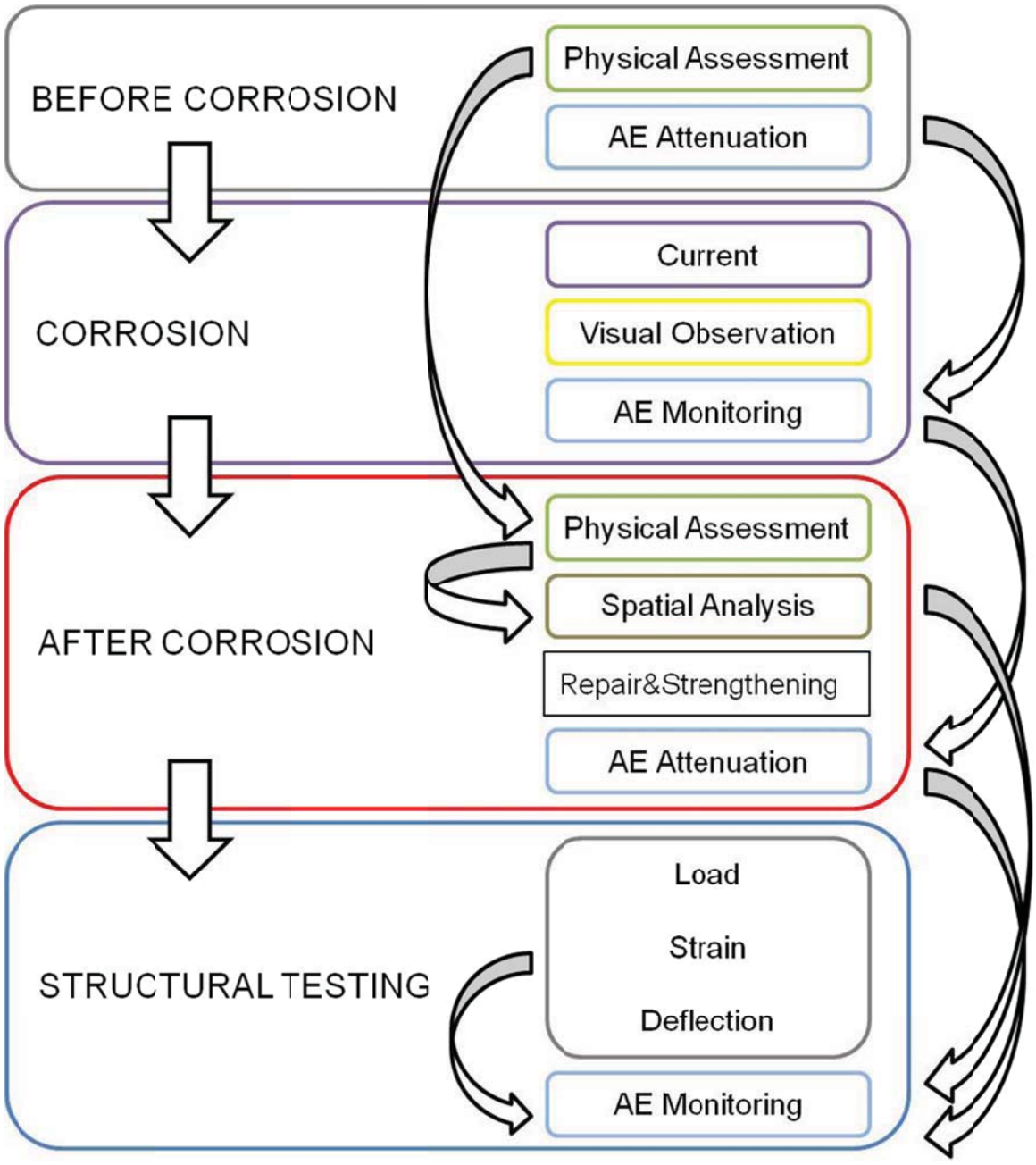

Figure 4.1 - Structure of Study III

4.2 Specimens and Specifications

RC beam specimens with section dimensions of 6 by 12 in. width [150 by 300 mm] and length 12 ft. [3.65 m] with a structural span limited to 10ft [3.05 m] for load testing. The beams were cast in a single batch of Type I Portland cement in May 2008 by a local concrete provider. In 2008, the concrete strength was determined by compression tests [ASTM C39, 2009] on 6 by 12 in. [150 by 300 mm] cylinders for a mean nominal value, f'_c, of 3900 psi [26.9 MPa] [Napoli et al., 2010]. In June 2010, three 6 in. [150 mm] cylinders were cored from each beam to conduct similar tests and provided a mean nominal value, f_c, of 4346 psi [30 MPa] with 13% standard deviation. Steel grade 60 was used for flexural longitudinal reinforcement existing of three steel #4 bars [12.7 mm] with 4 in. [100 mm] spacing and 1 in. [25 mm] concrete cover. The steel reinforcement ratio is determined on 0.98%. Specimens are designed such that no shear reinforcement is required in accordance with the 4 point bending tests. After corrosion, the tension surfaces are strengthened with two plies of CFRP [Table 4.1].

Table 4.1 - Reinforcement material specifications

	Elastic Modulus ksi	Thickness in.	Sectional Area in^2	Ultimate Strength ksi
Steel	29,000	3 #4	0.6	60
CFRP	11,900	0.04	0.96	91

4.3 Evaluation before Corrosion

4.3.1 AE Attenuation Testing

Attenuation tests are performed with the same apparatus and tools as used during the field bridge study; PAC Highway System II, R6I sensors, and aluminum brackets with grease as a contact agent. Detailed specifics can be found in Study II. CFRP laminates were applied on half of the width on the top of the specimens to assess differences in AE signal intensity between plain concrete and a double 0.04 in. [1.02 mm] thick layer of CFRP laminates as transmission interface (Figure 4.2). Sensors are placed at 17.14 in. [181 mm] distance, where sensors S1 to S8 on top of CFRP laminates and sensors S9 to S16 on plain concrete. 0.3 mm pencil lead breaks are carried out in the middle of the sensor spacing at 8.57 in. [217 mm] distances from neighboring sensors on 7 locations in the direction of A to K with a repetition of three times. The longest travel distance is 111 in. [2.82m]. Averages and standard deviations of Beam B0 attenuation tests are presented here, while the attenuation test results of Beam B1, B2 and B3 are reported in Appendix III.A with comparable results.

Figure 4.3 shows the attenuation of AE signal by pencil lead breaks in the form of Amplitude (dB) versus signal traveling distance (in.) made on concrete and CFRP and sensors recording from concrete and CFRP as interface. Standard deviations are given for all values. Dashed lines indicate sensors placed on other materials than where breaks are made. These signals are expected to be lower due to transmission losses by changing media. This only happens for sensors placed on CFRP laminates while breaks are made on concrete. Vice versa, AE amplitude appears to be higher for sensors placed on concrete while recording signals are made on CFRP laminates.

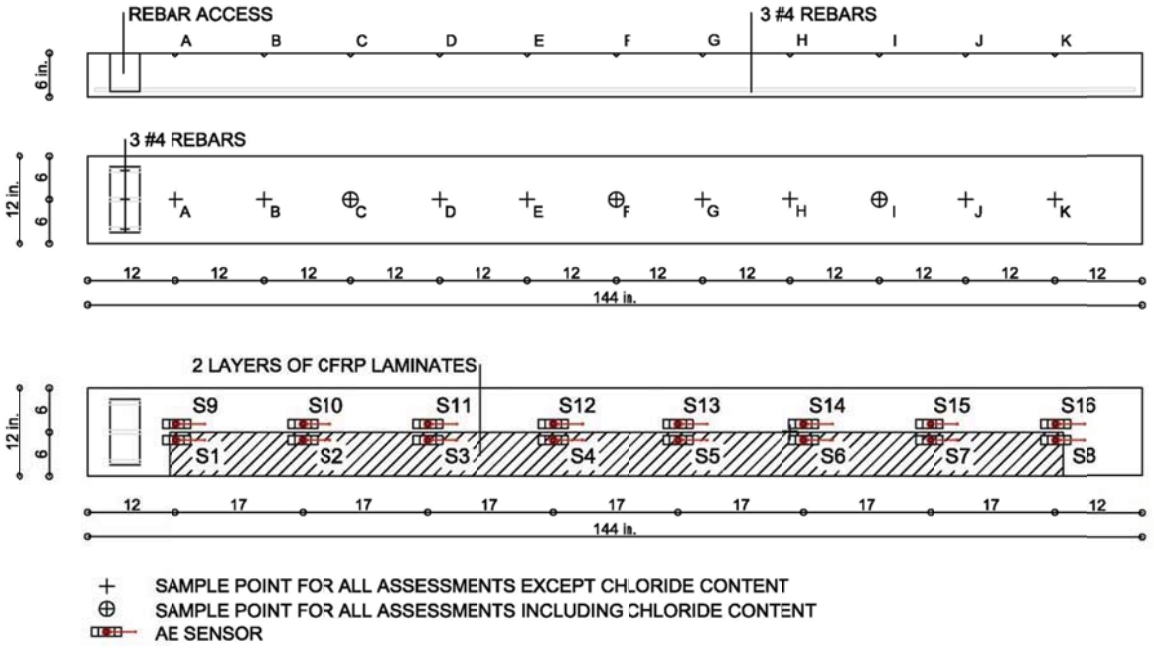

Figure 4.2 - Physical assessment and AE sample points (in.)

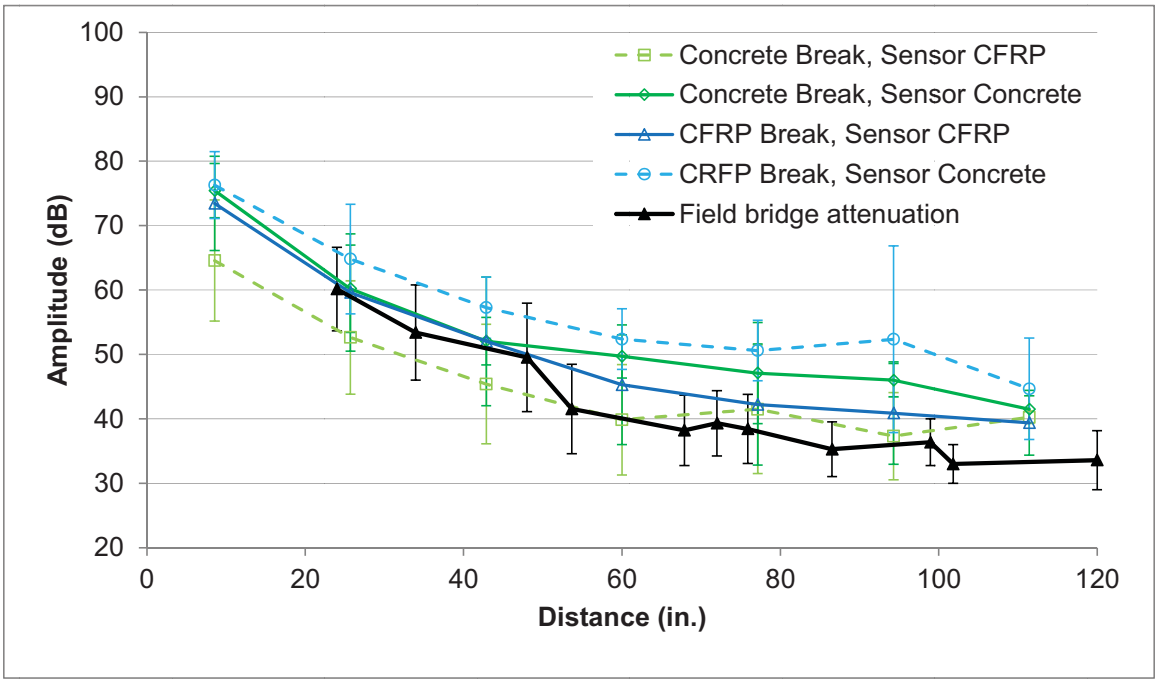

Figure 4.3 - AE attenuation Beam B0

The figure also shows that when a signal travels through its own material, concrete or CFRP, the Amplitude is at approximately similar intensity. Attenuation test results from the bridge test where breaks and sensors are placed only on CFRP laminates (Study II) are also plotted in this graph. The overall trend is recognized with parallel attenuation progress in relation to traveling distance. Up to a distance of 60 in. [1.5m], all sensor are able to record pencil lead break signals and conform the spacing of sensors and threshold of 40 dB. Pencil lead breaks made on the bottom are recorded on average 1 dB lower then on the top surface, traveling through 6 in. [150 mm] thick concrete material.

4.3.2 Physical Assessment Studies

The physical assessment program as performed for the bridge (Study I and II) is repeated on the 4 beams. One difference with the bridge study is that the chloride content layer (E) is included and the thermography layer (H) is excluded in the beam study. Methodology descriptions for each technique can be found in Study I and II. Sampling is performed with 12 in. [300 mm] spacing (Figure 4.2). Chloride content evaluation is limited to sample points C, F, and I. This is assumed to provide enough covering data for the entire specimens. The included physical assessment layers are given below:

A. Visual inspection;
B. Concrete carbonation;
C. pH level measurement;
D. Active corrosion potential;
E. Chloride content;
F. Crack map; and
G. AE attenuation conductivity

Visual inspection (A) before corrosion is limited to the observation that the beams are undamaged and show no visual cracks (F). No evidence for concrete carbonation (B) by 1% phenolphthalein in ethanol solution was detected. pH level measurement (C) was performed from three 5 mg powder samples from 1 in. [25 mm] deep drilled holes. pH level measurements result in values above 9.0, except for location B0-A, B0-J, and B0-K. The detection of active corrosion potential (D) was performed three times. The lowest average potential was found on location B1-A for -289 mV. Chloride samples were collected from the same drill holes and tested at an average temperature of 71.8 F [22.1°C], providing a mean value of 0.028% with standard deviation 0.0175%. All values are below 0.2% [ACI 222.3R, 2003]. AE Amplitude attenuation in relation to distance is translated by counting a maximum of seven recorded hits at each sensor location with a threshold of 40 dB (Figure 4.4). The least conductivity was found at B0-J where one out of seven signals was not recorded. Mean value of deterioration condition in terms of conductivity is 0.06 with standard deviation 0.049 on a normalized scale between 0 and 1. The combined results of physical assessment layers are normalized according to standards introduced in Table 3.3 to 3.9 in Study II. Figure 4.5 shows the combined normalized results of the four beams which, as expected, show a low corrosion damage probability (peak<0.17) before corrosion. Physical assessment results are reported in Appendix III.B.

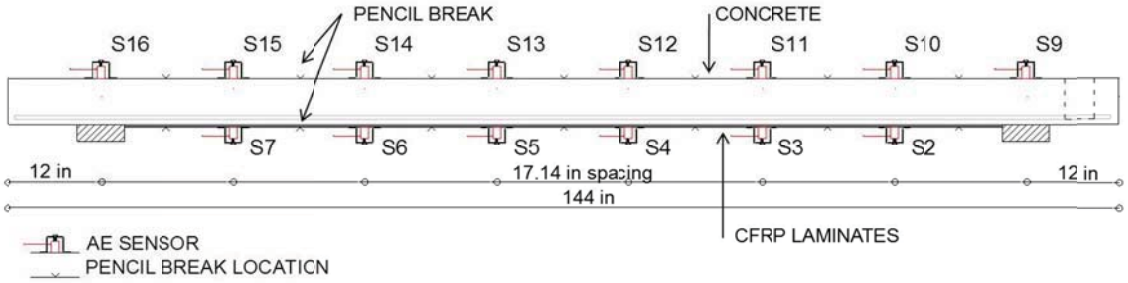

Figure 4.4 - AE attenuation test plan

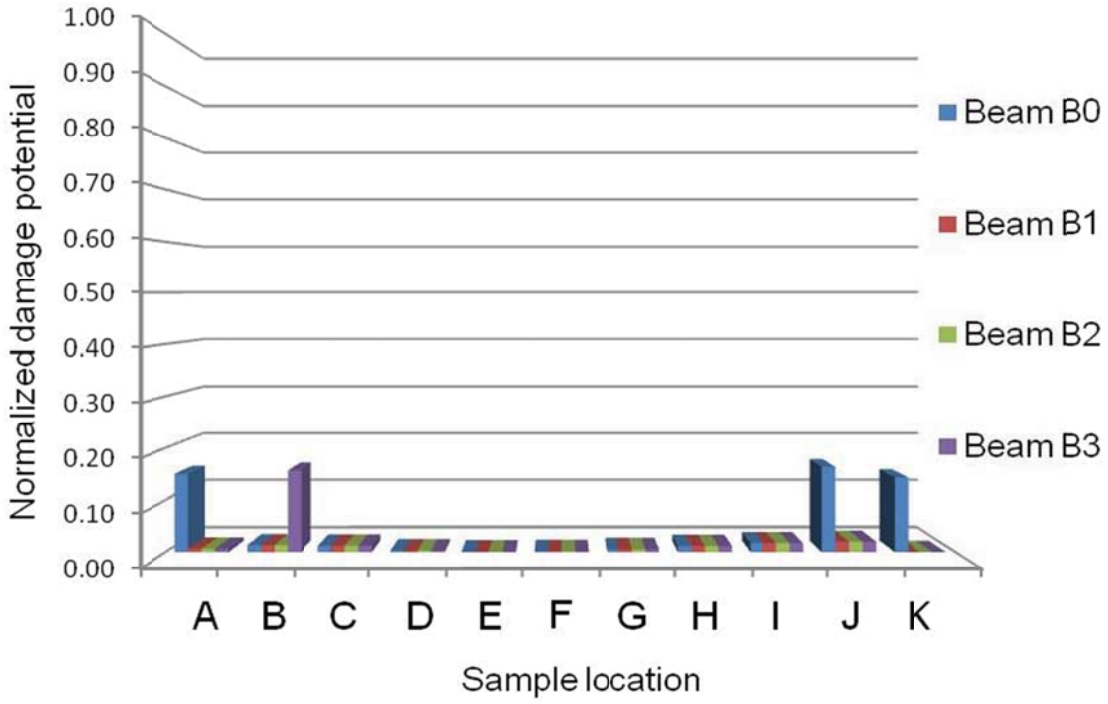

Figure 4.5 - Combined normalized results before corrosion

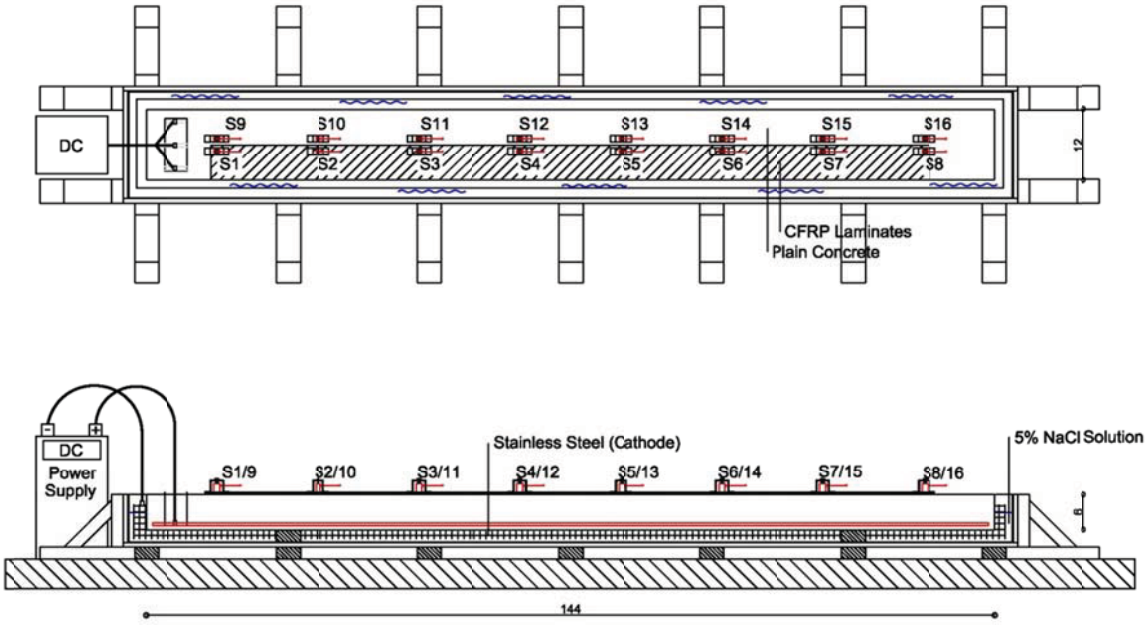

Figure 4.6 - Top and side view test setup corrosion conditioning

Figure 4.7 - Corrosion conditioning setup

4.4 Corrosion Conditioning

Accelerated corrosion conditioning is performed on three of the four beams. The specimens were laid in a 5% NaCl solution as an impressed current accelerated the corrosion process. Corrosion is induced by applying an electrochemical potential between the reinforcement steel (anode) and a cathode, connected together by an electrolyte. The three different beam specimens are exposed with different lengths of time to create three different levels of corrosion. Figure 4.6 and 4.7 shows the 12 ft beam specimen [3.65 m] in a wooden and Plexiglas fabricated container. CFRP plies are only applied on the top surface. Spread cathodic reaction is ensured by a stainless steel net placed continuous around the beam and hooked up to a negative power supply. To make sure the chloride solution has sufficient mass to penetrate, a 3 in. [75 mm] space is designed between the beam and box walls. The positive charge flow is connected directly to the #4 [12.7 mm] reinforcement bars. To create this direct connection, a hole from the top was made in the first foot length [300 mm] of the beam by coring, but carefully to maintain a water sealed space by the 1 in. [25 mm] thick cover. Power was supplied by three parallel connected Extech 80W Switching DC Power Supplies, each with a capacity of 16 Volts and 5 Amperes. They were used under current control at almost maximum capacity to maintain constant charge.

By Faraday's law in equation (1), the theoretical steel mass loss of developed rust per area ML (g/cm^2) was used to estimate the required time and current level to reach desired mass loss [Ahmad, 2009].

Equation (1) is a function of steel weight W which is taken as the ratio of atomic weight of iron to the valency of iron (27.925 g), I_{app} is the current density (Amp/cm^2), T is test duration (seconds), and F stands for the Faraday's constant (96487 Amp-sec).

$$ML = \frac{WI_{app}T}{F} \quad (1)$$

Another method used to determine mass loss is by weighing the reinforcement before and after corrosion. Weighing was performed after demolition and cleaning according to ASTM G01 [2003]. Table 4.2 gives weighing and theoretical mass loss established by Faraday's law. Calculated mass losses are higher for B1 and B2 and equal for B3. Faraday's law is chosen to indicate the level of corrosion for further study.

Table 4.2 - Steel mass loss

	Test Time	Current Density	Mass	Mass Loss	
	sec.	μAmp/cm^2	gram	Weight	Faraday
B0	0	0	12791	0%	0
B1	201660	3625	12156	5.00%	7.24%
B2	501540	2454	11793	7.80%	12.14%
B3	771480	2615	10206	20.30%	19.90%

4.4.1 AE Monitoring of Concrete Cracking

AE sensors S1 to S8 were placed on CFRP on the top surface and sensors S9 to S16 are placed on plain concrete right next to each other to evaluate differences in signal intensity in relation to the interface. AE graphs and an overview of most active sensors during corroding are reported in Appendix III.C. During testing, the most activity is found in the first 75 hours at specific sensors which was later verified for more visual corrosion.

4.4.2 Visual Inspection

Each beam is visually inspected after corrosion conditioning. Surfaces were cleaned and rust removed to inspect for cracks. Figure 4.8 shows in order Beam B1 with 7.24%, Beam B2 with12.14% and at the bottom Beam B3 with 19.90% steel mass loss. The specimens show transverse cracking and spall at the location of four transverse bars. The worst corrosion occurred on Beam B3 which shows longitudinal cracks throughout its length and transverse cracks at midspan. Focusing on Beam B3, sensor locations S11 and S14 were recognized with the highest AE Amplitude and Number of Hits. At sensor S14, the most severe corrosion was discovered and spall at the side surface showed that steel reinforcement was locally completely consumed. The transverse bar had more than half of its diameter dissolved and lay loose in the spall gap.

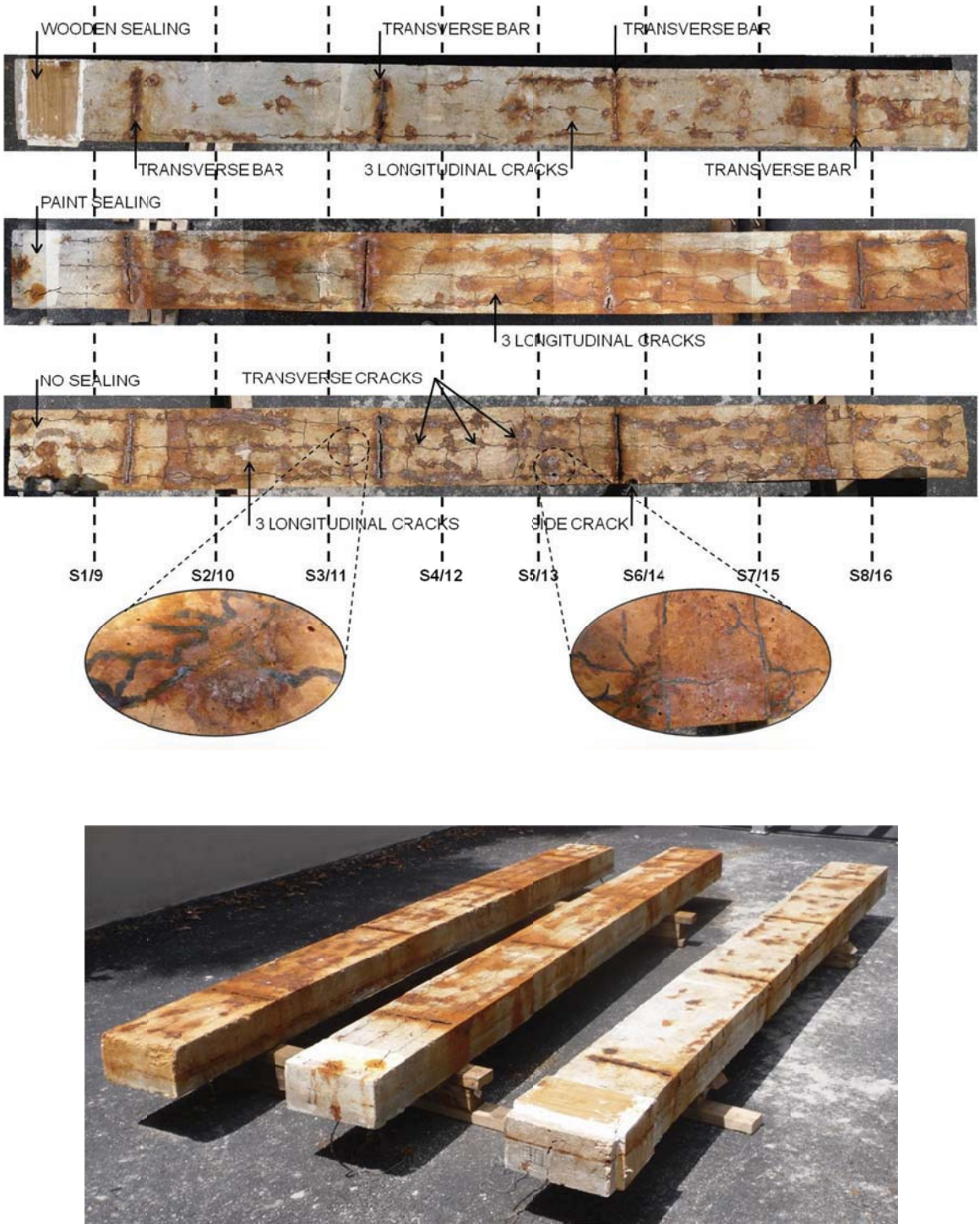

Figure 4.8 - Visual inspection after corrosion (B1 to B3)

4.5 Evaluation after Corrosion

Experimental work after corrosion consists of attenuation testing to evaluate changes in signal transmission due to corrosion and concrete damage, repeat physical assessment studies and finally spatial analysis to point out changing material properties at different levels of corrosion.

4.5.1 Physical Assessment Studies

The specimen's corrosion state relates to different physical parameters such as carbonation and active corrosion potential. Physical assessment studies (A) to (H) are performed at the same locations (Figure 4.2). Sample points are now located on the bottom surface where the corroded reinforcement is situated.

The first assessment layer is visual inspection (A). Table 4.3 gives a normalized ratio of consumed steel reinforcement by visual estimation. The average of three reinforcement bars per section at each sample point is considered. At locations where concerning corrosion was visually detected, the concrete cover was opened as part of the repair work and the remaining reinforcement was evaluated. For example, location B4-G and H are locations where, locally, a complete bar was consumed.

Table 4.3 - Visual inspection reinforcement results

	A	B	C	D	E	F	G	H	I	J	K
B0	0	0	0	0	0	0	0	0	0	0	0
B1	1	1	1	1	1	0	1	1	1	0	0
B2	1	0	0	1	1	1	1	1	0	0	0.1
B3	1	0	1	0.4	0.5	0.2	0.8	0.8	0	0.1	0

Concrete did not carbonate as much as expected. Only few locations on Beam B3 were rated for carbonation (Table 4.4). In addition, cores were drilled in the last foot

length [300 mm] and showed similar results (Appendix III.D). Only few additional locations are indicated with a pH level equal or lower than 9.0 (Table 4.5). Beam B1, Beam B2 and Beam B3 showed respectively 2, 3 and 1 additional sample locations with a pH level of ~9.0.

Table 4.4 - Carbonation detection results

	A	B	C	D	E	F	G	H	I	J	K
B0	0	0	0	0	0	0	0	0	0	0	0
B1	0	0	0	0	0	0	0	0	0	0	0
B2	0	0	0	0	0	0	0	0	0	0	0
B3	0	1	1	0	1	0	0	0	0	0	0

Table 4.5 - pH level results

	A	B	C	D	E	F	G	H	I	J	K
B0	9.0	11.0	11.0	10.7	10.0	11.0	10.3	11.0	10.0	9.0	8.3
B1	10.3	9.3	9.0	9.3	9.2	9.5	9.0	9.8	9.3	9.8	10.5
B2	9.0	9.0	8.8	11.0	11.7	11.7	11.7	11.7	11.3	11.7	10.0
B3	9.0	9.0	9.3	10.7	10.0	10.0	10.0	11.0	11.0	10.0	12.0

Active corrosion evaluation (E) by half-cell potential apparatus was performed 2, 3, and 7 days after accelerated corrosion conditioning. Table 4.6 shows highly increased numbers for all specimens compared to before corrosion occured (Appendix III.B). Results show active corrosion throughout the entire lengths of all corroded specimens.

Table 4.6 - Active corrosion potential results

	A	B	C	D	E	F	G	H	I	J	K
B0	0	0	0	0	0	0	0	0	0	0	0
B1	-649	-649	-647	-643	-647	-618	-626	-647	-627	-624	-607
B2	-545	-517	-533	-529	-510	-512	-498	-516	-515	-499	-485
B3	-422	-416	-406	-436	-448	-452	-430	-420	-419	-434	-448

Chloride content layer (F) gives indication of chemical binding of concrete with external salts such as found in marine environments. The mean value of each beam rose from 0.028% before corrosion to 0.178, 0.19, and 0.36% with standard deviations of 0.038, 0.052, and 0.05% after corrosion of specimens B1, B2 and B3 respectively. The specimens test duration exposure to the NaCl solution was able to raise the average chloride content bond with concrete material by 650%. According to ACI 222.3R [2003], reinforced concrete exposed to chloride in service is not allowed to have a chloride level higher than 0.2% at a depth of 1 in. [25.4 mm]. In the case of the beams study, chloride content locations with a higher level are B2-F, B3-C, B3-F, and B3-I (Table 4.7).

Table 4.7 - Chloride content results

	A	B	C	D	E	F	G	H	I	J	K
B0			0.00%			0.00%			0.00%		
B1			0.20%			0.20%			0.13%		
B2			0.15%			0.25%			0.17%		
B3			0.31%			0.41%			0.36%		

Crack density on bottom surface of the beams (G) is evaluated visually by counting cracks. Table 4.8 shows a range of 0 to 5, where 0 means no visual cracks, 3 stands in all cases for three longitudinal cracks, and 5 for three longitudinal cracks and two transverse cracks. Comparing Figure 4.8 with Table 4.7 gives clearness in how the severity of cracks per beam and location was evaluated and ranked.

Table 4.8 - Crack density results

	A	B	C	D	E	F	G	H	I	J	K
B0	0	0	0	0	0	0	0	0	0	0	0
B1	2	1	1	2	2	2	3	1	1	2	3
B2	3	3	3	3	3	3	4	3	3	3	3
B3	3	3	4	4	4	5	4	3	4	4	3

Last evaluation layer is the AE attenuation response in terms of conductivity. More detail will be given further on in this Study where attenuation tests are evaluated in more depth for comparison with attenuation results before corrosion. Figure 4.9 shows graphs where Amplitude attenuation is expressed vertically against time. Top figure 4.9a shows the attenuation evolution of each sensor before corrosion, while the bottom figure shows attenuation at approximately 19.90% corrosion. The compared figures give evident proof of diminished conductivity where Amplitude decreases much faster over its travel length, as in the case of sensor S13; the response disappears completely after ~43 in. [1.1m].

In numerical terms and with a similar threshold of 40 dB as before corrosion, conductivity decreases with a normalized mean value from 0.06 to 0.211 (352%), 0.156 (260%), and 0.443 (738%) for respectively Beam B1, B2 and B3. These parameters indicate diminished conductivity related to damage at various levels. Table 4.9 shows the average evaluation results of three attenuation tests translated to normalized values in a range from 0 to 1, where 0 indicates full conductive material properties and 1 indicates the most damaged condition. Beam B3 appears in the worst condition with values peaking at 0.69, which can be translated into an understanding that the sensor location was not able to record almost 5 out of 7 signals where it was able to record 7 out of 7 over a length of approximately 111 in. [2,820 mm] at the far end before corrosion.

Table 4.9 - AE attenuation conductivity results

	A	B	C	D	E	F	G	H	I	J	K
B0	0.05	0.10	0.09	0.02	0.01	0.01	0.04	0.08	0.12	0.14	0.00
B1	0.45	0.28	0.17	0.14	0.14	0.14	0.15	0.19	0.24	0.31	0.10
B2	0.12	0.15	0.16	0.14	0.14	0.14	0.14	0.14	0.14	0.24	0.19
B3	0.45	0.45	0.43	0.39	0.38	0.38	0.38	0.36	0.39	0.69	0.57

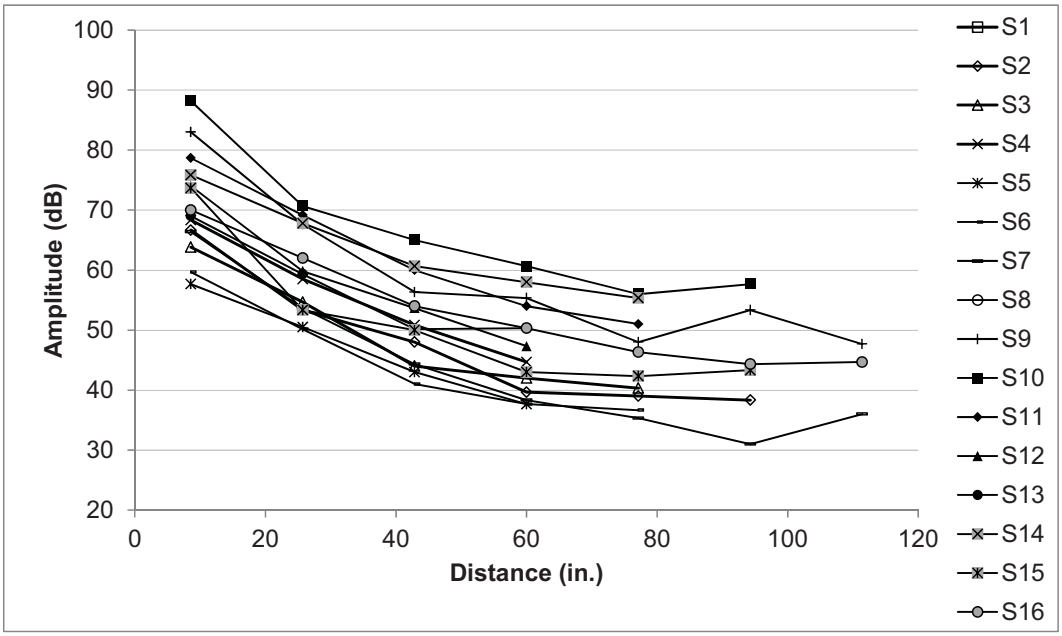

(a)

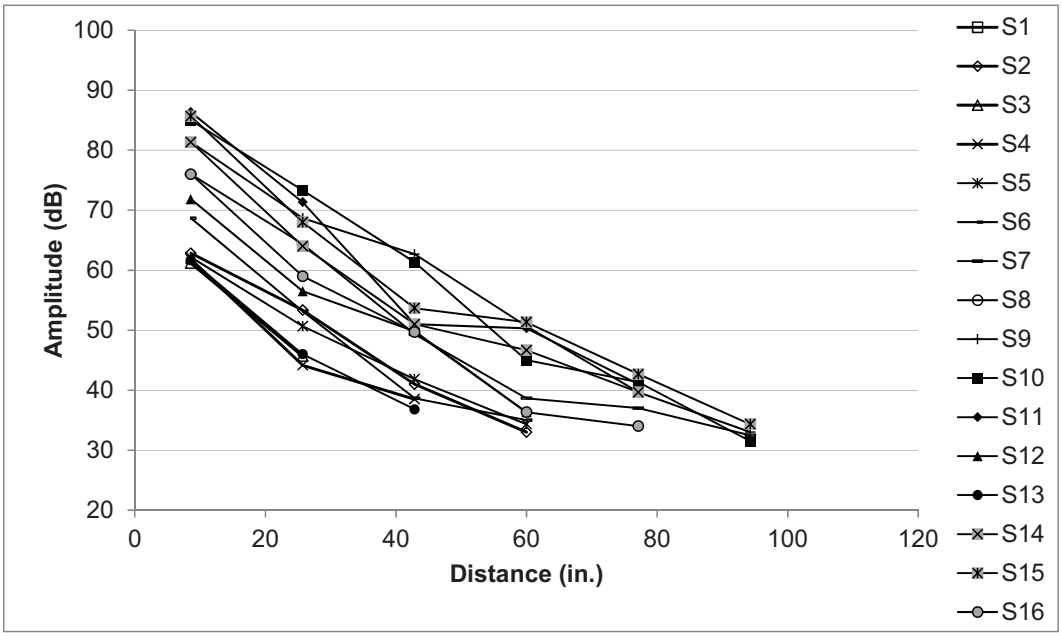

(b)

Figure 4.9 - Attenuation before (a) and after (b) corrosion (B3)

4.5.2 Spatial Analysis

Each assessment layer after corrosion conditioning is normalized as previously done with assessment layers before corrosion and the field bridge evaluation in Study II. One difference between the field evaluation and the laboratory study is that the layer with air voids is excluded and the chloride content evaluation is included in the spatial analysis. However, the number of included layers is equal and offers an example of enclosure of different assessment studies. As earlier mentioned, the threshold level set by ACI 222.3R [2003] is used to decide what level of chloride content is considered concerning. Table 4.10 shows the evaluation parameters and the corresponding translation. Cells where no chloride content samples are collected, adopt the chloride content ratios from the neighboring cell. This seems a consistent approach when analyzing results gathered in Beam B2 and Beam B3,

Table 4.10 - Numerical translation chloride content

Observation	$CC_{n,m}$
$\leq 0.2\%$	0
$> 0.2\%$	1

Combining all layers to establish mean value is performed by simple addition and normalization to a scale of 0 to 1 by dividing by the number of layers. In Study II, equations for mean and standard deviation are defined where the air void layer $AV_{Bi,n}$ is replaced by the chloride content layer $CC_{Bi,n}$. Numerical results for mean values are given in Table 4.11 and for standard deviations in Table 4.12. The peak value for corrosion damage potential before corrosion is 0.17. After corrosion, the peak value is 0.75 and found at location B3-A, B3-B and B3-C. Figure 4.10 shows combined normalized results

for damage potential due to induced corrosion, which can be directly compared to Figure 4.5 with combined results before corrosion. A visual increase in damage potential is evident by comparing both figures. The column plot also shows how each specimen classifies in the range of induced corrosion levels. Numerically, potential damage due to corrosion increases in mean value over the length of the beams from 0.05 in Beam B0 to 0.35, 0.41 to 0.58 in Beam B0 to B3 respectively. Damage potential levels of each beam increase along with the induced corrosion levels of 7.24%, 12.14% to 19.90% in Beam B0 to B3 respectively.

Table 4.11 - Mean values combined results (B0 to B3)

	A	B	C	D	E	F	G	H	I	J	K
B0	0.15	0.01	0.01	0.00	0.00	0.00	0.01	0.01	0.02	0.16	0.14
B1	0.41	0.35	0.48	0.36	0.36	0.22	0.54	0.34	0.35	0.24	0.24
B2	0.53	0.39	0.39	0.39	0.53	0.53	0.56	0.39	0.25	0.26	0.27
B3	0.72	0.72	0.75	0.51	0.67	0.51	0.57	0.54	0.46	0.51	0.45

Table 4.12 - Standard deviations combined results (B0 to B3)

	A	B	C	D	E	F	G	H	I	J	K
B0	0.38	0.04	0.03	0.01	0.00	0.00	0.01	0.03	0.04	0.37	0.38
B1	0.45	0.45	0.49	0.46	0.46	0.35	0.48	0.46	0.44	0.36	0.39
B2	0.48	0.44	0.43	0.47	0.48	0.48	0.50	0.47	0.37	0.38	0.37
B3	0.39	0.39	0.45	0.43	0.38	0.44	0.42	0.41	0.45	0.43	0.45

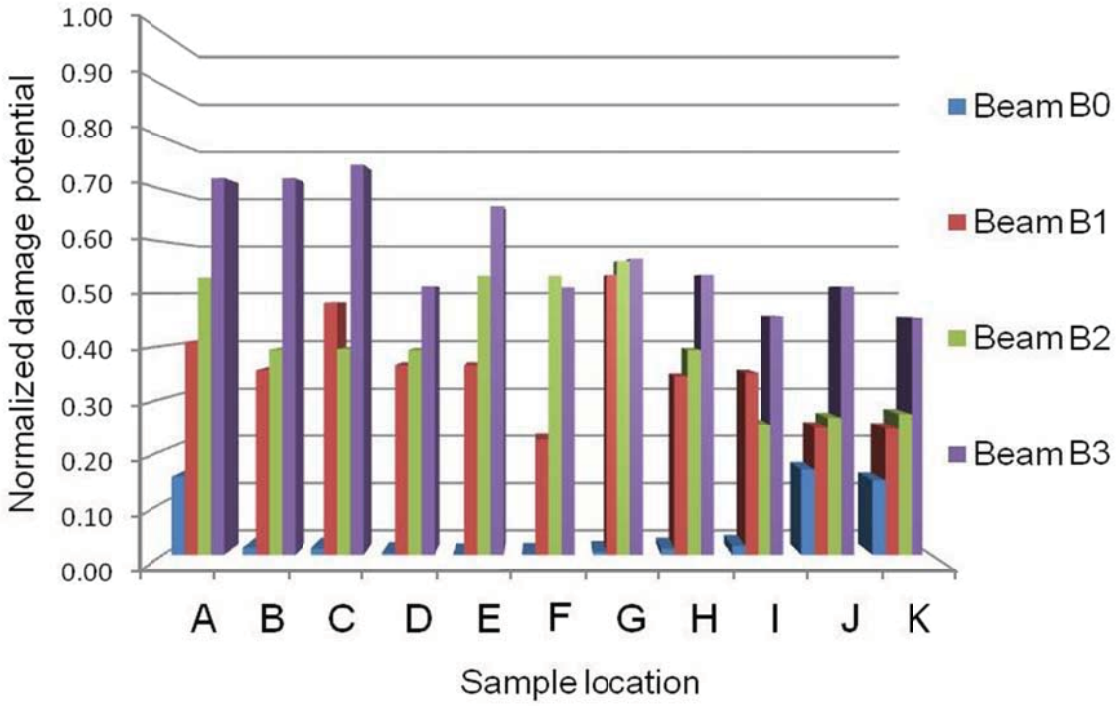

Figure 4.10 - Damage potential combined layers after corrosion

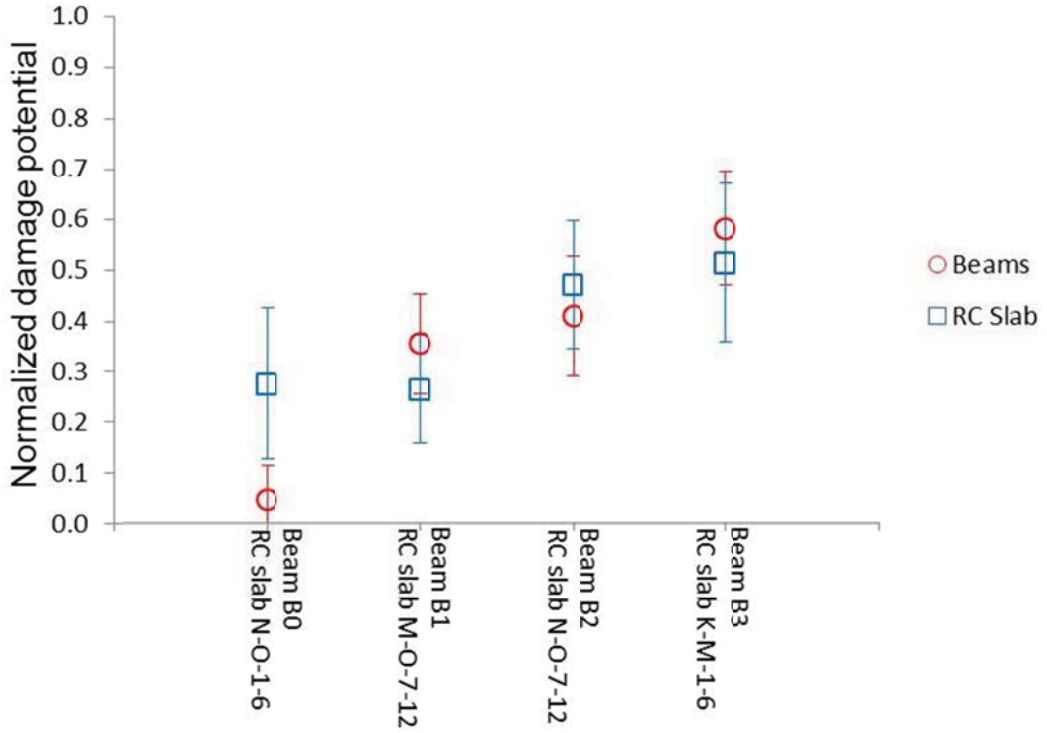

Figure 4.11 - Damage comparison RC slab and beams

Physical outcomes are put into perspective with spatial analysis results gathered in Study II. Peak values in the bridge study are at the level of 0.73 and 0.74 on a scale from 0 to 1 (Table 3.11). The beam study has peak values in Beam B3 of 0.72 and 0.75 (Table 4.11). The mean value of the area in South-West corner of the RC slab ranging from cells K-M-1-5 has mean normalized value of 0.54 with standard deviation 0.157 for 15 sample cells (Figure 4.11). Beam B3 has comparable corrosion damage potential indicated by a mean value of 0.58 and a standard deviation of 0.111 for 11 sample cells. The levels of concrete and corrosion damage of Beam B3 offer fair comparison with the bridge study for area K-M-1-5. This does not directly mean that the selected area in the RC bridge slab and Beam B3 have exactly similar physical conditions, corrosion level or damage. However, the rate of damage probability is similar. In addition, Beam B1 and B2 offer a matching range of evaluation levels by corrosion stages (Figure 4.11), except uncorroded specimen B0 which has a damage probability close to zero which is not found on the bridge.

In preparation of the load test cycles, spatial analysis is used to appoint the most severe areas to explore if failure location and localized highest AE activity matches the appointed cells with highest damage potential. Two approaches are used, where the first identifies the highest damage probability relative to the condition of all specimens. Equation (2) calculates Concrete Corrosion Damage Potential $CCDP_{B0-3,n}$ relative to specimens B0 to B3, where $\bar{x}_{Bi,n}$ is the mean value of each cell, and Max_{B0-3} is the maximum value of all specimens.

With this relationship, relative reclassification is established in the range between 0 and maximum mean values of all four specimens to allow for visual comparison with the visual output of the field bridge study (Figure 3.15). The visual output of equation (2) is given in Figure 4.12a and numerical values are given in Appendix III.E.

$$CCDP_{B0-3,n} = \frac{\bar{x}_{Bi,n}}{Max_{B0-3}} \tag{2}$$

$$CCDP_{Bi,n} = \frac{\bar{x}_{Bi,n} - Min_{Bi}}{Max_{Bi} - Min_{Bi}} \tag{3}$$

The second approach identifies areas with highest damage probability relative to the condition of each specimen. The Concrete Corrosion Damage Potential $CCDP_{Bi,n}$ relative to each single specimens is given in equation (3), where the difference of mean value of each cell ($\bar{x}_{Bi,n}$) and overall minimum of the specimen Min_{Bi} is divided by the range; maximum of each beam Max_{Bi} minus minimum Min_{Bi}. By this approach, a relative scale becomes visible for each beam to identify areas by damage potential and serves to identify areas for evaluation for higher AE activity and failure location.

Figure 4.12a shows the classification of the first approach in a perspective of all specimens. The scale from 0 to 10 is dominated by the highly damaged condition of Beam B3. The cell's gray scales can be directly related to Figure 3.15 in Study II. By visual estimation, concrete and corrosion damage potential estimates of beam specimens with outcomes of the RC slab can be compared.

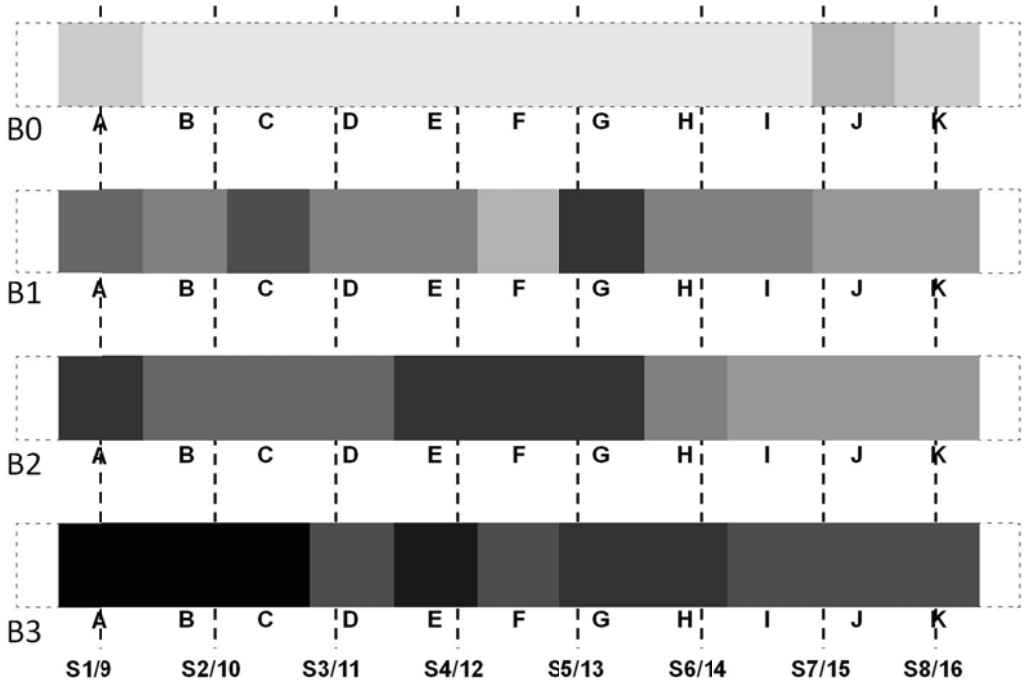

(a) Relative to all specimens

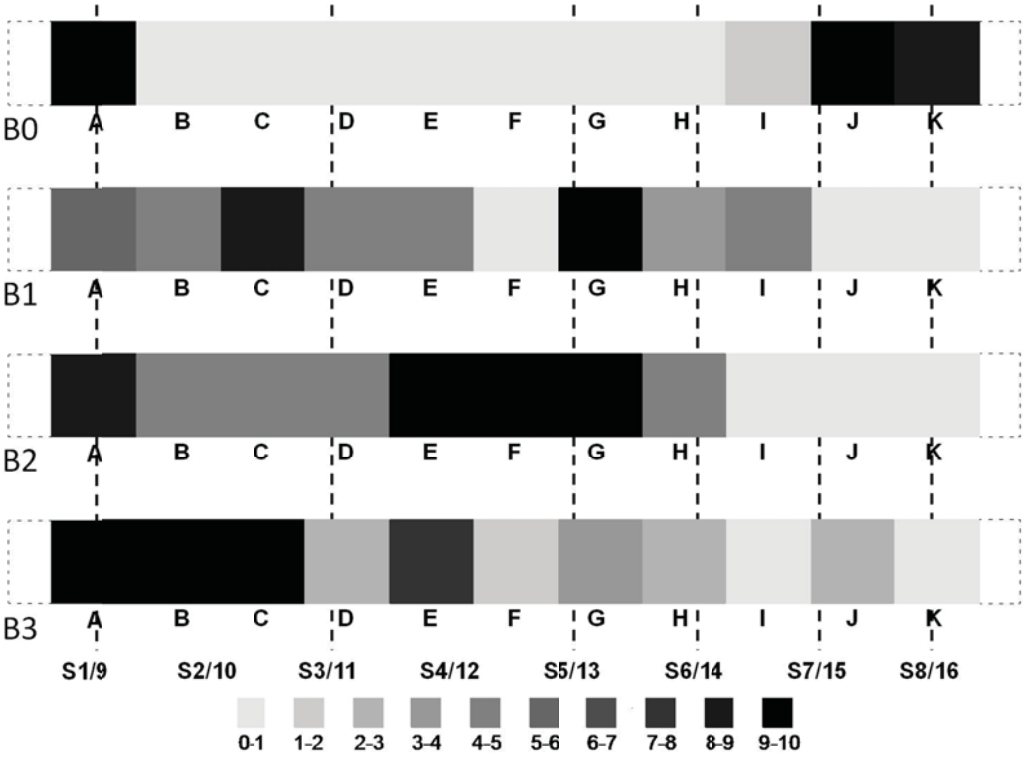

(b) Relative to each specimen

Figure 4.12 - Classification of damaged areas

Figure 4.21b gives indication of areas with the highest damage potential per beam. For each beam, an area can now be visually identified to predict failure location. The most severe areas are cells B0-A, J and K for Beam B0, B1-C and G for Beam B1, B2-A, E, F, and G for Beam B2, and B3-A, B and C for Beam B3. During the load tests, these locations are monitored for loading locations, failure location depending on possible mechanism like shear or flexure, cracking and propagation intensity compared to other locations.

4.5.3 AE Attenuation Testing

Pencil lead break tests are performed after repair and strengthening with CFRP laminates. The main objective of repeated attenuation before and after corrosion is to indicate AE attenuation differences in terms of Amplitude at different concrete and corrosion damage levels to be able to compare results with attenuation tests performed on the field bridge.

Collected attenuation data has been expressed in three sample average Amplitude (dB) against distance (in.) in Figure 4.13 to show the relationship between uncorroded, corroded at different levels, and the unknown damage level of the field bridge from sensors recording on CFRP. Figure 3.13 shows the results from breaks performed on the CFRP, while Figure 4.14 shows the results from breaks on the concrete surface. The graphs show that the most corroded Beam B3 has the highest attenuation, while Beam B2 has the lowest attenuation, but like the other specimens doesn't record signals from a larger distance than 77 in. [1.96m]. Only the uncorroded Beam B0 is able to record from greater distances.

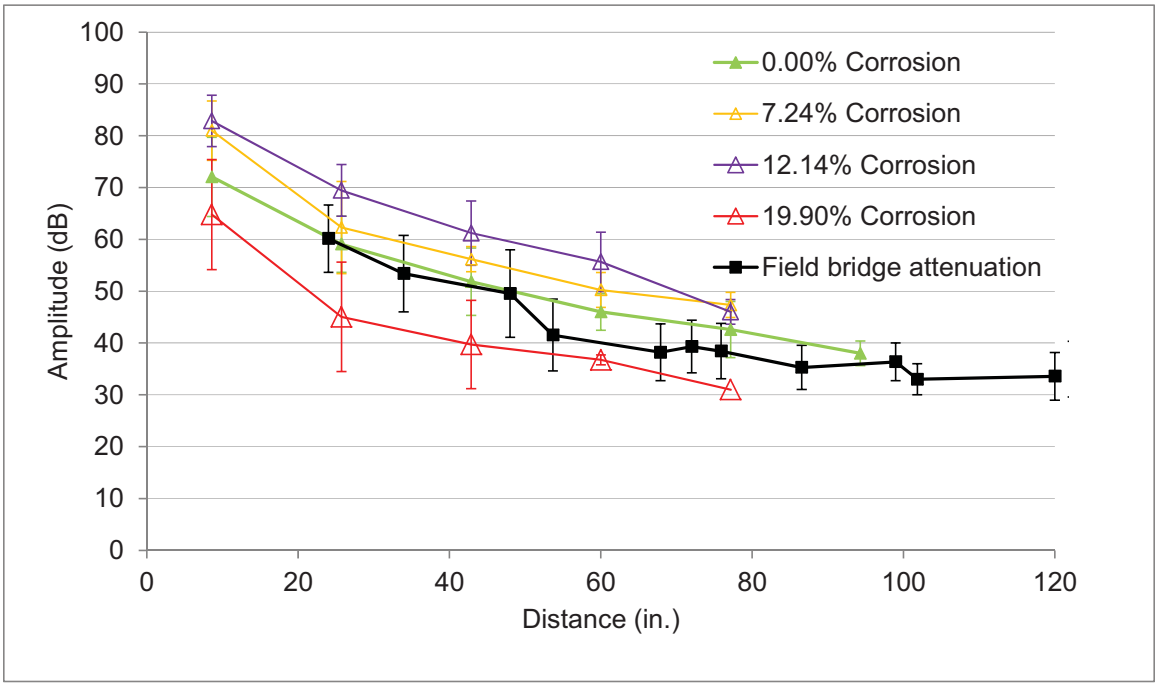

Figure 4.13 - Attenuation, sensors and breaks on CFRP

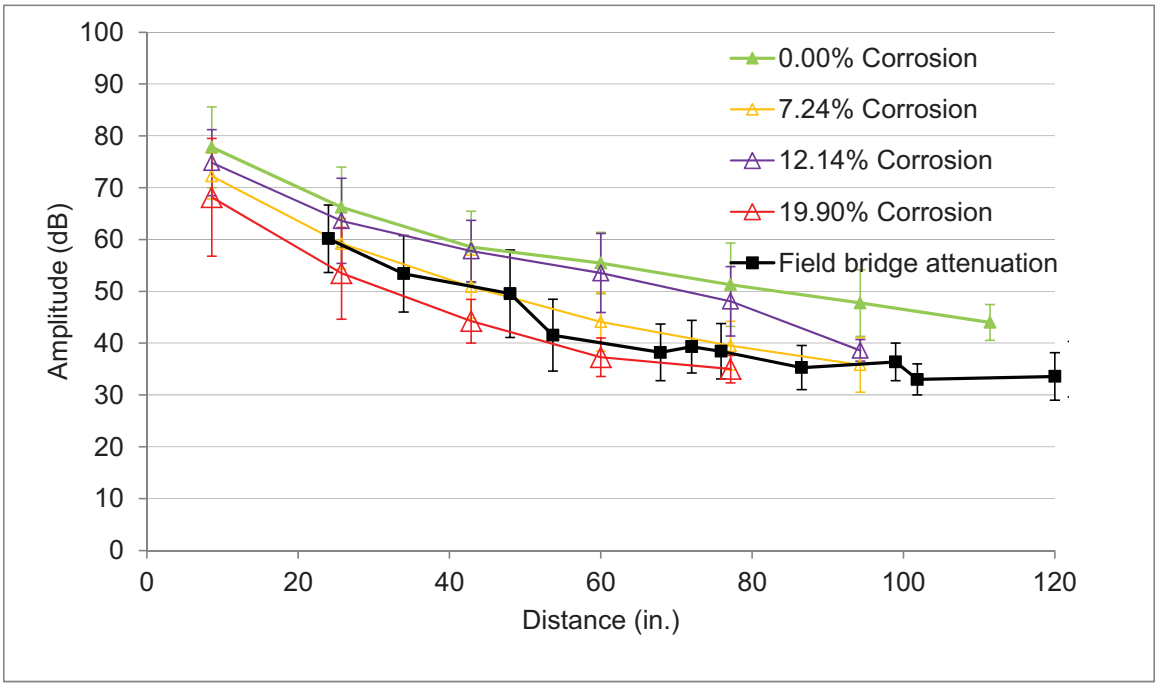

Figure 4.14 - Attenuation, sensors on concrete, breaks on CFRP

4.5.4 Repair & Strengthening

Repair and strengthening is performed after the visual inspection for spall of concrete cover, crack density and deterioration of concrete. Local removal of the concrete cover is done by impacting [Concrete Repair Manual, 1999]. Figure 4.15 shows local chipping on Beam B1, B2 and B3. Figure 4.16 shows locations of concrete cracks with corrosion bleeding and locations where steel reinforcement has been completely consumed. Specimens are prepared for repair by cleaning the remaining steel reinforcement and removing all attached concrete where the cover was locally removed as per ACI 220.3R [2003]. Immediately after cleaning procedures, the removed concrete cover is patched with cementious grout (Figure 4.17). Troweling and dry packing of 1 in. [25 mm] deep areas is performed using grout placement technique. After 7 days of curing, the entire surface of the specimens is prepared for CFRP laminate strengthening as per ACI 440.2R [2008]. Material specifications of the CFRP laminates can be found in Table 4.1.

Figure 4.15 - Local removal of concrete cover (B1 to B3)

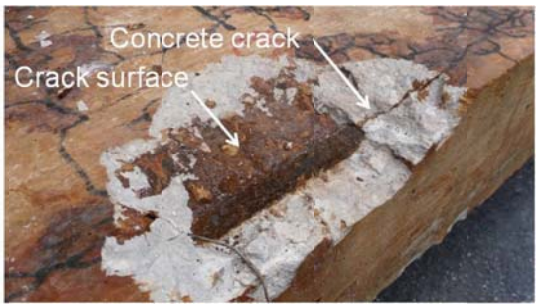

(a) Crack in concrete cover with bleeding surface

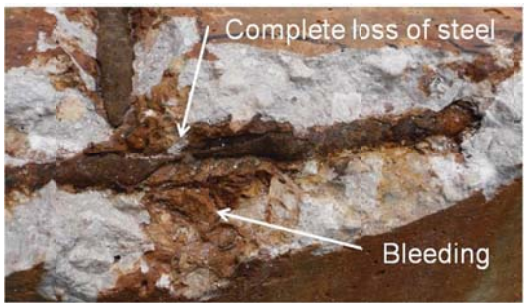

(b) Complete loss of steel reinforcement in Beam B3

Figure 4.16 - Corrosion observations

Figure 4.17 - Concrete patching chipped areas (B1 to B3)

4.6 Structural Testing

Four-point bending of three corroded and one uncorroded, repaired and CFRP strengthened RC beams is carried out in the laboratory with a hydraulic MTS 55 kip [245 kN] actuator (Figure 4.18). At midspan, one 5 mm strain gauge was adhered to the CFRP laminates and one 60 mm on the top concrete surface. A displacement transducer (LVDT) was placed at midspan, while two were placed at the supports to measure discrepancy. Strain and deflection were recorded with a 12 channel Data Acquisition System (DAQ) by National Instruments and Math Lab software with a sample rate of 10 Hz. As AE recording equipment was not linked to the DAQ, recording was started manually and simultaneously.

A prescribed load cycle program consisting of threefold loading series is designed to mimic service load behavior. Figure 4.19 shows load against time where percentage of ultimate load is given on the right vertical axis. The first load series peaks at about 2 kips [8.9kN] which is close to the cracking moment for all specimens. After threefold repetition, each series increases loading with approximately 1 kip [4.5kN]. Between 70 and 80% of ultimate load, steel yielding occurs. Several cycles later, the external reinforcement allows failure of the specimen. In relation to the bridge test, the applied load in the field was estimated at 16.31% of ultimate loading. For comparison, this load level is found between load cycle series A and B.

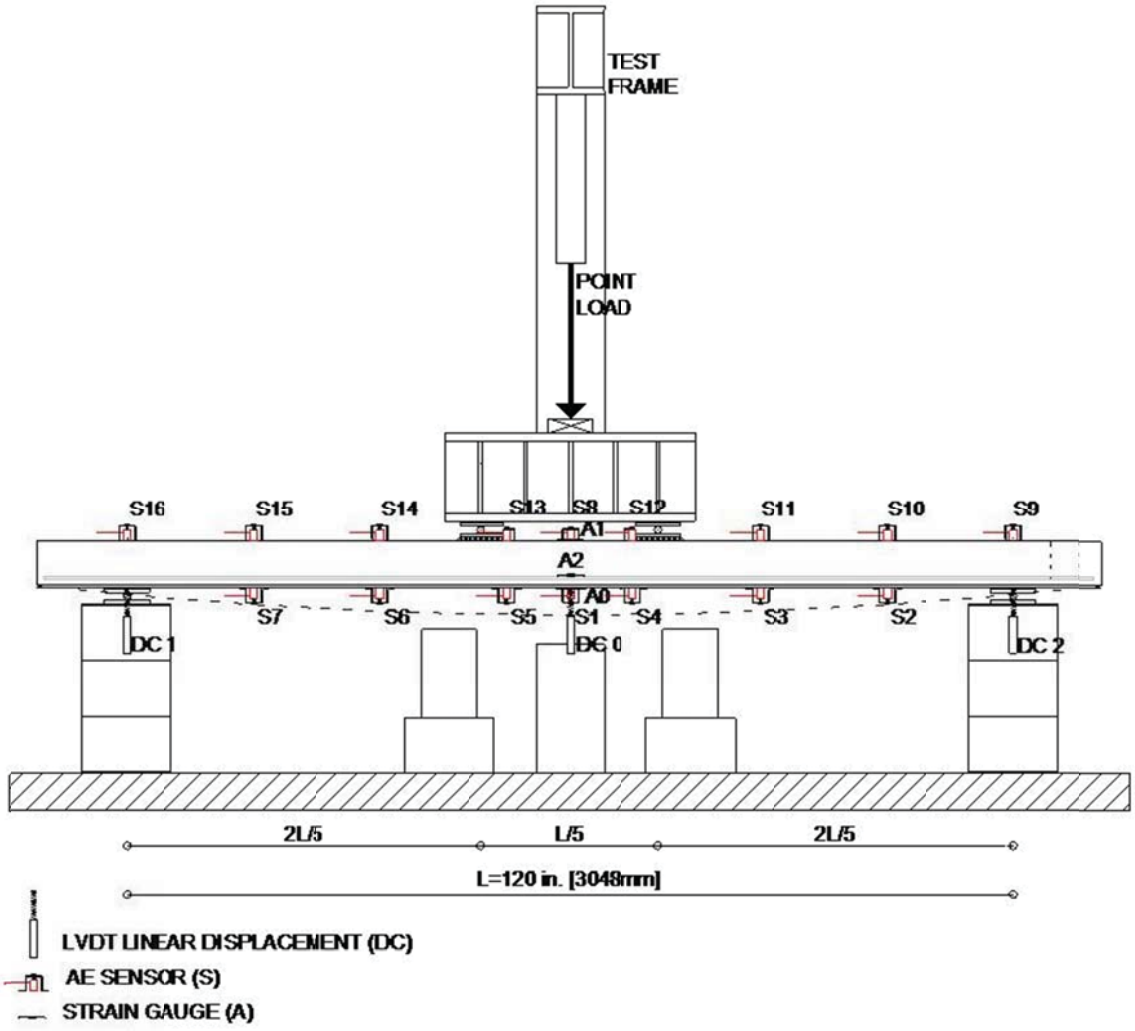

Figure 4.18 - Four-point bending test setup

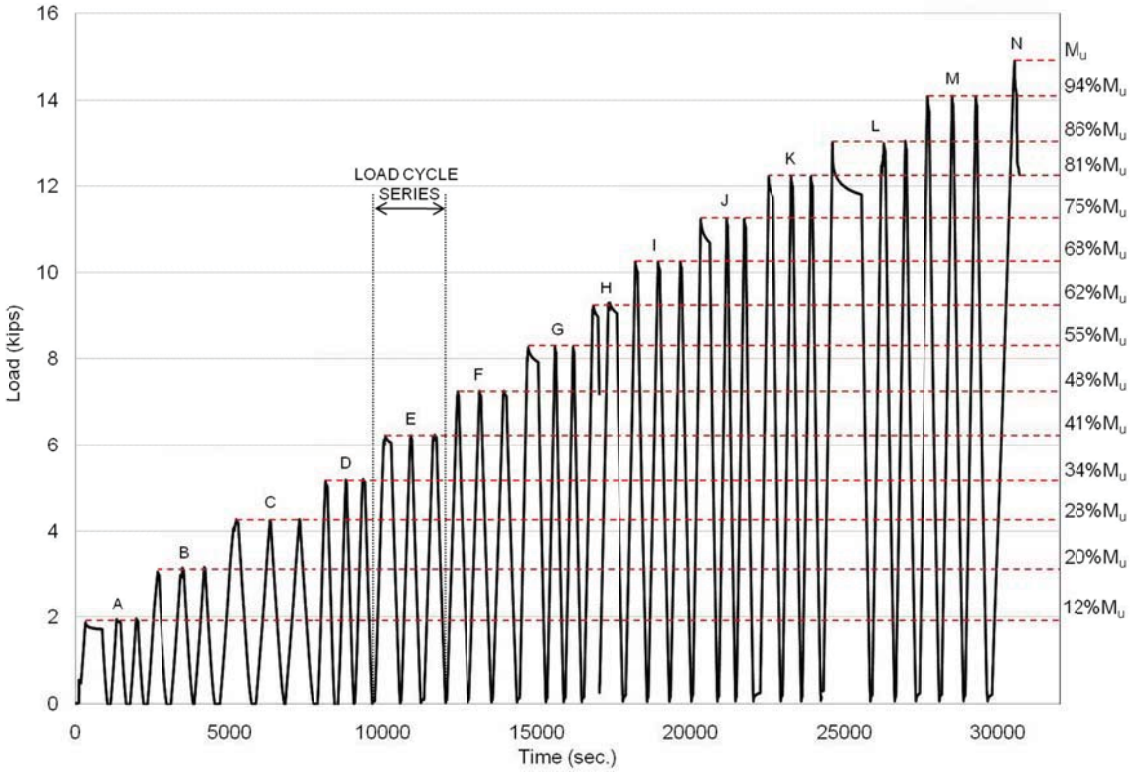

Figure 4.19 - Prescribed load cycle series program

4.6.1 Results and Discussion of Structural Response

The original uncorroded and unstrengthened specimens are designed according to ACI 318R-08 [2008] provisions, with failure being governed by crushing of concrete after steel yielding. External strengthening laminates are applied to attempt peeling failure. Table 4.13 gives next to experimental results of specimens B0 to B3, ACI estimations at estimated corrosion levels with two plies of CFRP strengthening (Appendix III.F), and in addition an uncorroded and unstrengthened specimen (C) [Napoli 2010].

Table 4.13 - Structural estimations and experimental results

		Corrosion Level	f'_c psi	M_y k-ft	$M_{y,i}/M_{y,c}$ %	M_u k-ft	$M_{u,i}/M_{u,c}$ %	w_y in.	w_u in.	Failure Mode
ACI, analytical	C	-	4346	12.6	-	13.2	-	1.18	3.26	YS-CC
	B0	-	4346	27.3	-	34.2	-	1.39	1.56	YS-LD
	B1	7.24%	4346	26.4	-	32.0	-	1.38	1.59	YS-LD
	B2	12.14%	4346	25.8	-	33.9	-	1.37	1.61	YS-LD
	B3	19.90%	4346	24.9	-	33.7	-	1.35	1.65	YS-LD
Experimental	C	-	3926	13.0	104%	17.4	132%	1.00	3.61	YS-CC
	B0	-	4346	26.0	95%	29.8	87%	1.21	2.33	YS-LD
	B1	7.24%	4346	24.1	91%	27.8	87%	1.21	1.67	YS-LD
	B2	12.14%	4346	25.2	97%	29.0	86%	1.21	1.61	YS-LD
	B3	19.90%	4346	22.0	88%	24.1	71%	1.15	1.29	CCD

YS = Steel Yielding, CC = Concrete Crushing, LD = Laminate Debonding,
CCD = Concrete Cover Debonding

Compression tests in 2008 and 2010 show compression strength increases of approximately 10.5%. Yielding moments of the 19.9% corroded specimen Beam B3 differs theoretically 9.6% and experimentally 18% with the uncorroded specimen Beam B0. Experimental and theoretical results differ by a maximum of 5% for yielding moment of the uncorroded specimens C and B0, and 12.14% for corroded B2. Beam B1 has its

yielding moment 9% and most corroded specimen B3 18% earlier than estimated. The ultimate moments of corroded specimens B0, B1 and B2 have a maximum difference of 18%, while specimen B3 fails 29% earlier than expected.

Load (kip) versus deflection (in.) is given for Beam B0 in Figure 4.20. The figure includes analytical load-deflection lines which show similarities. Eleven loading cycle series show elastic behavior till approximately 12.5 kip [56kN]. At this point, steel reinforcement starts to yield. Steel yielding is recorded by internal strain gauges on rebars for Beam B0 (Figure 4.21. Load in kips on the vertical axis and micro strain is found on the horizontal axis with steel strain in grey. Steel yielding is identified from about 12.5 kips loading. Strains turned out lower than expected (Table 4.14).

Table 4.14 - Experimental strain data

Specimen	Corrosion Level	f'_c psi	$\varepsilon_{y,s}$ ($\mu\varepsilon$)	$\varepsilon_{y,c}$ ($\mu\varepsilon$)	$\varepsilon_{y,f}$ ($\mu\varepsilon$)
C	0%	3926	18371	3970	-
B0	0%	4346	1733	2838	4146
B1	7.24%	4346	-	2461	4263
B2	12.14%	4346	-	2118	3869
B3	19.90%	4346	-	1484	2736

*Uncorroded specimen Beam B0 had an internal strain gauge on the steel reinforcement. Other specimens did not as the gauge corroded during the accelerated corrosion conditioning.

Strain behavior as a function of applied moment on the vertical axis shows two groups of strain envelope lines in Figure 4.22. The group with the highest increase is the positively expressed concrete strain which shows correlation with different corrosion levels. Strain is higher in order of corrosion level. The envelope line of experimental load-displacement relation of Beam B0 has a close relationship with the analytical evolution of Beam B0 in Figure 4.23.

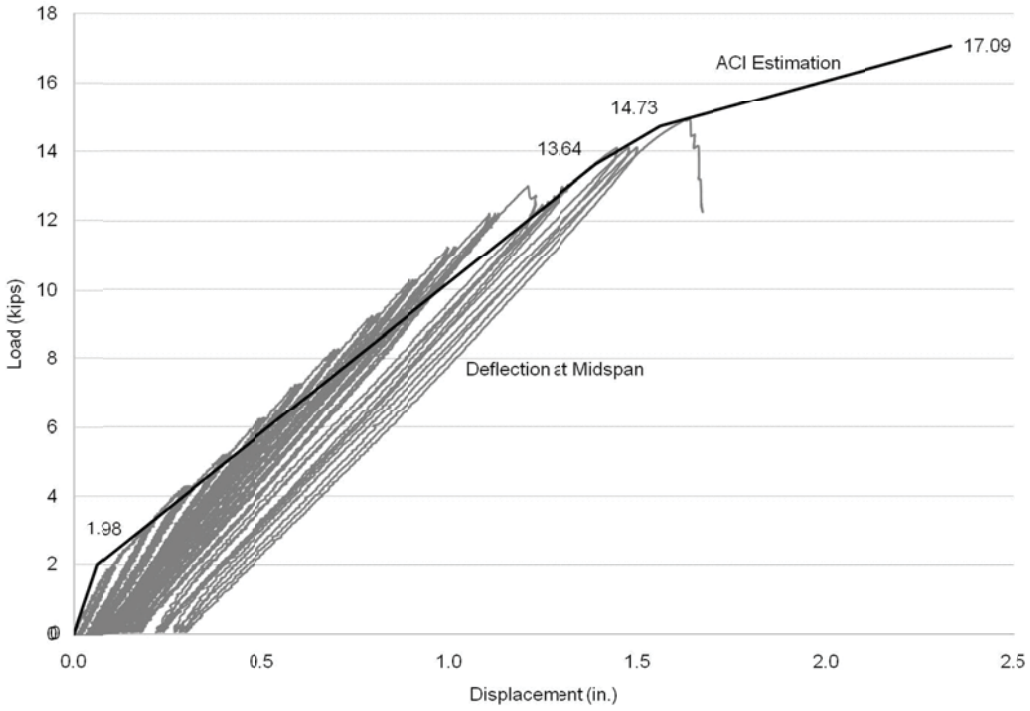

Figure 4.20 - Load-displacement (B0)

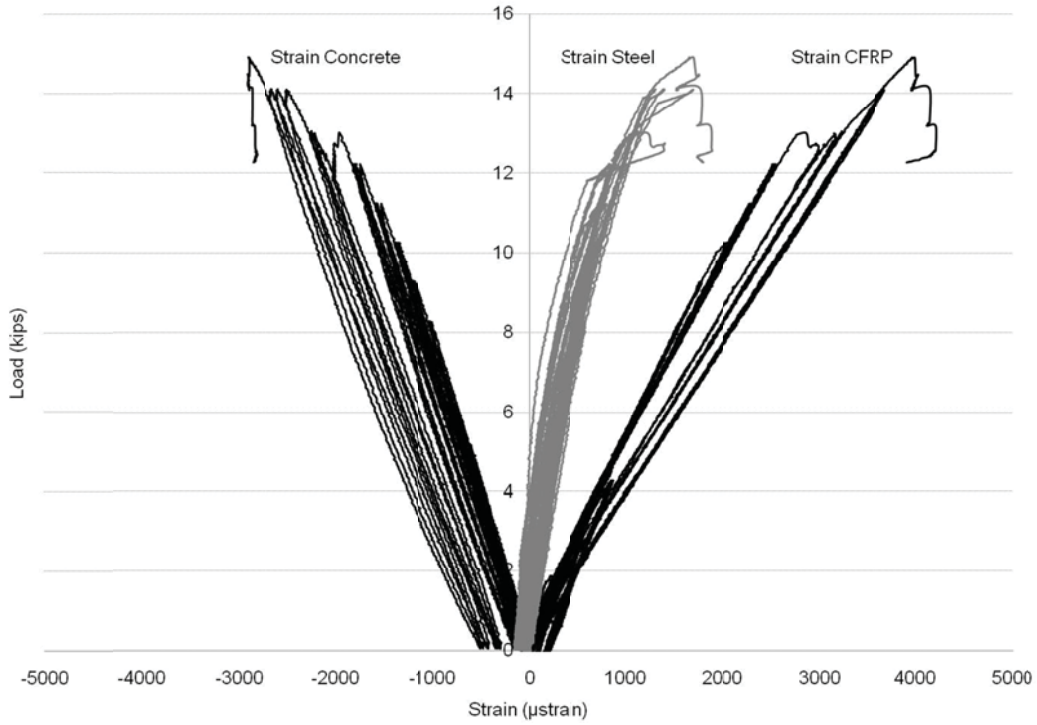

Figure 4.21 - Load-midspan strains (B0)

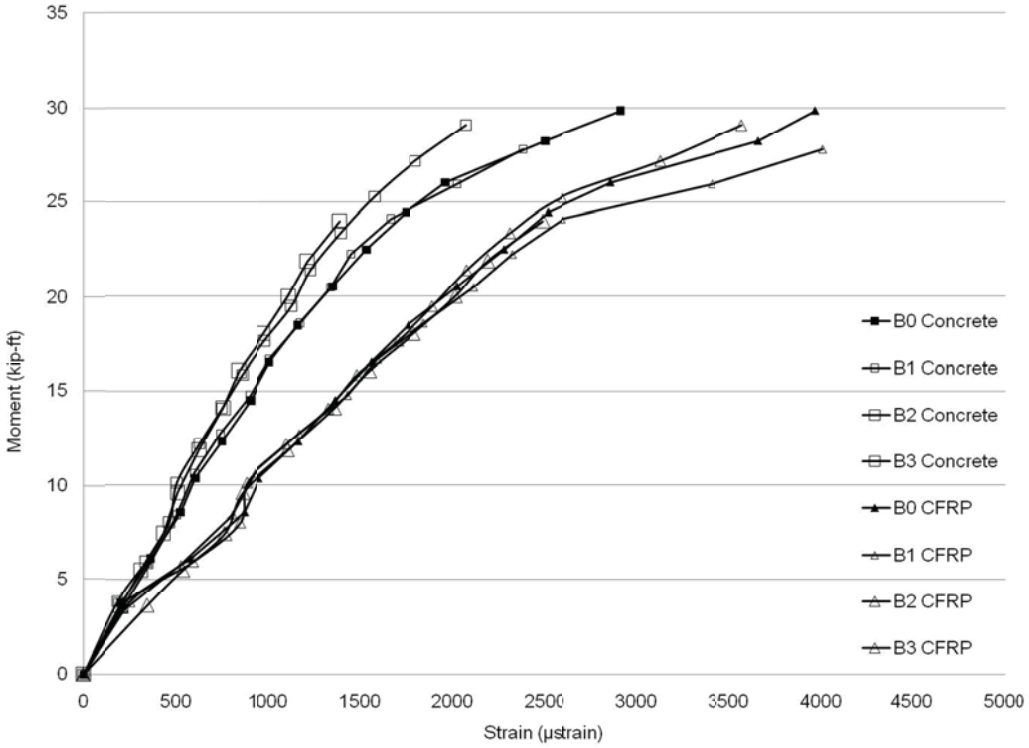

Figure 4.22 - Positive moment-strains (B0 to B3)

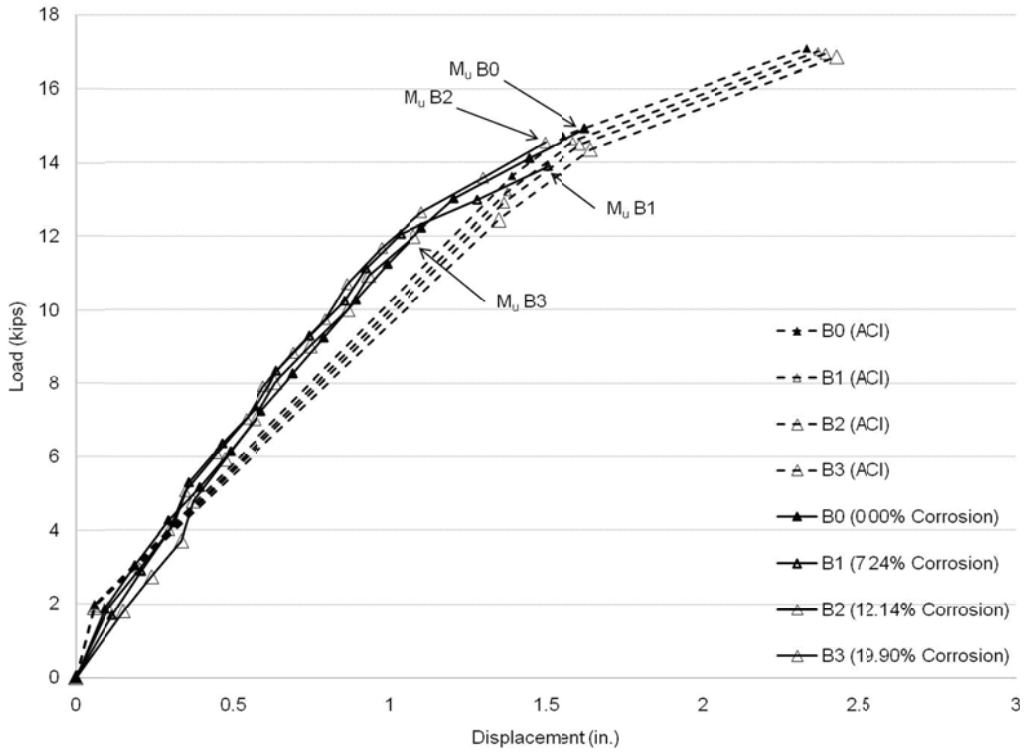

Figure 4.23 - Load-displacement (B0 to B3)

The load-deflection relation of all specimens follows almost similar evolution. The specimens have less deflection than estimated and probably have a higher stiffness than analytically assumed. The ACI nominal positive moment estimate is lower than the ultimate moment reached during the experimental investigation. The uncorroded specimen B0 fails 16% earlier than expected and at a similar percentage at lower bound fail corroded specimens B1 and B2. Specimen B3 fails at ~70% of the estimated nominal moment. The steel yielding moment comes in 13% earlier than estimated. The specimen fails by brittle concrete cover separation only 9.5% after experimental observed yielding and 3.3% before estimated analytical yielding.

Deflection and curvature in the test setup of one of the specimens close to failure is shown in Figure 4.24. The failure modes of specimens were all as expected by delamination of the CFRP sheets from the ends of the sheets after steel yielding (Figures 4.25a and b), except for Beam B3 (Table 4.13). This specimen showed sudden failure by brittle fracture (Figure 4.25c). This brittle failure by horizontal fracture most likely existed as a results of a combination of locally deteriorated material conditions and stress concentrations [Goa et al., 2007; Aram et al., 2008].

Inspection before repair showed bleeding surfaces and cracks from the level of reinforcement outward through the cover (Figure 4.25a). Closer inspection of the failure crack confirmed that, as the most likely initiator for failure, corrosion bleeding traces were observed in the failure crack (Figure 4.25d). Stress concentrations in combination with deteriorated material properties and existing longitudinal corrosion cracks may be the cause of this failure mode. As failure occurred at 60% of the ultimate analytically estimated load, this result requires further investigation.

Figure 4.24 - Test setup wit bended specimen close to failure

(a) Delamination B1

(b) Delamination B2

(c) concrete cover separation B3

(d) concrete cover delamination

Figure 4.25 - Failure modes beam specimens

4.6.2 Results and Discussion of AE monitoring

The relationship between strain and AE was found during crawl load testing in Study II in terms of peak Amplitudes, Energy, Duration, and Number of Hits. AE behavior of all load series is analyzed by same methods and parameters. Figure 4.26 shows test results of Beam B3 for all load cycle series A to K on the horizontal time axis. Strain is given on the left vertical axis, while AE Amplitude is given on the right vertical axis with a threshold of 40 dB. Cycle series each consist of three repeated loading cycles and high activity and intensity for Amplitude until 100 dB occurs for almost every first load cycle of each series. After steel yielding, more hits with higher Amplitudes are recorded. Figure 4.27 gives the same graph, but now only for load cycle series A to C. The reduced graph allows by the studying of the cycles and AE characteristics in greater detail, comparable at the load-capacity level of 16.3% of the estimated ultimate load of the bridge which lies here at the level between cycle A and B. Peak Amplitude measured during the bridge test is 67 dB at highest recorded strain. Beam specimens have peak recordings of 80 and 99 dB when loads are exceeded for the first time. The Kaiser Effect verifies that priory higher load levels have occurred on the field bridge than the tested one. For this reason, the field bridge tests did not see peak Amplitudes at similar levels as in the laboratory tests.

Figure 4.28 shows a similar graph of the complete test program of Beam B3, but now with AE Energy on the right vertical axis. This figure shows an obvious relationship between load cycles in terms of strain and AE activity. As in previous figures, energy peaks are discovered at every first load cycle of each series. Energy relative to Amplitude indicates that these events consist of primary cracks from within the structure, which are

likely to exist through concrete cracking at increasing load levels. The Kaiser Effect tells us that no AE hits should be recorded in reloading cycles where stresses are not exceeding previous applied stresses [ASTM E1316, 2010]. However, emissions with Amplitudes higher than 85 dB are recorded in reloading cycles B2, C2 and C3 of series A to C before 82% of steel yielding and 75% of the ultimate moment has taken place. The Kaiser Effect can unfortunately not be evaluated in its traditional fashion in terms of load against hits as the recording systems of AE and load, strain and displacement were not linked. In addition, Figure 4.29 gives the Energy relationship with measured strain as a function of time. Similar observations are noticed at greater detail and the relationship between Amplitude and Energy is clearer visible to indicate primary emissions.

Figure 4.30 and 4.31 show the same strain graph as a function of time for Beam B3. AE Hit results as history plot are given from the right vertical axis. The first figure shows load cycle series A to K, while the second figure only shows series A to C. The event rate of AE sensors at the bottom of the beam gives an immediate indication of micro cracking from the moment the load is applied [Maji and Sahu, 1994]. Micro cracks by first service level simulated load (B3 Cycle A1; 6.7% of M_u) is recorded as an event with a relatively high Number of Hits in both graphs. At the time that load reaches about 82% of yielding and 75% of the ultimate moment, an atypically high Number of Hits is recorded. Maji and Sahu [1994] have done similar observations and described this as occurring at about 80 to 90% of the ultimate load capacity. This observation complies also with the Felicity Effect [ASTM E1316, 2010], which specifies that a relationship between the Number of Hits and previously applied load levels exists. Felicity Effect indicates that at a certain load level, when a certain amount of damage has occurred, the Kaiser Effect is not viable

anymore and AE Hits will be recorded for none exceeding load cycles. Usually this effect starts occurring at around 70 to 80% of the ultimate moment. High Amplitude hits were recorded in reloading cycles before this level was reached and may relate to the damaged condition of specimen B3 due to corrosion. A high Number of Hits at failure directly relates to concrete failure cracks and CFRP debonding.

Figure 4.32 and 4.33 also show the Number of Hits, but now in a cumulative fashion as a function of time. The expectation of Cumulative Hits is usually to evaluate high increases of activity due to exceeding stresses. By the many cycles, this behavior is not clear in the first figure, but more obviously presented in the second. Increasing angles of evolution indicate increasing damage rates. The angle in the first figure is more sensitive to time. As the loading rate in load cycle series A-C is constant, comparisons can be made. The first load cycle increases the Number of Hits 35% of the three load cycle series. The first time increase of loading in the second and third cycle series made the Number of Hits increase approximately 16 to 20%. Every repeating cycle only increases the Number of Hits 4% in the first series, 6% in the second series and 8% in the third series. At repeated load cycles with increasing series, Cumulative Hits increase depending on the load level. Only Beam B3 is in the focus in this analysis, but similar findings were done in the other specimens and can be found in Appendix III.H.

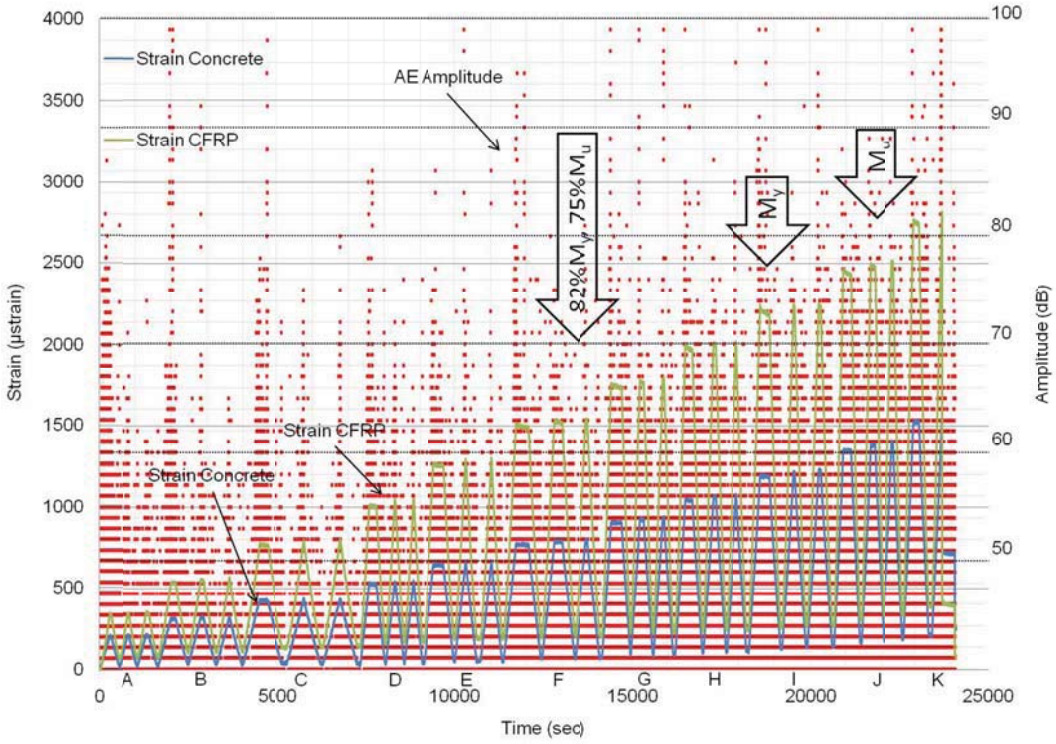

Figure 4.26 - Strain and AE Amplitude in time, complete test B3

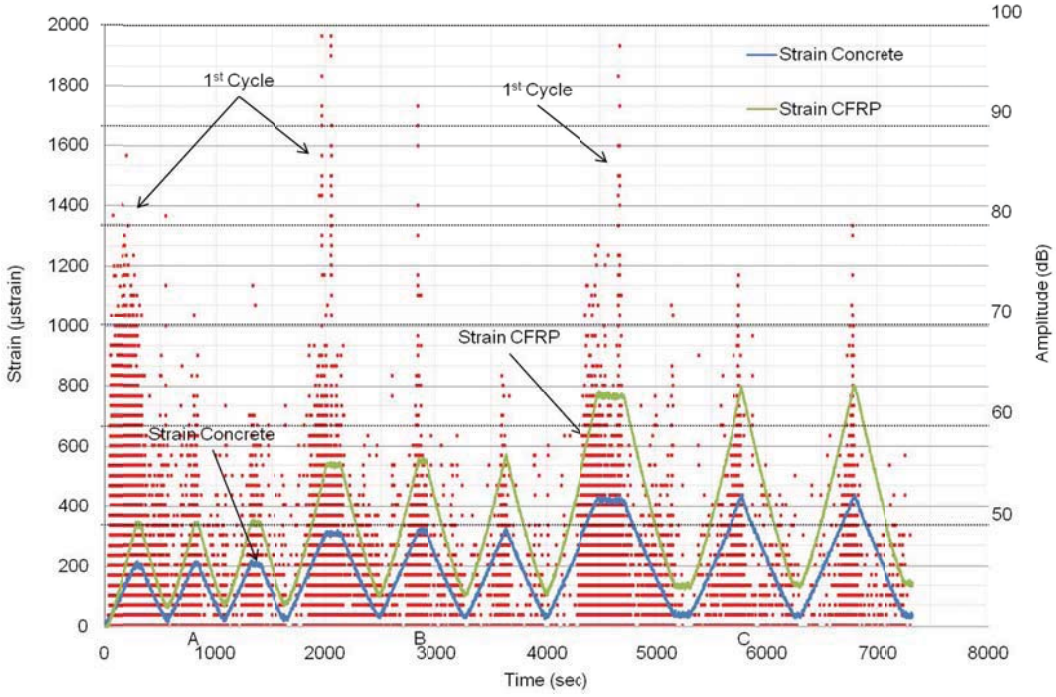

Figure 4.27 - Strain and AE Amplitude, B3 Series A-C

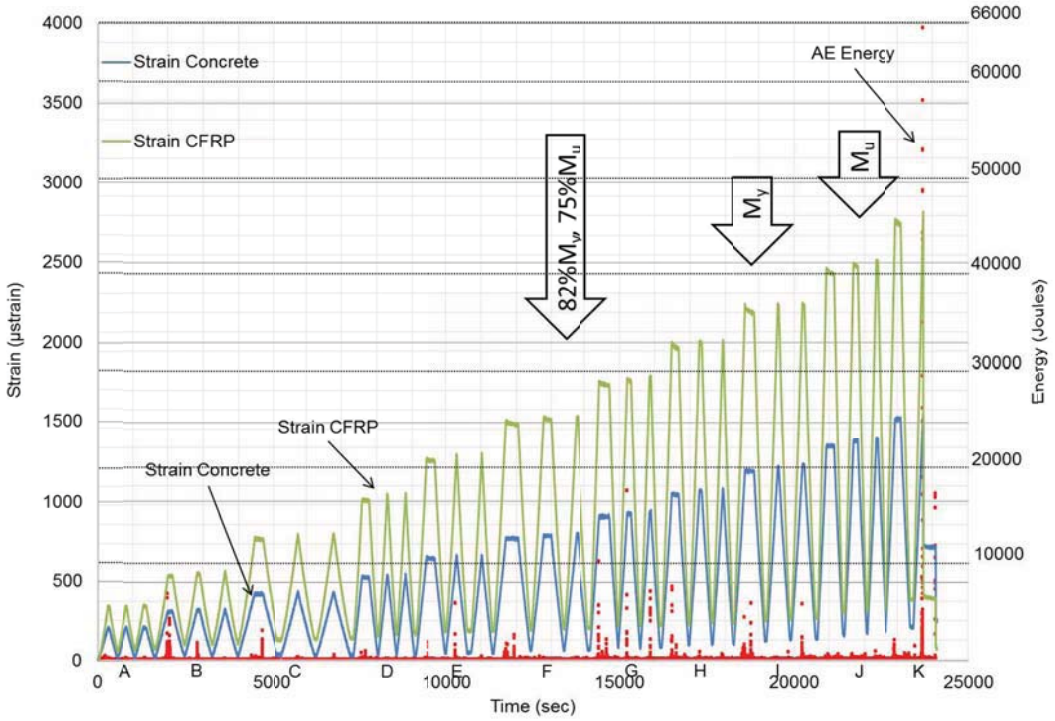

Figure 4.28 - Strain and AE Energy in time, complete test B3

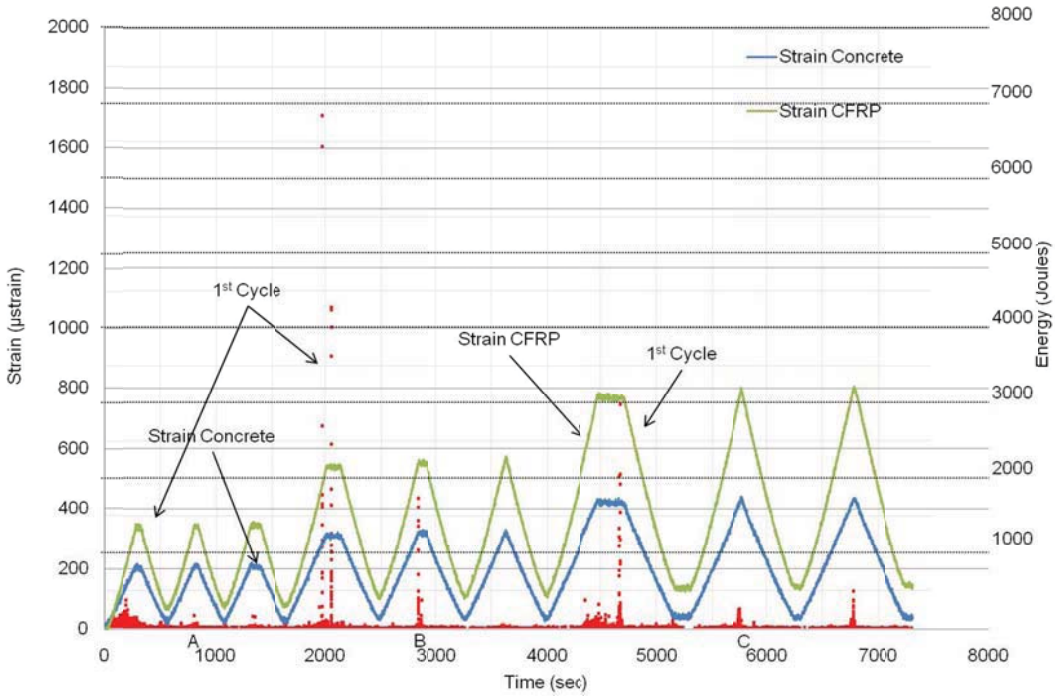

Figure 4.29 - Strain and AE Energy, B3 Series A-C

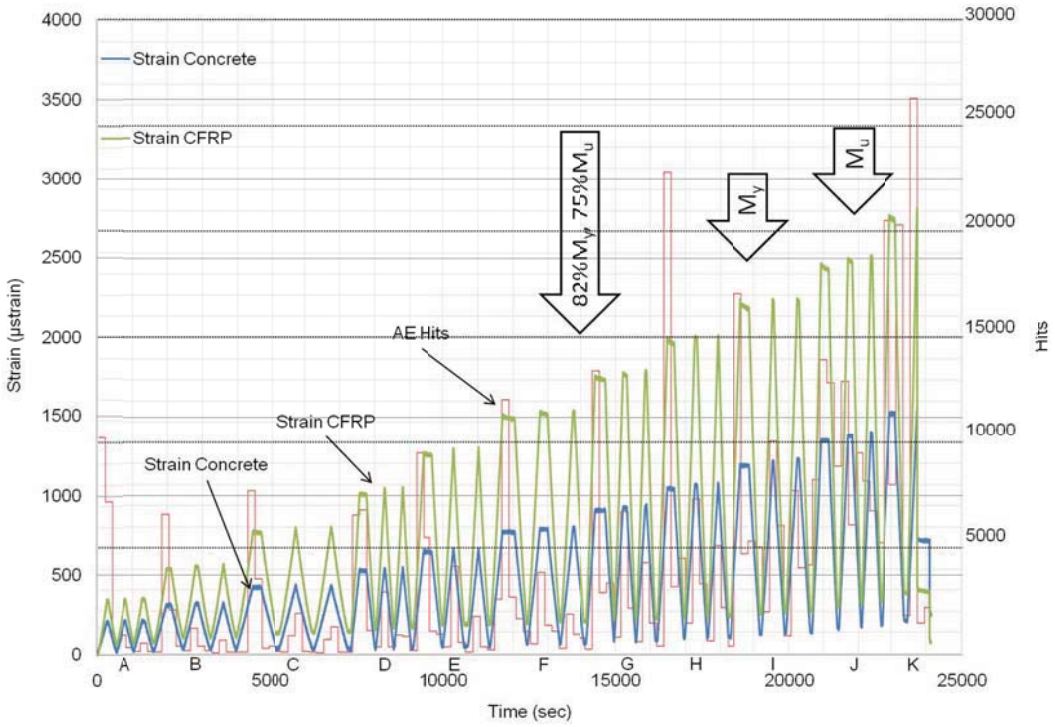

Figure 4.30 - Strain and AE Hits in time, complete test B3

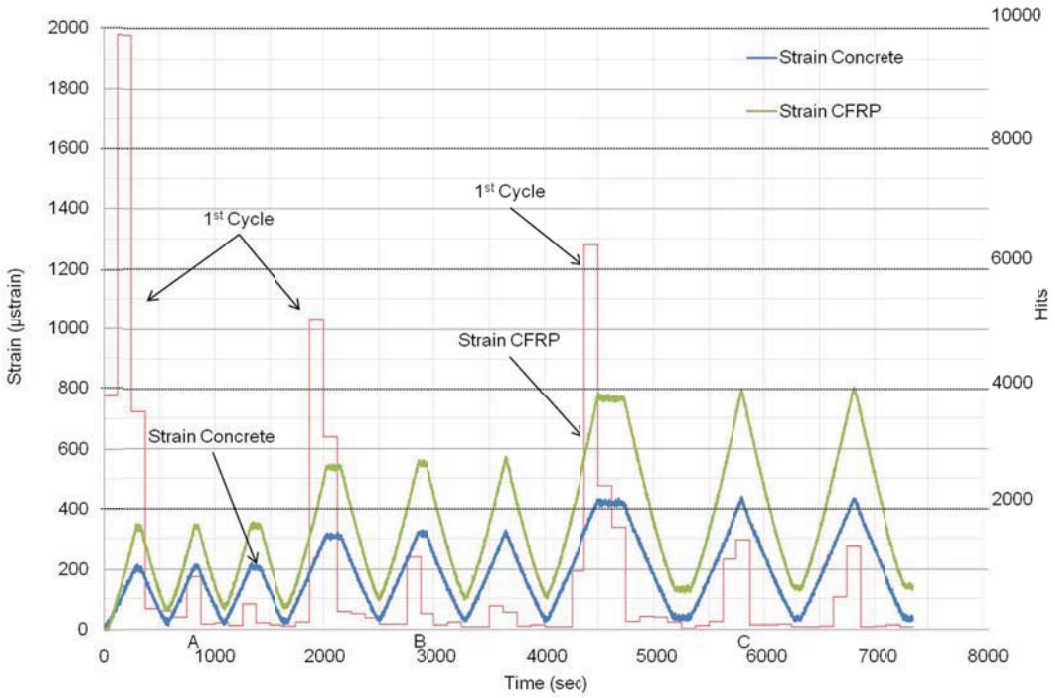

Figure 4.31 - Strain and AE Hits, B3 Series A-C

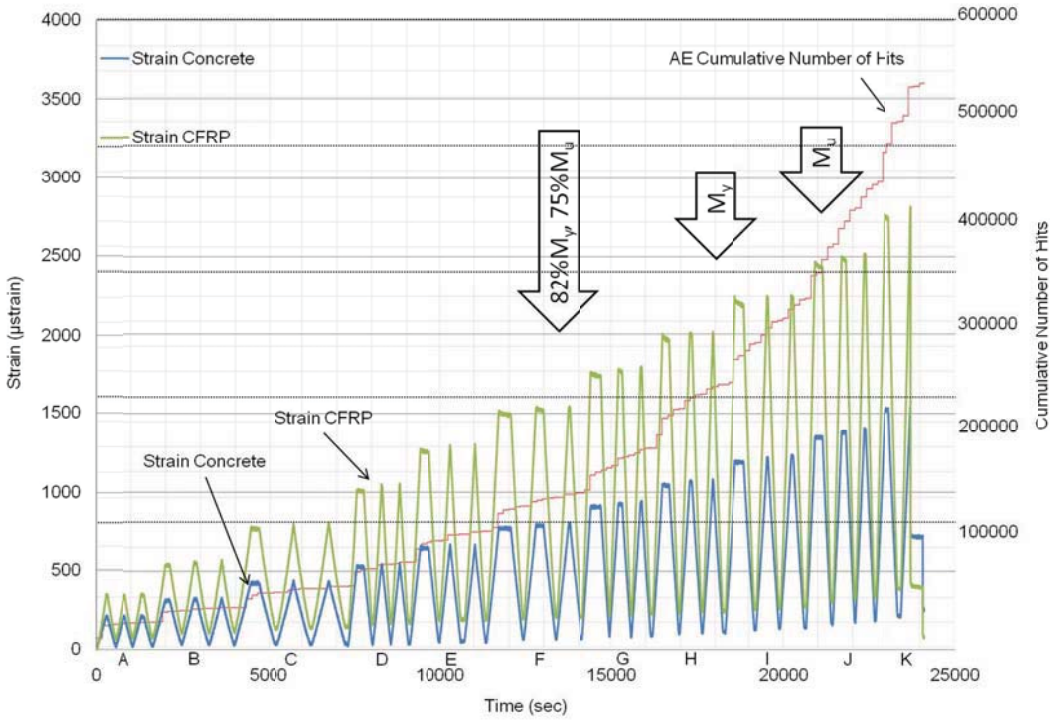

Figure 4.32 - Strain and AE Cumulative Hits, complete test B3

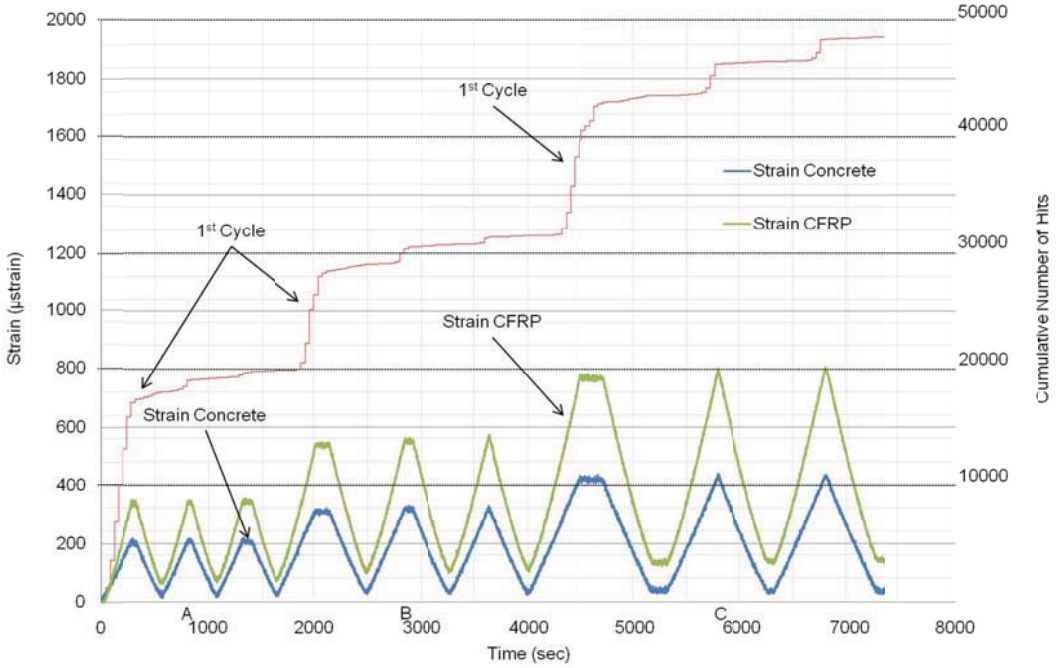

Figure 4.33 - Strain and AE Cumulative Hits, B3 Series A-C

4.6.3 Results and Discussion of Spatial Analysis and AE

Areas with relatively high potential damage due to corrosion, supported by NDT layers, are localized in each specimen (Figure 4.12). As done in Study II, statistical AE parameters are selected to point out areas of higher activity and intensity. Peak, mean and sum are able to indicate correlations between areas of high damage potential and high AE activity and intensity at relatively low level loading. For load and capacity comparison, only AE data of the first three load cycle series (A to C) are used.

Table 4.15 - Peak and mean value selection per specimen

	Amplitude (dB)		Energy (J.)		Duration (μsec.)		Nr. of Hits	
Test	Peak	Mean	Peak	Mean	Peak	Mean	Sum	Mean
B0	87	46	9	2.26	4707	243	9085	1.05
B1	99	47	7333	10.28	6241	237	9016	1.38
B2	99	47	4147	6.81	13202	341	9957	1.37
B3	99	46	6844	6.75	27958	276	10407	1.43

Table 4.15 shows selected statistical AE parameters, where specimen B0 has a peak Amplitude of 87 dB, while the corroded specimens all have 99 dB. At the same order, energy and duration recordings of the uncorroded specimen are considerably lower than corroded specimens. Especially for Duration, the order of magnitude seems to follow the rate of corrosion. The Number of Hits is discussed as the sum and the mean value. The mean is established by dividing the specific number of hits by the test duration. An increasing Number of Hits follows the rate of corrosion. A similar trend is found in the total Number of Hits of cycles A to N with 33, 40, 48, and 64 thousand hits per test for Beam B0, B1, B2 and B3 respectively.

The identification of the most active regions is done per sensor. Figure 4.34 shows sensor locations by dashed lines, where sensor S1 and S8 are placed in the center on top and bottom. Sensors S1 to S7 are placed on the bottom surface on CFRP laminates, while sensors S8 to S16 are placed on the top concrete surface. Table 4.16 gives, in relation to the previous table, sensors where peaks and highest sums per parameter are reported. The sensor indication seems consistent with what is seen in the bridge analysis. It is noted that sensors placed on the CFRP covered bottom surfaces record more activity and have higher peaks. Specimens B0, B1 and B2 are consistent in appointing most active areas using selected parameters, while Beam B3 has higher peak Amplitudes. After deeper investigation, it appeared that sensors S4, S11 and S14 showed peaks of 98 dB, which is 1 dB less than the opted sensors in the table.

Table 4.16 - Sensor selection highest AE activity per specimen

	Laboratory Beam Specimens, Cycle Series A-C				
		B0	B1	B2	B3
Peak	Amplitude	1	3	5, 6	1,8,12
	Energy	1	3	6	1
	Duration	12	5	6	14
Cumulative	Amplitude	1	4	12	8
	Energy	1	4	4	8
	Duration	1	4	4	8
	Hits	1	4	12	8
Result	Peak Sensors	1	3	6	1
	Cum. Sensor	1	4	4,12	8

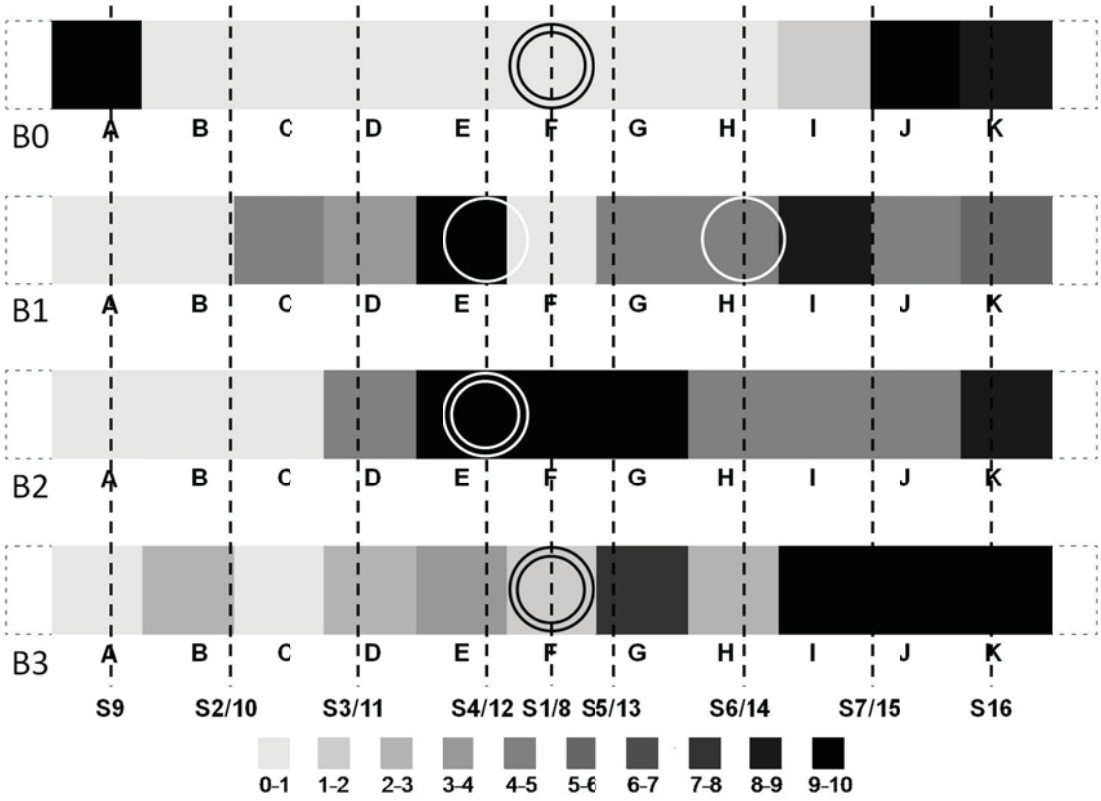

Figure 4.34 - Visual indication AE activity and spatial analysis

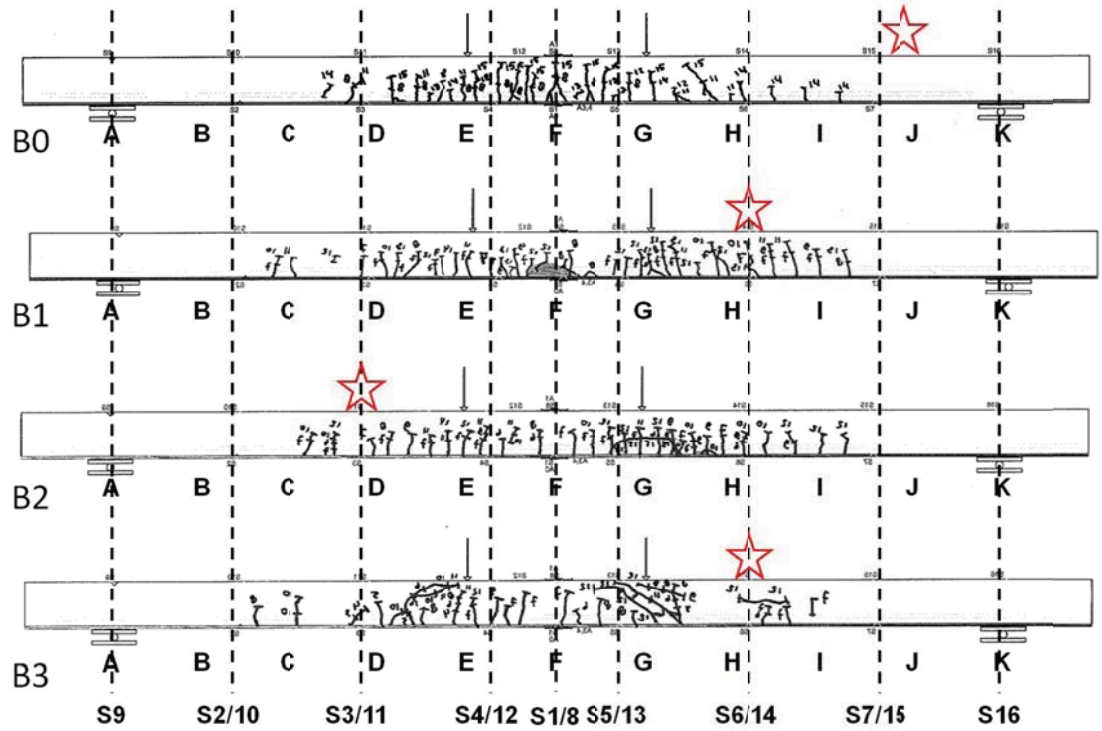

Figure 4.35 - Crack map with failure and AE sensor locations

Figure 4.35 correlates both assessments and visually identifies selected areas in relation to the physical evaluation outcomes. Note that Beam B1, B2 and B3 are mirrored as during load testing, AE sensors were placed in opposite numbering. Each ring stands for a sensor with dominating parameters in terms of occurrence [Table 4.16]. All beam specimens show the highest AE activity in the maximum constant moment zone between sensor locations 4/12 and 5/13, or cell locations E and G where the loads are applied. However, beams B1 and B2 show apparent spatial correlation with selected statistical parameters indicating high AE activity with high potential damaged areas (dark).

The specimens show more activity at the side were the beam was rated for diminished condition. The most corroded specimen, Beam B3, indicates that sensors with highest AE activity are situated in the constant moment zone at midspan where the largest deflections are measured. However, high Amplitude hits (90-100 dB) were recorded across the length of the specimen at relatively low level loads during first time loading and reloading. Figure 4.35 shows the crack maps and failure locations marked with a star. Visually detectable cracking only occurred from loads of 6 kips [26.7kN], which is approximately 41% of the ultimate load. AE was able to detect inferior areas earlier than the naked eye when cracks were opened by loading. All beam specimens show correlations with areas rated for high potential damage and failure location. Beam B3 failed by horizontal shear due to concrete cover separation and this appeared directly related to the physically deteriorated condition of the beam. Correlation between AE activity and failure location is not obviously visible. AE emissions appear to be related to the loading location with the highest stresses. Failure occurs at the weakest physical link where areas are rated for highest potential damage.

4.7 Conclusions

- Potential damage by spatial analysis of the bridge field test and the laboratory test showed similarity at different corrosion levels with the only difference that the bridge field test includes aid voids and the laboratory test includes chloride content. Moreover, similarity was found in the observation that localized areas rated for highest damage potential recorded most AE activity in terms of highest activity and intensity;
- Damage levels due to corrosion conditioning could be rated, identified and localized by spatial analysis combining different physical assessment layers;
- Failure occurred at locations with highest rating for physical deterioration, while Acoustic emission trends in terms of most active and intense parameters were able to indicate regions with highest stresses;
- Specimens with different corrosion level subjected to four-point bending tests show different failure modes in relation to the level of corrosion;
- AE attenuation was found to be especially influenced by interface properties, material, composition, level of corrosion damage, and sensor placement.

Chapter 5

5 Conclusions

This research investigates corrosion damage in concrete structures and AE. Physical assessment methods are generally accepted for field investigations to determine the condition of structural elements in a nondestructive fashion. Combining results, after normalizing, in spatial layered maps, offers a new tool to localize areas with high probability of corrosion and concrete damage with an increased confidence level. Overall, the investigation methods offer an improved means for decision making on maintenance, repair and replacement of concrete bridge structures with a resulting reduction of posting and closing. Additionally, the methods offer an improved and easy interpretable communication tool. Some specific observations include:

- Complexity of different material types, concrete designs and marine exposure deterioration are overcome by using combined NDE methods interpreted after spatial mapping.
- Spatial mapping identifies areas with high damage potential with higher level of confidence. This offers increased accuracy to effectively open up of the concrete cover for further inspections;
- ArcGIS is found a useful and accessible tool for the analysis of field assessments with layered maps and large amounts of data points;

- AE attenuation testing with repeatable signal characteristics offers a tool to investigate the composition and repair quality, independent of its composition and history, by AE signal conductivity of visual unreachable and undetectable areas covered with CFRP laminates. AE attenuation properties depend on interface material, structures composition, corrosion and damage level and sensor placement;
- AE monitoring gives indication in terms of signal activity and intensity of locations rated for high potential damage identified by spatial analysis of combined assessment layers;
- AE signal transmission is influenced and can be interrupted by local physical damages in a concrete structure. The method is therefore not yet reliable enough to be used as a standalone assessment tool to assess and monitor progressing damage of concrete structures. Together with tradition measurement methods, AE offers a good complementing method for life time monitoring.

Chapter 6

6 Future Work

New methods, incorporated methods and new technologies such as spatial analysis and AE should be further developed in order to provide enhanced evaluation tools for field inspections of concrete structures. Investigations and methods performed in this dissertation are mostly well accepted, but others need further verification. Suggestions are given for future research to advance field inspection methods of RC structures:

- Air voids under CFRP laminates may reduce the effectiveness of the strengthening layer and should be further investigated for numerical interpretation and related code descriptions;
- More specific approach and choice of assessment layers is desired in order to indicate specific physical processes and damage. Example is given by focusing on corrosion by making use of a minimum of three layers i.e. active corrosion detection by half-cell potential, pH-level, and carbonation. Investigations should be followed by visual inspection and corrosion level measurement to verify numerical results with existing assessment methods;
- Annual inspection of the study object Fair Isle Bridge is desired to verify physical damage location by means of established tradition methods like hammer tapping. At the time of demolition or failure, inspection should be carried out to verify high rated corrosion and concrete damage locations;

- Implementation of weight factors for different assessments layers should be investigated under laboratory conditions in order to specify more precise spatial analysis identification of damage potential;
- Fuzzy logic should be used for interpretation and analysis of physical assessment layers. This mathematical method offers advanced interpretation tools with relative normalized scaling;
- During accelerated corrosion conditioning by means of induced voltage, significant heat losses in the steel reinforcement were observed. Local temperature differences may introduce local steel volume expansion. This may cause cracking due to other sources than steel volume expansion related to corrosion and should be investigated to better understand and control the accelerated corrosion conditioning process;
- Pencil lead break testing can be used as a global assessment method to evaluate the structural composition in terms of AE amplitude attenuation and composition conductivity. This method should be further developed by means of simulated repeatable signals on a range of different surfaces, materials, and damage types with the use of signal generators and known inputs under laboratory conditions with the goal to generate a knowledge base of AE attenuation and conductivity properties relating to specific materials and structure types. Three dimensional expression to indicate the sensor range can be a valuable tool and should be further developed for field evaluations;

- Research to AE signal sources in RC structures should be further employed to establish more certainty in identifying AE signal sources in order to improve AE as a field monitoring tool. Above all, clearer differentiation should be made in signals with external and internal sources and recognition of causes by characterizing signal signatures. Investigation should be performed under laboratory conditions by simulating typical field sources like moving objects and impact loads to be able to identify the influence of these dynamic sources.
- AE recorded noise is to be investigated in order to justify threshold levels. Each AE signal has a source and needs to be analyzed in terms of recognizing source, signal's signature and source location in order to exclude unknown factors in field monitoring;
- Strain measurement showed correlation with AE signal activity and intensity. This relation offers the opportunity to fuse data streams to more significantly identify progressing damage and exclude insignificant AE recording. Fusing methods offers more effective field monitoring, reduction of data recording and processing, and reduction of cost. Strain, load, and displacement relations with AE need to be investigated and exploited with field simulations under laboratory conditions.

References

1 Alkhrdaji, T., and M. Frye (2009) "*Highway Bridge Pier Caps Strengthening with Fiber-Reinforced Polymer*," Concrete Repair Bulletin, Vol. July/August, pp. 17-20.

2 Alampalli, S., J. O'Connor, and A.P. Yannotti (2002) "*Fiber Reinforced Polymer Composites for the Superstructure of a Short-Span Rural Bridge*," Composite Structures, Vol. 58, pp. 21-27.

3 "*AASHTO Bridge the Gap, Restoring and Rebuilding the Nation's Bridges*," American Association of State Highway and Transportation Officials, 2008.

4 Colombo, S.I., M.C. Forde, I.G. Main, J. Halliday, and M. Shigeishi (2005) "*AE Energy Analysis on Concrete Bridge Beams*," Materials and Structures, Vol. 38, pp. 851-856.

5 "*NBIS, Code of Federal Regulations, No. 23CFR650*, " National Bridge Inspection Standards, U.S. Government Printing Office, Washington D.C., pp. 238-240, 1996.

6 Phares, B.M., Washer, G.A., Rolander, D.D., Graybeal, B.A., and Moore, M. (2004) "*Routine Highway Bridge Inspection Condition Documentation Accuracy and Reliability*," Journal of Bridge Engineering, ASCE, Vol., 9-4, pp. 403-413.

7 Moore, M.E., Phares, B.M., Graybeal, B.A., Rolander, D.D., and Washer, G.A. (2001) "*Reliability of Visual Inspection of Highway Bridges*," FWHA Rep. No. FHWA-RD-01-020, FHWA, U.S. Dept. of Transportation, Washington, D.C.

8 "*AASHTO, The Manual for Bridge Evaluation, First Edition*," American Association of State Highway and Transportation Officials, 2008.

9 Korenska, M., Stryk, J., Pazdera, L., and Vyroubal, P. (2008) "*Bridge Structure Diagnostics Using the Acoustic Emission Method*," Česká společnost pro nedestruktivní zkoušení materiálu 38, mezinárodní konference Defektoskopie 2008.

10 Carpinteri, A., Lacidogna, G. and Manuello, A. (2008) "*Localization Accuracy of Microcracks in Damaged Concrete Structures*," Acoustic Emission and Critical Phenomena, Taylor & Francis Group, London, Great Britain, pp. 101-124.

11 Matta, F., Ziehl, P.H., Galati, N., and Nanni, A. (2010), "*Static Methods for Assessment*," Chapter VI: Structural Health Monitoring and Assessment, in "*Inspection, Testing, and Monitoring of Buildings and Bridges*," in press, National Council of Structural Engineers Associations, Chicago, IL, USA.

12 Glennie, A.M.G., and Summerscales, J. (1986) "*Acoustic Emission Source Location in Orthotropic Materials*," British Journal of Non Destructive Testing, Vol. 28-1, pp. 17-22.

13 Schechinger, B., and Vogel, T. (2007) "*Acoustic Emission for Monitoring a Reinforced Concrete Beam Subject to Four-Point-Bending*," Construction and Building Materials, Vol. 21, pp. 483–490.

14 Lovejoy, S.C. (2008) "*Acoustic Emission Testing of In-Service Conventionally Reinforced Deck Girder Superstructure on Highway Bridges, Final Report*," Oregon Department of Transportation, Bridge and Engineering Section.

15 "*ASTM E 1316-10b, Standard Terminology for Nondestructive Examinations*," ASTM International, West Conshohocken, PA, 2010.

16 Cole, T.A., Lopez, M., and Ziehl, P.H. (2006) "*Fatigue Behavior and Nondestructive Evaluation of Full-Scale FRP Honeycomb Bridge Specimen*," Journal of Bridge Engineering, ASCE, Jul/Aug, pp. 420-429.

17 Lui, Z., and Ziehl, P.H. (2009) "*Evaluation of Reinforced Concrete Beam Specimens with Acoustic Emission and Cyclic Load Test Methods*," ACI Structural Journal, Vol. May-June, pp. 288-299.

18 Ziehl, P.H. (2008) "*Applications of Acoustic Emission Evaluation for Civil Infrastructure*," Proc. of SPIE, Vol. 6934, Acoustic-Ultrasound NDE, No. 69340I, pp. 1-8.

19 Hu, Q-W., Chen, Y-N., Zhou, Y., Xiong, C.L. (2009) "*An Overview on Open Source GIS Software with its Typical Applications*," Geomatics World, Vol. 01, pp. 208-218.

20 Hearn, S.W., and Shield, C.K. (1997) "*Acoustic Emission Monitoring as a Nondestructive Testing Technique in Reinforced Concrete*," ACI Materials Journal, Vol. November-December, pp. 510-519.

21 Ruggiano, D.J. (2008) "*Rehabilitation of Grove Isle Bridge over Biscayne Bay*," Report and Drawings of repair plan for Grove Isle Bridge by Metric Engineering, Inc. for Grove Isle Associates, LTD, Miami-Dade County, Florida.

22 Verma, N., and Balasubramaniam, R. (2009) "*Corrosion of Steel Reinforcement in Concrete*," Term Paper MME480, Indian Institute of Technology, Kanpur, Department of Materials and Metallurgic Eng.

23 Grubb, J.A., Hemant, S. Limaye, S., and Kakade, A.M. (2007) "*Testing pH of Concrete, Need for a Standard Procedure*," Concrete International, April 2007, pp. 78-83.

24 Matsushita, F., Aono, Y., and Shibata, S. (2000) "*Carbonation Degree of Autoclaved Aerated Concrete*," Cement and Concrete Research, Vol. 30, pp. 1741-1745.

25 Chang, C-F., Chen, J-W. (2004) "*The Experimental Investigation of Concrete Carbonation Depth*," Cement and Concrete Research, Vol. 36, pp. 1760– 1767.

26 Minor, J., and White, K.R. (1988) "*National Cooperative Highway Research Program Report 312, Condition Surveys of Concrete Bridge Components, User's Manual*," Transportation Research Board, National Research Council.

27 Otsuki, N.M., Miyazato, S-I., and Yodsudjai, W. (2003) "*Influence of Recycled Aggregate on Interfacial Transition Zone, Strength, Chloride Penetration and Carbonation of Concrete*," Journal of Materials in Civil Engineering, ASCE, Vol. September/October, pp. 443-451.

28 Elsener, B., and Böhni, H. (1988) "*Corrosion Rates of Steel in Concrete*," Proceeding Symposium Baltimore, Ed.: Berke, N.S., Chaker, V., and Whitening, D., ASTM G1, Ann Arbor, MI, pp. 143-156.

29 Malhotra, V.M., and Carino, N.J. (2004) "*Handbook on Nondestructive Testing of Concrete, 2nd Edition*," ASTM International, CRC Press LLC.

30 Neville, A. (1995) "*Chloride Attack of Reinforced Concrete: An Overview*," Materials and Structures, Vol. 28, pp. 63-70.

31 Bary, B., and Sellier, A. (2004) "*Coupled Moisture - Carbon Dioxide - Calcium Transfer Model for Carbonation of Concrete*, "Cement and Concrete Research, Vol. 34, pp. 1859 – 1872.

32 "*ASTM F 710-08, Standard Practice for Preparing Concrete Floors to Receive Resilient Flooring*," American Standard Test Method, 2008.

33 Räsänen, V., and Penttala, V. (2003) "*The pH Measurement of Concrete and Smoothing Mortar Using a Concrete Powder Suspension*," Cement and Concrete Research, Vol. 34, pp. 813-820.

34 Sergi, G., and Glass, G.K. (2000) "*A Method of Ranking the Aggressive Nature of Chloride Contaminated Concrete*," Corrosion Science, Vol. 42, pp.2043-2049.

35 Xinying, L., Li, C., and Zhang, H. (2001) "*Relationship Between the Free and Total Chloride Diffusity in Concrete*," Cement and Concrete Research, Vol.32, pp.323-326.

36 Thomas, M. (1996) "*Chloride thresholds in Marine Concrete*," Cement and Concrete research, Vol. 26-4, pp. 513-519.

37 Lindvall, A. (2007) "*Chloride Ingress Data from Field and Laboratory Exposure – Influence of Salinity and Temperature*," Cement & Concrete Composites, Vol. 29, pp. 88-93.

38 "*ASTM C 1152/C 1152M-04,* Standard Test Method for Acid-Soluble Chloride in Mortar and Concrete*,"* American Standard Test Method, 2004.

39 Shigeishi, M., Colombo, S., Broughton, K.J., Rutledge, H., Batchelor, A.J. and Forde, M.C. (2001) "*Acoustic Emission to Assess and Monitor the Integrity of Bridges*," Construction and Building Materials, Vol. 15, pp. 35-49.

40 Degala,S., Rizzo, P., Ramanathan, K., and Harries, K.A. (2009) "*Acoustic Emission Monitoring of CFRP Concrete Slabs*," Construction and Building Materials, Vol. 23, pp. 2016-2026.

41 "*ASTM D 3633-98, Standard Test Method for Electrical Resistivity of Membrane-Pavement Systems*," ASTM International, West Conshohocken, PA, 2006.

42 "*ASTM D 4580-03, Standard Practice for Measuring Delaminations in Concrete Bridge Decks by Sounding*," ASTM International, West Conshohocken, PA, 2003.

43 "*ASTM D 4788-03, Standard Test Method for Detecting Delaminations in Bridge decks Using Infrared Thermography*," ASTM International, West Conshohocken, PA, 2007.

44 Barde, V., Radlinska, A., Cohen, M., and Weiss, J. (2009) "*Relating Material properties to Exposure for predicting service life in Concrete Bridge decks in Indiana*," Joint transportation Research program, IDOT, Final Report.

45 Cusson, D., and Quin, S.Y. (2009) "*Ten-Year Field Evaluation of Corrosion-Inhibiting Systems in Concrete Bridge Barrier Walls*," ACI Materials Journal, Vol. 106-3, pp. 291-300.

46 Robertson, I.N., and Newtson, C. (2009) "*Performance of Corrosion Inhibitors in Concrete exposed to Marine Environment*," Concrete Repair, Rehabilitation and Retrofitting II, Taylor and Fracis Group, London, pp. 901-906.

47 Hawkins, G.F., Johnson, E., and Nokes J. (1999) "*Typical Manufacturing Flaws in FRP Retrofit Application*," Proceeding NIST Workshop NISTIR 6288, Vol. 3, Tucson, Arizona, pp.97-101.

48 Hsu, N.N. (1976) "*Acoustic Emission Simu*lator," US Patent 4 018 084.

49 Nielsen, A. (1980) "*Acoustic Emission Source Based on Pencil Lead Breaking*," The Danish Welding Institute Publication, Report 80-15.

50 Sanayei, M., and Saletnik, M. J. (1996) *"Parameter Estimation of Structures from Static Strain Measurements; I: Formulation,"* Journal of Structural Engineering, ASCE, Vol. 122-5, pp. 555-562.

51 Sanayei, M., Santini-Bell, E., Javdekar, C.N., Edelmann, J.L., and Slavsky, E. (2006) "*Damage Localization and Finite-Element Model Updating Using Multiresponse NDT Data*," Journal of Bridge Engineering, ASCE, Vol. 11-6, pp. 688-698.

52 Santini-Bell, E., Sanayei, M., Javdekar, C.N., and Slavsky, E. (2007) "*Multiresponse Parameter Estimation for Finite-Element Model Updating Using Nondestructive Test Data*," Journal of Structural Engineering, ASCE, Vol. 133-8, pp. 1067-1079.

53 "*ASTM C 876-09, Standard Test Method for Corrosion Potentials of Uncoated Reinforced Steel in Concrete*," American Standard Test Method, 2009.

54 Elsener, B., Andrade, J., Gulikers, R. Polder, R. and Raupach, M. (2003) "*Half-Cell Potential Measurements – Potential Mapping on Reinforced Concrete Structures*," Materials and Structures, Vol. 36, pp. 461-471.

55 Gulikers, J., and Elsener, B. (2009) "*Development of a Calculation Procedure For the Statistical Interpretation of the Results of Potential Mapping Performed on Reinforced Concrete Structures*," Materials and Corrosion, Vol. 60-2, pp.87-92.

56 Huston, D., Gucunski, N., Maher, A., Cui, J., Burns, D., and Jalinous, F. (2007) "*Bridge Deck Condition Assessment with Electromagnetic, Acoustic and Automated Methods*," Proceedings 6th International Workshop on Structural health Monitoring.

57 O'Sullivan, D., and Unwin, D.J. (2002) "*Geographic Information Analysis*," John Wiley & Sons, Hoboken, NJ, ISBN 978-0-470-28857-3.

58 Fotheringham, S., and Rogerson, P. (2002) "*Spatial Analysis and GIS*," Taylor & Francis Group, London, UK, ISBN 0-7484-0103-2.

59 Miles, S.B., and Ho, C.L. (1999) "*Applications and Issues of GIS as Tool for Civil Engineering Modeling*," Journal of Computing in Civil Engineering, Vol. 13-3, pp. 144-152.

60 Stevens, D., Dragicevic, S., and Rothley, K. (2006) "*iCity: A GIS – CA Modeling Tool for Urban Planning and Decision Making*," Environmental Modeling & Software, Vol. 22, pp. 761-773.

61 Yamazaki, F. (2001) "*Applications of Remote Sensing and GIS for Damage Assessment,*" Structural Safety and Reliability, Swets & Zeitlinger, pp. 1-12.

62 Vafeidis, A.T., Drake, N.A., and Wainwright, J. (2007) "*A Proposed Method for Modeling the Hydrologic Response of Catchments to Burning with the Use of Remote Sensing and GIS*," Catena, Vol. 70, pp. 396-409.

63 Carroll, J.M., Meutis, H.M., Convertino, G., Rosson, M.B., Ganoe, C.H., Sinha, H., and Zhao, D. (2007) "*Prototyping Collaborative Geospatial Emergency Planning*," Proceedings ISCRAM2007, pp. 105-113.

64 Kumaresan, V., Vasudevan, V., and Nambisan, S.S. (2009) "*Development of a GIS-Based Traffic Safety Analysis System*," Annual ESRI International User Conference, San Giego, CA, pp. 1-12.

65 Zheng, M.H., Guo, Y.R., Ai, X.Q., Qin, T., Wang, Q., and Xu, J.M. (2010) "*Coupling GIS with CFD Modeling to Simulate Urban Pollutant Dispersion*," Mechanic Automation and Control Engineering, pp. 1785-1788.

66 Kaiser, H., and Karbhari, V.M. (2004) "*Non-Destructive Testing Techniques for FRP Rehabilitated Concrete - I: a Critical Review*," International Journal of Materials and Product Technology, Vol. 21-5, pp. 349-384.

67 Hadidi, R., and Saadeghvaziri, M.A. (2005) "*Transverse Cracking of Concrete Bridge Decks: State-of-the-Art*," Journal of Bridge Engineering, ASCE, Vol. 10-5, pp. 503-510.

68 "*ACI 224R, Control of Cracking in Concrete Structures*," American Concrete Institute, Farmington Hills, MI, 2008.

69 Darwin, D., Browning, J., and Lindquist, W.D. (2004) "*Control of Cracking in Bridge Decks: Observations from the Field*," Cement, Concrete and Aggregates, Vol. 26-2, pp. 148-154.

70 "*ASTM E 2582-07, Standard Practice for Infrared Flash Thermography of Composite Panels and Repair Patches Used in Aerospace Applications*," ASTM International, West Conshohocken, PA, 2007.

71 "*ACI 440.2R-08, Guide for the Design and Construction of Externally Bonded FRP Systems for Strengthening Concrete Structures*," ACI Committee 440, 2008.

72 Jacobs, L.J., and Owino, J.O. (2000) "*Effect of Aggregate Size on Attenuation of Rayleigh Surface Waves in Cement-Based Materials*," Journal of Engineering Mechanics, Vol. 126-11, pp. 1124-1130.

73 "*ASTM E 976, Standard Practice for Reproducibility of Acoustic Emission Sensor Response*," ASTM International, West Conshohocken, PA, 2010.

74 Chen, H-L. (R.), and He, Y. (2001) "*Analysis of Acoustic Surface Waveguide for AE Monitoring of Concrete Beams*," Journal of Engineering Mechanics, ASCE, Vol. 127-1, pp. 1-10.

75 Chen, H-L. (R.), and Wissewapaisal, K. (2000) "*Study of Acoustic Waveguides on Reinforced Concrete Slabs*," Journal of Nondestructive Evaluation, Vol. 19-4, pp. 129-140.

76 Chang, C-F., Chen, J-W. (2004) "*The Experimental Investigation of Concrete Carbonation Depth*," Cement and Concrete Research, Vol. 36, pp. 1760– 1767.

77 Ormsby, T., Napoleon, E., Burke, R., Groessl, C., and Bowden, L. (2008) "*Getting to Know ArcGIS Desktop*," ESRI Press, Redlands, California, ISBN 978-1-58948-210-4.

78 Sanayei, M., Phelps, J.E., Sipple, J.D., Santini-Bell, E., and Brenner, B.R. (2010-1) "*Instrumentation, Nondestructive Testing, and FEM Updating for Bridge Evaluation Suing Strain Measurements*," (In Press).

79 Timoshenko, S., and Woinowski-Krieger, S. (1959) "*Theory of Plates and Shells*," McGraw-Hill, New York, ISBN 0-07-064779-8.

80 Sanayei, M., Santini-Bell, E., Brenner, B.R., Sipple, J.D., Phelps, J.D., and Lefebvre, P. (2010-2) "*Structural Health Monitoring and Baseline Model Updating using NDT Data*," 2010 ASCE Structures Congress, Orlando, Florida.

81 Chen, J., Wan, C., Xiao, C., Li, L. (2009) "*Research on Signal Processing for bridge Monitoring*," The Ninth International Conference on Electronic Measurement & Instruments, Vol. 4, pp.338-342.

82 Sanayei, M., Sipple, J.D., Phelps, J.E., Santini-Bell, E., Lefebvre, P.J., and Brenner, B.R. (2010-3) "*Bridge Instrumentation for Long Term Structural Health Monitoring*," (In Press).

83 Nair, A., and Cai, C.S. (2010) "*Acoustic Emission Monitoring of Bridges: Review and Case Studies*," Engineering Structures, Vol. 32, pp. 1704-1714.

84 Suma, A.B., Ferraro R.M., Metrovich, B., Matta, F., and Nanni, A., (in press) "*Non Destructive Evaluation Techniques and Acoustic Emission for Damage Assessment of Concrete Bridge in Marine Environment*," ACI Special Publications Journal, (In Press).

85 Mirmiran, A., and Philip, S. (2000) "*Comparison of Acoustic Emission activity in Steel-Reinforced and FRP-Reinforced Concrete Beams,"* Construction and Building Materials, Vol. 14, pp. 299-310.

86 Golaski, L. Gebski, P., and Ono, K. (2002) "*Diagnostics of Reinforced Concrete Bridges by Acoustic Emission,"* Journal of Acoustic Emission, Vol. 20, pp. 83-98.

87 Nair, A., and Cai, C.S. (2007) "*Acoustic Emission Monitoring of Field Bridges in Louisiana*," TRB 86th Annual Meeting Compendium of Papers, Transportation Research Board 86th Annual Meeting, Washington, CD-ROM, Paper #07-2940, pp.22.

88 El Maaddawy, T.A., and Soudki, K.A. (2003) "*Effectiveness of Impressed Current Technique of Steel Reinforcement in Concrete*," Journal of Materials in Civil Engineering, Vol. Jan/Feb, pp. 41-47.

89 Broomfield, J.P. (2007) "*Corrosion of Steel in Concrete, Understanding, Investigation and Repair, 2nd Edition*," Taylor and Francis, New York.

90 Angst, U., Elsener, B., Larsen, C.K., and Vennesland, Ø (2009) "*Critical Chloride Content in Reinforced Concrete – A Review*," Cement and Concrete Research, Vol. 39, pp. 1122-1138.

91 Nanni, A. (2000) "*Carbon Fibers in Civil Structures: Rehabilitation and New Construction*," Proc. The Global Outlook for Carbon Fiber 2000, Intertech., San Antonio, TX, pp. 1-6.

92 Van den Einde, L., Zhao, L., and Seible, F. (2003) "*Use of FRP Composites in Civil Structural Applications*," Construction and Building Materials, Vol. 17, pp. 389-403.

93 Bakis, C.E., Bank, L.C., Brown, V.L., Cosenza, E., Davalos, J.F., Lesko, J.J., Machida, A., Rizkalla, S.H., and Triantafillou, T.C. (2002) "*Fiber-Reinforced Polymer Composites for Construction – State-of-the-Art Review*," Journal of Composites for Construction, ASCE, pp. 73-87.

94 Hollaway, L.C. (2010) "*A Review of the Present and Future Utilization of FRP Composites in the Civil Infrastructure with Reference to their Important In-Service Properties*," Construction and Building Materials, Vol. 24, pp. 2419-2445.

95 Nanni, A. (2000) "*FRP Reinforcement for Bridge Structures*," Proc. Structural Engineering Conference, University of Kansas, Lawrence, KS, pp. 1-5.

96 De Luca, A., Nardone, F., Matta, F., Nanni, A., Lignola, P.L., and Prota, A. (2010) "*Structural Evaluation of Full-Scale FRP-Confined Reinforced Concrete Columns*," Journal of Composites for Construction, ASCE, Online, pp. 1-47.

97 Rocca, S., Galati, N. and Nanni, A. (2008) "*Review of Design Guidelines for FRP Confinement of Reinforced Concrete Columns of Noncircular Cross Sections*," Journal of Composites for Construction, ASCE, Jan/Feb, pp.80-92.

98 Galati, N., Tumialan, G. and Nanni, A. (2005) "*Strengthening with FRP Bars of UMR Walls Subject to Out-of-Plane Loads*," Construction and Building Materials, Vol. 20, pp. 101-110.

99 Khalifa, A., Gold, W.J., Nanni, A., and Aziz, A. (1998) "*Contribution of Externally Bonded FRP to Shear Capacity of Flexural Members*," Journal of Composites for Construction, ASCE, Vol. 2-4, pp. 195-203.

100 Ashour, A.F., El-RRefaie, S.A., and Garrity, S.W. (2004) "*Flexural Strengthening of RC Continuous Beams Using CFRP Laminates*," Cement & Concrete Composites, Vol. 26, pp' 765-775.

101 Arduini, M., Nanni, A., and Romagnolo, M. (2004) "*Performance of One-Way Reinforced Concrete Slabs with Externally Bonded Fiber-Reinforced Polymer Strengthening*," ACI Structural Journal, Mar/Apr, pp.193-201.

102 El Maaddawy, T., and Soudki, K. (2005) "*Carbon-Fiber-Reinforced Polymer Repair to Extend Service Life of Corroded Reinforced Concrete Beams*," Journal of Composites for Construction, ASCE, Mar/Apr, pp. 187-194.

103 Soudki, K., El-Salakawy, E., and Craig, B. (2007) "*Behavior of CFRP Strengthened Reinforced Concrete Beams in Corrosive Environment*," Journal of Composites for Construction, ASCE, May/Jun, pp. 291-298.

104 Masoud, S., Soudki, K., and Topper, T. (2001) "*CFRP-Strengthened and Corroded RC Beams under Monotonic and Fatigue Loads*,' Journal of Composites for Construction, ASCE, Nov, pp. 228-236.

105 Benjeddou, O., Ouezdou, M.B., and Bedday, A. (2007) "*Damaged RC Beams Repaired by Bonding of CFRP Laminates*," Construction and Building Materials, Vol. 21, pp. 1301-1310.

106 Gostautas, R.S., Ramirez, G., Peterman, R.J., and Meggers, D. (2005) "*Acoustic Emission Monitoring and Analysis of Glass Fiber-Reinforced Composites Bridge Decks*," Journal of Bridge Engineering, ASCE, Nov/Dec, pp. 713-721.

107 Maji, A.K., and Sahu, R. (1994) "*Acoustic Emissions from Reinforced Concrete*," Experimental Mechanics, pp. 379-388.

108 Ohtsu, M., Uchida, M. Okamoto, T., and Yuyama, S. (2002) "*Damage Assessment of Reinforced Concrete Beams Qualified by Acoustic Emission*," ACI Structural Journal, Jul/Aug, pp. 411-417.

109 Tensi, H.M. (2004) "*The Kaiser-Effect and Its Scientific Background*," EWGAE 2004, Keynote, DGZfP-Proceedings BB 90-CD, pp. 31-41.

110 Kaiser, J. (1950) "*Untersuchung über das Auftreten von Geräuschen beim Zugversuch*," Dr-Ing., Dissertation, Fakultät für Maschinenwesen und Elektrotechnik der Technischen Universität München (TUM); 15.2.

111 Kaiser, J. (1952), Patentschrift der Deutschen Patentamtes Nr. 852771, Klasse 42 k, Gruppe 3401 vom 20.10.1952, Materialprüfverfahren.

112 "*ASTM C39/C39M-09a, Standard Test Method for Compressive Strength of Cylindrical Concrete Specimens*," American Society for Testing and Materials, 2009.

113 Napoli, A., Matta, F., Martinelli, E., Nanni, A., and Realfonzo, R. (2010) "*Modelling and Verification of Response of RC Slabs Strengthened in Flexure with Mechanically Fastened FRP Laminates*," Magazine of Concrete Research, Vol. 62-8, pp. 593-605.

114 "*ACI 222.3R, Design and Construction Practices to Mitigate Corrosion of Reinforcement in Concrete Structures*, " American Concrete Institute, 2003.

115 Ahmad, S. (2009) "*Techniques for Inducing Accelerated Corrosion of Steel in Concrete*," The Arabian Journal for science and Engineering, Vol. 34-2C, pp. 95-104.

116 "*ASTM G1-03, Standard Practice for Preparing, Cleaning, and Evaluating Corrosion Test Specimens*," American Society for Testing and Materials, 2003.

117 "*ACI, ICRI, Concrete Repair Manual*, "American Concrete Institute, International Concrete Repair Institute, 1999.

118 "*ACI 318R-08, Building Code Requirements for reinforced* Concrete and Commentary, " American Concrete Institute, 2008.

119 Gao, B., Leung, C.K.Y., and Kim, J-K. (2007) "*Failure Diagrams of FRP Strengthened RC Beams*," Composite Structures, Vol. 77, pp. 493-508.

120 Aram, M.R., Czaderski, C., and Motavalli, M. (2008) "*Debonding Failure Modes of Flexural FRP-Strengthened RC Beams,*" Composites, Vol. 39-B, pp. 826-841.

Appendices

Appendix I – Study I

Appendix I.A – Physical Assessment Results at Deeper Level

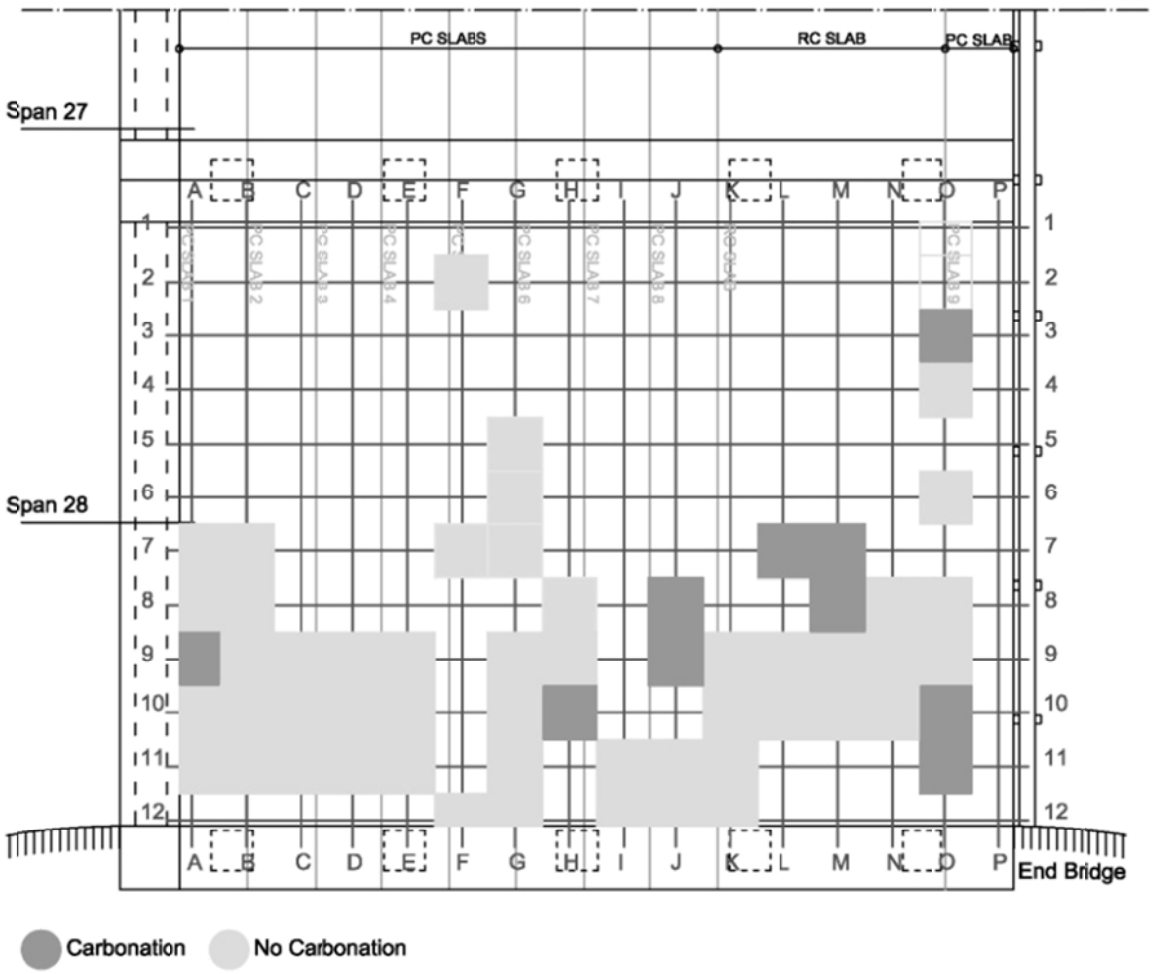

Figure I.A1 - Carbonation at 3 in. [76mm] depth

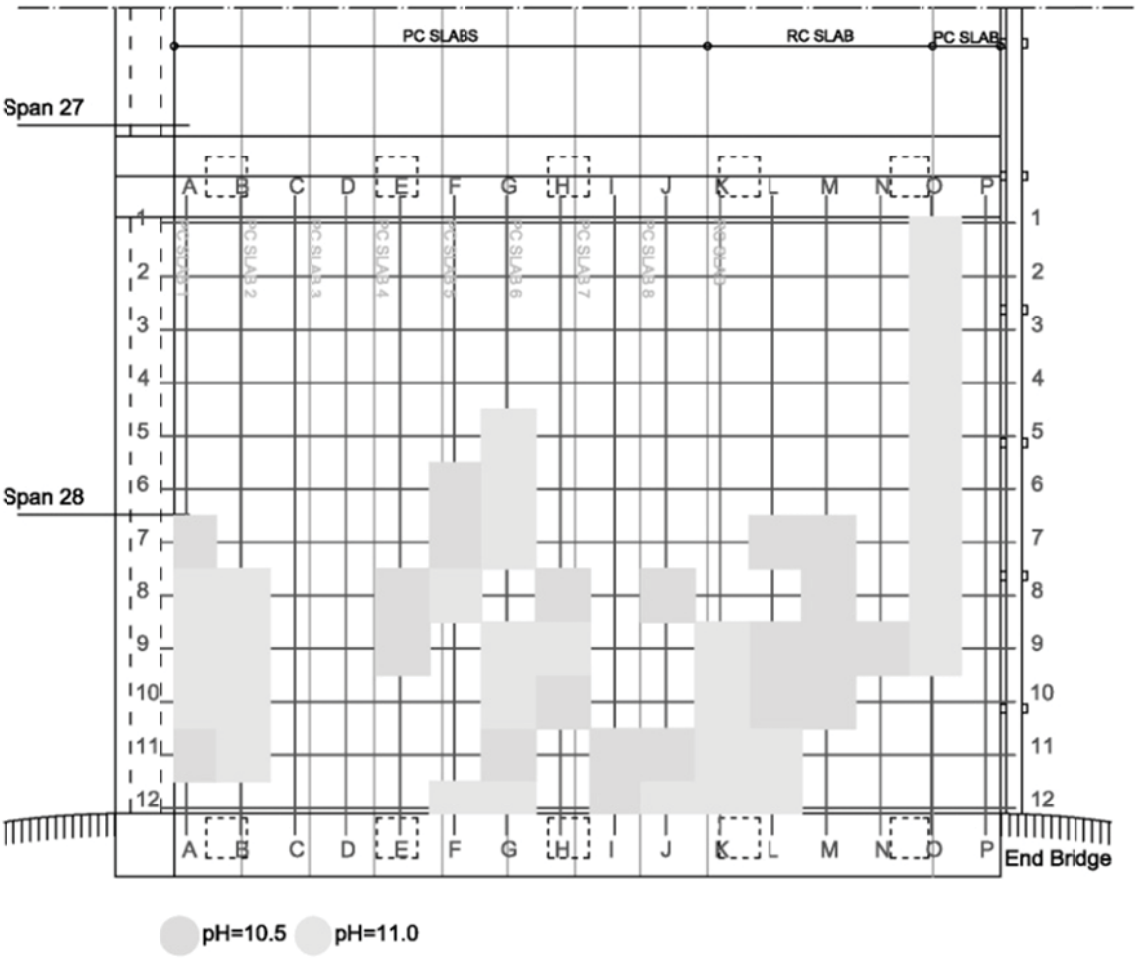

Figure I.A2 - pH level at 3 in. [76mm] depth

Appendix I.B – Chloride Content Results Fair Isle Bridge

Table I.B - Chloride content results Fair Isle Bridge

Sample	Material type	Age (years)	Temperature °F [°C]	Chloride content
1	RC	37	62.6 [17.0]	>2.0%
3	RC	37	62.6 [17.0]	>2.0%
5	Grout	11	63.3 [17.4]	>2.0%
6	RC	37	62.2 [16.8]	>2.0%
7	Grout	11	61.9 [16.6]	1.4%
10	PC	49	65.5 [18.6]	>2.0%
11	PC	49	61.9 [16.6]	>2.0%
12	PC	49	62.2 [16.8]	>2.0%
14	PC	49	64.0 [17.8]	0.5%
15	PC	49	61.9 [16.6]	>2.0%

Appendix II - Study II

Appendix II.A - Complete Crack Map

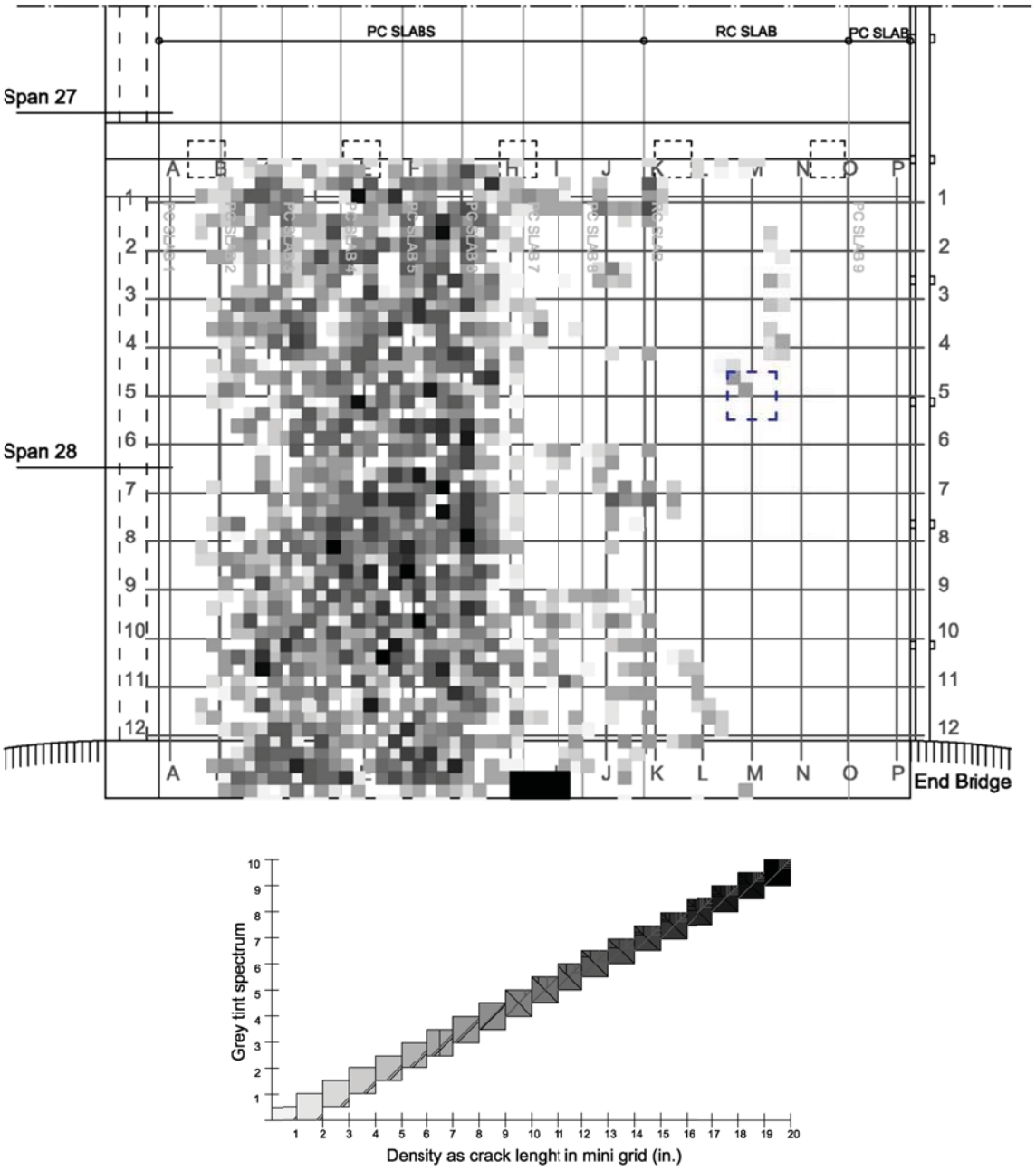

Figure II.A1 - Crack density map Fair Isle Bridge

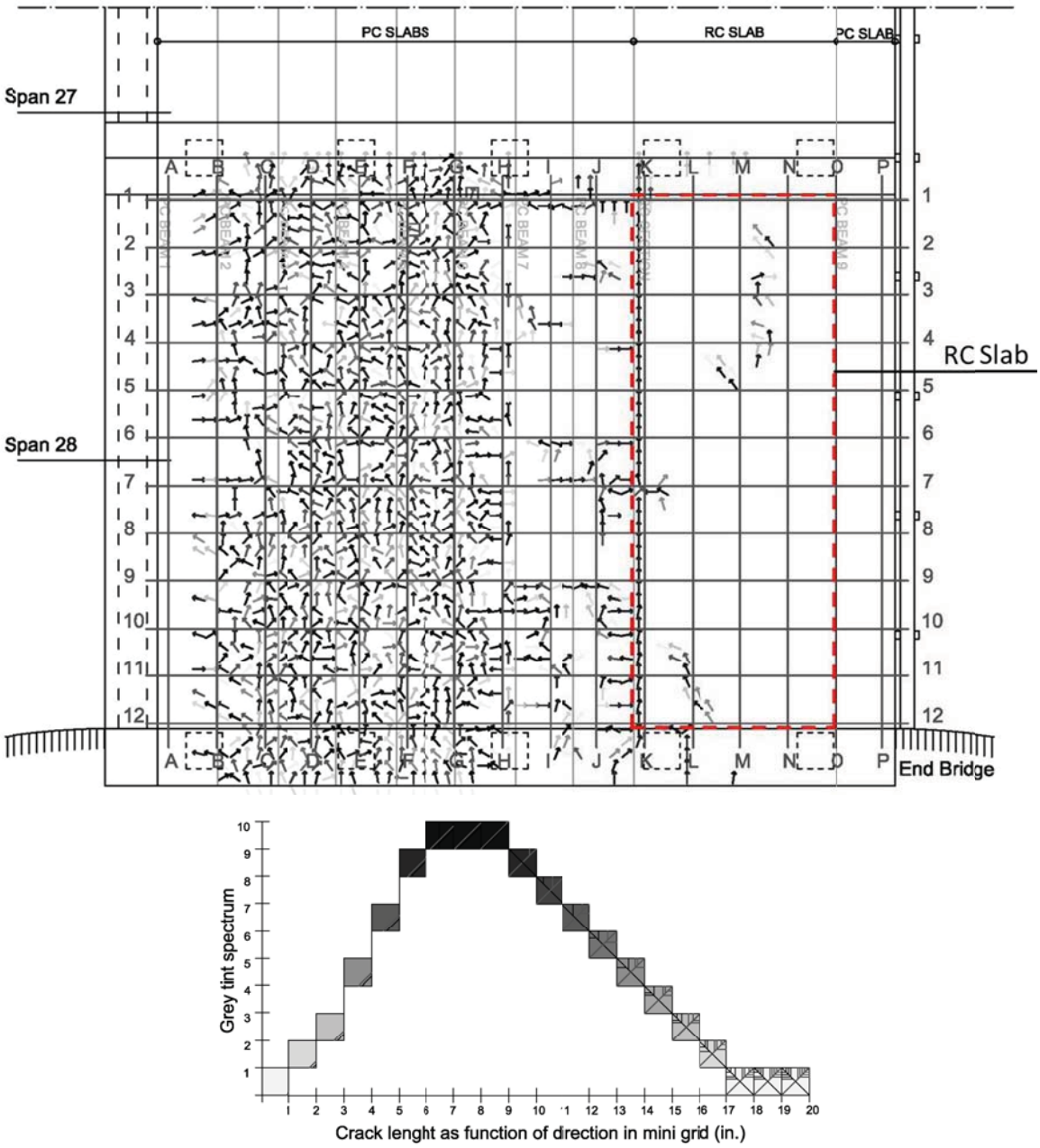

Figure II.A2 - Crack direction map of Fair Isle Bridge

Appendix II.B - Complete Air Voids Map

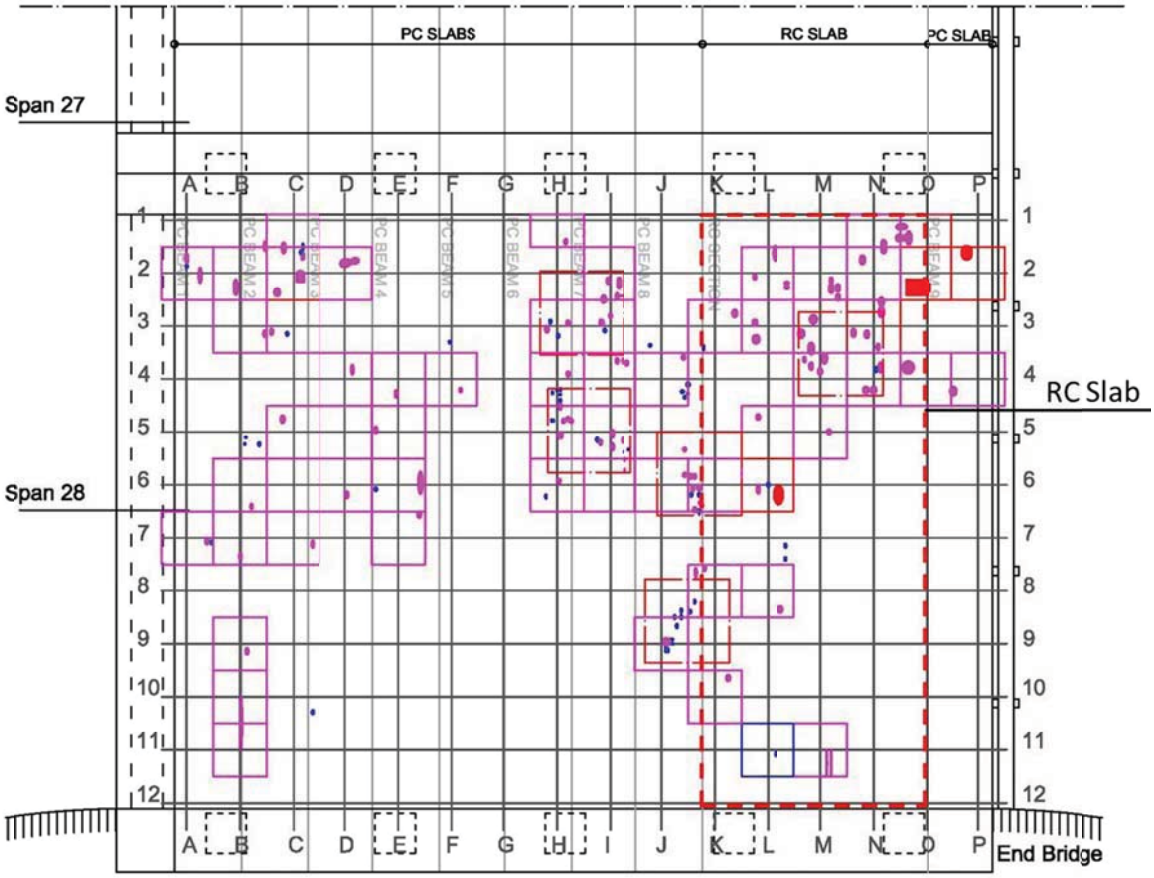

Figure II.B1 - Air void map of Fair Isle Bridge

Appendix II.C - Amplitude Results Attenuation Test

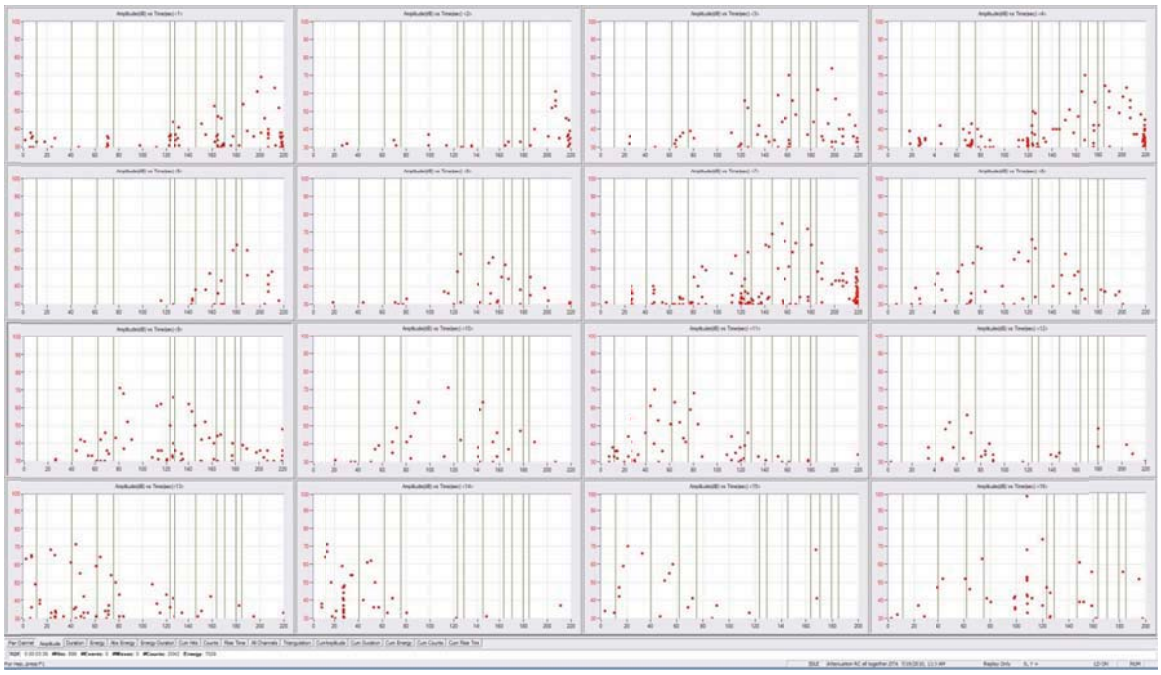

Figure II.C1 - AEWin output for AE Attenuation test Amplitude (dB) output

Table II.C1 - Average amplitude (dB) in parallel transmission

	Distance (in.)				
Sensor	24	48	72	120	144
S1	50.67	58.50	42.50	44.00	30.00
S2	50.67	40.00	33.00		
S3	62.50	59.00	46.00	39.00	32.00
S4	64.50	49.50	40.00	30.00	
S5	55.50	50.50	38.00		
S6	54.75	41.00	32.00	31.00	
S7	68.50	55.00	49.33	31.00	
S8	60.50	55.00	42.67	37.00	
S9	63.25	49.00	39.33	32.00	
S10	65.67	47.50	33.67	31.00	
S11	63.25	49.67	42.33	30.00	
S12	48.50	34.00	32.50	30.00	
S13	67.25	64.00	40.50	34.50	34.00
S14	61.50		41.00		
S15	65.33	41.00	37.00		
Average	60.16	49.55	39.32	33.59	32.00
St Dev.	6.49	8.42	5.06	4.60	2.00

Table II.C2 - Average amplitude in random direction for sensor 16

	Distance (in.)						
Distance	3.50	24.25	31.56	44.50	48.12	50.55	52.19
Average	99.00	63.00	44.00	41.00	56.50	39.00	42.50
St. Dev.			4.24		6.36		4.95

	Distance (in.)					
	72.58	74.86	96.06	105.81	120.05	121.73
Average	51.50	52.00	46.50	31.00	30.00	40.50
St. Dev.	6.36		13.44			12.02

Table II.C3. - Average amplitude (dB) in diagonal direction

	Distance (in.)		
Sensor	34	68	102
S1	53.50	49.44	
S2	43.50	31.00	
S3	50.50	40.00	33.00
S4	57.50	40.00	
S5	44.50	35.00	30.00
S6	44.50	36.00	
S7	64.75	47.50	36.00
S8	57.25	33.00	
S9	61.75	42.33	
S10	58.00	41.00	
S11	56.00	36.75	
S12	39.00		
S13	57.00	34.00	
S14	56.25	33.00	
S15	57.00	36.00	
Average	53.40	38.22	33.00
St Dev.	7.39	5.48	3.00

Table II.C4 - Average amplitude (dB) in random direction

	Distance (in.)							
Sensor	54	76	87	99	122	129	136	140
S1	38.00	49.50	36.00	40.00	36.00			
S2	36.00	33.00	31.00			30.00		
S3	42.50	40.25	36.00	38.00	35.00			
S4	43.75	44.50	39.67	34.00	35.00	35.00		43.00
S5	36.50	34.50		31.00				
S6	32.75	34.50			31.00			
S7	59.00	44.83	44.00	39.00	30.00		33.00	
S8	42.75	40.75	32.50	36.33	32.50			
S9	46.25	38.00	34.75	35.67	36.00	35.00		
S10	41.00	39.33	37.00	36.67	30.00			
S11	39.00	34.75	31.00	33.00	30.00	31.00		
S12	32.50	35.00			48.00			
S13	47.00	43.33	31.00	43.50	42.00			
S14	37.00	33.00						
S15	49.00	31.33		33.00	34.00			
Average	41.53	38.44	35.29	36.38	34.96	32.75	33.00	43.00
St Dev.	6.94	5.34	4.25	3.62	5.38	2.63		

Table II.C5 - Average amplitude (dB) in random direction

	Distance (in.)						
Sensor	144	146	152	161	170	193	217
S1	30.00						
S2							
S3	32.00		36.00				
S4							
S5							
S6							
S7							
S8							
S9				30.00			
S10							
S11							
S12					39.00		
S13	34.00	31.00			42.00	37.00	31.00
S14				31.00			
S15							
Average	32.00	31.00	36.00	30.50	40.50	37.00	31.00
St Dev.	2.00			0.71	2.12		

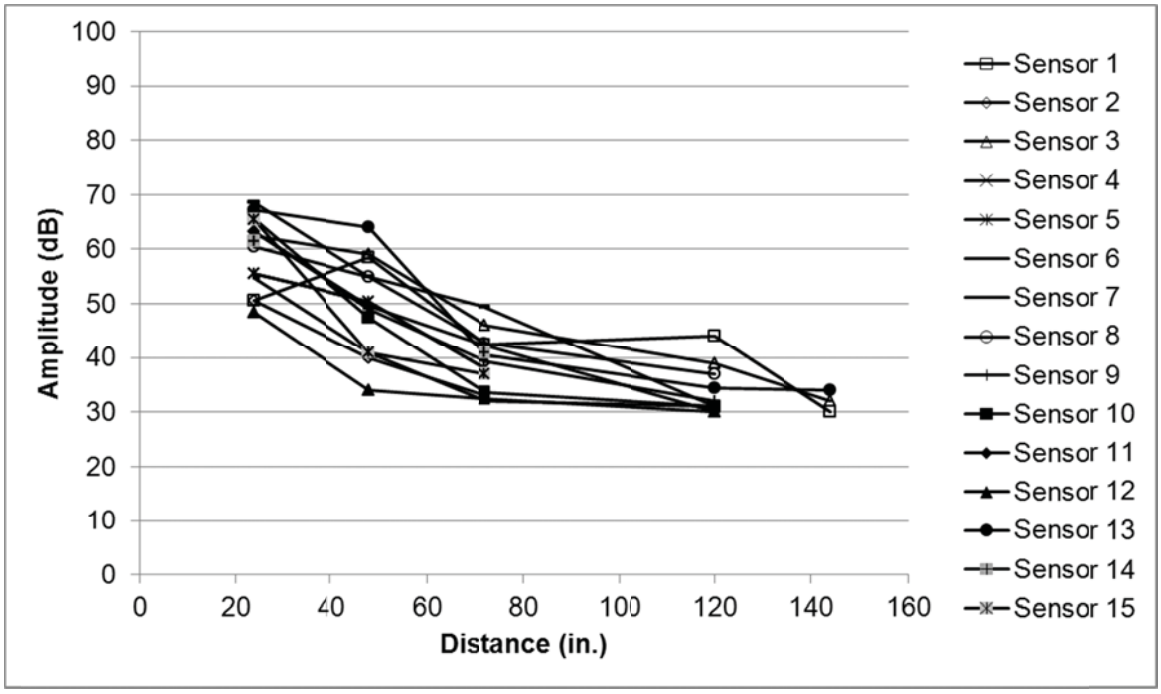

Figure II.C.2 - Attenuation signals in parallel direction

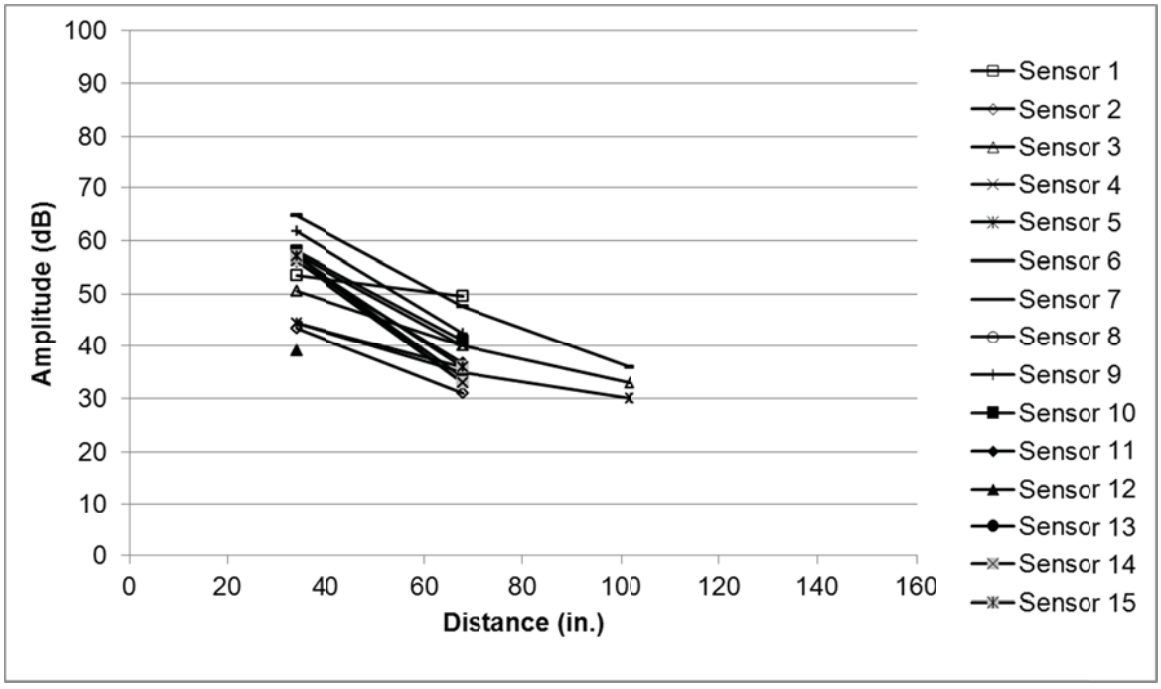

Figure II.C.3 - Attenuation signals in diagonal direction

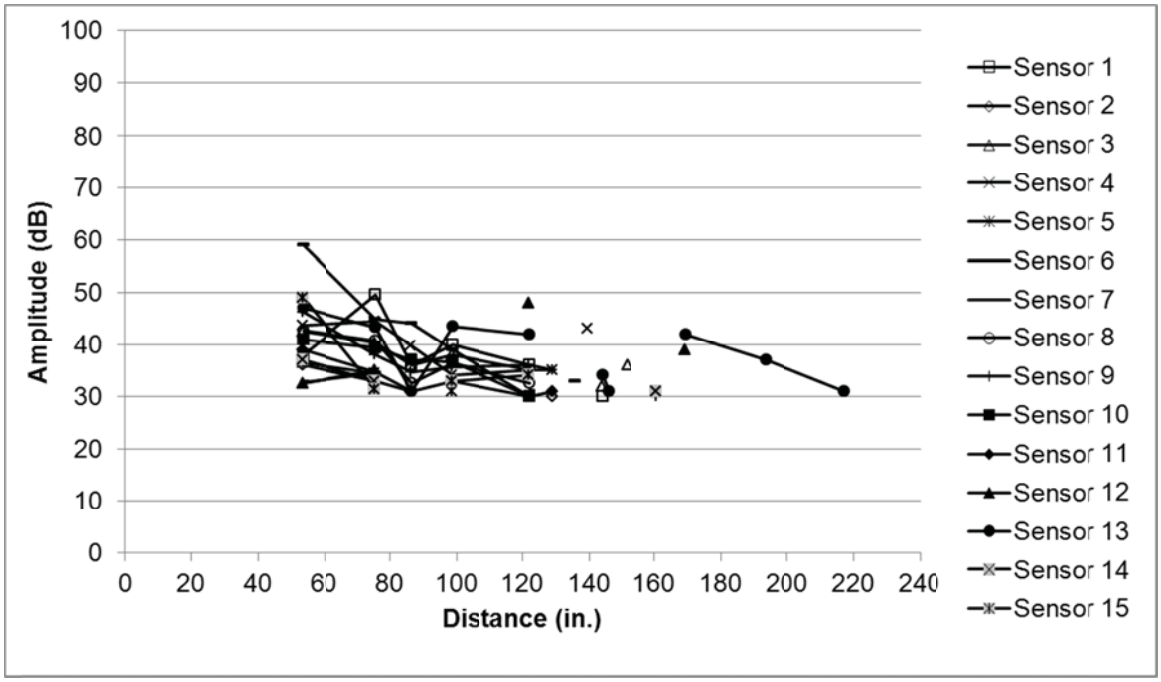

Figure II.C.4 - Attenuation signals in random direction

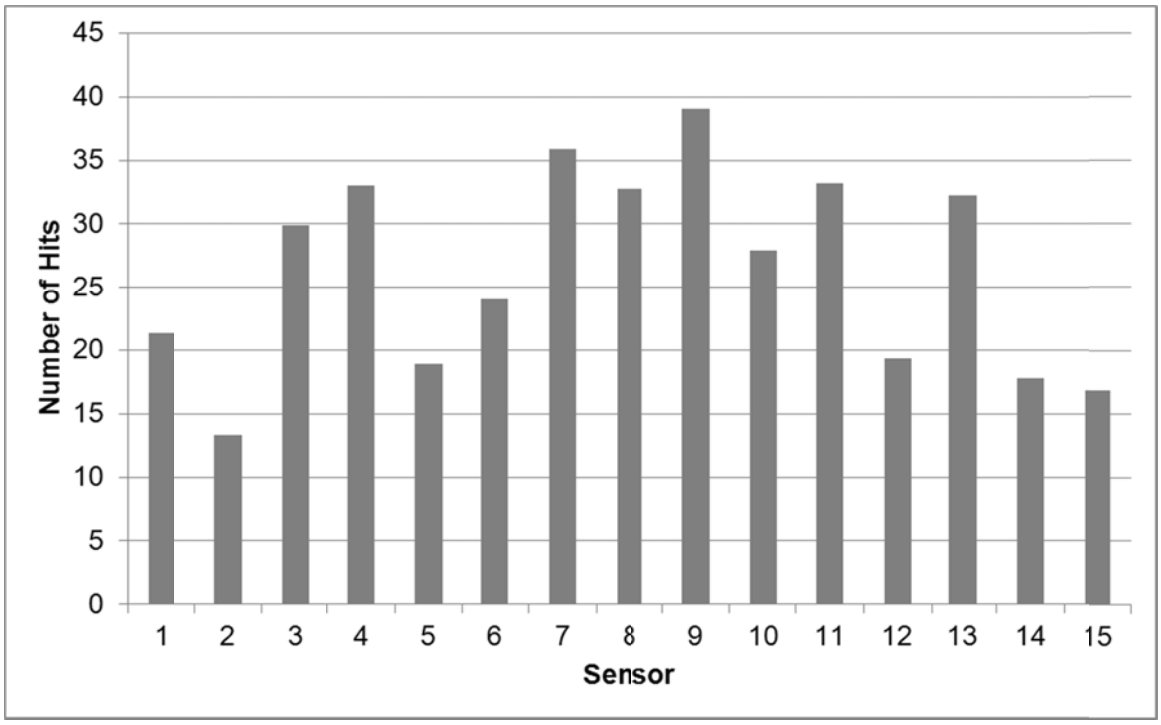

Figure II.C.5 - Number of hits per sensor of RC slab attenuation test

Appendix II.D - 3D Visualization AE Attenuation

3D visualized signal ranges of all sensors. The grey bottom volume is raised to threshold level and each sensor is indicated with a randomly chosen different color. The top view illustrates that when using a certain threshold, certain area of the RC deck can record pencil break events by specific sensor placement, spacing, and sensor types.

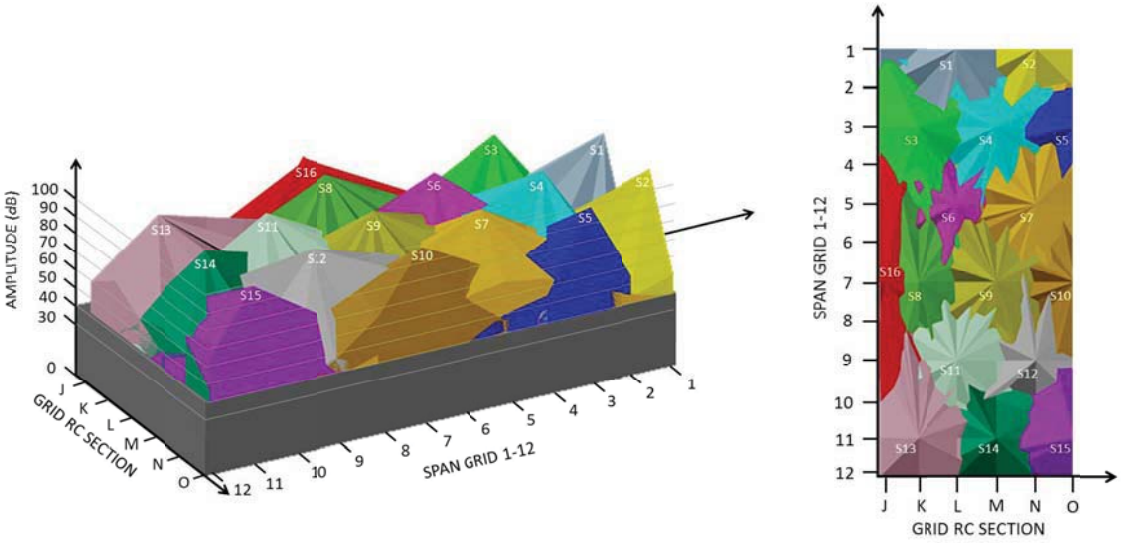

Figure II.D1 - AE signal ranges for sensors 1 to 16, threshold of 40 dB

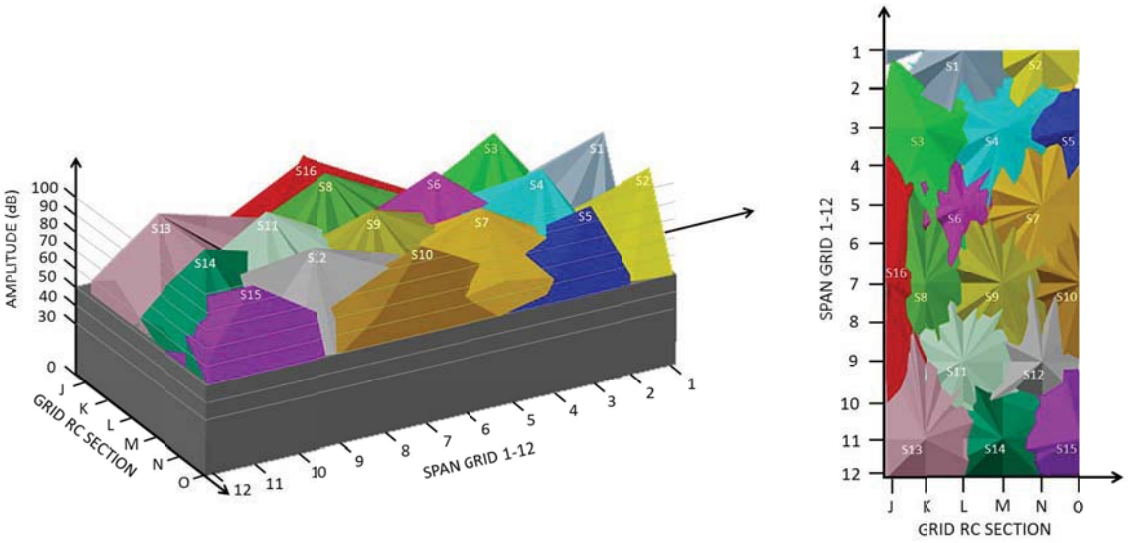

Figure II.D2 - AE signal ranges for sensors 1 to 16, threshold of 50 dB

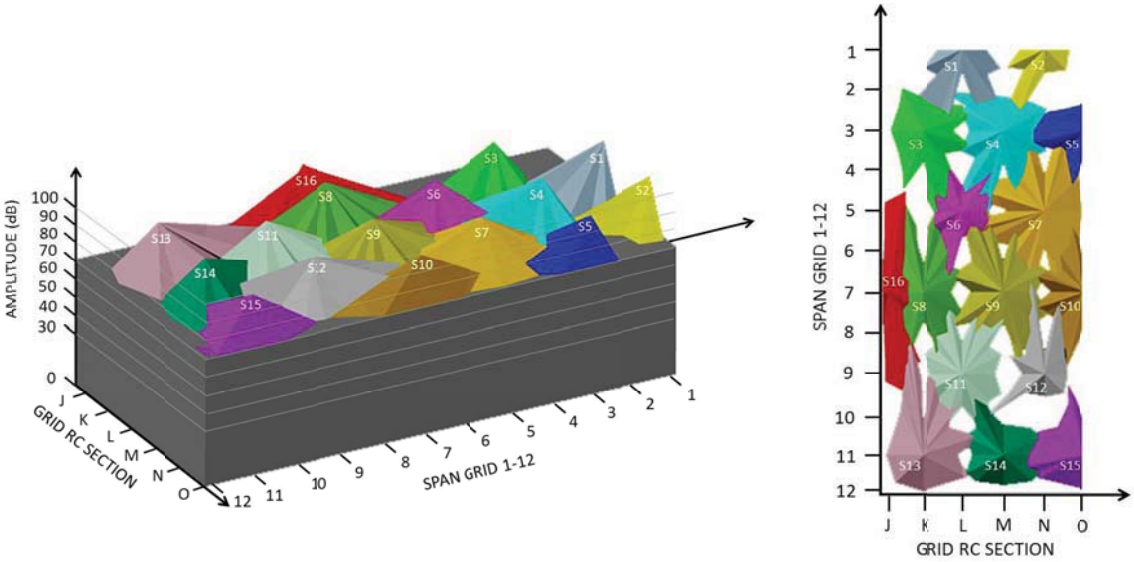

Figure II.D3 - AE signal ranges for sensors 1 to 16, threshold of 70 dB

Appendix II.E - Volumetric Attenuation Visualization

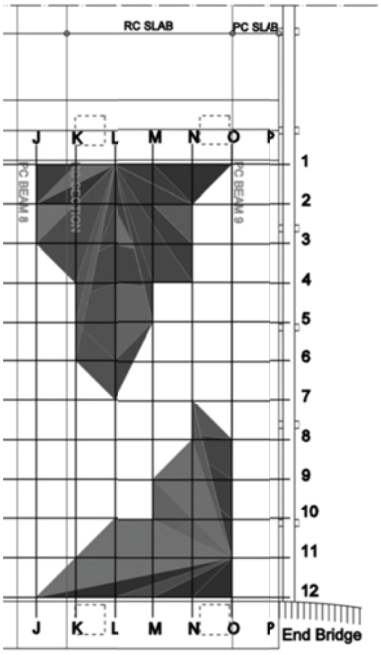

(a) sensor 1 (top) and 15 (bottom)

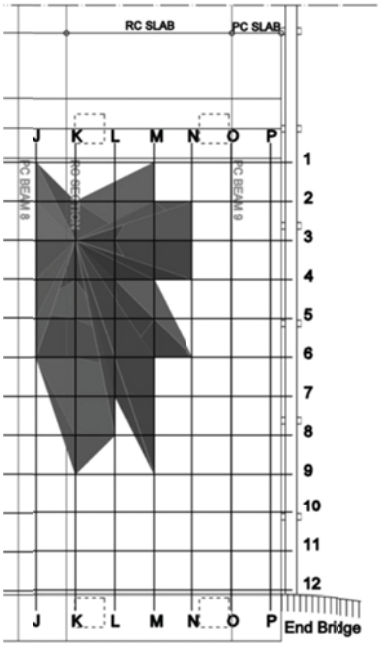

(b) sensor 3

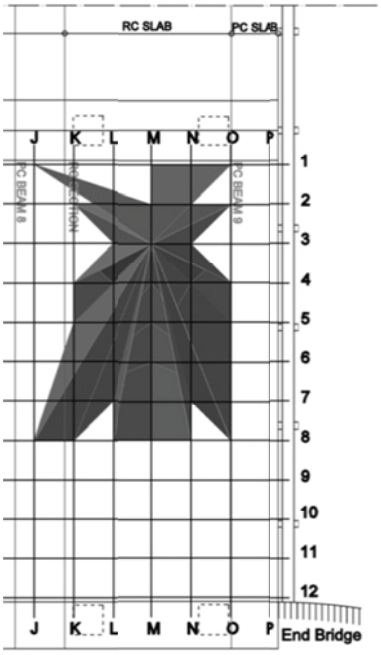

(c) sensor 4

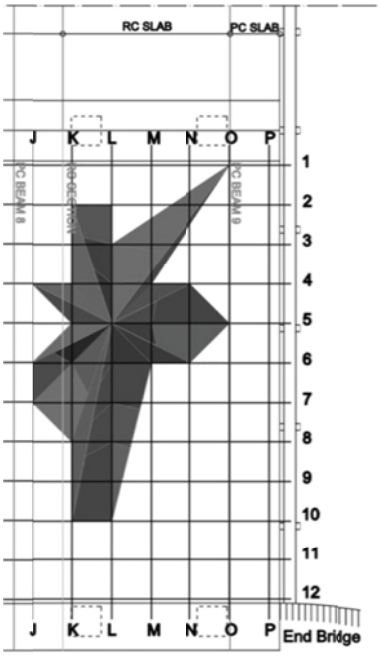

(d) sensor 6

Figure II.E.1 - Attenuation ranges sensors 1,3,4,6 and 15

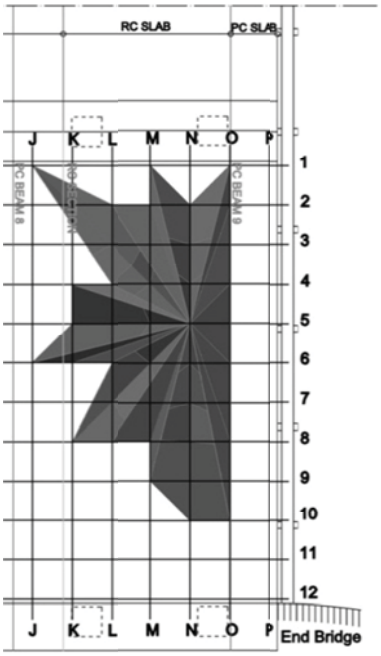

(a) sensor 7

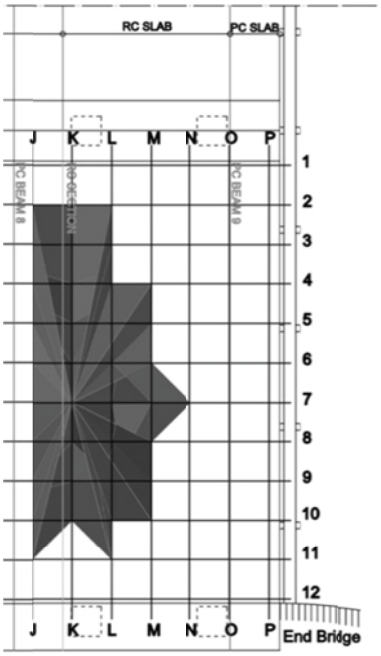

(b) sensor 8

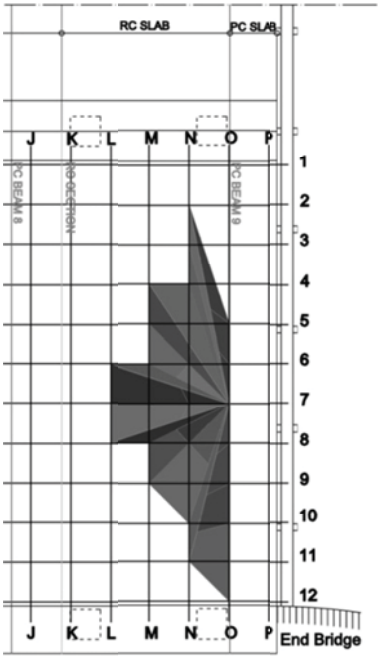

(c) sensor 10

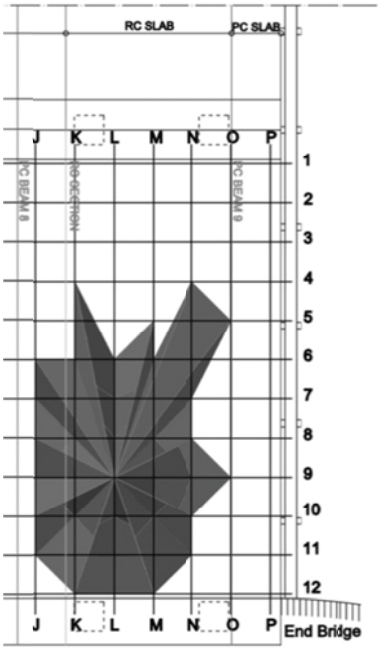

(d) sensor 11

Figure II.E.2 - Attenuation ranges sensors 7,8,10 and 11

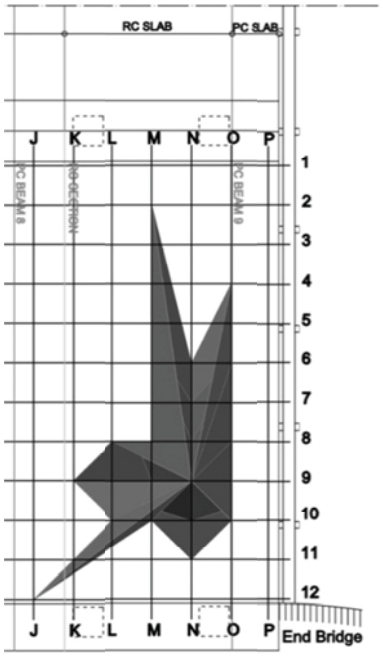

Figure 3II.E.3 - Attenuation range sensor 12

Appendix II.F - Matrices of Blocked Layers Before Repair

Tables II.F.1 - Combined layers before repair 1x1

	K	L	M	N	O
1	0.92	0.08	0.50	0.50	0.00
2	0.67	0.58	0.75	0.00	0.25
3	0.92	0.33	0.75	0.25	0.00
4	0.67	0.83	0.75	0.25	0.00
5	0.67	0.83	0.75	0.25	0.50
6	0.17	0.58	0.50	0.00	0.75
7	0.67	0.83	0.75	0.00	0.00
8	0.42	0.33	0.25	0.25	0.25
9	0.17	0.33	0.25	0.25	0.25
10	0.42	0.58	0.25	0.25	0.25
11	0.42	0.58	0.25	0.50	0.25
12	0.92	0.58	0.50	0.50	0.50

(a) Normalized means

	K	L	M	N	O
1	0.43	0.15	0.55	0.55	0.00
2	0.51	0.51	0.55	0.00	0.45
3	0.43	0.43	0.55	0.45	0.00
4	0.51	0.47	0.55	0.45	0.00
5	0.51	0.47	0.55	0.45	0.55
6	0.30	0.51	0.55	0.00	0.55
7	0.51	0.47	0.55	0.00	0.00
8	0.47	0.43	0.45	0.45	0.45
9	0.30	0.43	0.45	0.45	0.45
10	0.47	0.51	0.45	0.45	0.45
11	0.47	0.51	0.45	0.55	0.45
12	0.43	0.51	0.55	0.55	0.55

(b) Normalized standard deviations

Tables II.F.2 – Combined layers after repair 1x1

	K	L	M	N	O
1	0.50	0.30	0.19	0.39	0.56
2	0.36	0.35	0.38	0.38	0.52
3	0.49	0.31	0.51	0.51	0.26
4	0.28	0.14	0.68	0.62	0.35
5	0.54	0.24	0.31	0.07	0.11
6	0.61	0.33	0.11	0.15	0.22
7	0.48	0.11	0.15	0.22	0.26
8	0.65	0.31	0.11	0.19	0.22
9	0.69	0.11	0.15	0.11	0.19
10	0.62	0.18	0.15	0.19	0.30
11	0.49	0.36	0.35	0.22	0.30
12	0.50	0.39	0.22	0.26	0.30

(a) Normalized means

	K	L	M	N	O
1	0.45	0.51	0.32	0.35	0.51
2	0.34	0.31	0.16	0.16	0.50
3	0.08	0.27	0.43	0.43	0.45
4	0.25	0.17	0.29	0.40	0.31
5	0.41	0.25	0.17	0.13	0.19
6	0.35	0.58	0.19	0.26	0.38
7	0.50	0.19	0.26	0.38	0.45
8	0.31	0.27	0.19	0.32	0.38
9	0.27	0.19	0.26	0.19	0.32
10	0.11	0.23	0.26	0.32	0.51
11	0.43	0.34	0.31	0.38	0.51
12	0.45	0.35	0.38	0.45	0.51

(b) Normalized standard deviations

Tables II.F.3 - Combined layers before and after repair 1x1

	K	L	M	N	O
1	0.74	0.17	0.37	0.45	0.24
2	0.53	0.48	0.59	0.16	0.37
3	0.73	0.32	0.65	0.36	0.11
4	0.50	0.54	0.72	0.41	0.15
5	0.61	0.58	0.56	0.17	0.33
6	0.36	0.48	0.33	0.06	0.52
7	0.59	0.52	0.49	0.10	0.11
8	0.51	0.32	0.19	0.22	0.24
9	0.39	0.24	0.21	0.19	0.22
10	0.50	0.41	0.21	0.22	0.27
11	0.45	0.49	0.29	0.38	0.27
12	0.74	0.50	0.38	0.40	0.41

(a) Normalized means

	K	L	M	N	O
1	0.36	0.34	0.48	0.46	0.42
2	0.42	0.41	0.42	0.22	0.48
3	0.26	0.37	0.45	0.45	0.29
4	0.42	0.45	0.39	0.47	0.26
5	0.41	0.42	0.44	0.37	0.47
6	0.39	0.50	0.47	0.17	0.50
7	0.45	0.47	0.50	0.25	0.29
8	0.41	0.37	0.38	0.40	0.42
9	0.40	0.37	0.39	0.38	0.40
10	0.37	0.44	0.39	0.40	0.46
11	0.43	0.42	0.40	0.49	0.46
12	0.36	0.42	0.49	0.50	0.52

(b) Normalized standard deviations

Tables II.F.4 - Combined layers before and after repair 1x2

	K	L	M	N	O
1-2	0.63	0.33	0.48	0.31	0.30
3-4	0.61	0.43	0.68	0.39	0.13
5-6	0.48	0.53	0.45	0.12	0.43
7-8	0.55	0.42	0.34	0.16	0.17
9-10	0.45	0.32	0.21	0.21	0.25
11-12	0.59	0.49	0.34	0.39	0.34

(a) Normalized means

	K	L	M	N	O
1-2	0.39	0.40	0.45	0.38	0.44
3-4	0.36	0.41	0.41	0.44	0.27
5-6	0.41	0.45	0.45	0.28	0.48
7-8	0.42	0.42	0.45	0.33	0.35
9-10	0.38	0.40	0.37	0.37	0.42
11-12	0.41	0.40	0.43	0.47	0.48

(b) Normalized standard deviations

Tables II.F.5 - Combined layers before repair 1x3

	K	L	M	N	O
1-3	0.67	0.33	0.53	0.33	0.24
4-6	0.49	0.53	0.54	0.22	0.34
7-9	0.50	0.36	0.30	0.17	0.19
10-12	**0.**56	0.47	0.29	0.33	0.32

(a) Normalized means

	K	L	M	N	O
1-3	0.35	0.38	0.44	0.39	0.40
4-6	0.40	0.44	0.44	0.37	0.43
7-9	0.41	0.40	0.43	0.34	0.36
10-12	0.39	0.41	0.41	0.45	0.46

(b) Normalized standard deviations

Tables II.F.6 - Combined layers before repair 5x1

	K-O
1	0.39
2	0.43
3	0.43
4	0.46
5	0.45
6	0.35
7	0.36
8	0.30
9	0.25
10	0.32
11	0.38
12	0.49

(a) Normalized means

	K-O
1	0.44
2	0.41
3	0.42
4	0.42
5	0.43
6	0.43
7	0.44
8	0.39
9	0.37
10	0.41
11	0.42
12	0.45

(b) Normalized standard deviations

Tables II.F.6 - Combined layers before repair 1x6

	K	L	M	N	O
1-6	0.58	0.43	0.54	0.27	0.29
7-12	0.53	0.41	0.29	0.25	0.25

(a) Normalized means

	K	L	M	N	O
1-6	0.38	0.42	0.44	0.38	0.41
7-12	0.40	0.40	0.41	0.40	0.41

(b) Normalized standard deviations

Tables II.F.7 - Combined layers before repair 5x2

	K L M N O
1-2	0.41
3-4	0.45
5-6	0.40
7-8	0.33
9-10	0.29
11-12	0.43

(a) Normalized means

	K L M N O
1-2	0.42
3-4	0.42
5-6	0.43
7-8	0.41
9-10	0.39
11-12	0.44

(b) Normalized standard deviations

Tables II.F.8 - Combined layers before repair 5x3

	K-O
1-3	0.42
4-6	0.42
7-9	0.30
10-12	0.39

(a) Normalized means

	K-O
1-3	0.42
4-6	0.43
7-9	0.40
10-12	0.43

(b) Normalized standard deviations

Tables II.F.9 - Combined layers before repair 5x6

	K-O
1-6	0.42
7-12	0.35

(a) Normalized means

	K-O
1-6	0.42
7-12	0.42

(b) Normalized standard deviations

Appendix II.G - ArcGIS Visual Output Before and After Repair

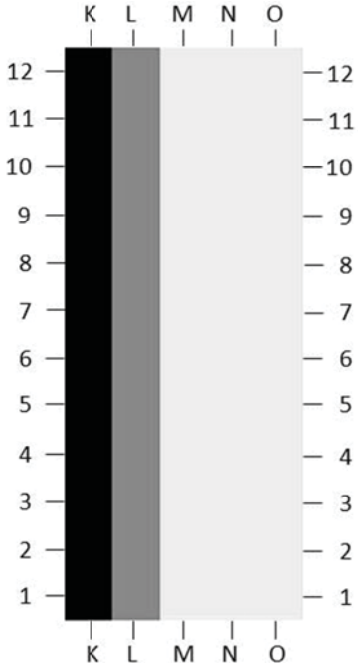

Lost reinforcement bars

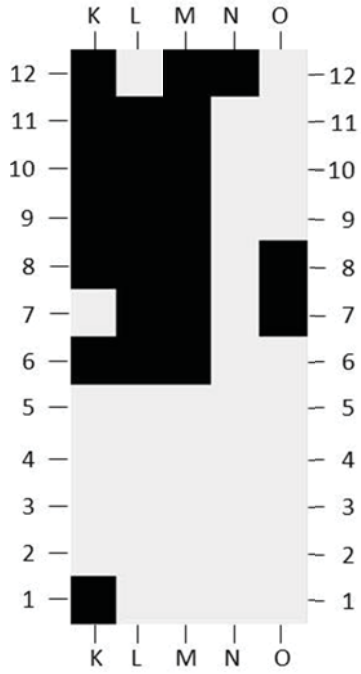

(B) Carbonation

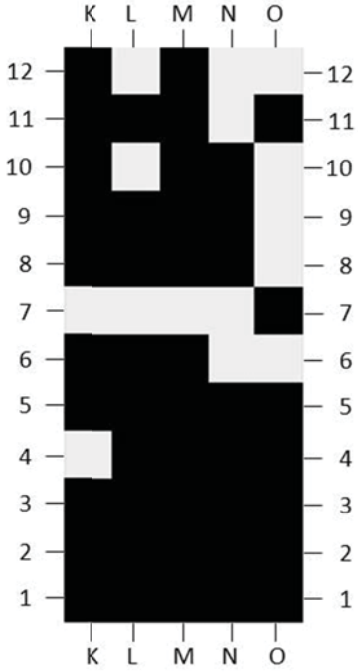

(C) Active corrosion potential

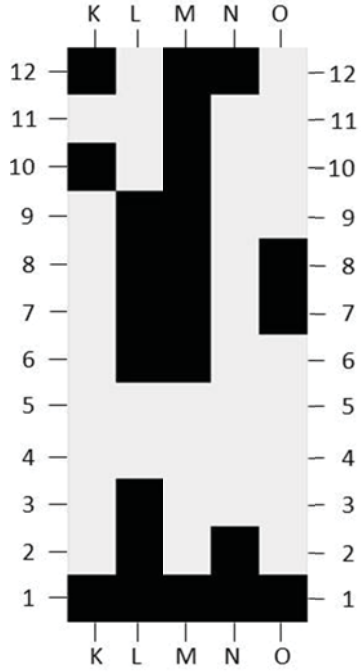

(D) pH level

Figure II.G.1 - Visual output assessment layers before repair by ArcGIS

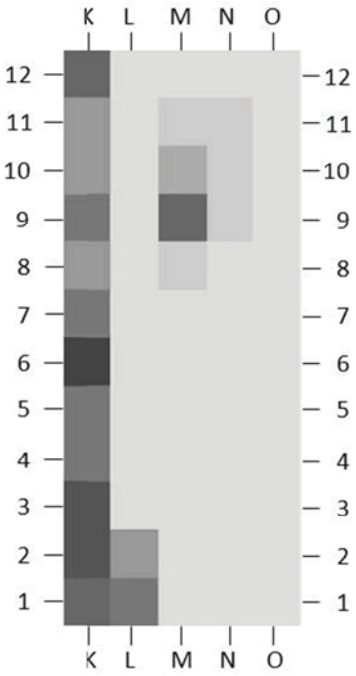

(F) Deck cracks

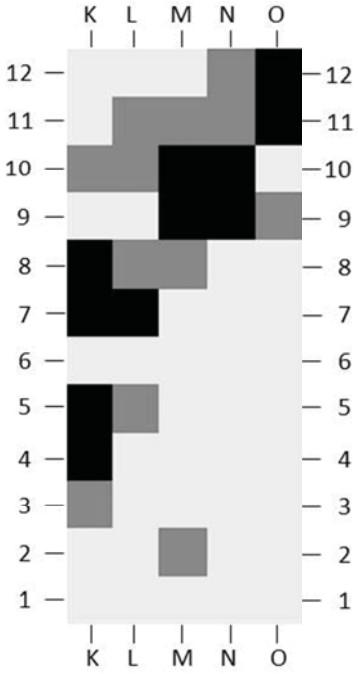

(G) Air voids

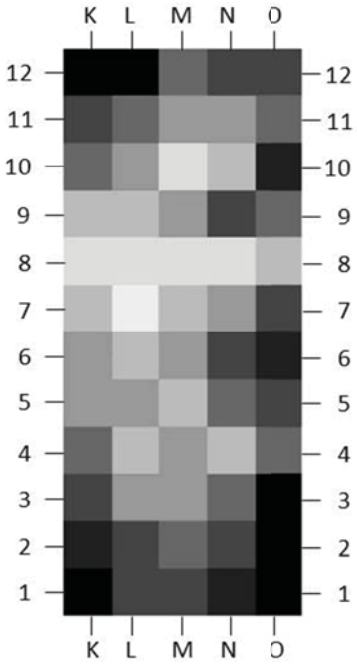

(H) AE attenuation conductivity

Figure II.G.2 - Visual output assessment layers after repair by ArcGIS

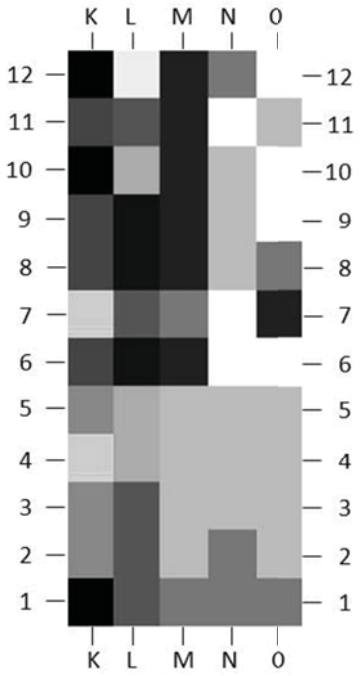

Combined assessment layers before repair

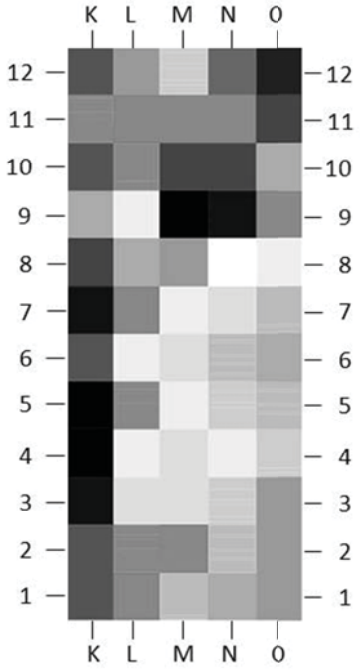

Combined assessment layers after repair

Figure II.G.3 - Visual output assessment layers combined by ArcGIS

Appendix II.H – Static Truck Load Test Results

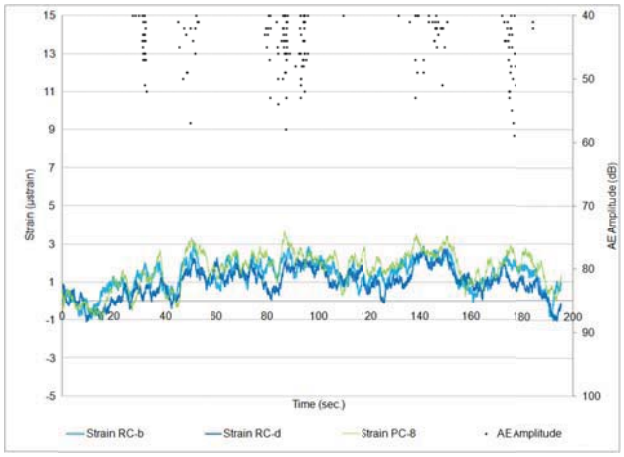

Figure II.H.1 - Strain and AE Amplitude, Test N-A1a

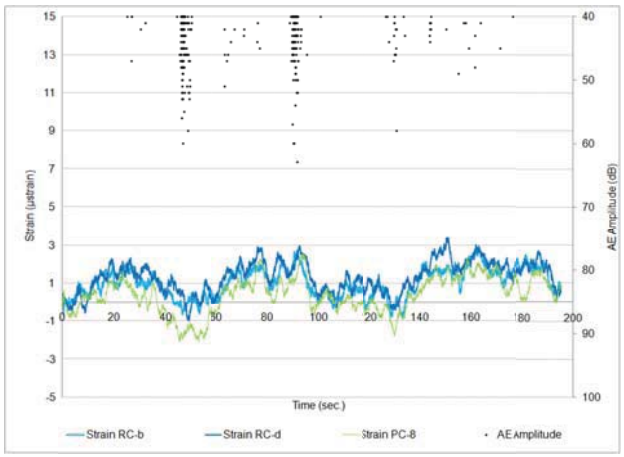

Figure II.H.2 - Strain and AE Amplitude, Test N-A1b

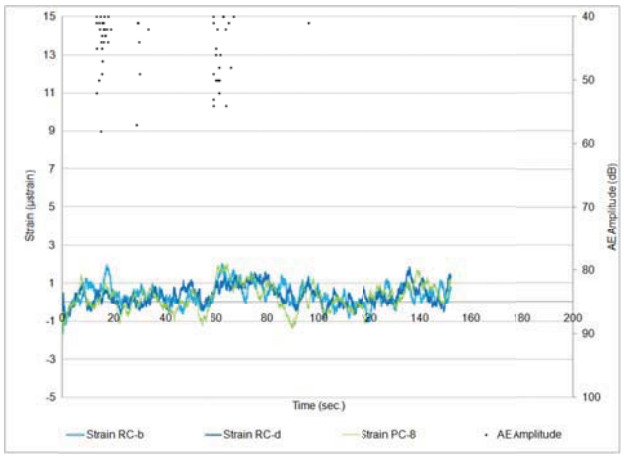

Figure II.H.3 - Strain and AE Amplitude, Test N-A1c

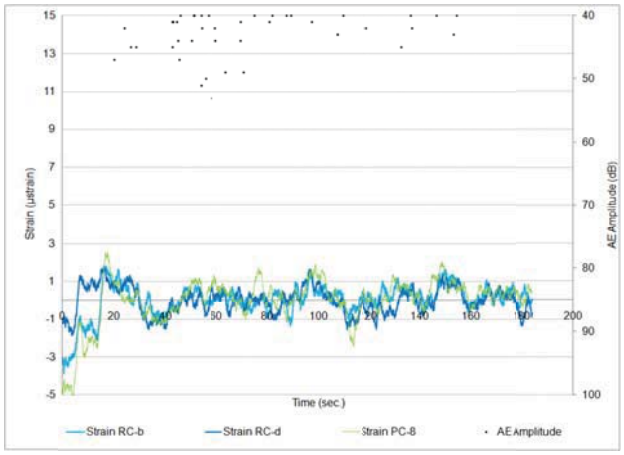

Figure II.H.4 - Strain and AE Amplitude, Test N-A2a

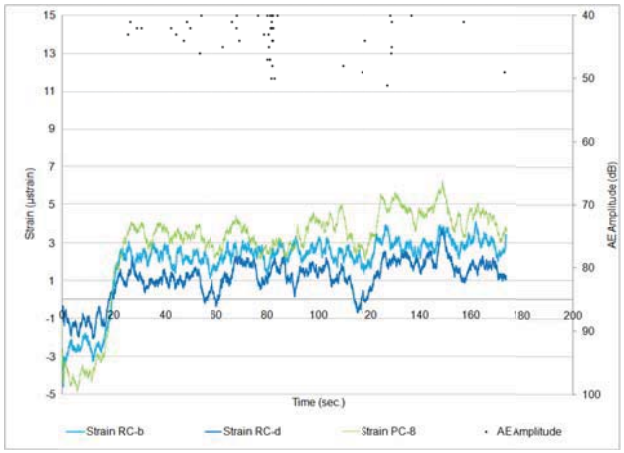

Figure II.H.5 - Strain and AE Amplitude, Test N-A2b

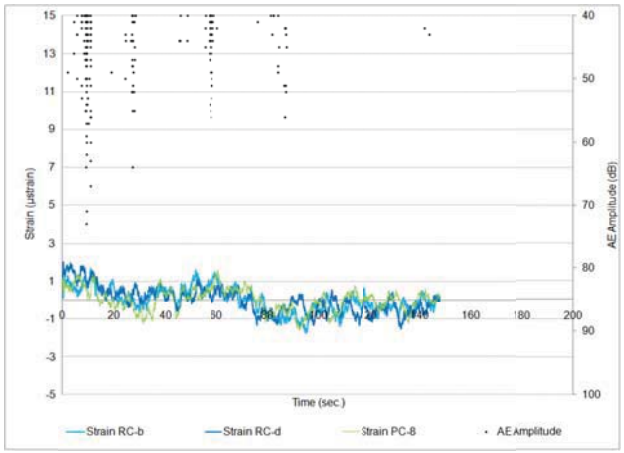

Figure II.H.6 - Strain and AE Amplitude, Test N-A2c

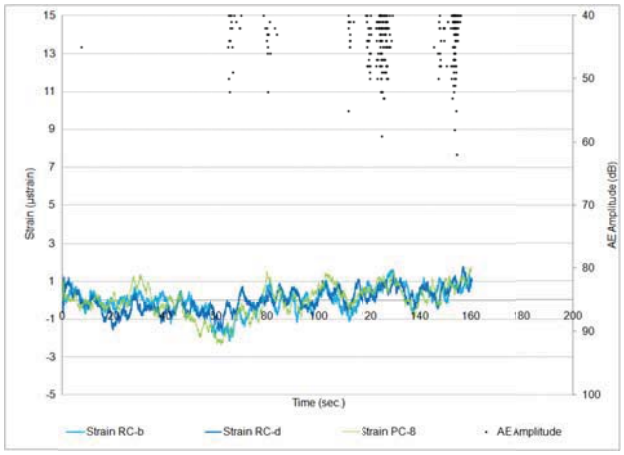

Figure II.H.7 - Strain and AE Amplitude, Test N-A3a

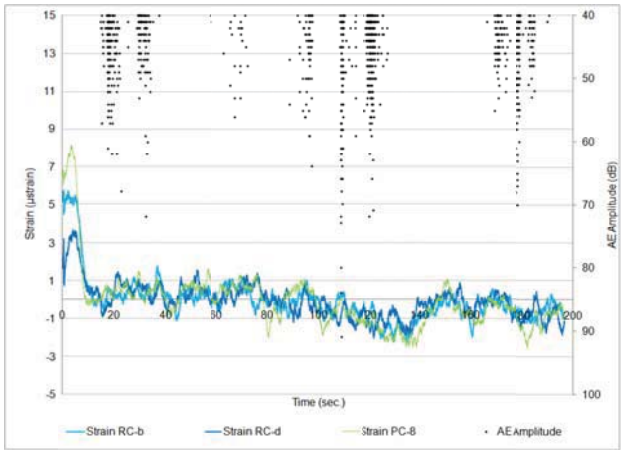

Figure II.H.8 - Strain and AE Amplitude, Test N-A3b

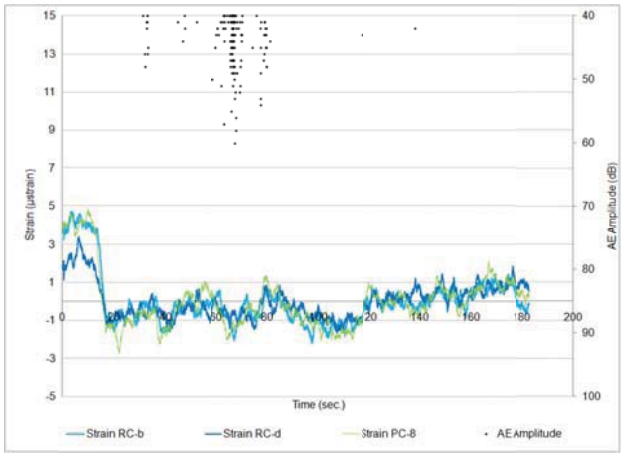

Figure II.H.9 - Strain and AE Amplitude, Test N-A3c

Appendix II.I – Truck Weight Documentation

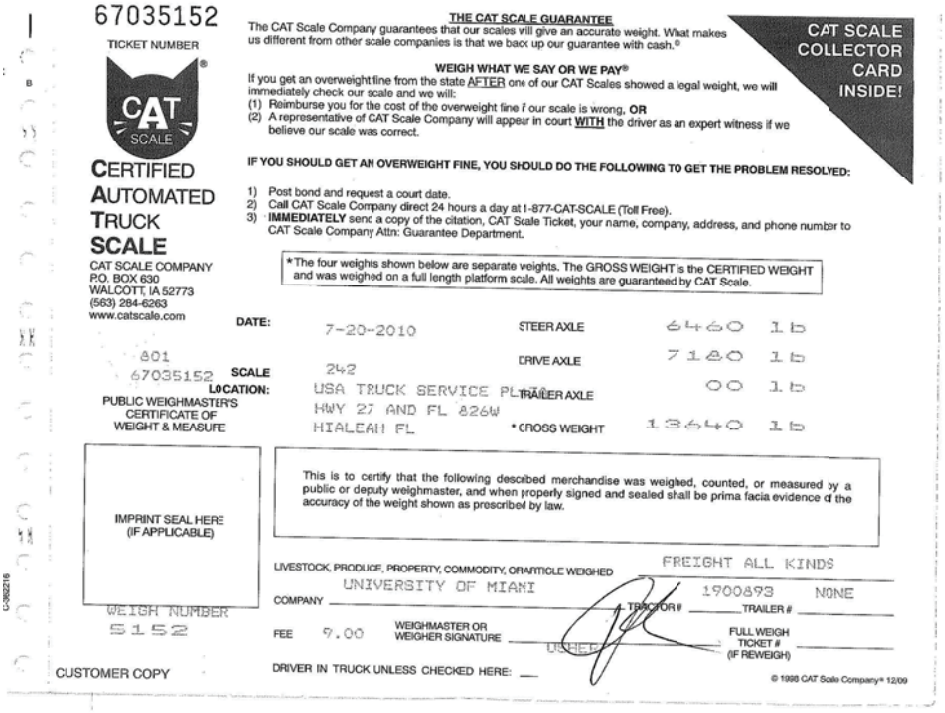

67035152

TICKET NUMBER

CERTIFIED AUTOMATED TRUCK SCALE

CAT SCALE COMPANY
P.O. BOX 630
WALCOTT, IA 52773
(563) 284-6263
www.catscale.com

801
67035152 SCALE
LOCATION: 242
USA TRUCK SERVICE PL
HWY 27 AND FL 826W
HIALEAH FL

PUBLIC WEIGHMASTER'S CERTIFICATE OF WEIGHT & MEASURE

IMPRINT SEAL HERE (IF APPLICABLE)

WEIGH NUMBER
5152

CUSTOMER COPY

THE CAT SCALE GUARANTEE

The CAT Scale Company guarantees that our scales will give an accurate weight. What makes us different from other scale companies is that we back up our guarantee with cash.®

CAT SCALE COLLECTOR CARD INSIDE!

WEIGH WHAT WE SAY OR WE PAY®

If you get an overweight fine from the state AFTER one of our CAT Scales showed a legal weight, we will immediately check our scale and we will:
(1) Reimburse you for the cost of the overweight fine if our scale is wrong, OR
(2) A representative of CAT Scale Company will appear in court WITH the driver as an expert witness if we believe our scale was correct.

IF YOU SHOULD GET AN OVERWEIGHT FINE, YOU SHOULD DO THE FOLLOWING TO GET THE PROBLEM RESOLVED:

1) Post bond and request a court date.
2) Call CAT Scale Company direct 24 hours a day at 1-877-CAT-SCALE (Toll Free).
3) IMMEDIATELY send a copy of the citation, CAT Scale Ticket, your name, company, address, and phone number to CAT Scale Company Attn: Guarantee Department.

*The four weighs shown below are separate weights. The GROSS WEIGHT is the CERTIFIED WEIGHT and was weighed on a full length platform scale. All weights are guaranteed by CAT Scale.

DATE: 7-20-2010

STEER AXLE	6460	lb
DRIVE AXLE	7180	lb
TRAILER AXLE	00	lb
*GROSS WEIGHT	13640	lb

This is to certify that the following described merchandise was weighed, counted, or measured by a public or deputy weighmaster, and when properly signed and sealed shall be prima facia evidence of the accuracy of the weight shown as prescribed by law.

LIVESTOCK, PRODUCE, PROPERTY, COMMODITY, OR ARTICLE WEIGHED: FREIGHT ALL KINDS

COMPANY: UNIVERSITY OF MIAMI

TRACTOR #: 1900893 TRAILER #: NONE

FEE: 9.00

WEIGHMASTER OR WEIGHER SIGNATURE: USHER

FULL WEIGH TICKET # (IF REWEIGH):

DRIVER IN TRUCK UNLESS CHECKED HERE: ___

© 1998 CAT Scale Company® 12/09

Figure 3.11.1 - Full weight truck measured before testing

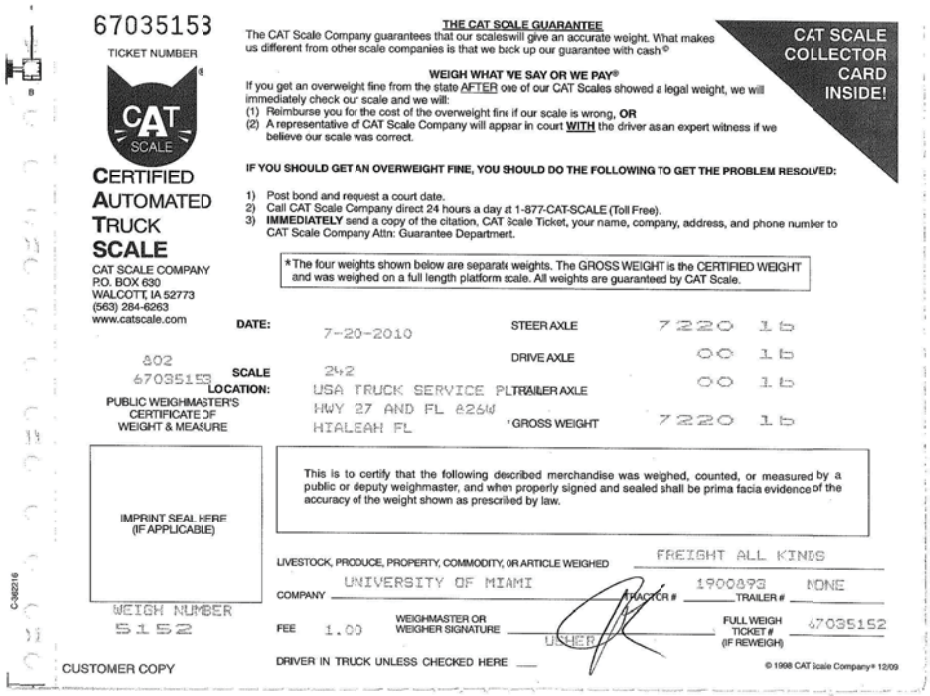

67035153

TICKET NUMBER

CERTIFIED AUTOMATED TRUCK SCALE

CAT SCALE COMPANY
P.O. BOX 630
WALCOTT, IA 52773
(563) 284-6263
www.catscale.com

802
67035153 SCALE
LOCATION: 242
USA TRUCK SERVICE PL
HWY 27 AND FL 826W
HIALEAH FL

PUBLIC WEIGHMASTER'S CERTIFICATE OF WEIGHT & MEASURE

IMPRINT SEAL HERE (IF APPLICABLE)

WEIGH NUMBER
5152

CUSTOMER COPY

THE CAT SCALE GUARANTEE

The CAT Scale Company guarantees that our scales will give an accurate weight. What makes us different from other scale companies is that we back up our guarantee with cash®

CAT SCALE COLLECTOR CARD INSIDE!

WEIGH WHAT WE SAY OR WE PAY®

If you get an overweight fine from the state AFTER one of our CAT Scales showed a legal weight, we will immediately check our scale and we will:
(1) Reimburse you for the cost of the overweight fine if our scale is wrong, OR
(2) A representative of CAT Scale Company will appear in court WITH the driver as an expert witness if we believe our scale was correct.

IF YOU SHOULD GET AN OVERWEIGHT FINE, YOU SHOULD DO THE FOLLOWING TO GET THE PROBLEM RESOLVED:

1) Post bond and request a court date.
2) Call CAT Scale Company direct 24 hours a day at 1-877-CAT-SCALE (Toll Free).
3) IMMEDIATELY send a copy of the citation, CAT Scale Ticket, your name, company, address, and phone number to CAT Scale Company Attn: Guarantee Department.

*The four weights shown below are separate weights. The GROSS WEIGHT is the CERTIFIED WEIGHT and was weighed on a full length platform scale. All weights are guaranteed by CAT Scale.

DATE: 7-20-2010

STEER AXLE	7220	lb
DRIVE AXLE	00	lb
TRAILER AXLE	00	lb
*GROSS WEIGHT	7220	lb

This is to certify that the following described merchandise was weighed, counted, or measured by a public or deputy weighmaster, and when properly signed and sealed shall be prima facia evidence of the accuracy of the weight shown as prescribed by law.

LIVESTOCK, PRODUCE, PROPERTY, COMMODITY, OR ARTICLE WEIGHED: FREIGHT ALL KINDS

COMPANY: UNIVERSITY OF MIAMI

TRACTOR #: 1900893 TRAILER #: NONE

FEE: 1.00

WEIGHMASTER OR WEIGHER SIGNATURE: USHER

FULL WEIGH TICKET # (IF REWEIGH): 67035152

DRIVER IN TRUCK UNLESS CHECKED HERE ___

© 1998 CAT Scale Company® 12/09

Figure 3.11.2 - Weight back axle truck measured before testing

Appendix II.J – Comparison of Moving Average Sampling

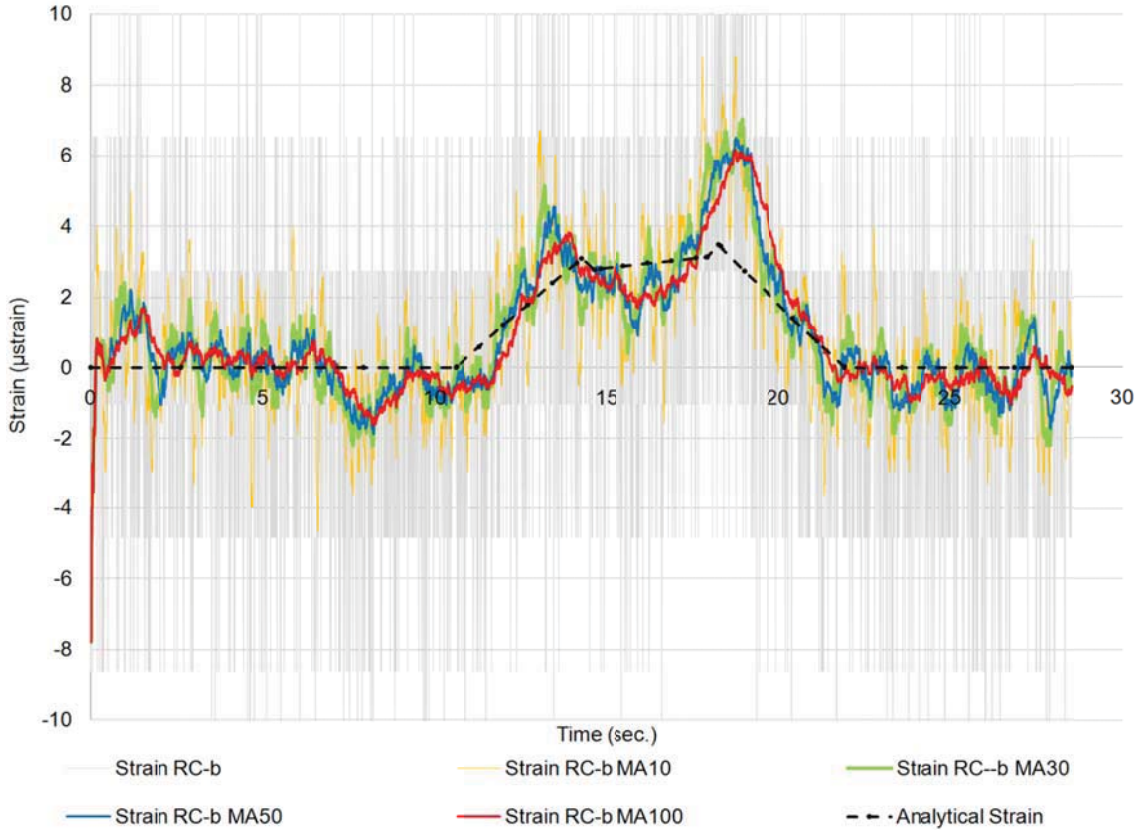

Figure II.J.1 - Superimposed strains with different sample count for moving average filtering

Appendix II.K - Crawling Speed Truck Load Tests Results

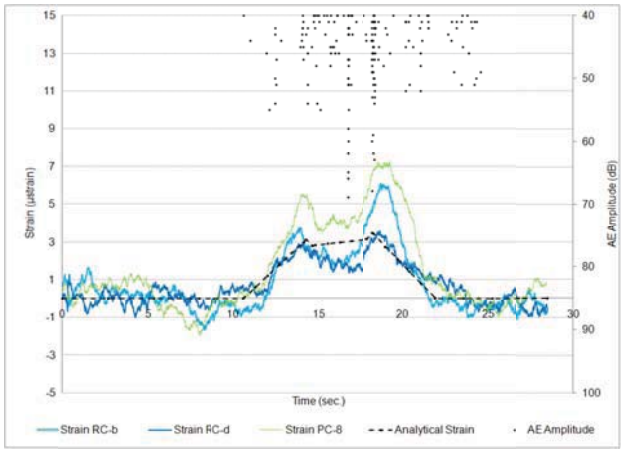

Figure II.K.1a - Strain and AE Amplitude, Test N-B1a

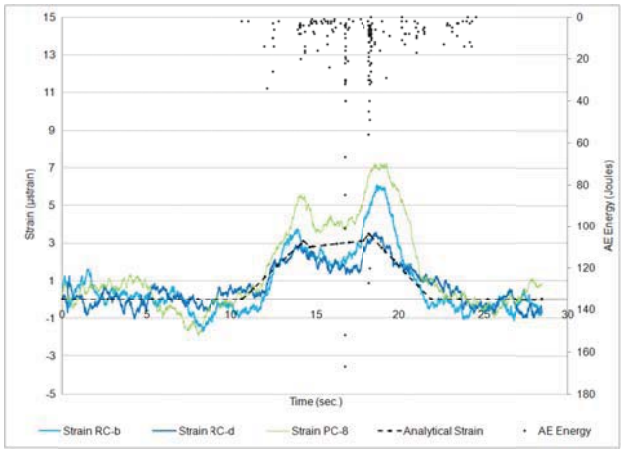

Figure II.K.1b - Strain and AE Energy, Test N-B1a

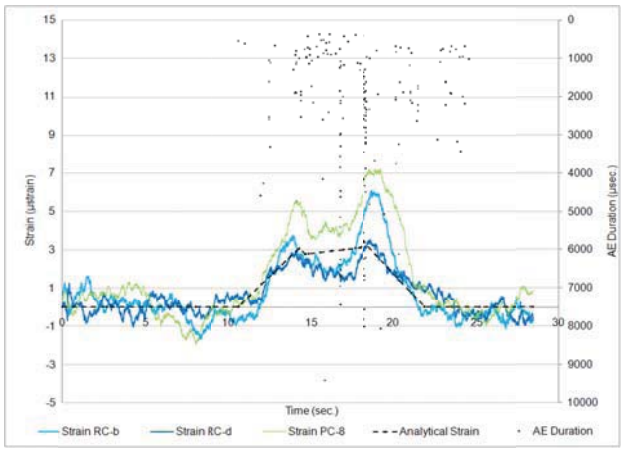

Figure II.K.1c - Strain and AE Duration, Test N-B1a

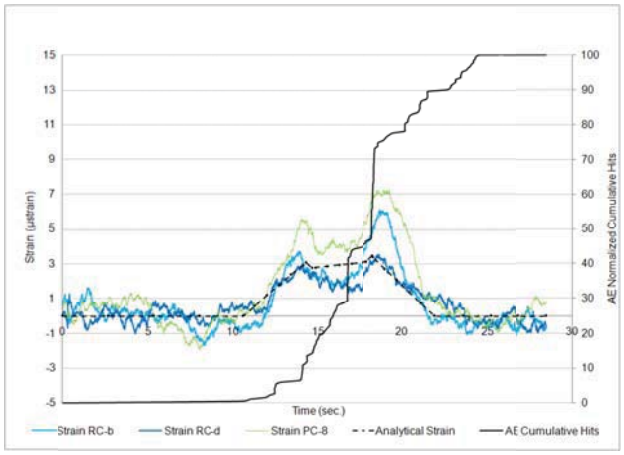

Figure II.K.1d - Strain and AE Cumulative Number of Hits, Test N-B1a

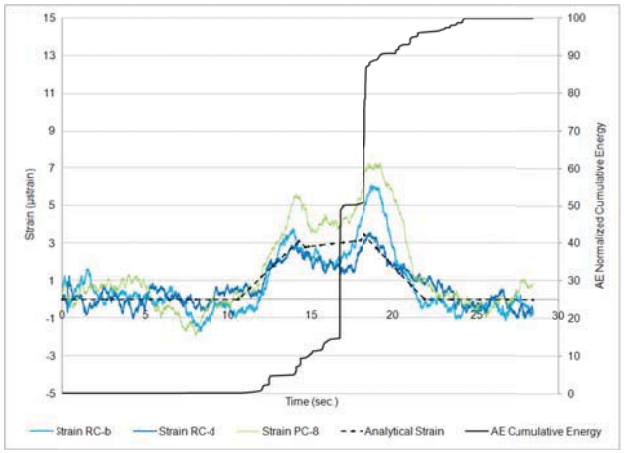

Figure II.K.1e - Strain and AE Cumulative Energy, Test N-B1a

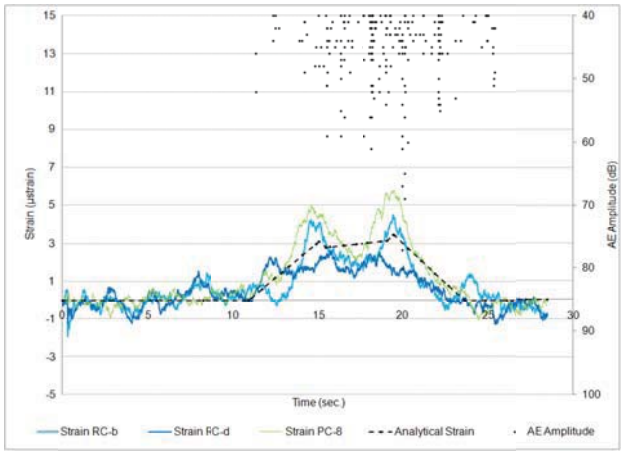

Figure II.K.2a - Strain and AE Amplitude, Test N-B1b

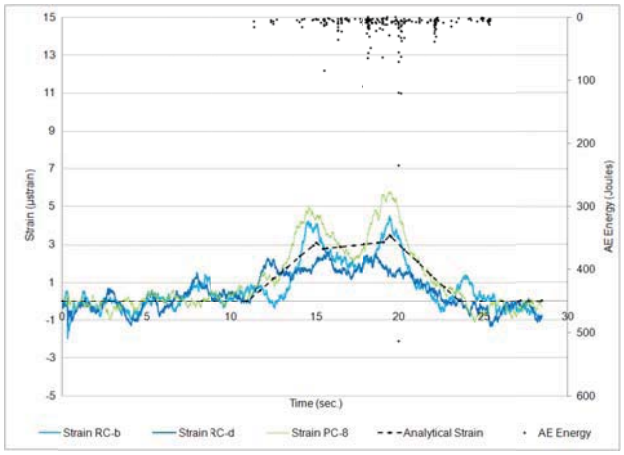

Figure II.K.2b - Strain and AE Energy, Test N-B1b

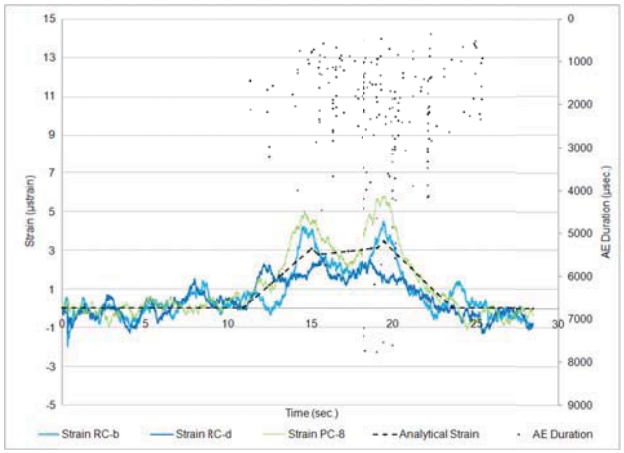

Figure II.K.2c - Strain and AE Duration, Test N-B1b

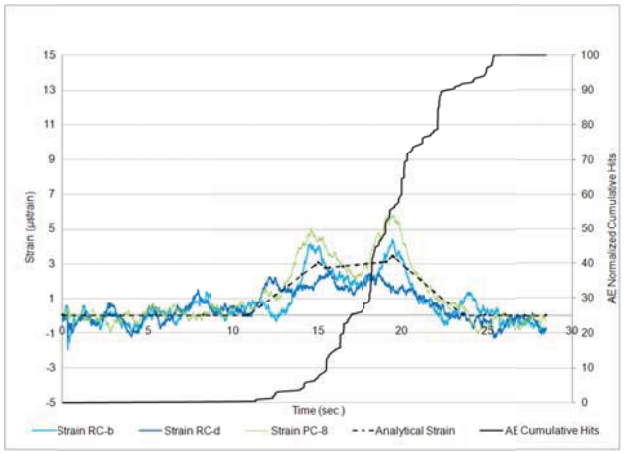

Figure II.K.2d - Strain and AE Cumulative Number of Hits, Test N-B1b

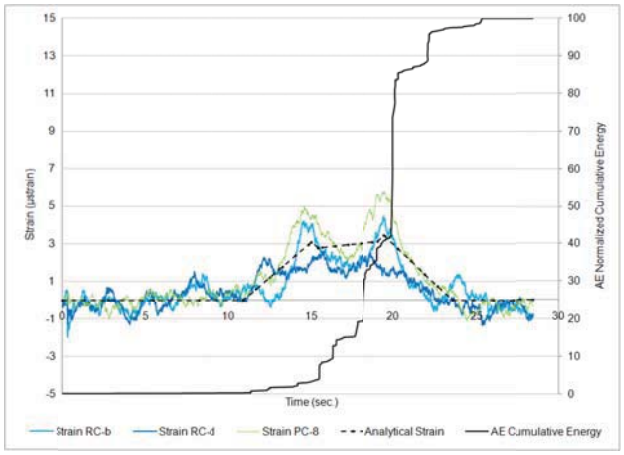

Figure II.K.2e - Strain and AE Cumulative Energy, Test N-B1b

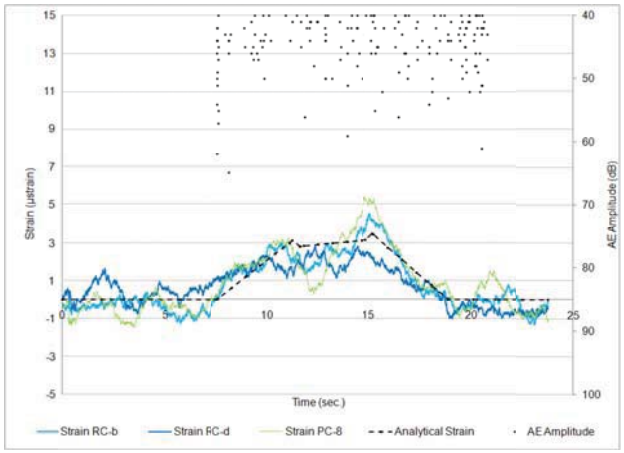

Figure II.K.3a - Strain and AE Amplitude, Test N-B1c

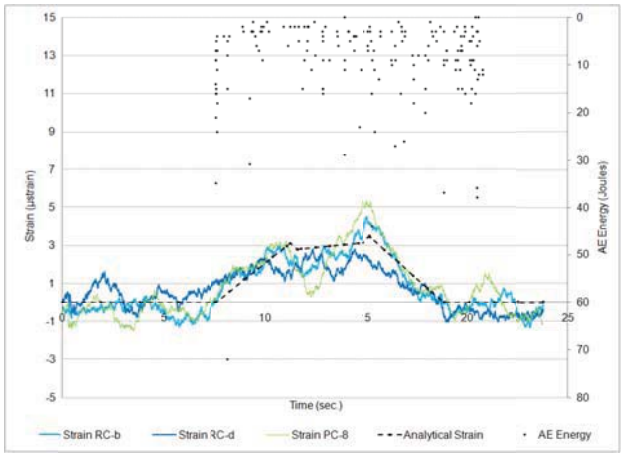

Figure II.K.3b - Strain and AE Energy, Test N-B1c

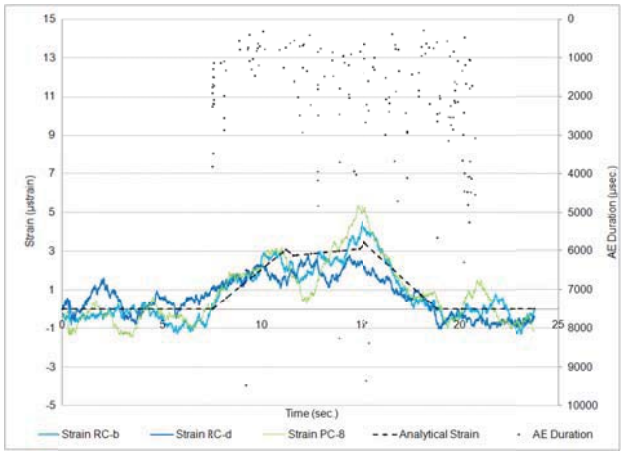

Figure II.K.3c - Strain and AE Duration, Test N-B1c

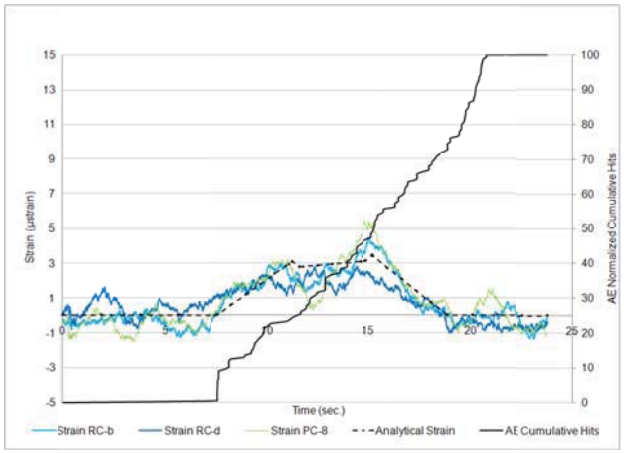

Figure II.K.3d - Strain and AE Cumulative Number of Hits, Test N-B1c

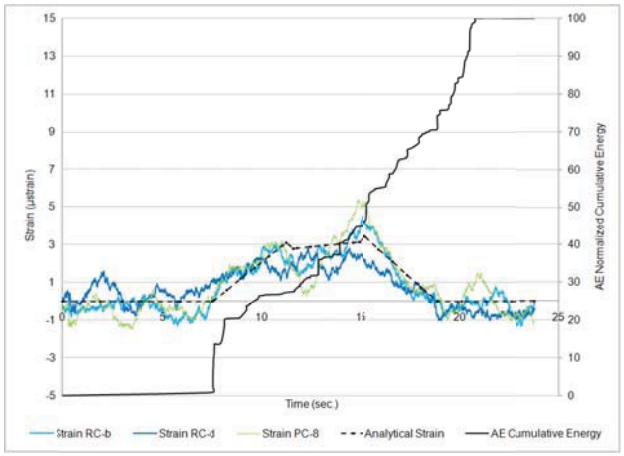

Figure II.K.3e - Strain and AE Cumulative Energy, Test N-B1c

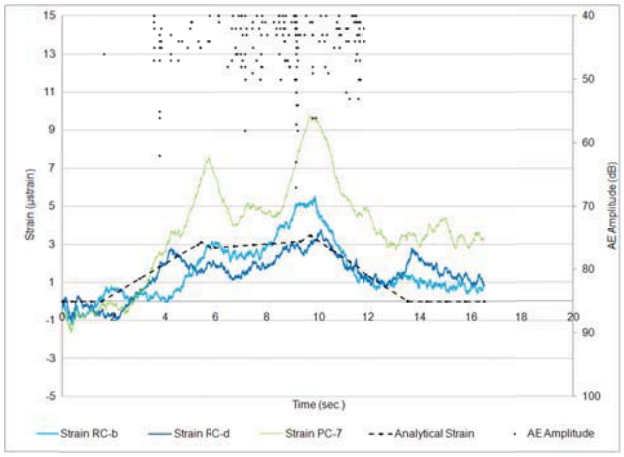

Figure II.K.4a - Strain and AE Amplitude, Test N-B2a

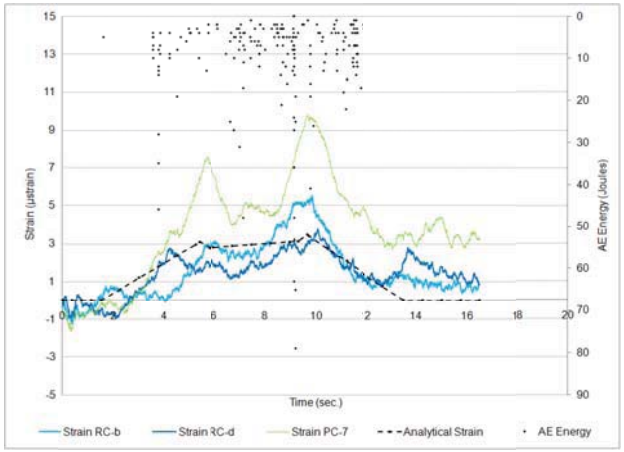

Figure II.K.4b - Strain and AE Energy, Test N-B2a

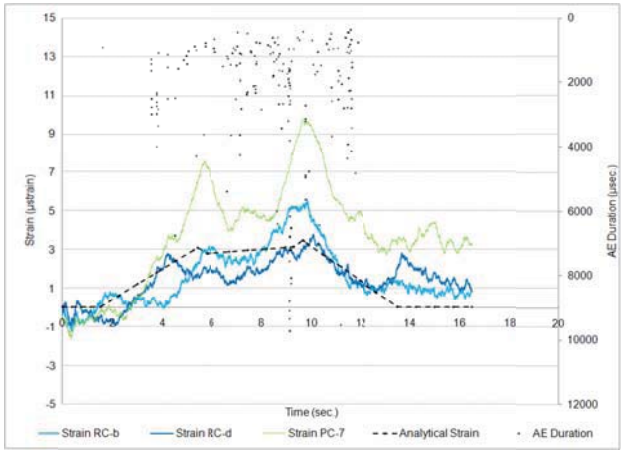

Figure II.K.4c - Strain and AE Duration, Test N-B2a

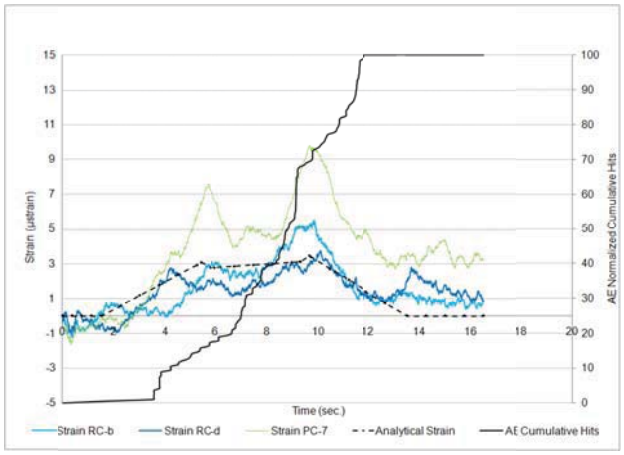

Figure II.K.4d - Strain and AE Cumulative Number of Hits, Test N-B2a

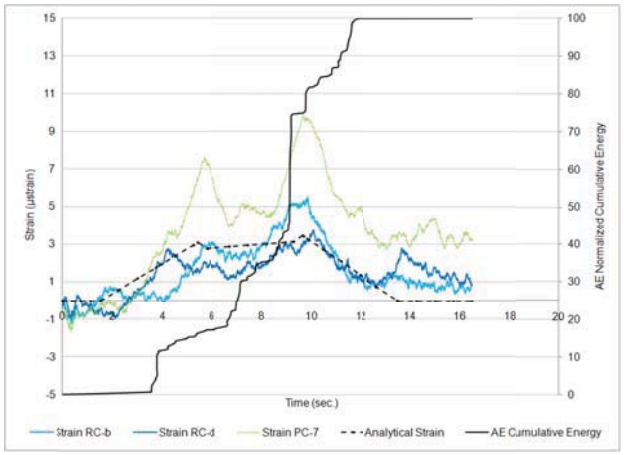

Figure II.K.4e - Strain and AE Cumulative Energy, Test N-B2a

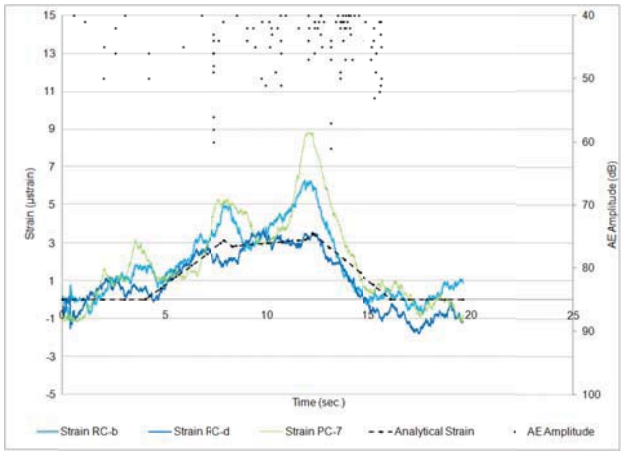

Figure II.K.5a - Strain and AE Amplitude, Test N-B2b

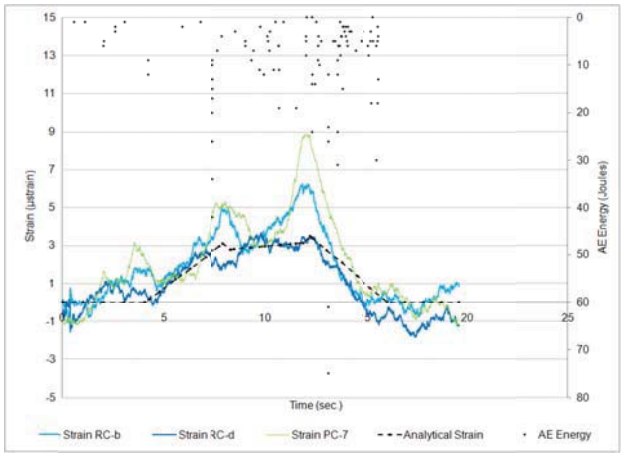

Figure II.K.5b - Strain and AE Energy, Test N-B2b

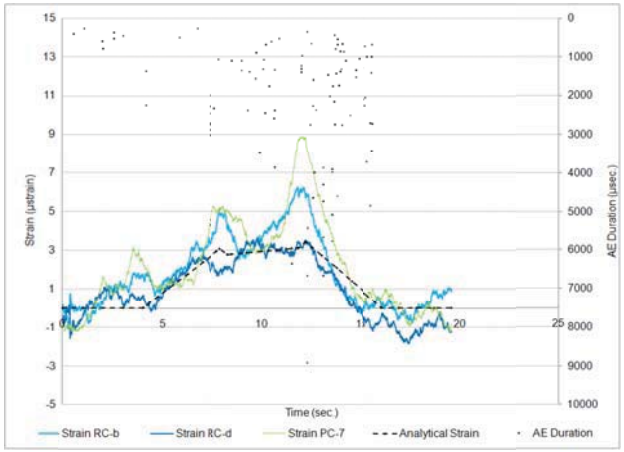

Figure II.K.5c - Strain and AE Duration, Test N-B2b

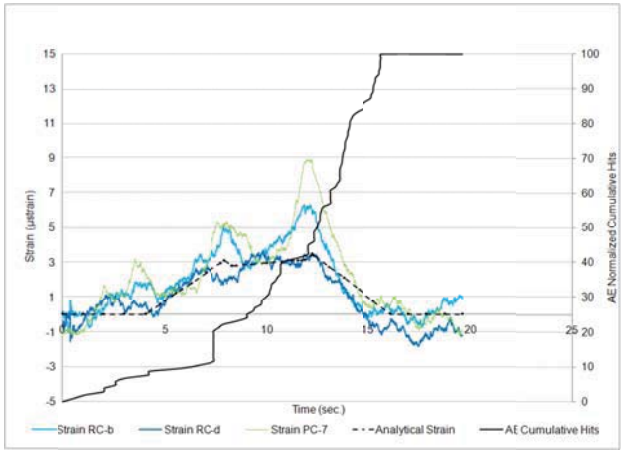

Figure II.K.5d - Strain and AE Cumulative Number of Hits, Test N-B2b

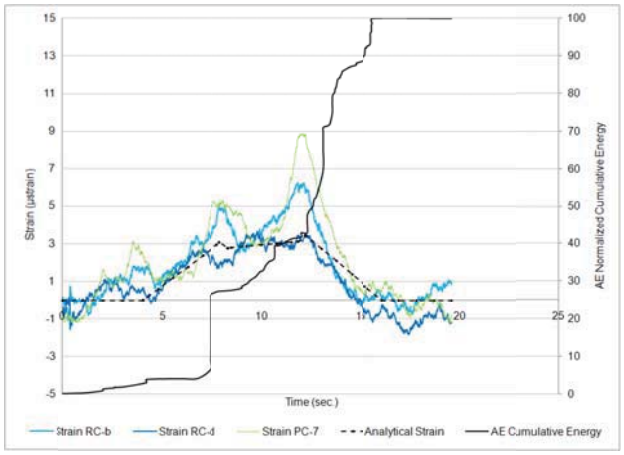

Figure II.K.5e - Strain and AE Cumulative Energy, Test N-B2b

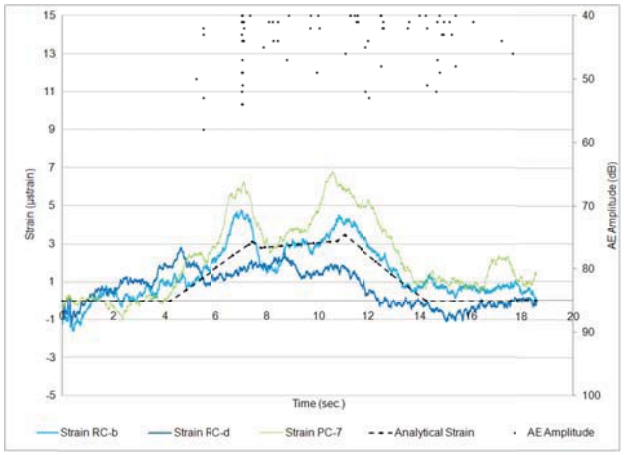

Figure II.K.6a - Strain and AE Amplitude, Test N-B2c

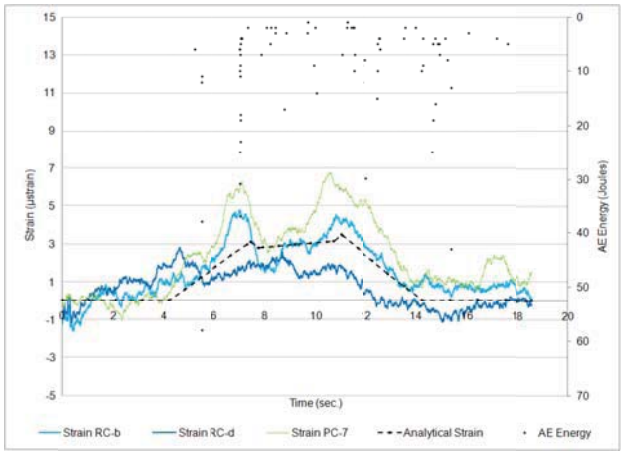

Figure II.K.6b - Strain and AE Energy, Test N-B2c

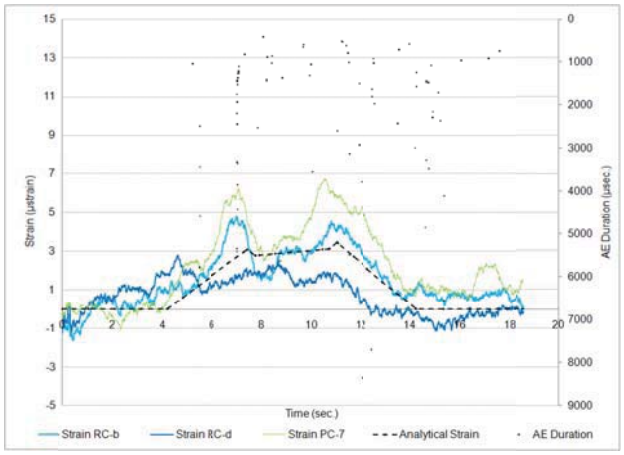

Figure II.K.6c - Strain and AE Duration, Test N-B2c

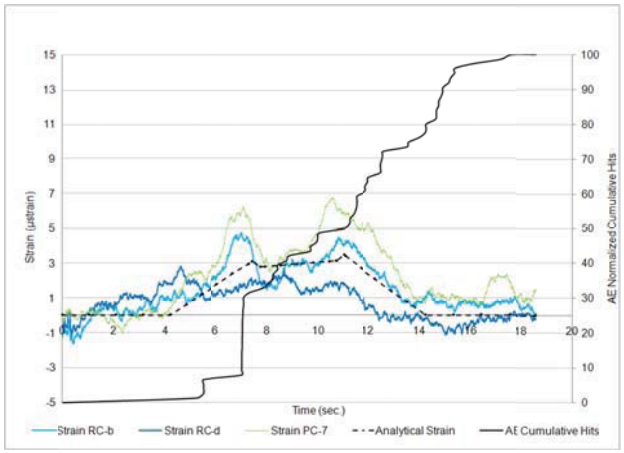

Figure II.K.6d - Strain and AE Cumulative Number of Hits, Test N-B2c

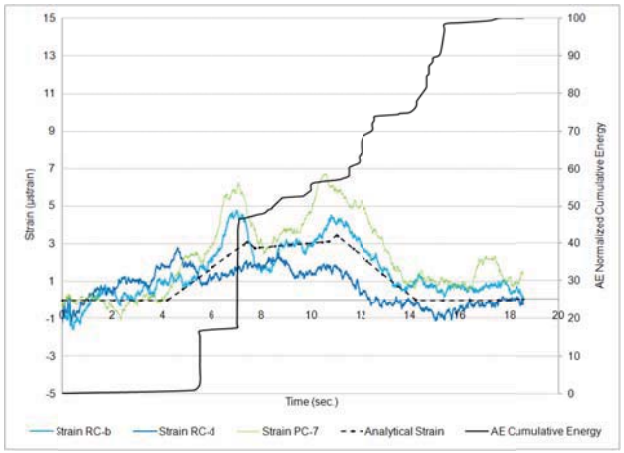

Figure II.K.6e - Strain and AE Cumulative Energy, Test N-B2c

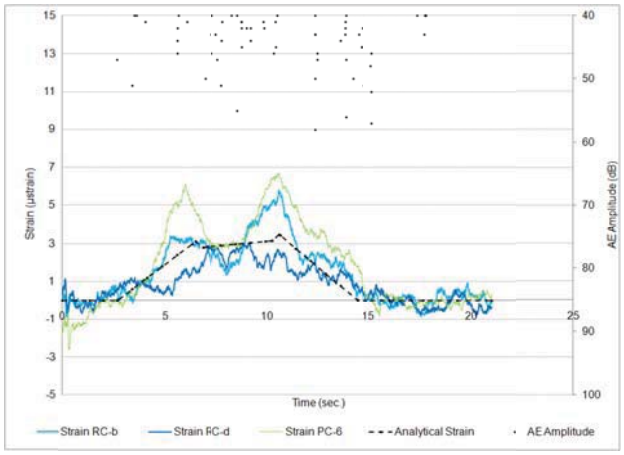

Figure II.K.7a - Strain and AE Amplitude, Test N-B3a

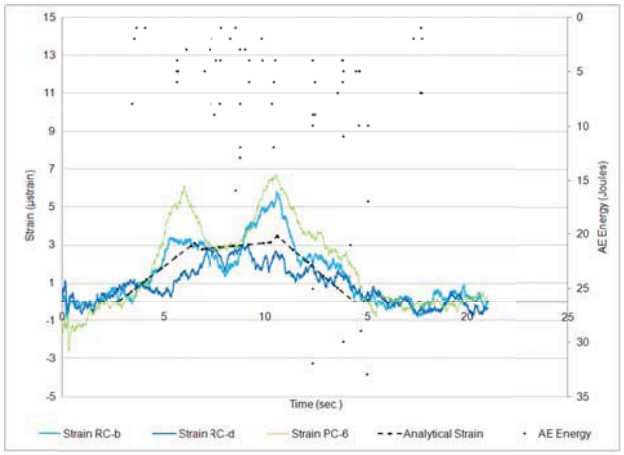

Figure II.K.7b - Strain and AE Energy, Test N-B3a

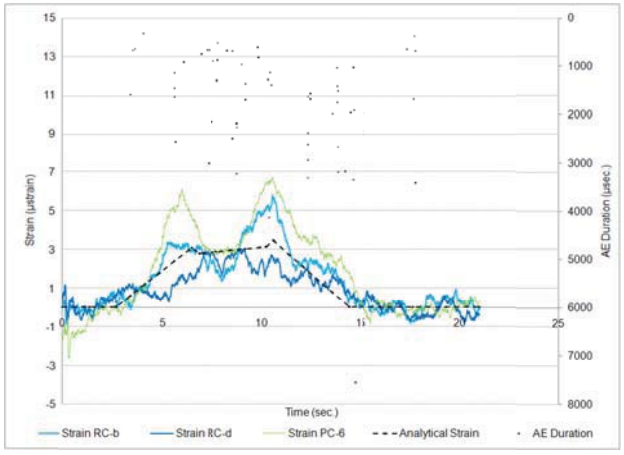

Figure II.K.7c - Strain and AE Duration, Test N-B3a

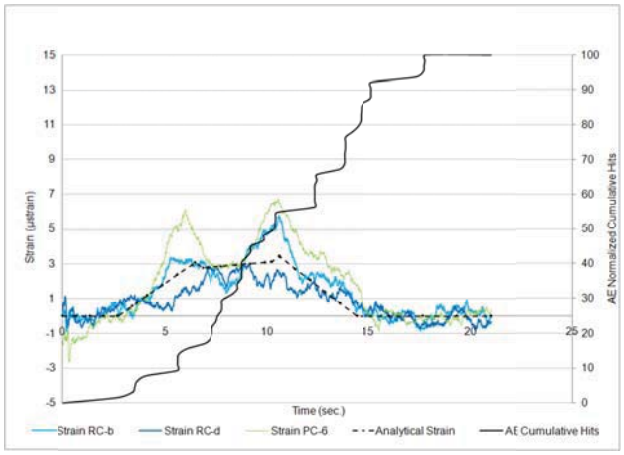

Figure II.K.7d - Strain and AE Cumulative Number of Hits, Test N-B3a

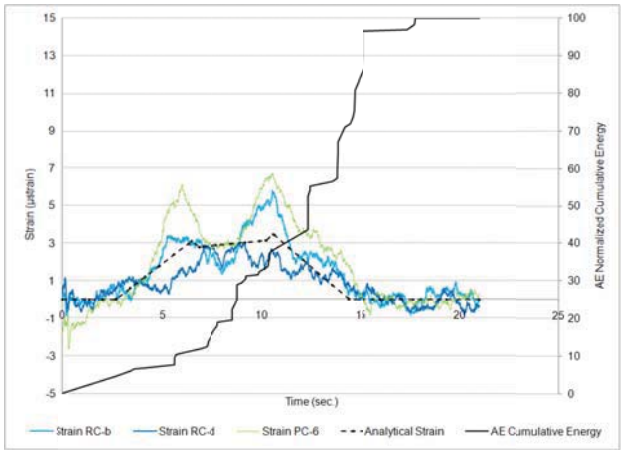

Figure II.K.7e - Strain and AE Cumulative Energy, Test N-B3a

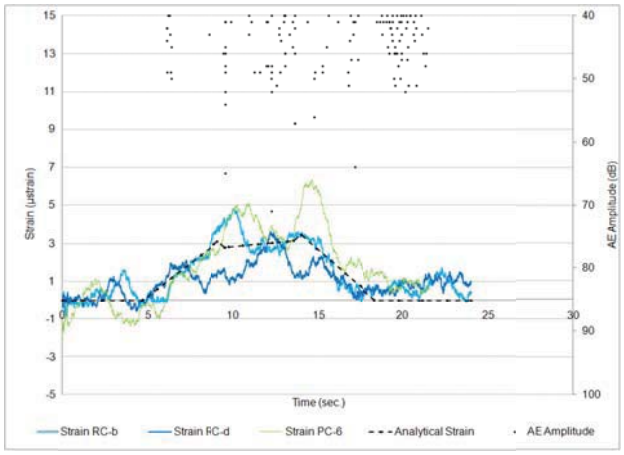

Figure II.K.8a - Strain and AE Amplitude, Test N-B3b

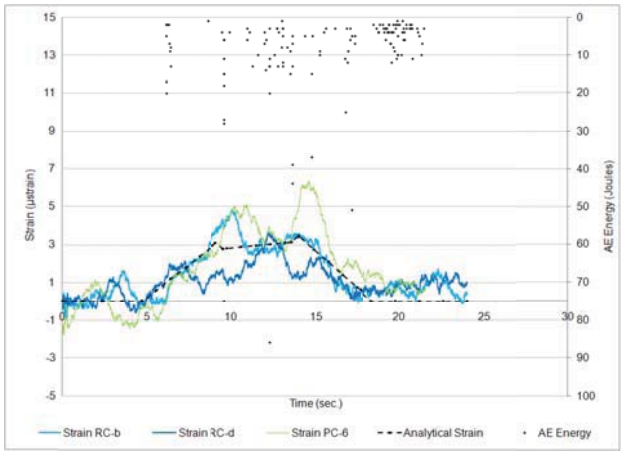

Figure II.K.8b - Strain and AE Energy, Test N-B3b

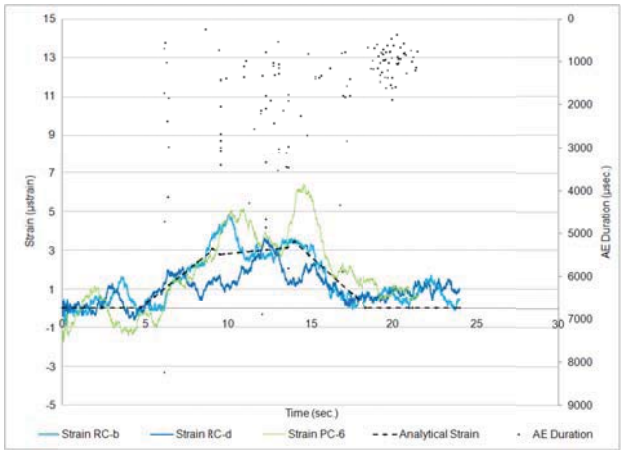

Figure II.K.8c - Strain and AE Duration, Test N-B3b

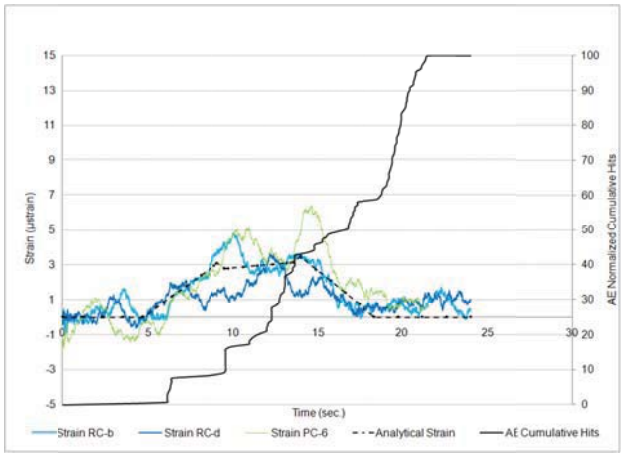

Figure II.K.8d - Strain and AE Cumulative Number of Hits, Test N-B3b

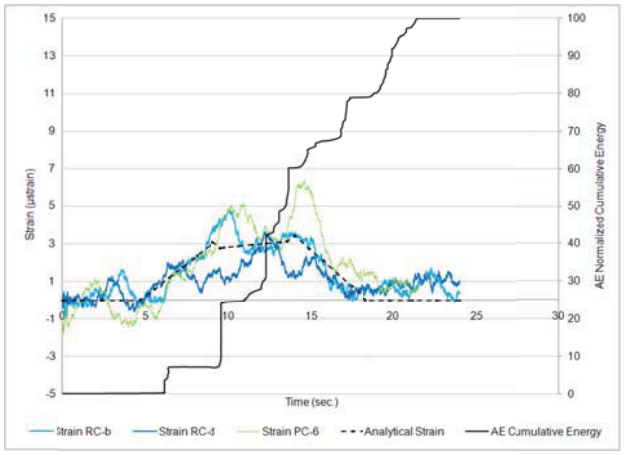

Figure II.K.8e - Strain and AE Cumulative Energy, Test N-B3b

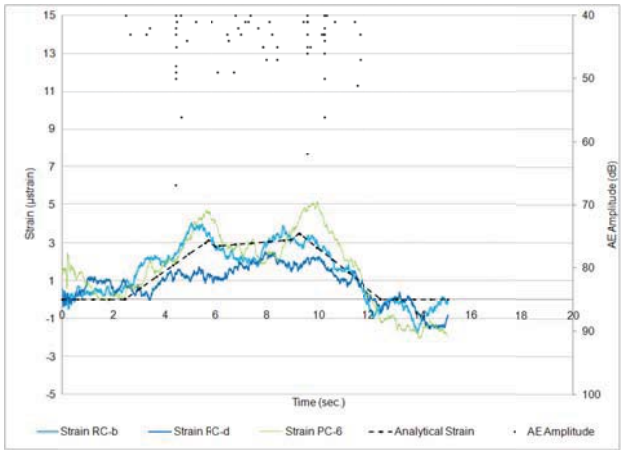

Figure II.K.9a - Strain and AE Amplitude, Test N-B3c

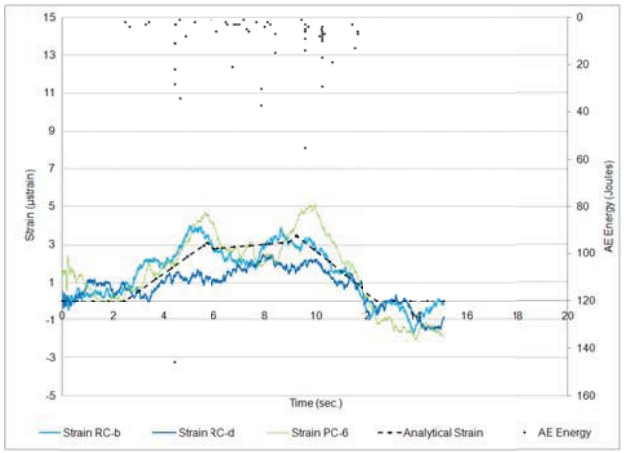

Figure II.K.9b - Strain and AE Energy, Test N-B3c

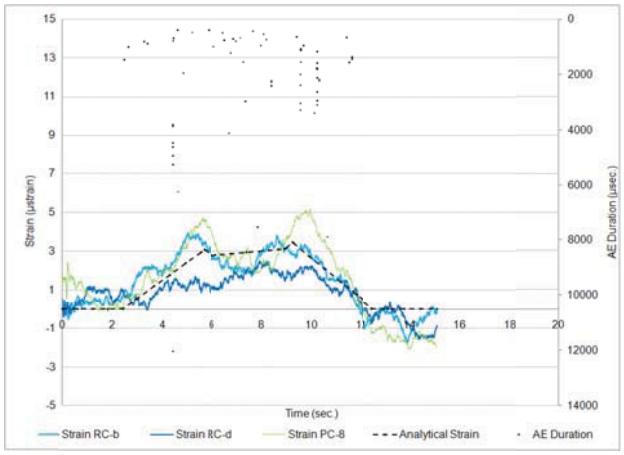

Figure II.K.9c - Strain and AE Duration, Test N-B3c

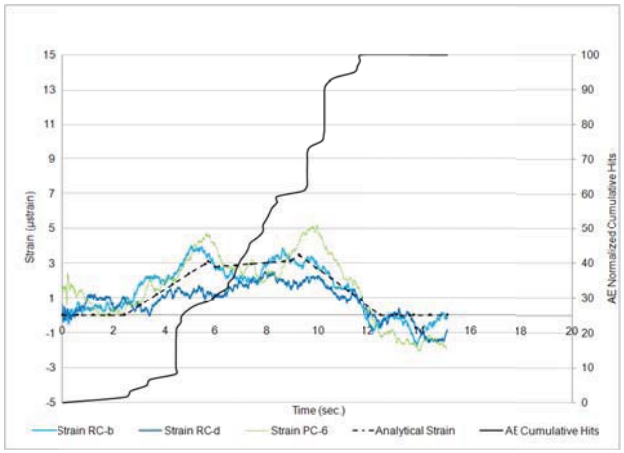

Figure II.K.9d - Strain and AE Cumulative Number of Hits, Test N-B3c

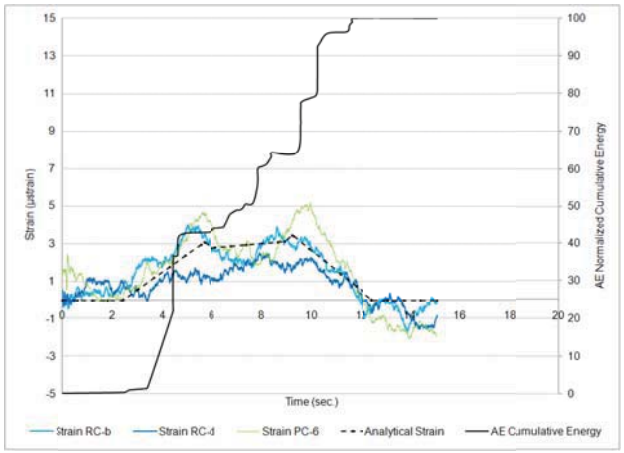

Figure II.K.9e - Strain and AE Cumulative Energy, Test N-B3c

Appendix III - Study III

Appendix III.A - Attenuation Test Results Before Corrosion

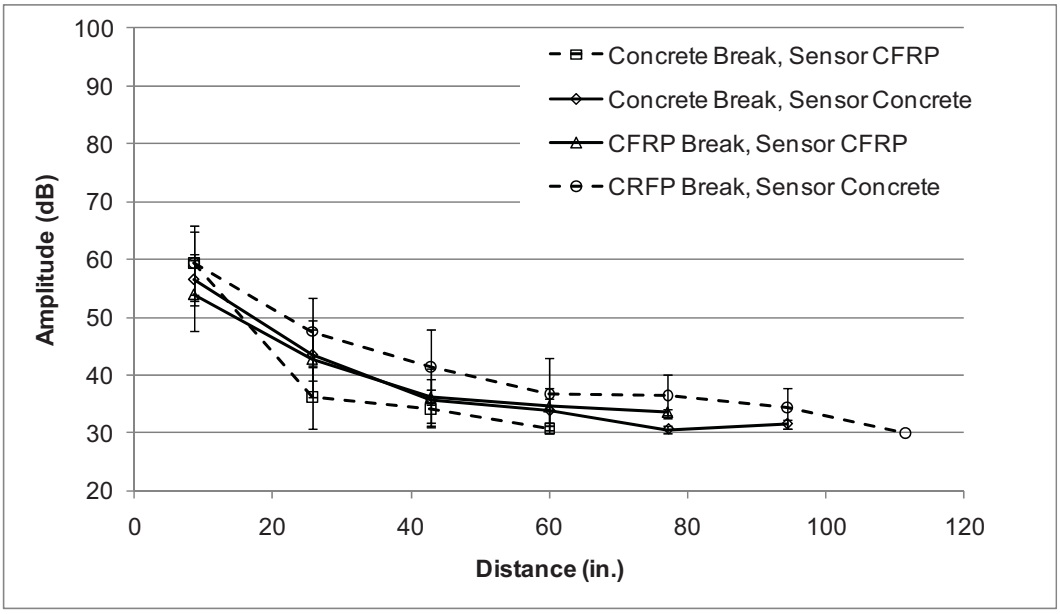

Figure III.A.1 - Attenuation results Beam B1

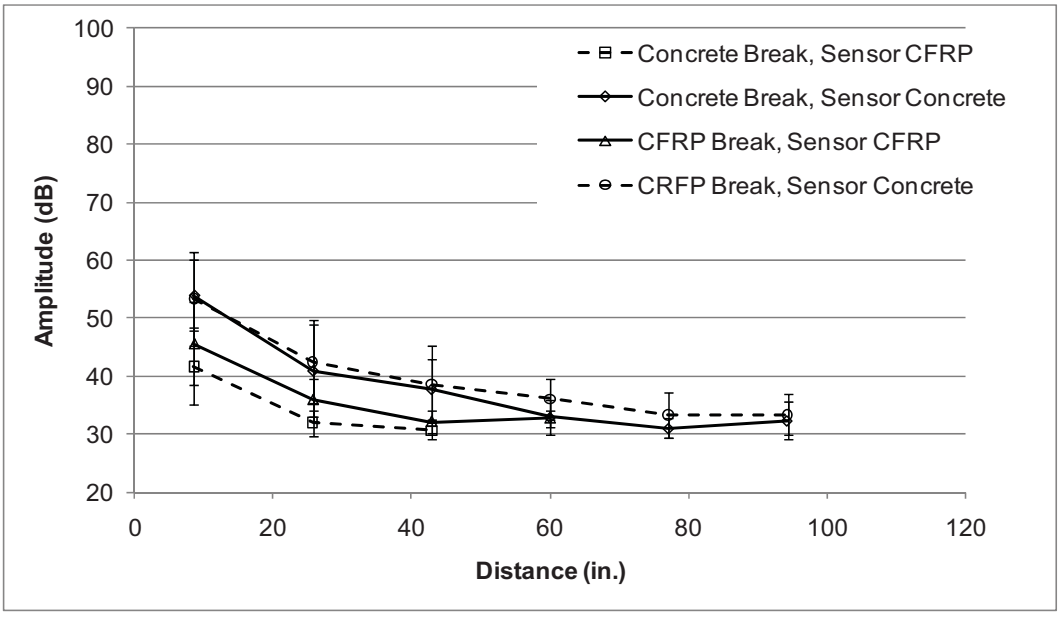

Figure III.A.2 - Attenuation results Beam B2

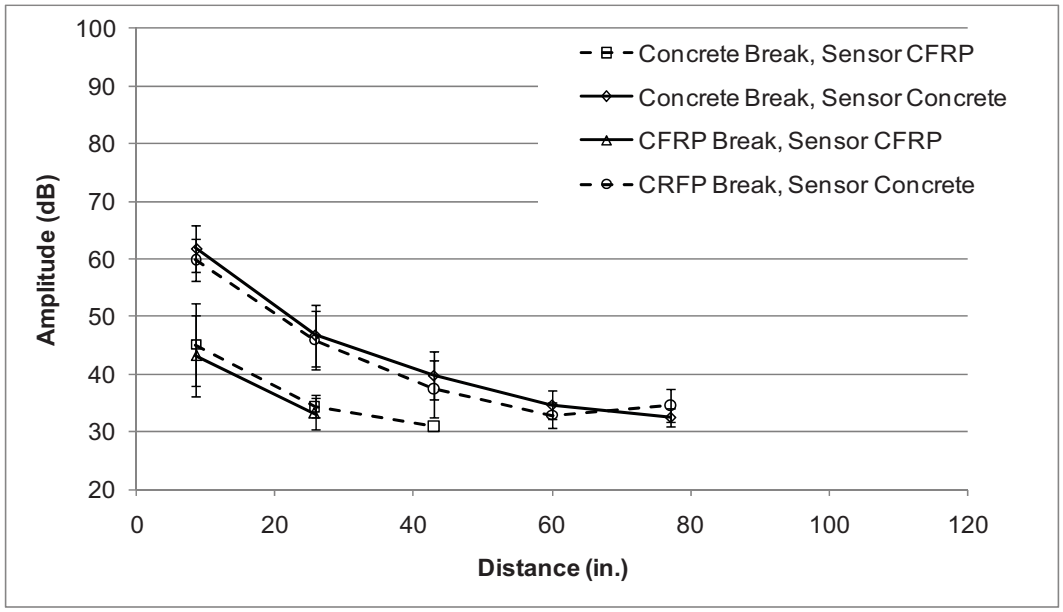

Figure III.A.3 - Attenuation results Beam B3

Appendix III.B - Physical Assessment Results Before Corrosion

The physical assessments before repair had results equal to zero for the layers crack map, reinforcement loss, and carbonation. These layers and data are not illustrated below.

Table III.B.1 - pH level

	A	B	C	D	E	F	G	H	I	J	K
B0	9.0	11.0	11.0	10.7	10.0	11.0	10.3	11.0	10.0	9.0	8.3
B1	11.0	11.0	11.0	11.0	11.0	11.0	11.0	11.0	11.0	11.0	11.0
B2	11.0	11.0	11.0	11.0	11.0	11.0	11.0	11.0	11.0	11.0	11.0
B4	11.0	9.0	10.0	11.0	11.0	11.0	11.0	11.0	11.0	11.0	11.0

Table III.B.2 - Active corrosion potential

	A	B	C	D	E	F	G	H	I	J	K
B0	-233	-178	-129	-120	-144	-110	-99	-28	-61	-56	-118
B1	-289	-213	-111	-28	17	13	28	3	-109	-40	-96
B2	-276	-179	-82	-37	-37	-6	9	-20	40	33	26
B4	-284	-202	-117	-136	-104	-65	-111	-98	-118	-104	-128

Table III.B.3 - Chloride content

	A	B	C	D	E	F	G	H	I	J	K
B0			0.06%			0.05%			0.02%		
B1			0.04%			0.04%			0.02%		
B2			0.04%			0.01%			0.01%		
B4			0.02%			0.01%			0.02%		

Table III.B.4 - Attenuation conductivity

	A	B	C	D	E	F	G	H	I	J	K
B0	0.05	0.10	0.09	0.02	0.01	0.01	0.04	0.08	0.12	0.14	0.00
B1	0.04	0.01	0.09	0.04	0.02	0.01	0.04	0.02	0.01	0.01	0.04
B2	0.06	0.02	0.01	0.02	0.01	0.01	0.02	0.08	0.12	0.02	0.00
B4	0.01	0.10	0.09	0.02	0.01	0.01	0.04	0.10	0.12	0.10	0.01

Appendix III.C - AE Monitoring Corrosion Conditioning

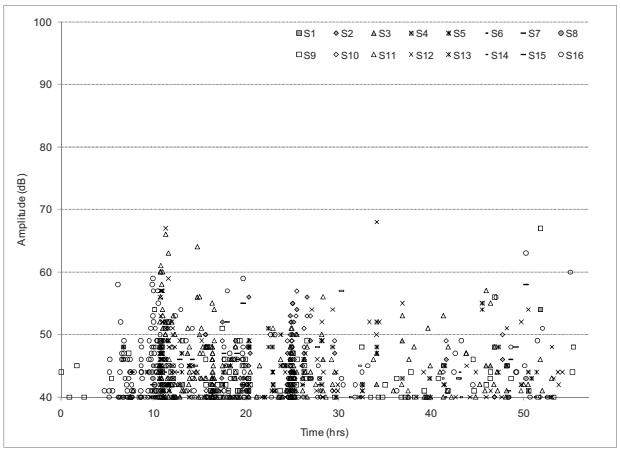

Figure III.C1a – AE Amplitude corrosion Beam B1

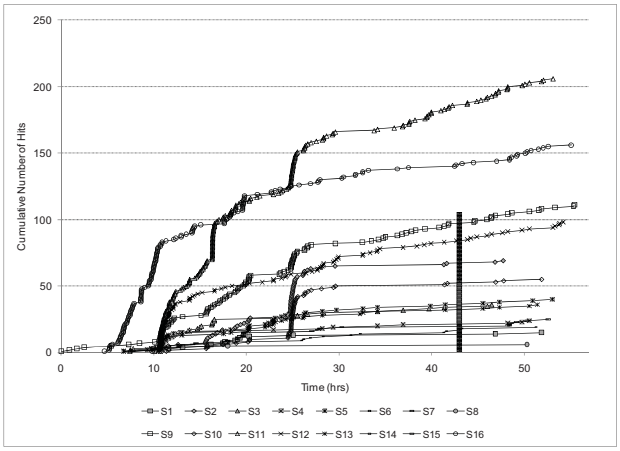

Figure III.C1b - AE Amplitude corrosion Beam B1

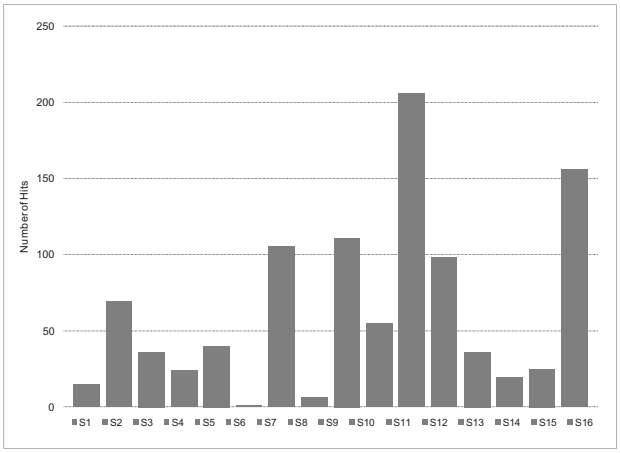

Figure III.C1c - AE Number of Hits Beam B1

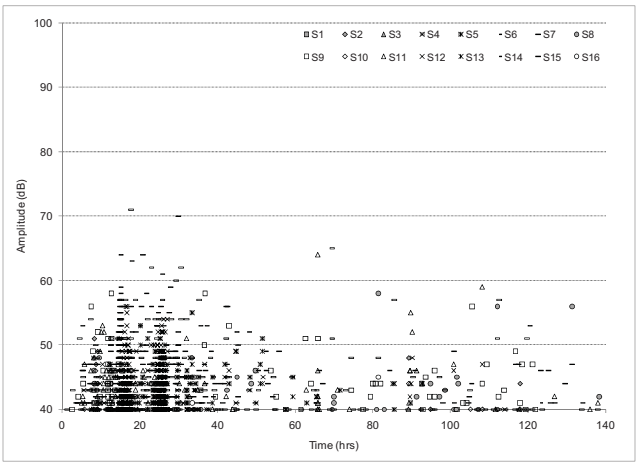

Figure III.C2a - AE Amplitude corrosion Beam B2

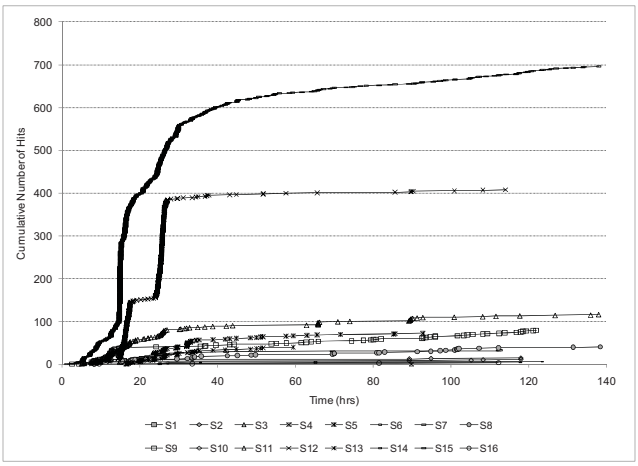

Figure III.C2b - AE Amplitude corrosion Beam B2

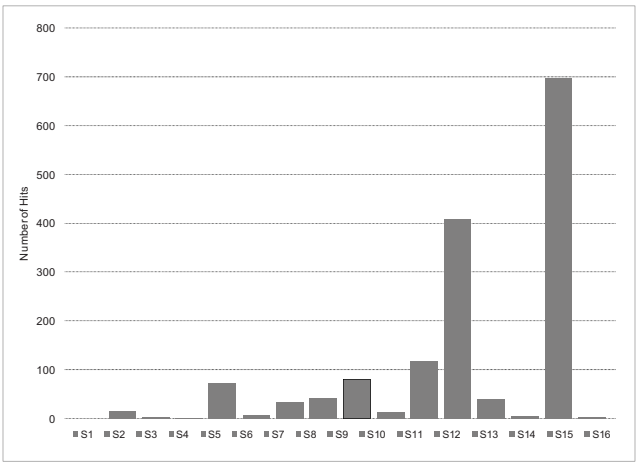

Figure III.C2c - AE Number of Hits Beam B2

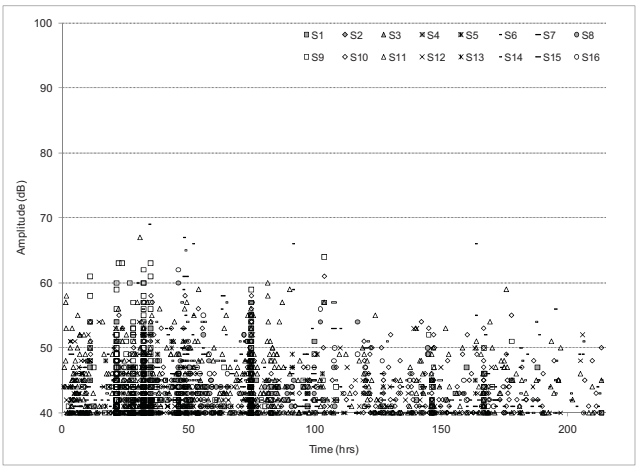

Figure III.C3a - AE Amplitude corrosion Beam B3

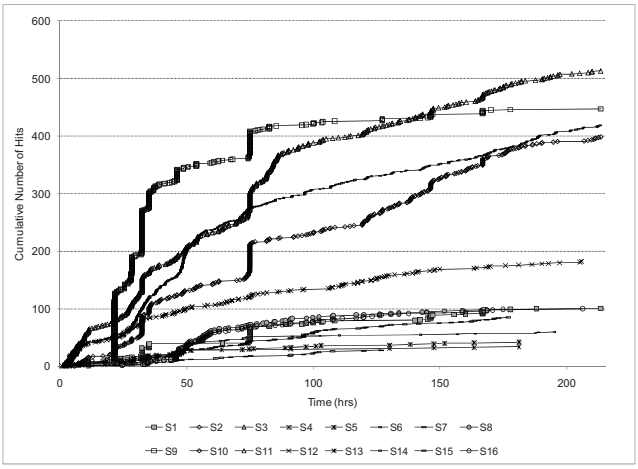

Figure III.C3a - AE Amplitude corrosion Beam B3

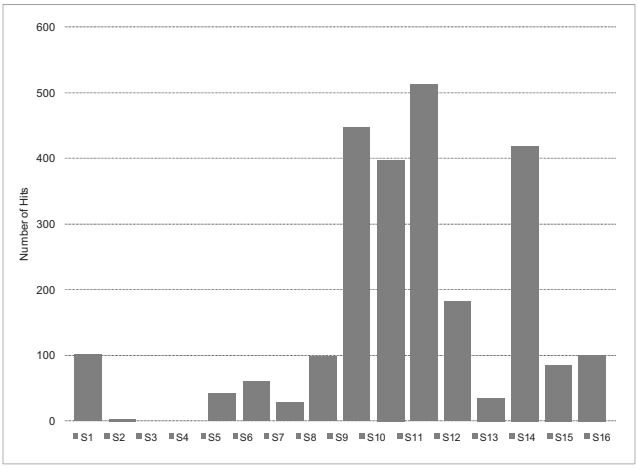

Figure III.C3c - AE Number of Hits Beam B3

Table III.C1 - Most active sensors during corrosion conditioning

		Acoustic Emission		Observations		Visual
		Amplitude	Number of Hits	Initiation	Activity	Inspection
Beam B1	7.24%	S12 S11 S9	S11 S16 S9			S13
Beam B2	12.14%	S15 S11	S15 S12 S11	S9 S15	S9 S12 S15	S12 S13
Beam B3	19.90%	S14 S11 S9 S10	S9 S11 S15 S10	S13 S14	S13 S14	S11 S12 S13 S14

Appendix III.D - Visual Inspection and Carbonation

Figure III.D.1 - Visual inspection Beam B0 to B4 before corrosion

Figure III.D.2 - Core evaluation of concrete carbonation before corrosion

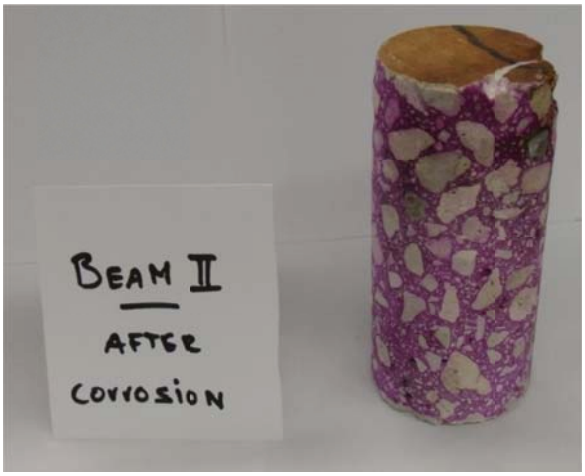

Figure III.D.3 - Core evaluation of concrete carbonation after corrosion

Appendix III.E - Normalized Assessments Results After Repair

Translated results for visual inspection, carbonation and AE attenuation conductivity layers can be found in Table 4.3, 4.4 and 4.9.

Table III.E.1 - pH level

	A	B	C	D	E	F	G	H	I	J	K
B0	1	0	0	0	0	0	0	0	0	1	1
B1	0	0	1	0	0	0	1	0	0	0	0
B2	1	1	1	0	0	0	0	0	0	0	0
B4	1	1	0	0	0	0	0	0	0	0	0

Table III.E.2 - Active corrosion potential

	A	B	C	D	E	F	G	H	I	J	K
B0	0	0	0	0	0	0	0	0	0	0	0
B1	1	1	1	1	1	1	1	1	1	1	1
B2	1	1	1	1	1	1	1	1	1	1	1
B4	1	1	1	1	1	1	1	1	1	1	1

Table III.E.3 - Chloride content

	A	B	C	D	E	F	G	H	I	J	K
B0	0	0	0	0	0	0	0	0	0	0	0
B1	0	0	0	0	0	0	0	0	0	0	0
B2	0	0	0	0	1	1	1	0	0	0	0
B4	1	1	1	1	1	1	1	1	1	1	1

Table III.E.4 - Crack density

	A	B	C	D	E	F	G	H	I	J	K
B0	0.0	0.0	0.0	0.0	0.0	0.0	0.0	0.0	0.0	0.0	0.0
B1	0.4	0.2	0.2	0.4	0.4	0.4	0.6	0.2	0.2	0.4	0.6
B2	0.6	0.6	0.6	0.6	0.6	0.6	0.8	0.6	0.6	0.6	0.6
B4	0.6	0.6	0.8	0.8	0.8	1.0	0.8	0.6	0.8	0.8	0.6

Appendix III.F - Example Calculation for Beam Specimens

BEAM TEST PREPARATATION

FLEXURAL STRENGTHENED RC CONCRETE BEAM WITH A CFRP SYSTEM

Geometrical data

$N_b := 3$	Number of bars
$X := 100\%$	Percentage steel present
$h := 6 \cdot in$	Height
$h_{tot} := h = 6 \cdot in$	Height with deck
$c_{over} := 1 in$	Cover
$d_b := 0.5 in$	Bars diameter
$d := h - c_{over} - 0.5 \cdot d_b = 4.75 \cdot in$	Effective depth
$d_f := h = 6 \cdot in$	Depth till FRP
$b_w := 12 in$	Width of the slab
$L_{span} := 10 ft$	Span
$A_s := X \cdot N_b \cdot 2 in^2 = 0.6 \cdot in^2$	Total area bars
$A_g := b_w \cdot h = 72 \cdot in^2$	Area concrete section
$l := 12 \cdot ft$	Length of the laminate
$w_b := 12 in$	Width of FRP strips
$t_f := 0.04 in$	Tickness of FRP strips
$n_f := 2$	Number of FRP strips
$A_f := n_f \cdot w_b \cdot t_f = 0.96 \cdot in^2$	Total area of FRP strips
$I := b_w \cdot \frac{h^3}{12} = 216 \cdot in^4$	Moment of inertia
$I_g := b_w \cdot \frac{d^3}{12} = 107.172 \cdot in^4$	Effective moment of inertia

Material data

$f_s := 60 \cdot ksi$ — Steel strength

$f_c := 4.346 \cdot ksi$ — Concrete strength

$f_r := 7.5 \cdot \sqrt{f_c \cdot psi} = 0.494 \cdot ksi$ — Concrete fiber rupture strenght

$f_{f.u} := 91 ksi$ — FRF rupture strength

$E_s := 29000 \cdot ksi$ — Elastic modulus of steel

$E_c := 57000 \sqrt{f_c \cdot psi} = 3.758 \times 10^3 \cdot ksi$ — Elastic modulus of concrete

$E_f := 11900 ksi$ — Moculus of elasticity of FRP

$n_s := \frac{E_s}{E_c} = 7.718$ — Composite ratio steel concrete

$n_{of} := \frac{E_f}{E_c} = 3.167$ — Composite ratio FRP concrete

$\varepsilon_{cu} := 0.003$ — Maximum compression strain concrete

$\varepsilon_{cr} := \frac{f_r}{E_c} = 1.316 \times 10^{-4}$ — Maximum tensile strain concrete

$\varepsilon_s := \frac{f_s}{E_s} = 2.069 \times 10^{-3}$ — Ultimate strain steel

$\varepsilon_{f.u} := 0.0085$ — Rupture strain CFRP

Step 1: Calculate the FRP system design material properties

$\psi_f := 1$ — FRP strenght reduction factor

$C_e := 1$ — FRP environ. reduction factor

$f_{fu} := C_e \cdot f_{f.u} = 91 \cdot ksi$ — Reduced rupture stress

$\varepsilon_f := C_e \cdot \varepsilon_{f.u} = 8.5 \times 10^{-3}$ — Reduced rupture strain

$w_D := \frac{h_{tot} \cdot b_w}{ft^2} \cdot 150 \frac{lbf}{ft} = 75 \cdot \frac{lbf}{ft}$ — Dead load

$M_{DL} := \frac{\left(w_D \cdot L_{span}^2\right)}{8} = 0.937 \cdot kip \cdot ft$ — Moment from dead load beam

$\varepsilon_{fd} := 0.083 \cdot \sqrt{\frac{f_c}{n_f \cdot E_f \cdot t_f}} \cdot in^{0.5} = 5.608 \times 10^{-3}$ — Debonding strain level FRP <0.9*εf.u
εf.u=0.0085 * 0.9 = 0.00765
Otherwise debonding is failure

$\varepsilon_{fu} := \begin{cases} \varepsilon_{fd} & \text{if } \varepsilon_{fd} < \varepsilon_{f.u} \\ \varepsilon_f & \text{otherwise} \end{cases} = 5.608 \times 10^{-3}$ — Ultimate strain FRP

Step A: Cracking Moment

$\iota_{cr} := .34525$ $\quad x_{cr.0} := \iota_{cr} \cdot h = 2.071 \cdot in$

$\varepsilon_{c.t} := \frac{f_r}{E_c} = 1.316 \times 10^{-4}$ Rupture tensile concrete

$\varepsilon_{f.cr} := \varepsilon_{c.t} = 1.316 \times 10^{-4}$ < 0.005321

$\varepsilon_{s.cr} := \frac{(d - x_{cr.0})}{(h - x_{cr.0})} \cdot \varepsilon_{c.t} = 8.971 \times 10^{-5}$ < 0.002

$\varepsilon_{c.cr} := \frac{x_{cr.0}}{(h - x_{cr.0})} \cdot \varepsilon_{c.t} = 6.938 \times 10^{-5}$ < 0.00175

$f_{s.cr} := E_s \cdot \varepsilon_{s.cr} = 2.602 \cdot ksi$ $\quad f_{f.cr} := E_f \cdot \varepsilon_{f.cr} = 1.566 \cdot ksi$

$f_{c.cr} := E_c \cdot \varepsilon_{c.cr} = 0.261 \cdot ksi$ Average concrete pressure

$\varepsilon_{oc.cr} := 1.7 \cdot \varepsilon_{c.cr} = 1.179 \times 10^{-4}$ Strain corresponding to stress concrete

$\beta_{1.cr} := \frac{4\varepsilon_{oc.cr} - \varepsilon_{c.cr}}{6 \cdot \varepsilon_{oc.cr} - 2 \cdot \varepsilon_{c.cr}} = 0.707$ Beta 1

$\alpha_{1.cr} := \frac{\left(3 \cdot \varepsilon_{oc.cr} \cdot \varepsilon_{c.cr} - \varepsilon_{c.cr}^2\right)}{3 \cdot \beta_{1.cr} \cdot \varepsilon_{oc.cr}^2} = 0.669$ Alpha 1

$x_{cr} := \frac{\left(A_s \cdot f_{s.cr} + A_f \cdot f_{f.cr}\right)}{\alpha_{1.cr} \cdot f_{c.cr} \cdot \beta_{1.cr} \cdot b_w} = 2.071 \cdot in$ Calculation for x.cr, should equal assumption x.cr0

$y_{cr} := d - x_{cr} = 2.679 \cdot in$

$I_0 := \frac{1}{12} \cdot b_w \cdot h^3 + n_s \cdot A_s \cdot \left(d - \frac{h}{2}\right)^2 + n_{of} \cdot A_f \cdot \left(\frac{h}{2}\right)^2 = 257.543 \cdot n^4$

$M_{n.cr} := f_r \cdot \frac{I_0}{y_{cr}} = 3.961 \cdot kip \cdot ft$ Moment

$\kappa_{cr} := \frac{\left(\varepsilon_{c.cr} + \varepsilon_{f.cr}\right)}{h} = 3.349 \times 10^{-5} \cdot \frac{1}{in}$ Curvature

$EI_0 := \frac{M_{n.cr}}{\kappa_{cr}} = 1.419 \times 10^{9} \cdot lbf \cdot in^2$ Stiffness

$w_{cr} := -0.5 \cdot \frac{\left[M_{n.cr} \cdot \left(0.5 \cdot L_{span}\right)^2\right]}{EI_0} = -0.06 \cdot in$ Defection

Step B: Steel Yielding Moment

$\iota_y := .34525$ $\quad x_{y.0} := \iota_y \cdot h = 2.071 \cdot in$

$\varepsilon_{s.y} := \frac{f_s}{E_s} = 2.069 \times 10^{-3}$ Yielding steel

$\varepsilon_{c.y} := \frac{x_{y.0}}{(d - x_{y.0})} \cdot \varepsilon_{s.y} = 1.6 \times 10^{-3}$ < 0.00175

$\varepsilon_{f.y} := \frac{(h - x_{y.0})}{d - x_{y.0}} \cdot \varepsilon_{s.y} = 3.035 \times 10^{-3}$ < 0.005321

$f_s = 60 \cdot ksi$ $\quad f_{f.y} := E_f \cdot \varepsilon_{f.y} = 36.111 \cdot ksi$

$f_{c.y} := E_c \cdot \varepsilon_{c.y} = 6.013 \cdot ks$ Average concrete pressure

$\varepsilon_{oc.y} := 1.7 \cdot \varepsilon_{c.y} = 2.72 \times 10^{-3}$ Strain corresponding to stress concrete

$\beta_{1.y} := \frac{4\varepsilon_{oc.y} - \varepsilon_{c.y}}{6 \cdot \varepsilon_{oc.y} - 2 \cdot \varepsilon_{c.y}} = 0.707$ Beta 1

$\alpha_{1.y} := \frac{\left(3 \cdot \varepsilon_{oc.y} \cdot \varepsilon_{c.y} - \varepsilon_{c.y}^2\right)}{3 \cdot \beta_{1.y} \cdot \varepsilon_{oc.y}^2} = 0.669$ Alpha 1

$x_y := \frac{\left(A_s \cdot f_s + A_f \cdot f_{f.y}\right)}{\alpha_{1.y} \cdot f_{c.y} \cdot \beta_{1.y} \cdot b_w} = 2.071 \cdot in$ Calculation for x.y, should equal assumption x.y0

$M_{ns.y} := A_s \cdot f_s \cdot \left[d - \frac{(\beta_{1.y} \cdot x_y)}{2}\right] = 12.053 \cdot kip \cdot ft$ Steel contribution to bending

$M_{nf.y} := A_f \cdot f_{f.y} \cdot \left[d_f - \frac{(\beta_{1.y} \cdot x_y)}{2}\right] = 15.217 \cdot kip \cdot ft$ FRP contribution to bending

$M_{n.y} := M_{ns.y} + M_{nf.y} = 27.27 \cdot kip \cdot ft$ Moment

$\kappa_y := \frac{(\varepsilon_{c.y} + \varepsilon_{f.y})}{h} = 7.724 \times 10^{-4} \cdot \frac{1}{in}$ Curvature

$EI_y := \frac{M_{n.y}}{\kappa_y} = 4.236 \times 10^8 \cdot lbf \cdot in^2$ Stiffness

$w_y := -0.5 \cdot \frac{\left[M_{n.y} \cdot (0.5 \cdot L_{span})^2\right]}{EI_y} = -1.39 \cdot in$ Defection

Step C : Concrete Crushing Moment

$\iota_{c1} := .3367$ $\quad x_{c1.0} := \iota_{c1} \cdot h = 2.02 \cdot in$

$\varepsilon_{c.c1} := 0.00175$ Concrete starts crushing

$\varepsilon_{s.c1} := \frac{(d - x_{c1.0})}{x_{c1.0}} \cdot \varepsilon_{c.c1} = 2.365 \times 10^{-3}$ < 0.002 Yielded steel

$\varepsilon_{f.c1} := \frac{(h - x_{c1.0})}{x_{c1.0}} \cdot \varepsilon_{c.c1} = 3.448 \times 10^{-3}$ < 0.005321

$f_{s.c1} := f_s = 60 \cdot ksi$ $\quad f_{f.c1} := E_f \cdot \varepsilon_{f.c1} = 41.025 \cdot ksi$

$f_{c.c1} := E_c \cdot \varepsilon_{c.c1} = 6.576 \cdot ksi$ Average concrete pressure

$\varepsilon_{oc.c1} := 1.7 \cdot \varepsilon_{c.c1} = 2.975 \times 10^{-3}$ Strain corresponding to stress concrete

$\beta_{1.c1} := \frac{4\varepsilon_{oc.c1} - \varepsilon_{c.c1}}{6 \cdot \varepsilon_{oc.c1} - 2 \cdot \varepsilon_{c.c1}} = 0.707$ Beta 1

$\alpha_{1.c1} := \frac{\left(3 \cdot \varepsilon_{oc.c1} \cdot \varepsilon_{c.c1} - \varepsilon_{c.c1}^2\right)}{3 \cdot \beta_{1.c1} \cdot \varepsilon_{oc.c1}^2} = 0.669$ Alpha 1

$x_{c1} := \frac{\left(A_s \cdot f_s + A_f \cdot f_{f.c1}\right)}{\alpha_{1.c1} \cdot f_{c.c1} \cdot \beta_{1.c1} \cdot b_w} = 2.02 \cdot in$ Calculation for x.c1, should equal assumption x.c10

$M_{ns.c1} := A_s \cdot f_s \cdot \left[d - \frac{(\beta_{1c1} \cdot x_{c1})}{2}\right] = 12.107 \cdot kip \cdot ft$ Steel contribution to bending

$M_{nf.c1} := A_f \cdot f_{f.c1} \cdot \left[d_f - \frac{(\beta_{1.c1} \cdot x_{c1})}{2}\right] = 17.347 \cdot kip \cdot ft$ FRP contribution to bending

$M_{n.c1} := M_{ns.c1} + M_{nf.c1} = 29.454 \cdot kip \cdot ft$ Moment

$\kappa_{c1} := \frac{(\varepsilon_{c.c1} + \varepsilon_{f.c1})}{h} = 8.663 \times 10^{-4} \cdot \frac{1}{in}$ Curvature

$EI_{c1} := \frac{M_{n.c1}}{\kappa_{c1}} = 4.08 \times 10^8 \cdot lbf \cdot in^2$ Stiffness

$w_{c1} := -0.5 \cdot \frac{\left[M_{n.c1} \cdot (0.5 \cdot L_{span})^2\right]}{EI_{c1}} = -1.559 \cdot in$ Defection

Step E: Ultimate Concrete Moment

$\iota_{cu} := .3859$ $\quad x_{cu.0} := \iota_{cu} \cdot h = 2.315 \cdot in$

$\varepsilon_{cu} = 3 \times 10^{-3}$ Ultimate concrete strain

$\varepsilon_{s.cu} := \frac{(d - x_{cu.0})}{x_{cu.0}} \cdot \varepsilon_{cu} = 3.154 \times 10^{-3}$ < 0.002 Yielded steel

$\varepsilon_{f.cu} := \frac{(h - x_{cu.0})}{x_{cu.0}} \cdot \varepsilon_{cu} = 4.774 \times 10^{-3}$ < 0.005321

$f_{f.cu} := E_f \cdot \varepsilon_{f.cu} = 56.811 \cdot ksi$

$f_{s.cu} := f_s = 60 \cdot ksi$

$f_c = 4.345 \cdot ksi$

$\varepsilon_{oc} := 1.7 \cdot \frac{f_c}{E_c} = 1.966 \times 10^{-3}$ Strain corresponding to stress concrete

$\beta_{1.cu} := \frac{4\varepsilon_{oc} - \varepsilon_{cu}}{6 \cdot \varepsilon_{oc} - 2 \cdot \varepsilon_{cu}} = 0.839$ Beta 1

$\alpha_{1.cu} := \frac{\left(3 \cdot \varepsilon_{oc} \cdot \varepsilon_{cu} - \varepsilon_{cu}^2\right)}{3 \cdot \beta_{1.cu} \cdot \varepsilon_{oc}^2} = 0.893$ Alpha 1

$x_{cu} := \frac{(A_s \cdot f_{s.cu} + A_f \cdot f_{f.cu})}{\alpha_{1.cu} \cdot f_c \cdot \beta_{1.cu} \cdot b_w} = 2.315 \cdot in$ Calculation for x.cu, should equal assumption x.cu0

$M_{ns.cu} := A_s \cdot f_s \cdot \left[d - \frac{(\beta_{1.cu} \cdot x_{cu})}{2}\right] = 11.335 \cdot kip \cdot ft$ Steel contribution to bending

$M_{nf.cu} := A_f \cdot f_{f.cu} \cdot \left[d_f - \frac{(\beta_{1.cu} \cdot x_{cu})}{2}\right] = 22.854 \cdot kip \cdot ft$ FRP contribution to bending

$M_{n.cu} := M_{ns.cu} + M_{nf.cu} = 34.189 \cdot kip \cdot ft$ Moment

$\kappa_{cu} := \frac{(\varepsilon_{cu} + \varepsilon_{f.cu})}{h} = 1.296 \times 10^{-3} \cdot \frac{1}{in}$ Curvature

$EI_{cu} := \frac{M_{n.cu}}{\kappa_{cu}} = 3.166 \times 10^8 \cdot in^2 \cdot lbf$ Stiffness

$w_{cu} := -0.5 \cdot \frac{\left[M_{n.cu} \cdot (0.5 \cdot L_{span})^2\right]}{EI_{cu}} = -2.332 \cdot in$ Defection

Appendix III.G - Strain and AE Results B0, B1 and B2

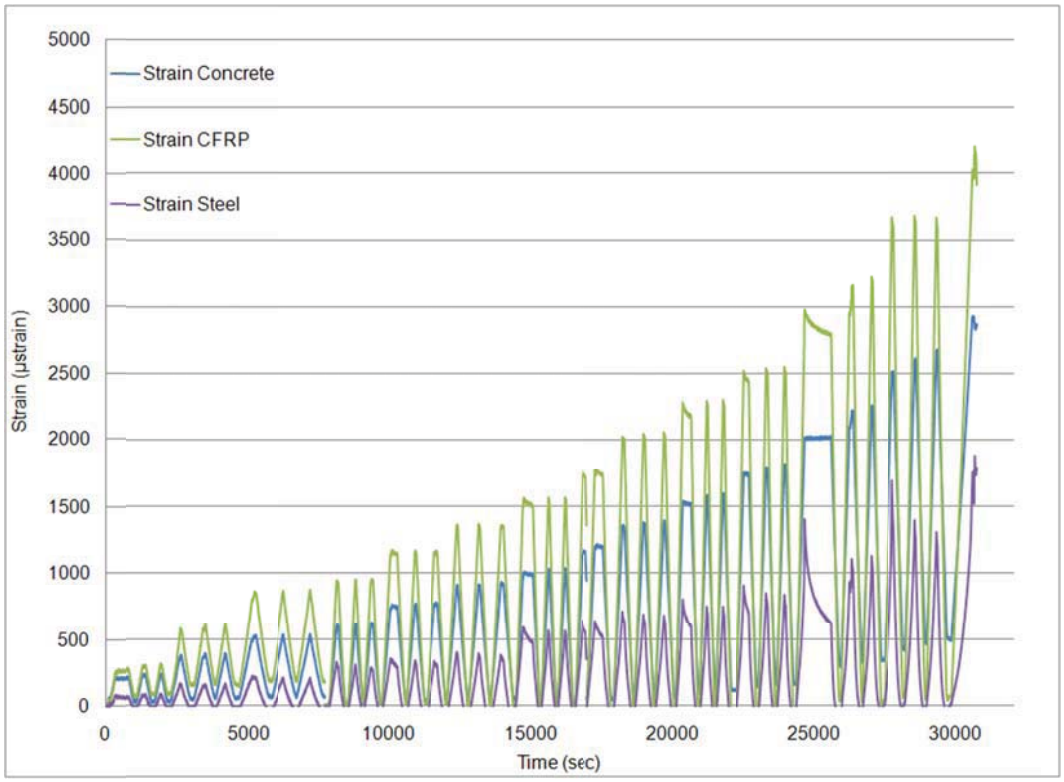

Figure III.G.1a - Strain in time, Test B0

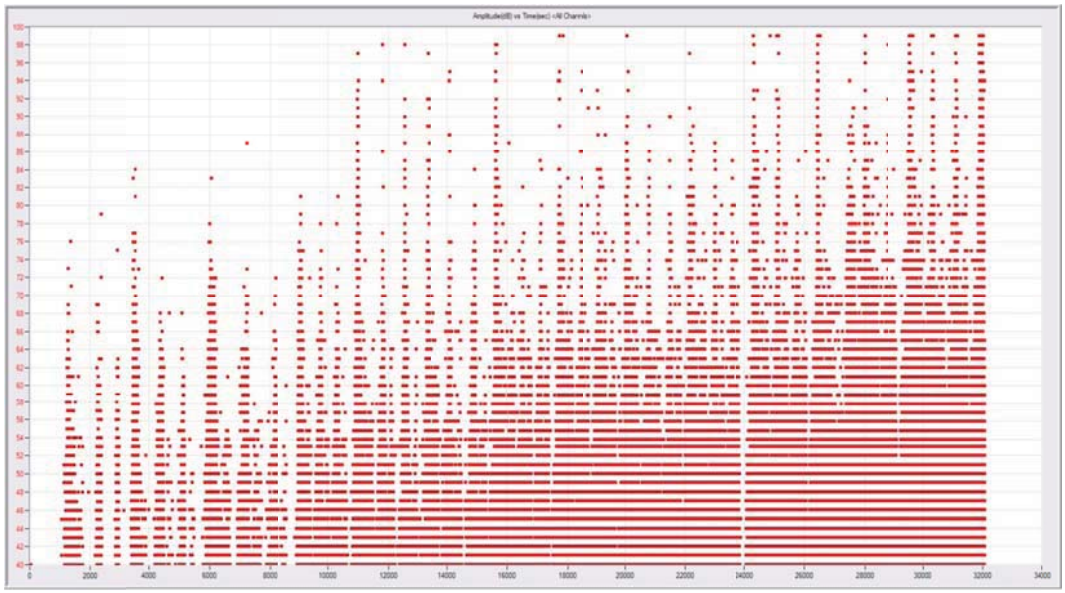

Figure III.G.1b - AE Amplitude (dB) in time, test B0

Figure III.G.1c - AE Energy (Joules) in time, test B0

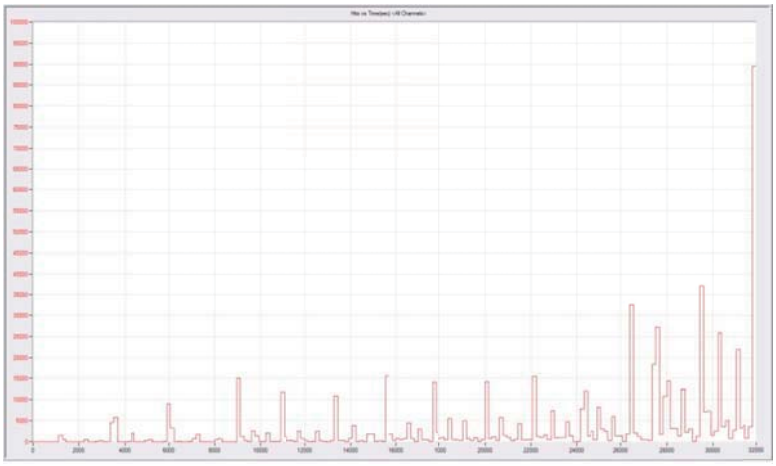

Figure III.G.1d - AE Hits in time, test B0

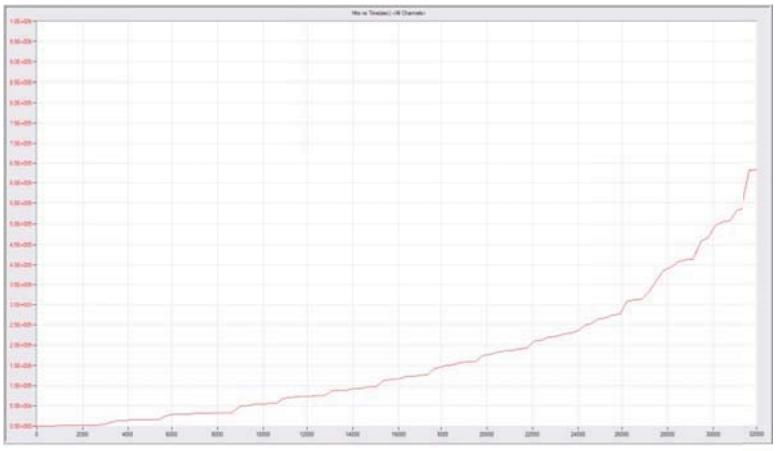

Figure III.G.1e - AE Cumulative Hits in time, test B0

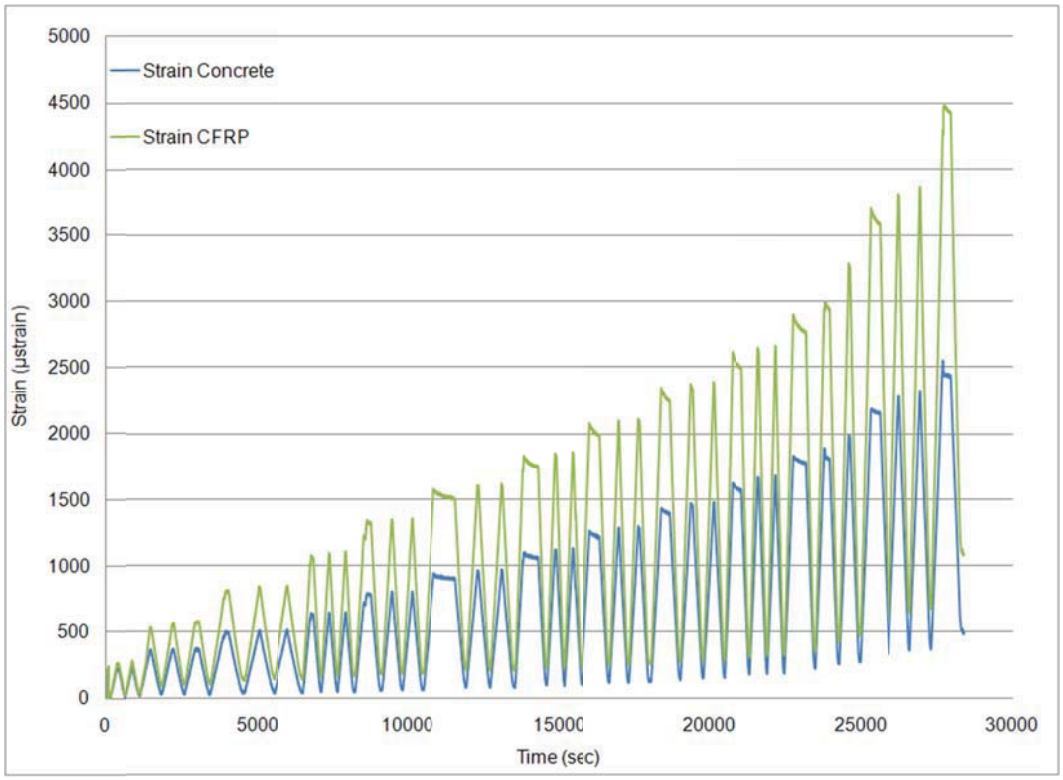

Figure III.G.2a - Strain in time, test B1

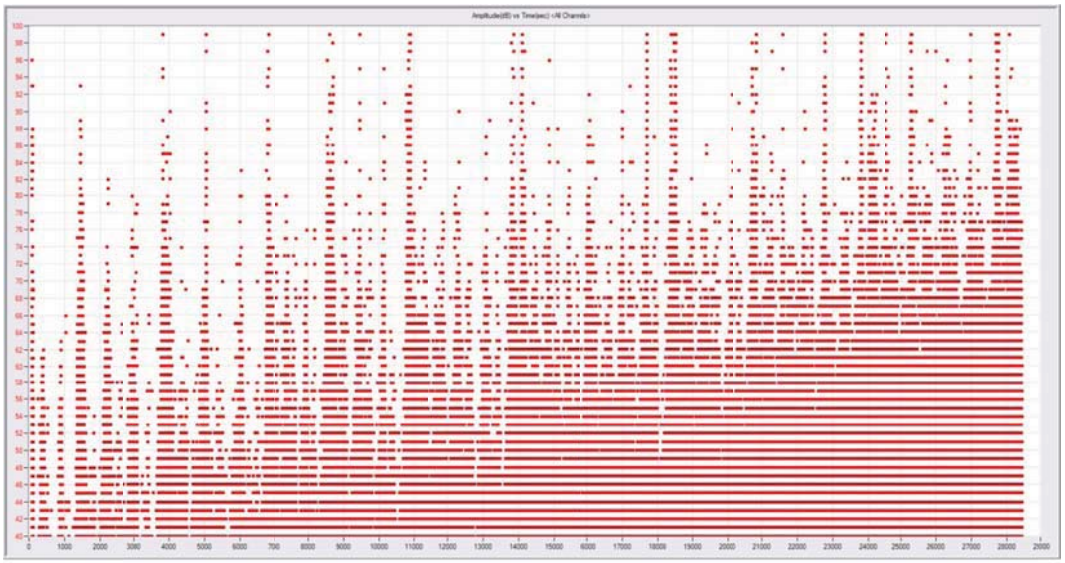

Figure III.G.2b - AE Amplitude (dB) in time, test B1

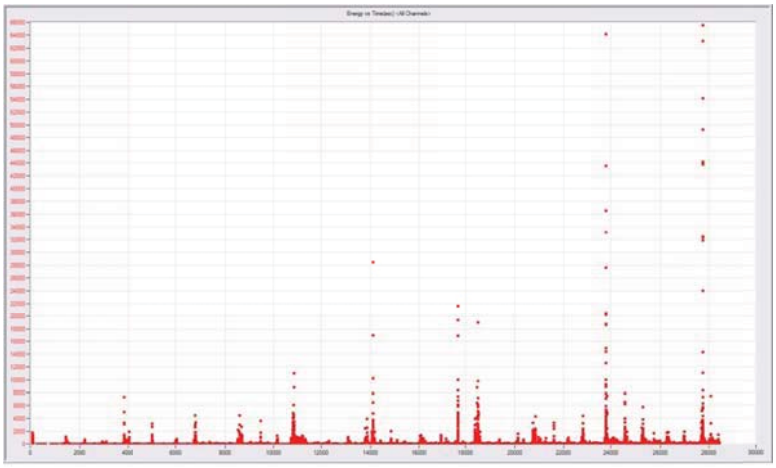

Figure III.G.2c - AE Energy (Joules) in time, test B1

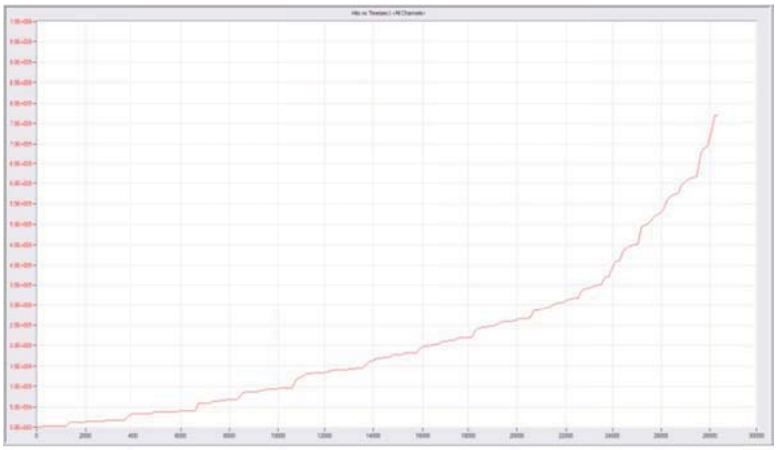

Figure III.G.2d - AE Hits in time, test B1

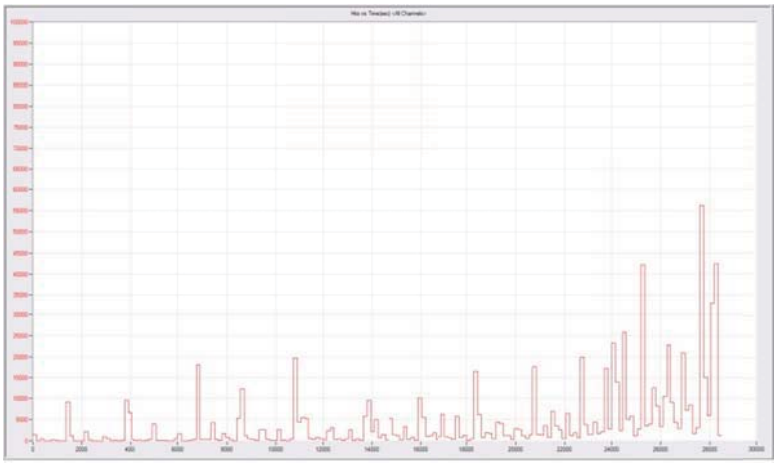

Figure III.G.2e AE Cumulative Hits in time, test B1

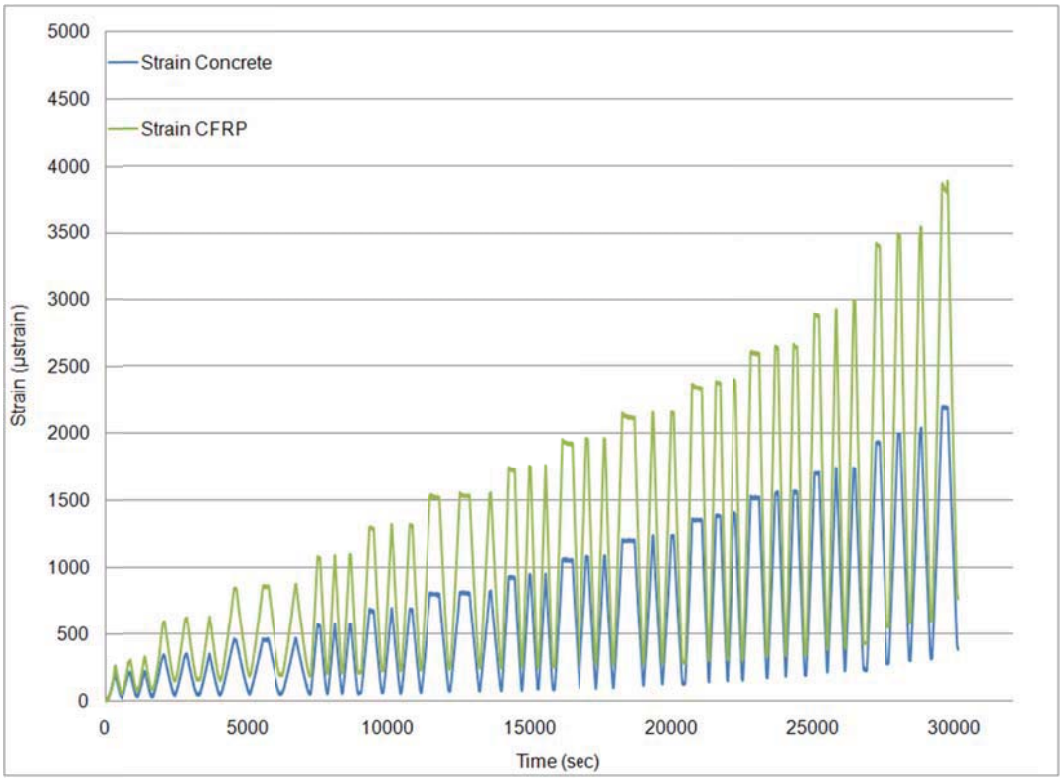

Figure III.G.3a - Strain in time, test B2

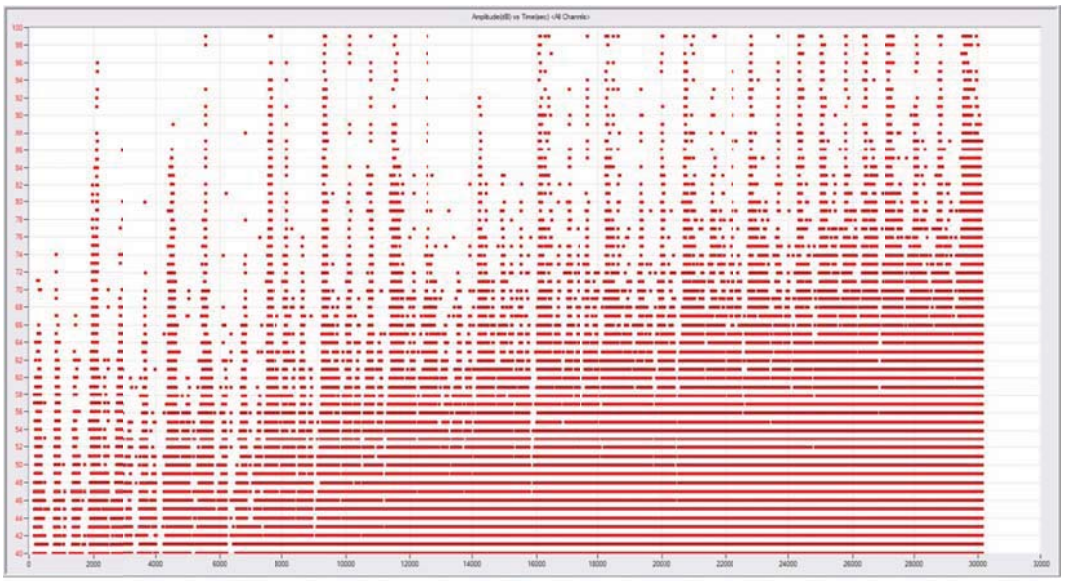

Figure III.G.3b - AE Amplitude (dB) in time, test B2

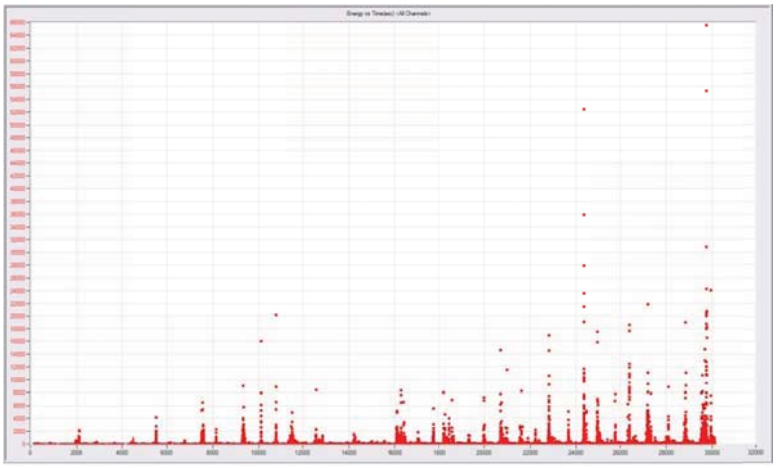

Figure III.G.3c - AE Energy (Joules) in time, test B2

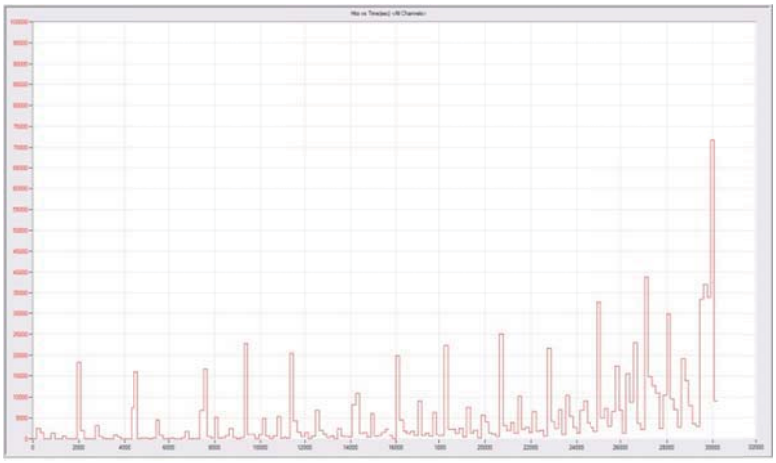

Figure III.G.3d - AE Hits in time, test B2

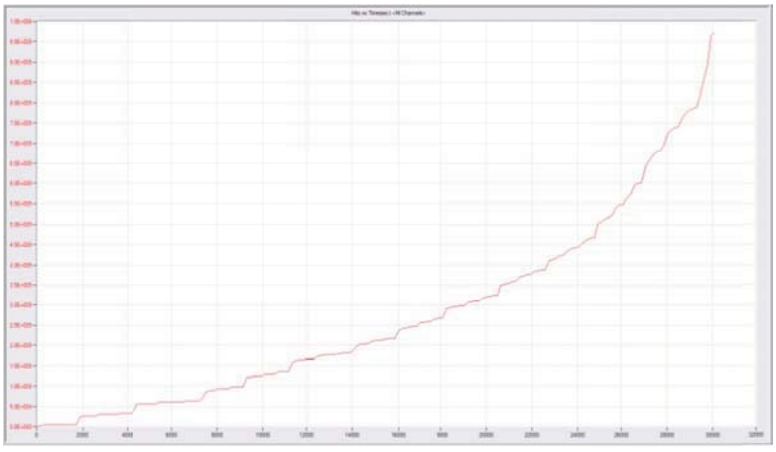

Figure III.G.3e - AE Cumulative Hits in time, test B2